Behaviour of helical anchors subjected to cyclic loadings

José Antonio Schiavon

l'université nantes angers le mans
PÔLE DE RECHERCHE ET D'ENSEIGNEMENT SUPÉRIEUR

USP

ECN Centrale Nantes

Thèse de Doctorat

José Antonio SCHIAVON

Mémoire présenté en vue de l'obtention du
grade de Docteur de l'Ecole Centrale de Nantes
Docteur de la Universidade de São Paulo
sous le label de L'Université Nantes Angers Le Mans

École doctorale : Sciences Pour l'Ingénieur, Géosciences, Architectures

Discipline : Génie Civil
Unité de recherche : ***Institut Français des Sciences et Technologie des Transports de l'Aménagement et des Réseaux***

Soutenue le 30 septembre 2016

Behaviour of helical anchors subjected to cyclic loadings

JURY

Président :	**Márcio ALMEIDA**, Professeur, Universidade Federal do Rio de Janeiro
Rapporteurs :	**Daniel DIAS,** Professeur des universités, Université Grenoble Alpes **Márcio ALMEIDA**, Professeur, Universidade Federal do Rio de Janeiro
Invité(s) :	**Amy CERATO,** Professeur, University of Oklahoma
Directeur de Thèse : Co - directeur de Thèse :	**Luc THOREL,** Directeur de Recherche, IFSTTAR **Cristina TSUHA,** Professeur, Universidade de São Paulo

l'université nantes angers le mans

PÔLE DE RECHERCHE ET D'ENSEIGNEMENT SUPÉRIEUR

Centrale Nantes

Thèse de Doctorat

José Antonio SCHIAVON

Behaviour of helical anchors subjected to cyclic loadings
Comportement des ancrages helicöidaux soumises à des chargements cycliques

Résumé

Les ancrages hélicoïdaux, largement utilisés pour résister à des efforts de traction pour une variété d'applications comme les pylônes électriques, les pipelines, les structures offshore, etc., sont soumis à des chargements cycliques qui influent sur la performance d'ancrage et peuvent induire une rupture par fatigue. Cependant, l'influence des sollicitations cycliques sur le comportement d'ancrage hélicoïdal est mal connue. Une évaluation approfondie de l'effet de charges cycliques sur la réponse effort – déplacement des ancrages avec une seule hélice dans les sols sableux est présentée, incluant un diagramme d'interaction pour aider à évaluer l'impact des différentes conditions de chargement cyclique. La partie expérimentale de cette thèse comprend des essais en centrifugeuse géotechnique et des essais de chargement *in situ*. Les essais en centrifugeuse ont été effectués sur des modèles réduits d'ancrages hélicoïdaux dans du sable, à l'IFSTTAR (Nantes, France). Les essais de chargement *in situ* ont été réalisés sur des ancrages hélicoïdaux installés dans le sol tropical résiduel du site expérimental de l'Université de São Paulo (São Carlos, Brésil). De plus, la modélisation numérique a été utilisée pour prédire les réponses pré et post-cycliques des ancrages d'une hélice testée en centrifugeuse. Les principales conclusions de cette recherche sont: (a) le comportement d'un ancrage hélicoïdal est régi par la capacité portante de l'hélice, et aucune perte de capacité portante d'hélice n'a été observée pour la gamme de charges cycliques testée, (b) la dégradation de la résistance par frottement latéral sur le fut a été remarquée principalement pendant les 100 premiers cycles, lorsque l'accumulation des déplacements permanents est plus importante, (c) un diagramme d'interaction montrant les différentes conditions de stabilité cyclique est proposé à partir des résultats des données expérimentales, (d) des valeurs modifiées du facteur de capacité portante (N_q) sont proposées pour l'estimation de la capacité et post-cyclique des ancrages avec une hélice dans du sable, (e) l'effet de l'installation de l'ancrage doit être pris en compte dans le modèle numérique afin d'obtenir des prédictions fiables de la performance de l'ancrage hélicoïdal.

Mots clés

Ancrages hélicoïdaux, capacité portante en traction, sable, chargement cyclique, modélisation en centrifugeuse, essais de chargement *in situ*, modélisation numérique, sols tropicaux résiduels.

Abstract

Helical anchors, used widely to resist uplift loading for a variety of applications, including in transmission towers, pipelines, offshore structures, etc., are subjected to environmental cyclic loads that influence the anchor performance and may induce fatigue failure. However, the influence of cyclic loading on helical anchor behaviour is unknown. A comprehensive evaluation of the effect of cyclic loading on the load-displacement response of single-helix anchors in sandy soils is presented here, including an interaction diagram to help designers evaluate the impact of different conditions in cyclic loadings. The experimental work of this thesis includes geotechnical centrifuge modelling and field load tests. The centrifuge model tests were carried out with reduced scale models of helical anchors in sand, at IFSTTAR (Nantes, France). The field load tests were performed on helical anchors installed in a tropical residual soil of the Experimental Site of the University of São Paulo (São Carlos, Brazil). In addition, numerical modelling was used to predict the pre- and post-cyclic responses of the single-helix anchors tested in a centrifuge. The main findings of this research are: (a) helical anchor behaviour is governed by helix bearing resistance, and no loss of helix bearing capacity was observed in the range of cyclic loadings tested, (b) the degradation of shaft resistance was noticed mainly during the first 100 cycles, when the accumulation of permanent displacements is more significant, (c) an interaction diagram showing the different conditions of cyclic stability is proposed from the results of the experimental data, (d) modified values of the bearing capacity factor in tension (N_q) are suggested for the estimation of post-cyclic uplift capacity of single-helix anchors in sand, (e) the installation effect of the anchor should be taken into account in the numerical model in order to obtain reliable predictions of the helical anchor performance.

Key Words

Helical anchors, uplift capacity, sand, cyclic loading, centrifuge modelling, field load tests, numerical modelling, tropical residual soil.

Dedicated to my parents.

Acknowledgements

I would like to express deep gratitude to Professor Cristina Tsuha for believing in me and for giving me the opportunity to conduct this study. I only have to thank her for all that I have learned on work, scientific methodology, analysing, reasoning and writing. Without her guidance, encouragement, enthusiasm and support, this research would not have happened. I would also thank her for all the efforts made to materialize the Brazilian-French joint supervision of this thesis.

I thank Professor Luc Thorel, not only for co-supervising this research, but for the invaluable experience shared while I was a visiting student at IFSTTAR, and for the trips to Brazil to organize this research. I appreciate the discussions, suggestions, collaborations with this research and also the efforts made during all the process to conclude the joint supervision process.

I would like to thank all the professors of the Department of Geotechnical Engineering of the University of São Paulo, especially to Prof. Cintra and Prof. Orencio. I would also like to thank all the technicians and staff of the Department of Geotechnical Engineering of the University of São Paulo: Oscar, Zé Luiz, Dito, Antonio, Décio, Clever, Maristela, Neiva, Álvaro, Herivelto and Toninho.

I would like to thank to Mathieu Blanc, Alberto Bretschneider and Sandra Escoffier for the agreeable fellowship during my stay at IFSTTAR. I am greatly thankful to the IFSTTAR Centrifuge Team: Patrick, Alain, Philippe, Stéphane, Damien and Claude. These guys are awesome!

I thank to Prof. Daniel Dias and Prof. Marcio Almeida who accepted to be the rapporteurs of this thesis. I appreciate the evaluations and suggestions made by these Professors. I would also like to thank the evaluation and suggestions made by Prof. Nelson Aoki during the qualifying exam. I also appreciate the help of Prof. Christophe Dano with triaxial tests and tomography performed at the Ecole Centrale de Nantes.

I acknowledge the financial support provided by the program USP-COFECUB grant No. UcMa 132/12, by the Brazilian Agency CAPES (Ministry of Education) and by the French Institute of Science and Technology for Transport, Development and Networks (IFSTTAR), France.

I thank to Vercon Industrial and Vértice Engenharia by providing the material, staff and equipment to carry out the field tests.

Special thanks to my friends who accompanied me during my doctoral research in USP/Brazil (especially to João, Thaise, Diego, Milena, Luis Neto, Philippe, Roberto and Zorany) and in France (especially to Mathieu P., Catalina, Milia, Prof. Ana Furlan, Yingjie, Xiaoting and Peter).

A loving thanks to my wife Karen, my parents, brother, sister, sisters-in-law, brothers-in-law and parents-in-law, who always supported and encouraged me.

ABSTRACT

SCHIAVON, J.A. **Behaviour of helical anchors subjected to cyclic loadings**. 2016. 300 p. Doctoral Thesis under joint supervision between the University of Sao Paulo and Nantes Angers and Le Mans University, Sao Paulo, Sao Carlos, SP, 2016.

Helical anchors, used widely to resist uplift loading for a variety of applications, including in transmission towers, pipelines, offshore structures, etc., are subjected to environmental cyclic loads that influence the anchor performance and may induce fatigue failure. However, the influence of cyclic loading on helical anchor behaviour is unknown. A comprehensive evaluation of the effect of cyclic loading on the load-displacement response of single-helix anchors in sandy soils is presented here, including an interaction diagram to help designers evaluate the impact of different conditions in cyclic loadings. The experimental work of this thesis includes geotechnical centrifuge modelling and field load tests. The centrifuge model tests were carried out with reduced scale models of helical anchors in sand, at IFSTTAR (Nantes, France). The field load tests were performed on helical anchors installed in a tropical residual soil of the Experimental Site of the University of São Paulo (São Carlos, Brazil). In addition, numerical modelling was used to predict the pre- and post-cyclic responses of the single-helix anchors tested in a centrifuge. The main findings of this research are: (a) helical anchor behaviour is governed by helix bearing resistance, and no loss of helix bearing capacity was observed in the range of cyclic loadings tested, (b) the degradation of shaft resistance was noticed mainly during the first 100 cycles, when the accumulation of permanent displacements is more significant, (c) an interaction diagram showing the different conditions of cyclic stability is proposed from the results of the experimental data, (d) modified values of the bearing capacity factor in tension (N_q) are suggested for the estimation of post-cyclic uplift capacity of single-helix anchors in sand, (e)

the installation effect of the anchor should be taken into account in the numerical model in order to obtain reliable predictions of the helical anchor performance.

Key Words

Helical anchors, uplift capacity, sand, cyclic loading, centrifuge modelling, field load tests, numerical modelling, tropical residual soil.

RESUMO

SCHIAVON, J.A. **Comportamento de ancoragens helicoidais submetidas a carregamentos cíclicos**. 2016. 300 p. Tese de Doutorado em cotutela entre a Universidade de São Paulo e a Universidade Nantes Angers e Le Mans, São Paulo, São Carlos, SP, 2016.

As estacas helicoidais são largamente utilizadas para resistir a carregamentos de tração em uma variedade de aplicações como torres de linhas de transmissão de energia, dutos enterrados, estruturas *offshore*, etc. Estes tipos de estruturas são normalmente submetidos a carregamentos cíclicos que influenciam o desempenho de fundações por estacas helicoidais submetidas a esforços de tração, e podem induzir ruptura por degradação da capacidade de carga. Contudo, a influência do carregamento cíclico no comportamento das estacas helicoidais (ou ancoragens helicoidais, quando submetidas apenas a esforços de tração) é pouco conhecida. Uma avaliação abrangente do efeito de carregamentos cíclicos sobre o comportamento das ancoragens helicoidais é apresentada nesta tese, incluindo um diagrama de interação para auxiliar na avaliação do impacto de diferentes condições de carregamento cíclico. O trabalho experimental desta tese inclui modelagem em centrífuga geotécnica e ensaios de carregamento cíclico em estacas na grandeza real em campo. Os ensaios em centrífuga foram realizados com modelos reduzidos de estacas helicoidais em areia, no IFSTTAR (Nantes, França). Os ensaios de campo foram realizados em ancoragens helicoidais instaladas no solo residual tropical do Campo Experimental de Fundações da Universidade de São Paulo (São Carlos, Brasil). Além disso, modelos numéricos foram utilizados para simular os resultados do comportamento das ancoragens helicoidais ensaiadas em centrífuga nas condições pré- e pós-ciclos. Os principais resultados desta pesquisa são: (a) a capacidade de carga à tração da ancoragem helicoidal é controlada pela capacidade de carga da hélice, (b) a degradação da resistência por atrito lateral foi observada principalmente durante os primeiros

100 ciclos, período em que a acumulação dos deslocamentos permanentes é mais significante, (c) um diagrama de interação mostrando as diferentes condições de estabilidade cíclica é proposto a partir dos resultados experimentais em centrífuga, (d) valores modificados do fator de capacidade de carga em tração (N_q) são sugeridos para estimativa da capacidade pós-ciclos de ancoragens helicoidais com uma hélice em areia, (e) o efeito da instalação da ancoragem deve ser levado em consideração no modelo numérico para que se obtenha previsões confiáveis do desempenho de ancoragens helicoidais.

Palavras-chave

Ancoragens helicoidais, capacidade de carga à tração, areias, carregamento cíclico, modelagem física em centrífuga, provas de carga, modelagem numérica, solo residual tropical.

RESUME

SCHIAVON, J.A. **Comportement des ancrages helicöidaux soumises à des chargements cycliques**. 2016. 300 p. Thèse de Doctorat en cotutelle entre l'Université de Sao Paulo et l'Université Nantes Angers Le Mans, Sao Paulo, Sao Carlos, SP, 2016.

Les ancrages hélicoïdaux, largement utilisés pour résister à des efforts de traction pour une variété d'applications comme les pylônes électriques, les pipelines, les structures offshore, etc., sont soumis à des chargements cycliques qui influent sur la performance d'ancrage et peuvent induire une rupture par fatigue. Cependant, l'influence des sollicitations cycliques sur le comportement d'ancrage hélicoïdal est mal connue. Une évaluation approfondie de l'effet de charges cycliques sur la réponse effort – déplacement des ancrages avec une seule hélice dans les sols sableux est présentée, incluant un diagramme d'interaction pour aider à évaluer l'impact des différentes conditions de chargement cyclique. La partie expérimentale de cette thèse comprend des essais en centrifugeuse géotechnique et des essais de chargement *in situ*. Les essais en centrifugeuse ont été effectués sur des modèles réduits d'ancrages hélicoïdaux dans du sable, à l'IFSTTAR (Nantes, France). Les essais de chargement *in situ* ont été réalisés sur des ancrages hélicoïdaux installés dans le sol tropical résiduel du site expérimental de l'Université de São Paulo (São Carlos, Brésil). De plus, la modélisation numérique a été utilisée pour prédire les réponses pré et post-cycliques des ancrages d'une hélice testée en centrifugeuse. Les principales conclusions de cette recherche sont: (a) le comportement d'un ancrage hélicoïdal est régi par la capacité portante de l'hélice, et aucune perte de capacité portante d'hélice n'a été observée pour la gamme de charges cycliques testée, (b) la dégradation de la résistance par frottement latéral sur le fut a été remarquée principalement pendant les 100 premiers cycles, lorsque l'accumulation des déplacements permanents est plus importante, (c) un diagramme d'interaction montrant les différentes conditions de stabilité

cyclique est proposé à partir des résultats des données expérimentales, (d) des valeurs modifiées du facteur de capacité portante (N_q) sont proposées pour l'estimation de la capacité et post-cyclique des ancrages avec une hélice dans du sable, (e) l'effet de l'installation de l'ancrage doit être pris en compte dans le modèle numérique afin d'obtenir des prédictions fiables de la performance de l'ancrage hélicoïdal.

Mots-clés

Ancrages hélicoïdaux, capacité portante en traction, sable, chargement cyclique, modélisation en centrifugeuse, essais de chargement *in situ*, modélisation numérique, sols tropicaux résiduels.

TABLE OF CONTENTS

Notations and Abbreviations

EESC is the São Carlos School of Engineering

IFSTTAR is the French Institute of Science and Technology for Transport, Development and Networks

USP is the University of São Paulo

c is the soil cohesion

d is the shaft diameter

d_{50} is the average grain-size

e_{max} is the maximum void ratio

e_{min} is the minimum void ratio

f is the cyclic loading frequency

f_s is the skin friction resistance

k is the anchor axial stiffness

$k_{(N=1)}$ is the anchor axial stiffness at the 1st cycle

p is the helix pitch

t_h is the helical plate thickness

w is the effective helical radius

z_D is the helix embedment depth

A_h is the helix net area

A_s is the effective shaft surface area

B is the square plate width

C_u is the coefficient of uniformity

D is the regular plate or helical plate diameter

$D_{lower\ helix}$ is the diameter of the lower helical plate of a multi-helix anchor

$D_{upper\ helix}$ is the diameter of the upper helical plate of a multi-helix anchor

G_s is the specific gravity of the sand particles

I_D is the sand density index

K_u is the lateral earth pressure coefficient in uplift

N is the number of cycles

N_f is the number of cycles to failure

N_q is the bearing capacity factor

$N_{q\text{-}pc}$ is the post-cyclic helix bearing capacity factor

Q is the tensile load on the anchor head

$Q_{applied}$ is the tension force applied on the anchor head

Q_{cyclic} is the axial cyclic load amplitude

Q_{helix} is the tension force registered by the force gauge above the helix

Q_{max} is the maximum cyclic load

Q_{mean} is the mean axial cyclic load

Q_{min} is the minimum cyclic load

Q_{pre} is the tension force applied on the anchor head that simulates the field pre-cyclic load

Q_{shaft} is the shaft friction resistance

Q_T is the ultimate tensile load

Q_{T1} is the ultimate tensile load obtained from the 1st monotonic tension load test

Q_{TN} is the ultimate tensile load obtained from the Nth monotonic tension load test

$Q_{T\text{-}pc}$ is the post-cyclic ultimate tensile load

$Q_{T\ (0.1D)}$ is the assumed tensile capacity for an uplift displacement of 10%D

$Q_{T\ (peak)}$ is the peak tensile capacity

R_{max} is the maximum surface roughness

T is the period of the cyclic loading

$T_{avg\text{-}3D}$ is the average torque for the final distance of penetration equal to three times the helix diameter

T_f is the final installation torque

T_{helix} is the resistant torque acting on the helical plates

T_{shaft} is the torque generated by the contact between soil and pile shaft in the final of installation

U is the vertical displacement

U_{acc} is the accumulated vertical displacement

$U_{(peak)}$ is the vertical displacement at the peak force value

δ is the interface friction angle

ϕ is the soil friction angle

γ is the soil unity weight

γ' is the soil effective unity weight

γ_d is the dry unity weight

$\gamma_{d(max)}$ is the maximum dry unity weight

$\gamma_{d(min)}$ is the minimum dry unity weight

$\gamma_{d(avg)}$ is the average unity weight of the sand samples

$\rho_{d(max)}$ is the maximum dry density

$\rho_{d(min)}$ is the minimum dry density

$\rho_{d(avg)}$ is the average dry density of sand samples

1. INTRODUCTION

Helical anchors have been widely used as foundation of power transmission towers in many countries. In Brazil, the use of helical anchors in the electrical power industry has increased markedly in recent years.

This type of foundation is normally used to support structures, such as transmission towers, submerged pipelines, decks, offshore constructions, wind farms, etc. In these cases, the helical anchors are subjected to a series of loading and unloading cycles during their service life. These cyclic loadings change the soil conditions close to the anchor, and consequently affect the helical anchor behaviour.

However, despite the increasing use of helical foundations in the aforementioned applications, there are no studies that investigate and propose procedures to estimate the influence of cyclic loadings on helical anchor behaviour. In addition, there is no design instruction for the prediction of helical foundations' responses under cyclic loadings.

In investigations about the behaviour of conventional piles under tension cyclic loading, the cyclic response has been classified based on the displacement accumulation and on the degradation of shaft resistance. For high amplitude tension cyclic loadings, few cycles are sufficient to cause complete pile skin friction degradation and failure under tensile loading. On the other hand, in cases of compression cyclic loadings with low cyclic amplitudes, a densification of the soil below the pile tip is observed, that causes an increase in pile capacity mainly due to a gain in base resistance.

The cyclic response of foundations or anchors depends on the characteristics of the cyclic loading, soil type and installation process.

In the case of helical anchors, the cyclic response is composed of two distinct parts: shaft resistance response and helix bearing response. As the soil around the anchor is sheared and displaced (loosened) during installation, a tensile cyclic loading is supposed to cause the

densification of the soil above the helix, consequently improving the helix bearing response during static loading. However, the shaft resistance may degrades faster compared to conventional piles, since the soil around the anchor shaft is disturbed by the installation process and is in a less dense condition. Therefore, to address these questions, the study reported here is focused on the behaviour of single-helix anchors subjected to tensile cyclic loadings.

The main motivations of this thesis are to contribute to the current unsatisfactory understanding of helical foundations behaviour and to help foundation designers predict helical anchors cyclic response, as the construction of guyed towers for Brazilian power transmission lines is increasing rapidly.

1.1. Objectives

Considering the need for a better understanding of the behaviour of helical anchors under cyclic loading, the main objective of the research reported here is to evaluate the effects of different combinations of cyclic loadings and of the number of cycles on the accumulation of anchor displacement and on the uplift capacity of single-helix anchors in sand.

1.1.1. Secondary objectives

- Evaluate the scale effects on the prototype results of the physical modelling of helical anchors in sand;

- Evaluate the contribution of shaft resistance to the uplift capacity of single-helix anchors;

- Verify the influence of the soil disturbance caused by the installation process on the cyclic behaviour of helical anchors in sand and in residual tropical soil;

- Development of numerical modelling to simulate the pre- and post-cyclic helical anchor response considering the soil disturbance caused by the installation process.

1.1.2. Justification

The fact that a large amount of helical foundations has been employed to support cyclic loadings of power transmission towers, added to the fact that the installation process of helical anchors causes soil disturbance, which directly affects the anchor's capacity and stiffness, indicates that it is necessary to understand in detail the performance of helical foundations under cyclic loadings.

1.2. Thesis organization

- Chapter 1 shows the motivations and the objectives of this thesis
- Chapter 2 provides background information on the principal topics involved in this research. The failure mechanism of single-helix anchors under tension is briefly discussed as well as the effects of the helical anchor installation on the anchor capacity. The physical phenomena that influences the behaviour of foundations under cyclic loading is also included in a literature review about previous research on foundations under cyclic loading. Additionally, a brief description of centrifuge physical model tests and the scale effects that can affect the modelling results is presented.
- Chapter 3 presents the materials and methods employed in this work. This chapter is subdivided into three sections: centrifuge modelling, field experiments and numerical modelling.
- Chapter 4 presents and discusses the experimental and numerical results. This part is subdivided into three sections.

- Chapter 5 offers propositions to guide the prediction of the cyclic loading response of single-helix anchors in sand. In this chapter, Interaction Diagrams, recommendations concerning the numerical modelling of helical anchors, and equations to predict the cyclic accumulated displacement in sand are presented. In addition, values of post-cyclic bearing factors ($N_{q\text{-}pc}$) are proposed for the calculation of the post-cyclic uplift capacity of helical anchors in sand. Also, the results of post-cyclic bearing factors ($N_{q\text{-}pc}$) are compared to the pre-cyclic bearing factors (N_q).
- Chapter 6 presents the main conclusions of the thesis and suggestions for future research on this subject.

2. LITERATURE REVIEW

2.1. Helical anchors

Helical anchors have been employed as foundations of structures subjected to vertical and horizontal actions (Figure 1b to 1e). In Brazil, this type of foundation has normally been used as a foundation for towers for power transmission lines, as guyed masts and self-supporting towers.

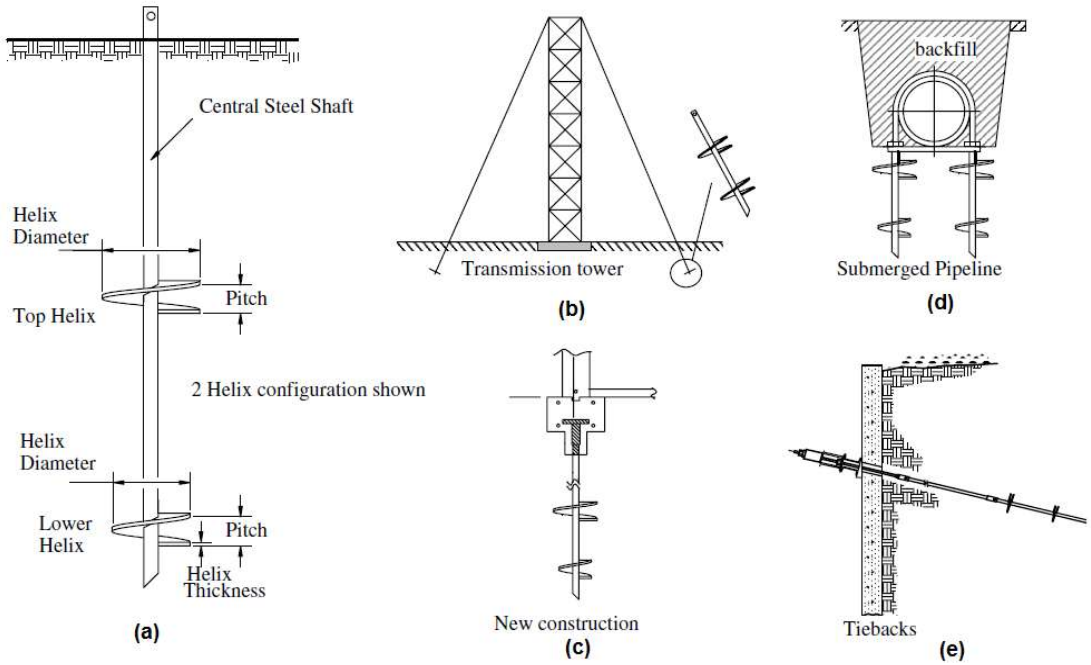

Figure 1. (a) helical anchor configuration; (b), (c), (d), and (e) the use of helical anchors as anchors (Merifield, 2011).

A helical anchor consists of a steel shaft with a tubular or square cross-section, with one or more helical plates welded along the shaft (Figure 1a). The number of helical plates depends on the soil conditions and on the required capacity. These anchors are installed into the soil by means of torque application to the upper end of the shaft by mechanical means (Figure 2). Initially, together with torque effort, a downward force is applied to assist in the advancement of installation. This downward force must be sufficient to ensure that the anchor advances into the ground with a feed rate of 80 to 100% of the helix pitch. Insufficient force

leads to a lower advance rate which can cause augering and affects the anchor uplift capacity (Perko H. , 2000).

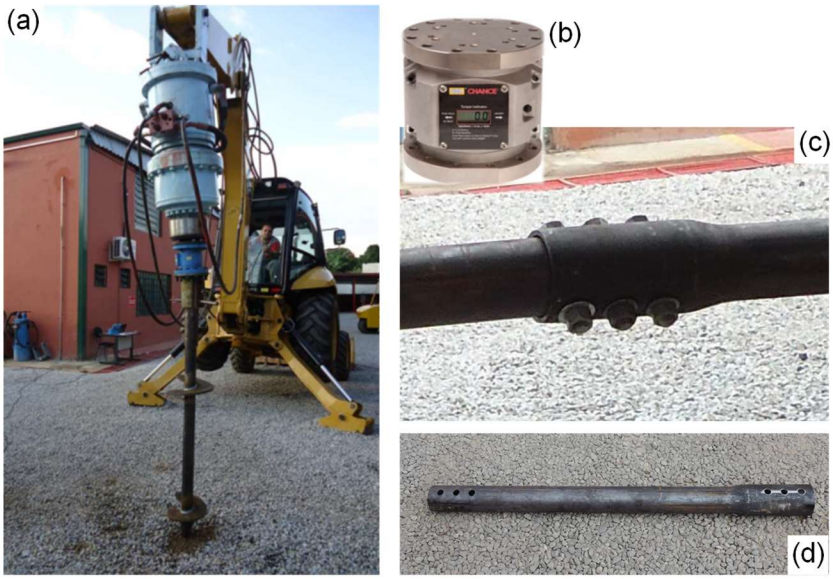

Figure 2. (a) installation equipment, after Schiavon *et al.* (2015); (b) torquemeter, after AB Chance Co. (2013); (c) coupling between extension segments, after Santos Filho (2014); (d) extension segment (own author).

According to various researchers (Hoyt & Clemence, 1989; Narasimha Rao *et al.*, 1989; Ghaly & Hanna, 1991; Ghaly *et al.*, 1991; Perko, 2000; Tsuha & Aoki, 2010; Sakr, 2014), the uplift capacity of helical anchors can be correlated with the final installation torque. The torque measured at the end of installation (final penetration corresponding to 3 helix diameters) represents an indirect strength measure of sheared soil by helices (Hoyt & Clemence, 1989). The installation of the helical anchor is supposed to finish when the installation torque reaches the design value.

Perko *et al.* (2000) list the main advantages of helical anchors compared to other types of foundation:

- The uplift capacity can be estimated using the installation torque;
- The anchors are removable and can be reused;
- Easy transportation to places difficult to access, compared to concrete;

- Can be installed under the water table;
- Less time to be installed compared to other types of deep foundation;
- Can be installed with small equipment in inaccessible places;
- Noise and vibration during installation are minimal;
- Can be galvanized to resist corrosion;
- There is no need for concrete moulds;
- This pile can be loaded immediately after installation;
- There is no soil residue;
- It is less harmful to the environment.

Perko (2009) reported that there are over 50 helical anchor manufacturing companies in at least twelve countries on four continents, and in the United States there are over 2000 installation contractors. Brazil is among such manufacturing countries, where companies have been installing helical anchors for nearly 15 years in Brazilian territory, primarily used as anchors of guyed masts and foundations of self-supporting towers (Tsuha C. , 2007). These types of structures are subject to a series of loading and unloading cycles of variable load amplitudes, mainly due to environmental changes. In this case, the helical anchors should support cyclic loadings which largely depend on variation in wind force. Also, in the case of guyed towers, the cycles of temperature variation can cause length variation in electrical conductors and guy cables, and consequently cause variation in uplift loading. These cyclic loadings modify the stress condition in the soil mass close to the pile, and consequently change the helical anchor tensile and compressive capacities.

2.1.1. Behaviour of helical anchor foundations under uplift axial loading

When conventional piles are subjected to tensile loads, the pile capacity depends on the shear resistance at the interface pile-soil (shaft resistance). However, the failure mechanism of helical anchors under tensile loading differs from the mechanism of conventional piles (cylindrical shape) mainly because: 1) generally the helix bearing resistance is more important than the shaft resistance, 2) the soil around the shaft is significantly disturbed by the helix penetration during installation.

2.1.1.1. Effects of helical anchor installation

During helical anchor installation, the soil around the shaft is traversed and disturbed by the passage of the helices (shearing and displacing the soil laterally and vertically), and consequently some characteristics of the soil are modified and the shaft resistance is affected.

Helical anchor installation disturbs the soil structure and changes the stresses in the soil mass above the helical plates. Tsuha *et al*. (2012a) observed a considerable influence of the different degrees of disturbance of sand penetrated one, two or three times by the helical plate. However, for the anchor installed in loose sand, the final state of the sand above each one of the three helices was similar. The hypothesis explaining the effect of sand density is illustrated in Figure 3.

The different shades of grey in Figure 3 identify two different groups of sand condition: initial state of undisturbed sand and the final state of a sand mass penetrated by the helices. In Figure 3b, the different shades of grey correspond to four different groups of sand condition, which vary with the number of helical plates that penetrate through a particular zone of soil.

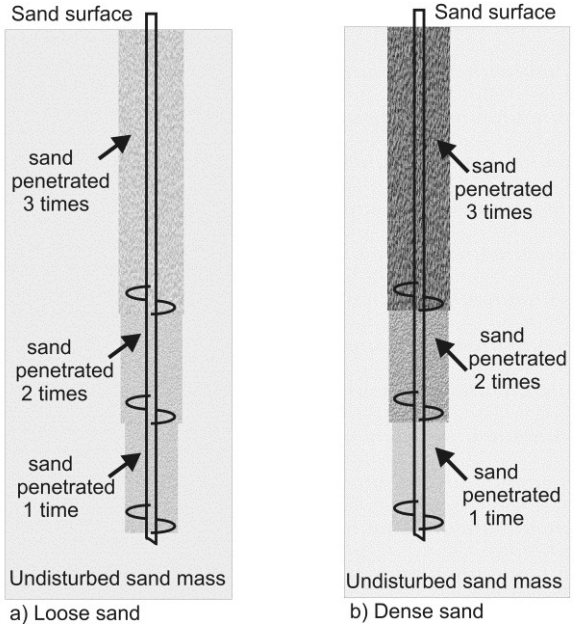

Figure 3. Hypothesis for sand disturbance after installation of a three-helix anchor: (a) loose sand; (b) dense sand (Tsuha C. , Aoki, Rault, Thorel, & Garnier, 2012a).

The movement of soil particles around a helical plate during the installation of a helical anchor was verified with a video by Kanai (2007). The author observed that the soil at the lower edge of the helical plate starts moving towards the upper edge of the plate during anchor penetration. Figure 4 illustrates the mechanism observed.

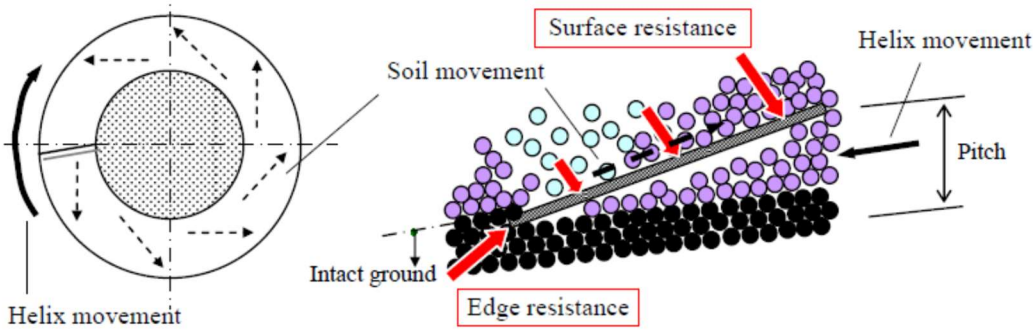

Figure 4. Model for the movement of soil particles around a helical plate during installation, after Kanai (2007).

Komatsu (2007) carried out model tests on a small scale helical anchor (shaft of 40 mm diameter and 80 mm of helix diameter) in a cylindrical testing vessel to examine the effect of the anchor installation on soil. In Figure 5, the displacement of the soil mass can be visualized

after the installation of a single-helix model anchor. This author observed the following: (i) the soil above the blade of the pile rises upwards, (ii) the soil close to the pile shaft is pulled down due to the shaft friction, and (iii) the soil beneath the blade is compressed.

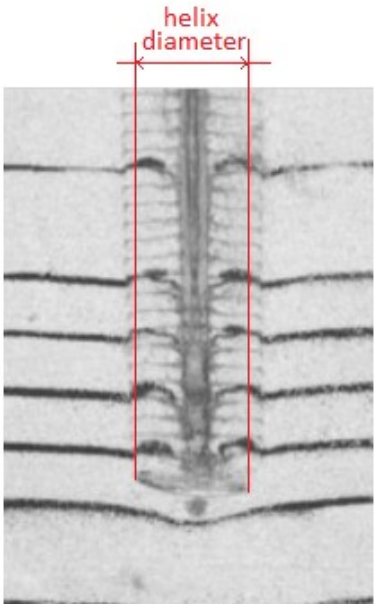

Figure 5. Model anchor (one-helix) installed in sand, after Komatsu (2007) – adapted.

Kulhawy (1985) mentioned that significant disturbance does occur within the cylindrical installation zone of the helical anchor, and the disturbance effect can be approximated by relating the disturbed properties to the in-situ soil properties. For the prediction of the anchor uplift capacity, Kulhawy recommended considering the disturbance effect on the shearing resistance along the disturbed cylinder.

A large increase in lateral stress around a helical anchor model was observed by Clemence and Pepe (1984) after installations in dense soils. When the anchor was loaded to failure the lateral stress increased further. The authors attributed this increase to arching stresses and soil dilatant behaviour developed when the anchor traversed and sheared the soil.

Concerning the effect of installation on the shaft resistance of piles, Vesic (1970) observed a reduction in the shear stresses mobilized along the shaft at a given depth in the ground as the pile tip penetrates further. This behaviour has been referred to as “friction

fatigue" (Heerema, 1978). During pile driving, the friction experienced by the pile shaft is presumed as large in the beginning and decreases gradually because of the abrasion between soil grains and shaft surface while the pile moves down due to the driving. The gradual decrease of shaft skin friction is a consequence of horizontal stress decrease of the surrounding soil. White and Bolton (2004) observed that soil particles had broken in the interface zone adjacent to the pile shaft models when high stresses were generated below the model base, causing high irretrievable volume reduction. While the shearing along the pile-soil interface proceeds, this zone tends to exhibit further contraction, leading to a mechanism of shaft friction degradation.

2.1.1.2. Helical anchor uplift capacity

The behaviour of single-helix anchors is dependent on the helix embedment depth. When the helical anchors are installed with the helix at shallow depths, a significant soil movement at the ground surface is observed at failure (shallow anchor behaviour).

Figure 6 presents the schemes of the failure surfaces in tests on multi-helix model anchors observed by Mitsch and Clemence (1985). Although these experiments have been carried out on multi-helix anchors, the mechanism of shallow anchor failure is clearly illustrated in the zone above the top helix in Figure 6a. In this situation, the anchor's capacity depends considerably on the depth of the top helix and the load is transmitted to the ground exclusively by the helices (Trofimenkov & Mariupolskii, 1964; Ghaly *et al.*, 1991; Clemence *et al*., 1994). The shallow anchor behaviour occurs until a certain critical helix embedment depth. When the helix depth exceeds this critical value (H_{cr}), the soil movement in the ground surface is not observed (deep anchor behaviour). In this case, the soil mobilization occurs in the zone around the helix (Figure 6b). The uplift capacity of helical anchors is dependent on

the helix depth, and the load is transmitted to the soil by the helix and shaft (Trofimenkov & Mariupolskii, 1964; Ghaly *et al*., 1991; Clemence *et al*., 1994; Tsuha & Aoki, 2010).

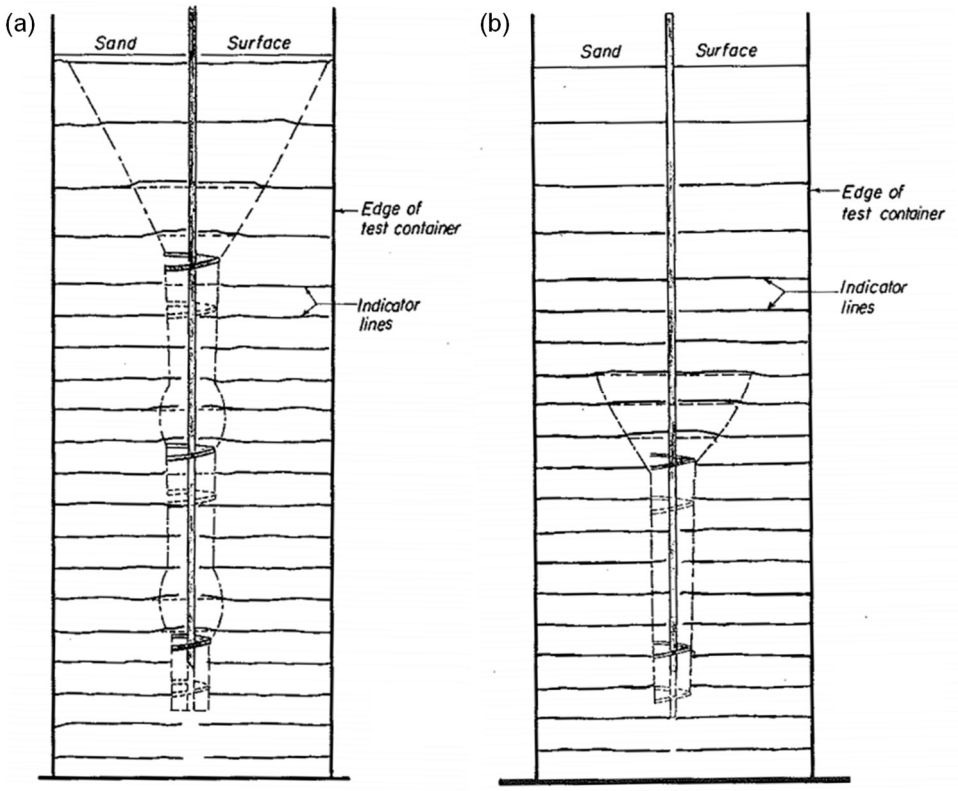

Figure 6. Failure surface in multi-helix model anchors, after Mitsch and Clemence (1985): (a) shallow top helix; (b) deep top helix.

The methods for the prediction of the helical anchor uplift capacity consist of theoretical approaches or empirical relationships. The most common theoretical methods are based on limit state analysis; such methods assume the individual bearing resistances of the helices. Theoretical methods based on the cylindrical shear model, which assumes that a cylindrical failure surface is mobilized between the top and the bottom helices (Figure 6), are not discussed in this document, since the current study is focused on the behaviour of single helix anchors.

In practice, these theoretical methods are used to define the dimensions of helical anchors, such as the quantity and diameter of helical plates and the shaft (Perko H. , 2009).

Perko *et al.* (2000) suggest that, when possible, engineers' decisions should be based on these methods in conjunction with installation torque measurements.

2.1.1.3. Individual bearing method: helix bearing and shaft resistances

According to Trofimenkov and Mariupolskii (1964), the value of the critical helix depth (H_{cr}) for the characterization of shallow and deep anchor behaviour is around 4-5 times the helix diameter (D). Healy (1971) found values of the critical depth equal to 5D. Various authors have evaluated the value of the critical helix depth of anchors.

Mitsch and Clemence (1985) reported a critical embedment ratio value of 5D for helical anchors in sand with relative density (D_r) between 44 and 90%. Trofimenkov and Mariupolskii (1964) and Vesic (1971) argue that the critical embedment ratio depends on the soil shear strength. Figure 7 presents the values of critical helix depth suggested by Das (1990).

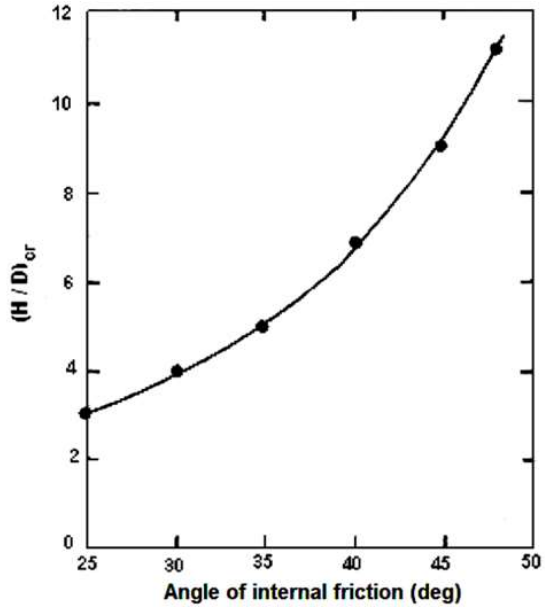

Angle of internal friction (deg)	$(H / D)_{cr}$
25	3
30	4
35	5
40	7
45	9
48	11

Figure 7. Critical embedment depth a function of the angle of internal friction of soil, after Das (1990).

Ghaly *et al.* (1991) proposed values for the critical helix depth depending on the angle of friction and on the helix diameter. Hanna *et al.* (2007) proposed the existence of a

transition zone between deep and shallow behaviour. Hanna *et al.* (2007) used Ghaly's *et al.* (1991) criterion to delineate the lower bound for deep anchors and added a transition zone, as observed in Figure 8. The limits proposed by Hanna *et al.* (2007) are expressed in Eq. 1 and Eq. 2.

$$H < H_{cr} = D(0.4\phi' - 5) \quad \text{(for shallow anchors)} \qquad \text{Eq. 1}$$

$$H > D(0.4\phi' - 3) \quad \text{(for deep anchors)} \qquad \text{Eq. 2}$$

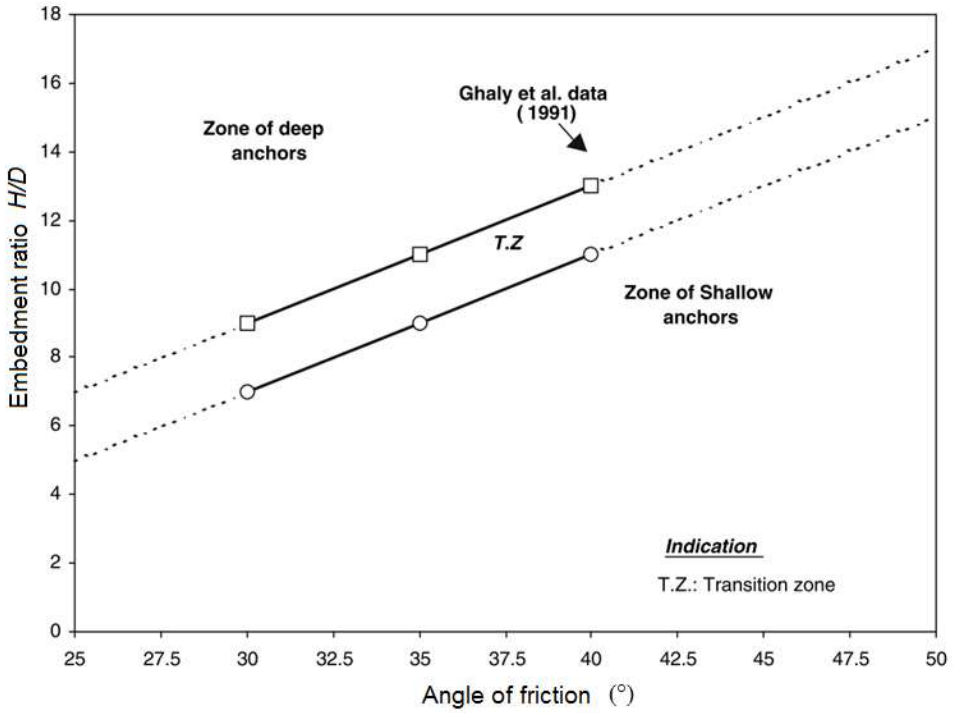

Figure 8. Variation of critical depth with angle of friction and helical plate diameter, after Hanna *et al.* (2007).

Trofimenkov and Mariupolskii (1964) were the first authors to present a formula (Eq. 3) expressing the uplift helix bearing capacity of a helical anchor as a function of dimensionless capacity factors (similar to Terzaghi's bearing capacity equation).

$$q_{ult} = Ac + B\gamma' z_D \quad \text{Eq. 3}$$

where,

q_{ult} is the ultimate bearing pressure;

c is the soil cohesion;

A and B are bearing capacity dimensionless factors (Figure 9);

γ' is the soil unity weight;

z_D is the helix embedment depth.

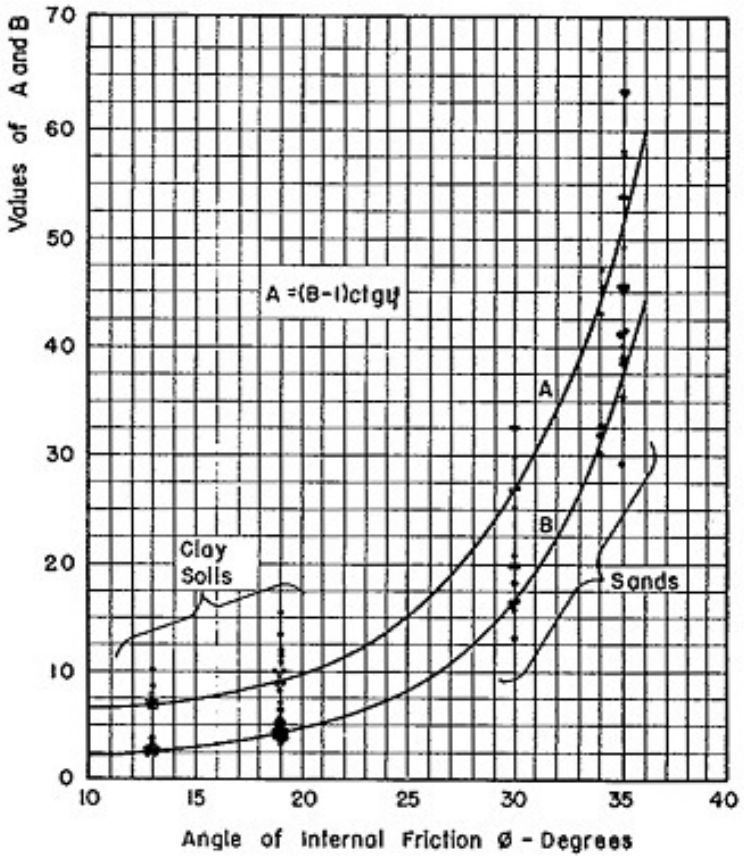

Figure 9. Bearing capacity factors for helical anchors, after Trofimenkov and Mariupolskii (1964).

Mitsch and Clemence (1985) grouped experimental results of uplift tests on plate anchors and helical anchors, from various authors and presented values of uplift capacity factor (N_q) for helical anchors in sand (Figure 10). Thus, the helix bearing capacity can be given by Eq. 4.

$$q_{ult} = \gamma' \times z_D \times N_q \qquad \text{Eq. 4}$$

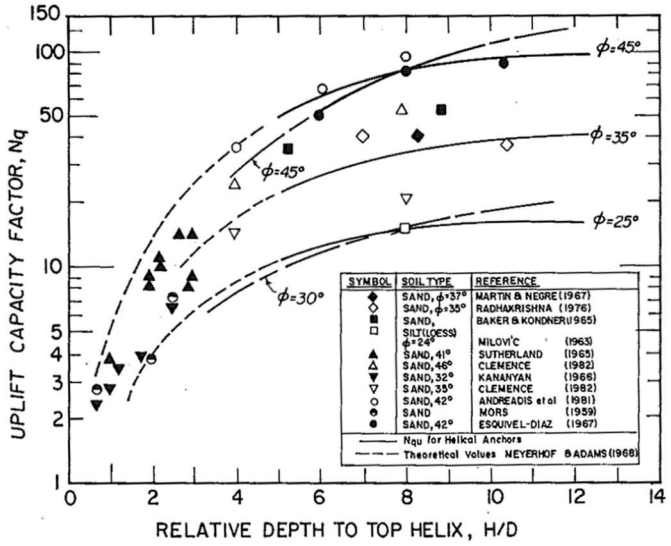

Figure 10. Bearing capacity factors for helical anchors in sand, after Mitsch and Clemence (1985) – adapted.

For deep behaviour helical anchors, Mitsch and Clemence (1985) propose to determine the shaft friction resistance based on the theoretical expression proposed by Tomlinson (1971) for shaft resistance of piles in sand (Eq. 5). For helical anchors, Mitsch and Clemence (1985) presented values for the lateral earth pressure coefficient in uplift (Table 1).

$$f_s = \bar{q} K_u \tan\delta \qquad \text{Eq. 5}$$

where,

$\bar{q}$ is the effective average (or mid-height) vertical stress $\gamma' z_i$ on the element of the shaft length ΔL;

γ' is effective unit weight of soil;

z_i is the ground depth i;

K_u is the lateral earth pressure coefficient in uplift (see Table 1);

δ is the interface friction angle.

Table 1. K_u values recommended by Mitsch and Clemence (1985).

Angle of internal friction of soil (º)	K_u recommended values for helical anchors
25	0.70
30	0.90
35	1.50
40	2.35
45	3.20

Therefore, the uplift capacity of a single helix anchor can be expressed by the combination of the helix bearing resistance with the shaft resistance as presented in Eq. 6.

$$Q_T = q_{ult} \times A_h + \sum_{1}^{n} \left(f_s \times A_s \right) \quad \text{Eq. 6}$$

where,

A_h is the helix net area $(D^2 - d^2)\times\pi/4$;

A_s is effective shaft surface area of each shaft segment with ΔL length on which f_s acts, and n is the number of shaft segments.

2.2. Foundations subjected to cyclic axial loadings

Over time, some structures are subjected to different types of actions of varying magnitude. Transmission towers, chimneys and other tall structures are submitted to a series of loading and unloading cycles due to wind action. Offshore platforms are structures subjected to wave action, characterized as a load which fluctuates during the structure's service life. Thus, foundations are required to support these cyclic loadings. However, foundation behaviour under cyclic loadings differs from monotonic behaviour.

A quasi-static cyclic loading is characterized by a condition in which the initial forces generated by low loading frequency can be assumed as negligible. For large loading frequencies, the inertia forces are relevant and the loading is dynamic (Wichtmann, 2005).

Youd (1972) observed no influence of the loading frequency within the tested range from 0.2 to 1.9 Hz. The limit between quasi-static and dynamic loading is also dependent on the cyclic loading amplitude. However, according to Wichtmann (2005), often this amplitude dependence is disregarded and the limit between quasi-static and dynamic loading is considered to be within about 5 Hz.

For the analysis of foundations under cyclic loadings, the main characteristics of the cyclic loading are: the number of cycles (N), the frequency of cycles (f), the mean load (Q_{mean}) and the cyclic amplitude (Q_{cyclic}). Figure 11 illustrates these parameters of cyclic loadings.

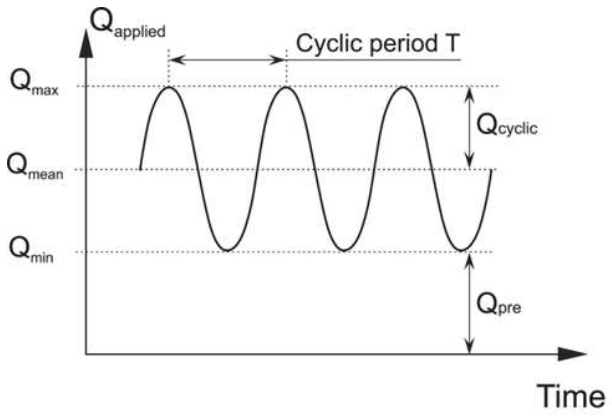

Figure 11. Cyclic loading parameters, after Tsuha *et al.* (2012b) - adapted.

In the case of anchor guyed cables of cell or transmission towers, a minimum load is applied under "no-wind" condition. In Figure 13, this pre-load (Q_{pre}) corresponds to the minimum value of the tensile load that the anchor is subjected. The pre-load (Q_{pre}) maintains the guy cable stretched during the tower service life.

The axial cyclic loading can involve one or two directions of loading. For one-way (OW) cycling the load is applied in only one way (compression or tension). For two-way (TW) cyclic loadings, tension and compression load is applied alternately. The path of the load may follow different functions, exhibiting linear, square, sinusoidal or other functions.

Previous investigations have demonstrated that cyclic loading on piles can induce degradation in shaft resistance, and in some situations in pile base resistance (Turner & Kulhawy, 1990; Al-Dhouri & Poulos, 1995; Le Kouby *et al*., 2004; D'Aguiar *et al*., 2011; Li *et al*., 2012; Tsuha *et al*., 2012b; Thomassen, 2016). Even in small load amplitudes, cyclic failure has been observed in one and two-way cyclic loadings.

Chan and Hanna (1980) relate that failure can occur under one-way loading for a maximum load (Q_{max}) of 30% of the ultimate static value. Gudehus and Hettler (1981) presents the results of model tests in sand indicating that a maximum load, as small as 10% of the ultimate static load, can lead to pile failure. At higher cyclic load levels, e.g. 30%Q_T, failure occurs within about 40 cycles. In these experiments performed by Gudehus and Hettler (1981), failure was characterized by an increasing accumulation of permanent displacement with increasing numbers of cycles. Van Weele (1979) deduced that displacement accumulation is due to continuous re-arrangement and crushing of particles. According to Poulos (1989), two phenomena related to cyclic axial loading may influence the failure of a pile foundation: a) cyclic degradation (or reduction) of shaft skin friction and base resistance; b) accumulation of permanent displacement with increasing load cycles.

A description of the stress-strain response of soils according to three characteristic zones was proposed by Jardine (1992), as illustrated in Figure 12. Zone I corresponds to perfectly linear plastic behaviour delineated by the kinematic yield surface Y_1. This yield surface Y_1 falls within a larger Y_2 surface where the stress-strain behaviour is non-linear though full recoverable behaviour is observed for complete load-unload cycles. According to Jardine (1992), the stress-strain loops typically involve hysteresis in which the dissipated energy is thought to be a result of local yielding and wearing at the inter-particle contacts. According to Tsuha *et al.* (2012), load cycling within the Y_2 surface does not lead to significant strain accumulation. If the cyclic shear strain amplitude during the cyclic loading

exceeds a certain threshold value (and the Y_2 surface is engaged) the soil microstructure is irreversibly altered resulting in stiffness and soil volume variations (Vucetic, 1994). The stress paths move out towards the large scale Y_3 yield surface with the soil exhibiting increasingly plastic and irrecoverable behaviour (Tsuha, et al., 2012b).

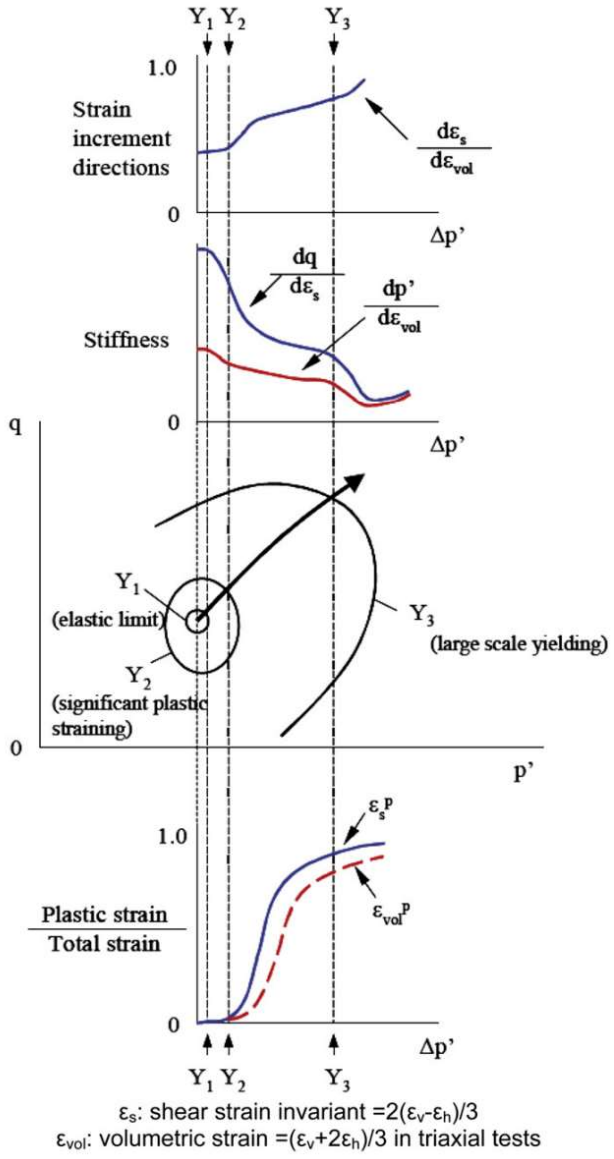

Figure 12. Multiple yield surface, after Tatsuoka *et al.* (1997b).

2.2.1. Stability of pile foundations under axial cyclic loadings

The number of cycles of loading needed to provoke pile cyclic failure depends on the mean cyclic load, the cyclic load amplitude, and the shaft and base resistances. An illustration of the influence of cyclic loading effects on shaft capacity of axially loaded piles in sand could be represented by an interaction diagram.

Karlsrud *et al.* (1986) and Poulos (1988) were pioneers in presenting interaction diagrams (Figure 13) in which foundation cyclic stability can be evaluated. In this diagram, the mean and cyclic axial loads on a pile were plotted, and three regions were identified for a specified number of cycles (*N*): (1) a cyclically stable zone A in which no reduction in load capacity after *N* cycles is observed; (2) a metastable zone B in which cyclic loading causes some limited reduction of load capacity after *N* cycles; and (3) an unstable zone C in which cyclic loading results in failure of the pile within *N* cycles or less.

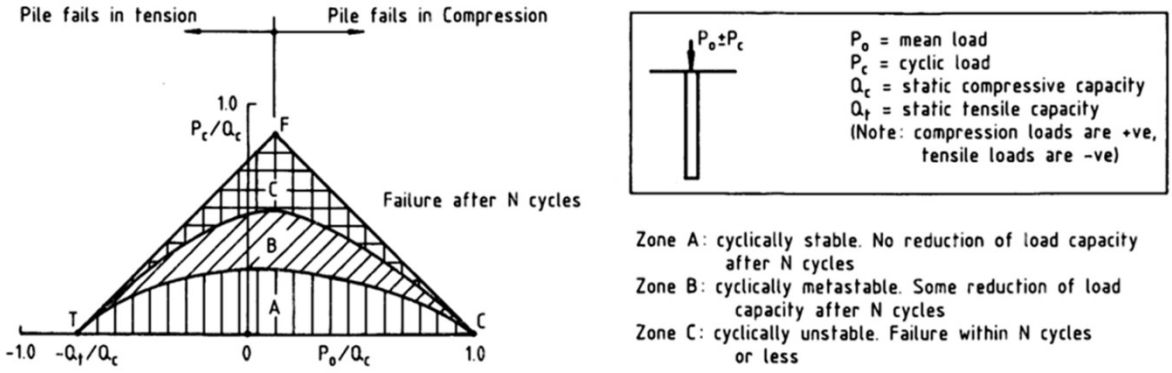

Figure 13. Main features of cyclic stability diagram (Poulos, 1988) - adapted.

The results of cyclic load–controlled tests performed on model piles in calcareous sand by Al-Douri and Poulos (1995) showed from the tests carried out-on 'virgin' piles (not previously failed) that the cyclic response is better than in piles that had been failed. In pre-failed piles the cyclic loading led to failure in a small number of cycles.

Jardine and Standing (2000) report results of field experiments into cyclic loading with full-scale piles in sand focusing mainly on axial shaft resistance in tension. One of the analyses reported by these authors explored the contours of number of cycles to failure in the cyclic loading coordinates $Q_{mean}/Q_{max\ static}$ and $Q_{cyclic}/Q_{max\ static}$ (Figure 14).

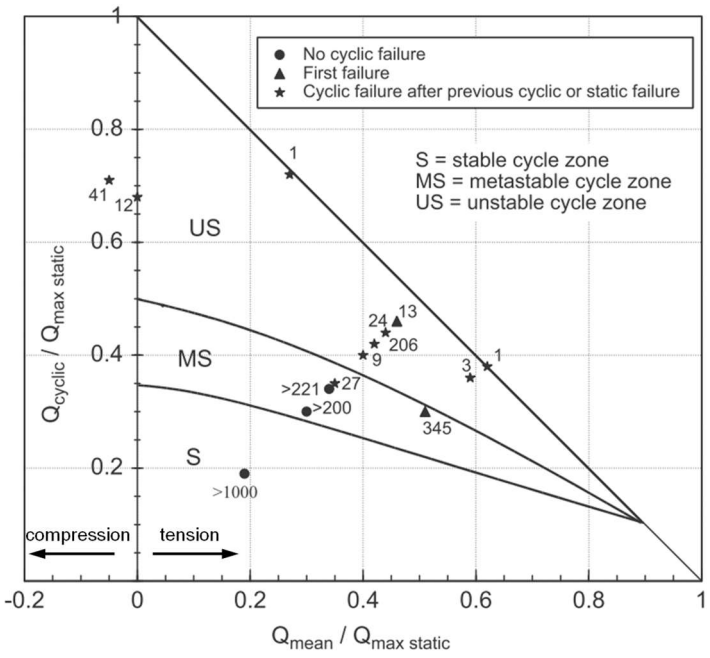

Figure 14. Interaction diagram presented by Jardine and Standing (2000) after studies evaluating the skin friction degradation of piles in sand under tensile cyclic loading (adapted).

An evaluation of the behaviour of displacement model piles in sand under cyclic axial loading was presented by Tsuha *et al*. (2012b) in model tests in a calibration chamber. A cyclic interaction diagram was used by these authors to identify categories of cyclic loading responses. Stable, Meta-Stable and Unstable cyclic responses were established according to the number of cycles necessary to pile failure under tension (shaft resistance). In this study, cyclic failure occurs when:

a) accumulated displacements (U_{acc}) are equal or greater than 10% of the pile diameter or,

b) there is a sharp increase in the displacement rates (U/N).

Displacement rates are considered slow when the tests exhibit less than 1 mm/10^4 cycles, or are considered fast with axial displacements of 1mm/100 cycles or more. The styles of cyclic responses are:

- Stable: no failure occurs before 1000 cycles, with slow or decreasing rates of displacement accumulation.
- Unstable: failure develops with less than 100 cycles.
- Meta-Stable: failure is observed between 100 and 1000 cycles, or accumulated displacements do not stabilize at slow rates.

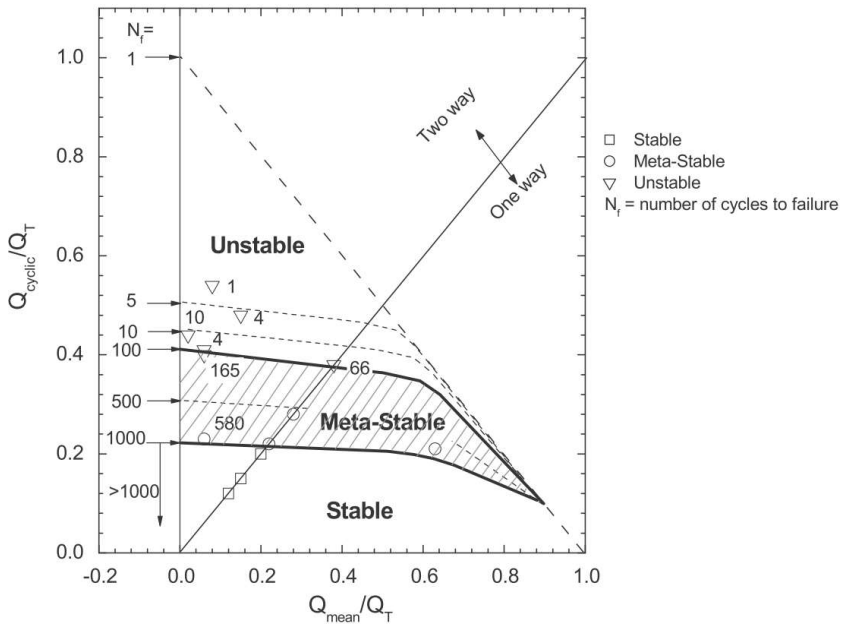

Figure 15. Cyclic interaction diagram, after Tsuha *et al.* (2012b).

Interaction diagrams obtained from cyclic tests in bored piles (compression) and in driven piles (tension) installed in sand are presented by Puech *et al.* (2013). These authors performed cyclic tests in centrifuge, calibration chamber and *in situ* (full scale tests). For the driven piles subjected to tensile cyclic loadings, Puech *et al.* (2013) adopted the same failure criteria used by Tsuha *et al.* (2012), for the interpretation of shaft friction cyclic behaviour.

According to Puech *et al.* (2013), the failure criteria definition for piles under cyclic compression loads is more complicated.

According to Benzaria *et al.* (2013), displacements are accompanied by a progressive mobilization of the pile toe capacity, therefore, the displacements generally tend to stabilize. Therefore, the failure criteria should be defined in terms of an allowable displacement. In addition, the criteria can be attained in both increasing and decreasing rates of displacement accumulation. Figure 16 presents the displacement rates in the compression cyclic tests reported by Puech *et al.* (2013).

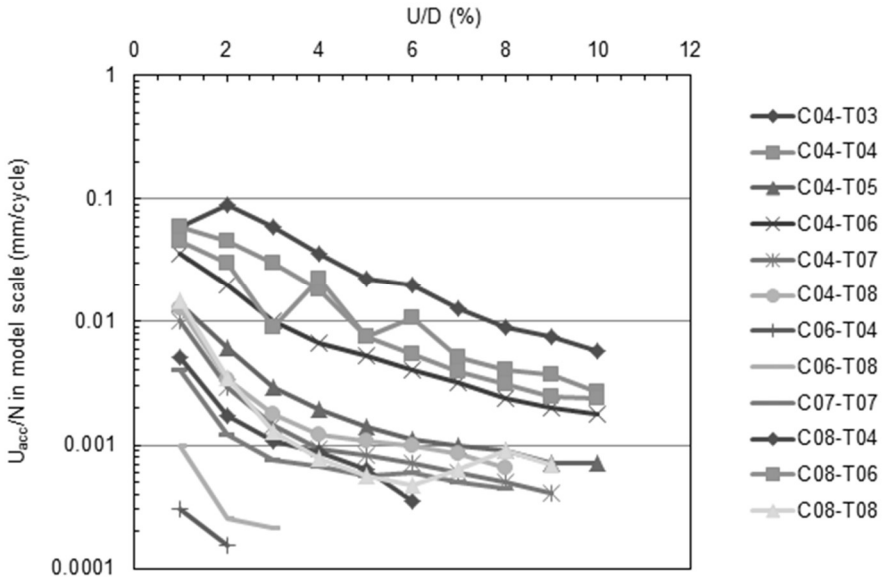

Figure 16. Displacement rate of cyclic compression tests in centrifuge simulating bored piles, after Puech *et al.* (2013) - adapted.

2.2.2. Skin friction degradation in one-way cyclic loading

According to the findings of many researchers (Boulon & Foray, 1986; Poulos, 1989; Lehane *et al*., 1993, Al-Dhouri & Poulos, 1995; Foray *et al*., 1998; Fioravante, 2002; Lehane *et al*., 2005; Mortara *et al*., 2007), the skin friction response of piles in sand is mainly influenced by:

a) the interface friction angle;
b) the variation of lateral stress, which is governed by the interdependence between the interface volumetric behaviour and the deformability of the sand around the pile shaft;
c) the stiffness imposed by the soil on the interface, which depends on the pile radius and deformability of the soil;
d) the initial stress level, which influences the dilation response of the interface;
e) the type of loading (monotonic of cyclic), which determines dilation or contraction of the sand at the interface.

The shaft resistance is related to the soil tendency to dilate at the interface, that is a function of soil mineralogy, soil density, stress level, grain-size, pile diameter and interface roughness (Foray, 1991). The ratio of the dilatant zone thickness to the pile diameter is responsible for the large shaft resistance observed in small diameter piles; however, for relatively smooth steel piles the dilatant properties of the soil may be less important (Houlsby, 1991).

Regarding cyclic conditions in sand, Bowman and Soga (2005) argued that cyclic perturbations may allow friction slippage of particles, which would tend to accelerate the onset of volumetric dilation during soil creep. In contrast, Rimoy and Jardine (2011) observed that low-level cycling accelerates the progression of creep but the volumetric strains are no longer reversed.

With respect to sand-steel interfaces, Mortara *et al.* (2007) observed a marked increase of the stress ratio (τ/σ) in low amplitude cycling in constant normal stiffness (CNS) direct shear tests. These observations are similar to those made by Yoshimi and Kishida (1981) Uesugi *et al.* (1989) and DeJong *et al.* (2003). Yoshimi and Kishida (1981) and Mortara *et al.* (2007) observed homogeneous deformations of the sand specimen for low shear

displacements. For higher values of shear displacement, strong distortions of the sand close to the interface were observed. All of these cited authors found a marked effect of densification at low amplitudes, leading to a stress ratio increase, which limits the decrease in normal stress, and results in a lower degradation rate.

Experiments performed on pile models in clay have shown that the degradation of shaft resistance occurs when the cyclic displacement exceeds 0.2% of the pile diameter (Poulos H. , 1982). Increasing cyclic displacement generates degradation and a loss of shaft resistance, reaching a limiting value for cumulative displacements about 1.5% of the pile diameter, after the first 10 or 20 cycles (Poulos H., 1982).

Urabe *et al*. (2015) reported through centrifuge testing that the shaft resistance reached an ultimate value when the pile head displacement was about 6-13% of the shaft diameter of model pile, and reduced significantly with increasing displacements. Li *et al.* (2012) verified that the majority of skin friction reduction occurs within the first 10 cycles in jacked and pre-jacked model piles. However, Poulos (1982) mentions that the onset of degradation can vary considerably. According to Poulos (1989), the shaft resistance degradation begins when the cyclic amplitude displacement exceeds the displacement required for full slip under static load test.

Based on the results of field tests at the Dunkirk site, Stuyts *et al.* (2012) observed that progressive densification of the soil around the pile occurs for cyclic axial loadings with an amplitude greater than 25% of the shaft resistance. In consequence of soil densification, the effective radial stresses on the pile-soil interface are reduced, resulting in a decrease of the normal stress on the pile-soil interface as well as the shaft capacity.

The reduction of radial stress during pile installation is possibly dependent on volume changes and stress level (D'Aguiar, Modaressi, Santos, & Lopez-Caballero, 2011). White and Lehane (2004) and Gavin and O'Kelly (2007) relate the friction fatigue degradation to the

number of shearing cycles during the pile penetration in the installation process. Therefore, comparing jacked and driven piles, the rate of degradation should be more significant in driven piles experiencing high blow counts. On the other hand, for continuous jacking piles, the rate of degradation should be considerably less.

Gavin and O'Kelly (2007) reported that cyclic loading caused no effect on the pile base resistance (or base stiffness) of displacement piles installed in dense sand. However, the shaft resistance of monotonically installed jacked piles, which had exhibited significantly high shaft resistance, showed large degradation during the initial load cycles, and at higher cyclic load levels. Furthermore, the horizontal effective stress at failure, acting monotonically and cyclically, were indistinguishable after a relatively small number of working load cycles.

Urabe *et al*. (2015) observed that the shaft resistance of piles under cyclic tensile loadings exhibited greater degradation than in cyclic compressive loadings. According to these authors, the shear deformation during the downward movement increases the effective stress around the pile, while the uplift movement results in effective stress decrease.

The cyclic load amplitude causes significant influence on the cyclic degradation of shaft resistance. Le Kouby *et al.* (2004) observed that friction degradation increases for greater displacement amplitudes (tests conducted with a displacement control). On the other hand, an increase in shaft resistance was observed after a few cycles of small cyclic amplitudes. Similar observations were made by D'Aguiar *et al.* (2009).

The initial stress level does not influence significantly the cumulative contraction of sand within the shear zone surrounding the pile interface (Li *et al.,* 2012). These authors reported that the skin friction degradation exhibited similar trend for model piles installed in different manners: pre-jacked, monotonically jacked and cyclically jacked. Li *et al.* (2012) concluded that independently of the installation procedure, similar amplitude cyclic loadings tend to provoke a similar decrease in radial stress with consequent shaft resistance decrease.

2.2.3. Behaviour of the pile base resistance in one-way cyclic loadings

Studies on pile base resistance under cyclic loading can contribute to the understanding of the behaviour of helical anchors. The largest contribution to the helical anchor's capacity is given by the helix bearing resistance, similar to the pile base capacity. Therefore, some observations about the degradation of pile base resistance, and also about the bearing resistance of footings, can be useful in the study of helical anchors.

Poulos and Chua (1985) reported an effective reduction in the base capacity in model footings tests on sand as a result of large accumulated displacements at relatively high cyclic stress levels. Due to the scantly available data at that time, Poulos (1989) suggested to ignore the cyclic degradation of base resistance in cyclic axial loading analysis in sand.

Li *et al.* (2012) observed that although jacking installation causes densification of soil under the pile tip, a softening behaviour of the load-displacement response was observed during displacement-controlled cyclic loading on a jacked pile model in centrifuge. This softening is commonly expected for pre-jacked model piles (simulating buried piles) since the installation of this type of pile does not induce soil densification. For both cases of jacked and pre-jacked piles, the softening in the pile base resistance is due to a gap between the pile model base and the soil developed during the cyclic loading. However, for the case of jacked model piles, the softening phenomenon occurred after cyclic tests with larger settlements (65 mm for jacked piles and 5-20 mm for pre-jacked piles, both models with 63.5 mm diameter in prototypes), indicating that the large-amplitude cyclic axial loads can cause further densification of the zone of sand at the base of the jacked pile. Previous studies have indicated that the sand subjected to cyclic shear experiences a net reduction in volume with the number of cycles, until reaching a maximum density, even for dense sands with I_D around 90% (Ansell & Brown, 1978; Airey *et al*. 1992).

When the settlement is larger than 20 mm for the pre-jacked model piles, Li *et al.* (2012) observed that the pile base resistance increased with increasing settlement. Similar observations were made by Le Kouby *et al.* (2004) and Benzaria (2013). According to Le Kouby *et al.* (2004), the soil around the pile is not remoulded as in the case of the jacked pile. Therefore, the cyclic loading causes soil densification, leading to a reduction in the pile base-sand particles contact and consequently a decrease in the stress at the pile base.

In two-way centrifuge cyclic tests, Urabe *et al.* (2015) observed an increase in the base resistance when a wing pile model (similar to a helical pile) is in the pushing direction, possibly because the sand moves beneath the base during the tension load and afterwards is densified during the compression load.

2.3. Plate anchors in sand subjected cyclic loadings

Plate anchors are used to support structures subjected to repeated uplift loadings as dry dock floors, transmission towers and offshore structures. This type of anchor essentially is comprised of a high strength rod fixed to a plate anchor installed by excavating the ground to the required depth followed by back filling and compacting with a good quality soil, different from helical anchors, for which the soil around the anchor was previously disturbed by the installation. The anchor's initial condition can be pre-stressed or dead (zero load). The reason for pre-stressing the anchors lies in the belief that this technique allows a reduction in the adverse effects of repeated loadings (Hanna, Sivapalan, & Senturk, 1978). When subjected to cyclic loadings, dead anchors exhibit non-recoverable displacements, and the anchor's life will depend primarily on the load range for a particular limiting displacement. As the cyclic loads are applied, a progressive modification of the stress state occurs along the foundations resulting in a change in the anchor behaviour (Hanna, Sivapalan, & Senturk, 1978).

Cyclic tests carried out by Hanna *et al.* (1978) on model dead anchors in sand revealed that the anchor experiences large displacements in the initial cycles with an increase in permanent displacements. In a bi-logarithmic plot with the rate of anchor displacement *versus* the number of cycles, the authors observed a decreasing linear trend of the displacement accumulation. With an increase in the number of cycles, the rate of displacement accumulation decreases but does not cease, and failure in the form of a sudden pull-out never occurs. The cyclic laboratory tests conducted by Petereit (1987) on anchor model plates in fine saturated sand showed a continuous anchor displacement even at maximum cyclic loads of 15%Q_T.

The anchor pre-stressing during the proof loading stage aims to reduce creep effects and stiffen the anchor system. Hanna *et al.* (1978) also investigated the effects of pre-loading the anchor with 75% of the anchor's uplift capacity (Q_T), and they observed that pre-loading does not produce any permanent stiffening effect. In contrast, when the anchor was subjected to 20,000 cycles with the applied loading varying from zero to 50%Q_T, a significant stiffening was noticed in the following cyclic loading (from 25%Q_T to zero).

Hanna and Al-Mosawe (1981) showed that the use of a pre-stress load significantly reduces the displacements under the first cyclic loading and increases the anchor's life duration, by decreasing the permanent displacements at any cycle in comparison with the dead anchors. Hanna and Al-Mosawe (1981) also noticed that cyclic loadings with low mean loads (Q_{mean}) tend to be more severe, i.e., a cyclic loading ranging from zero to 60%Q_T will generate greater accumulated displacements than a 30-80%Q_T cyclic loading.

Beard (1980) proposed contours limiting the number and magnitude of loading cycles to prevent failure due to cyclic creep, and suggests that the cyclic loadings with $2Q_{cyclic}$ (double cyclic amplitude) lower than 5%Q_T can be ignored. Based on experimental observations, Andreadis and Harvey (1981) proposed a hyperbolic equation to describe the anchor response

under cyclic loadings. In the case in which the permanent displacement experienced by a previous cyclic loading is known, these authors also propose a hardening ratio-total relative cyclic movement relationship.

Regarding the uplift resistance of wing plates of model piles under two-way cyclic loadings, Urabe *et al.* (2015) reported a significant decrease in the wing bearing resistance for piles with small ring area, under cyclic displacement amplitudes more than ±65 mm (in prototype values). This decrease was caused by the disturbance of the soil above the wing. Urabe *et al.* (2015) also show that the shaft resistance controls the cyclic tension response of the model pile for cyclic displacements less than ~30 mm. However, for larger displacement amplitudes, the wing plate controls the cyclic tension response.

Chow *et al*. (2015) employed a macro-element modelling approach to interpret the behaviour observed in cyclic tests on plate anchors in dense sand. In this approach, an allowable combination of horizontal load (H), vertical load (V) and moment (M) acting on the anchor is represented by a surface in the H'-V'-M' space (Figure 17). To reproduce the effects of cyclic loadings, additional features should be considered in the model. If the soil experiences cyclic loading, the density and fabric changes and imposes an expansion of the yield surface (Tatsuoka, Jardine, Lo Presti, Di Bennedetto, & Kodaka, 1997b). Similar behaviour was described by Chow *et al*. (2015), with the anchors exhibiting changes in sand density and fabric, causing an expansion of the bounding and memory surfaces. However, the effects of density and fabric changes tend to disappear with large amounts of deformation, a situation in which both bounding and memory surfaces approach the ultimate failure surface (Chow, O'Loughlin, Corti, Gaudin, & Diambra, 2015).

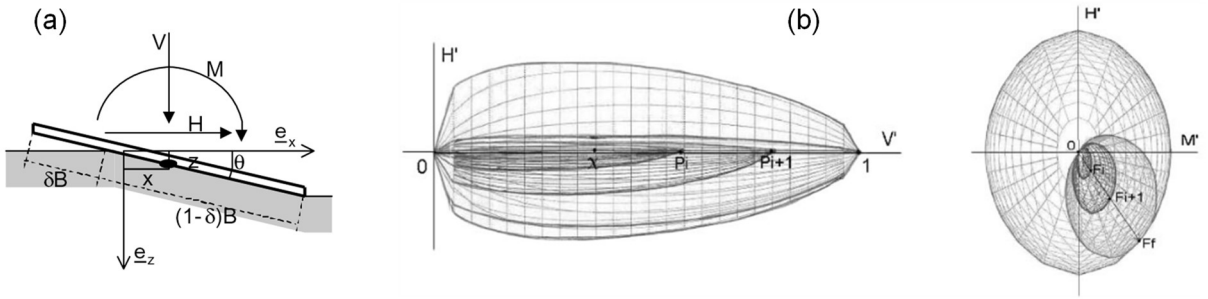

Figure 17. Displacement rate of cyclic compression tests on bored piles: (a) system definition; (b) loading surface in the H-V-M space, after Cremer *et al.* (2001) - adapted.

2.4. Cyclic behaviour of helical anchors in sand

The influence of cyclic loadings on the skin friction degradation of piles has been addressed by many studies in the literature. Also, the effect of cyclic loading on soils has been evaluated by triaxial tests on uniform samples. According to Ishihara *et al.* (1975), sand responses to monotonic and cyclic shearing depend on their fabric, initial state (void ratio and stresses) and degree of shearing.

For helical piles, the cyclic failure of the soil under the bottom plate (intact sand) in compressive cyclic loading could be evaluated with triaxial tests (the uniform and intact soil under the bottom plate). However, the cyclic response of helical piles under tension depends on the shear resistance of a soil-disturbed above the plates.

El Sharnouby and El Naggar (2011) present results of 15 compressive load cycles on a helical pile. According to the authors, the pile stabilized after a few cycles with a mean cyclic load and a maximum load respectively equals to 57 and 70% of the ultimate load. Improvement of the monotonic load-displacement response was observed due to the performed load cycles, occurring an increase in stiffness.

The most prominent feature of helical anchor uplift capacity is the shear resistance of the disturbed soil in the cylinder above the plates. When this type of anchor is submitted to

cyclic loadings, the resisting forces are concentrated in the interface between intact soil and disturbed soil. Therefore, the cyclic response of helical anchors in sand depends of the shear resistance between disturbed soil and intact soil.

Probably, after a certain number of loading cycles (depending on the cyclic load amplitude), in one-way cyclic (in tension), the disturbed soil within the cylinder will be densified. In two-way cyclic (tension and compression), the pile response depends on the densification of the soil disturbed above the plates, and on the intact soil under the bottom plate. In that way, the behaviour of helical anchors under cyclic loading is complex.

Previous studies on helical anchors have related that cyclic loading promotes degradation on both coarse-grain and fine-grain soils and anchor performance. A reduction in horizontal stress occurs during the cyclic loading because of the sand particles movement from the edge of the helix to below the helix during repeated loading. As a consequence, a significant reduction in the anchor's capacity occurs (Clemence & Smithling, 1984). In the case of an expected inflow of soil into the cavity, Trofimenkov and Mariupolskii (1964) mentioned that the limiting value of the applied load cyclic conditions should be limited to between 60 and 70% of the anchor's uplift capacity in one-way cyclic loading, and from 30 to 40% of the uplift capacity in two-way cyclic loading. However, repeated load applications increased the stiffness of the soil-anchor system in some cases (Andreadis, Harvey, & Burley, 1981).

According to Cerato and Victor (2009), cyclic loadings at a relatively high cyclic/static load ratio may significantly increase uplift capacities and reduces long-term creep. If no pre-loading is performed, the anchors could present excessive displacements even at low loadings. A general recommendation is to keep cyclic loads below 25% of the ultimate capacity of the anchor to minimize long-term creep (Cerato & Victor, 2009; Ghaly & Clemence, 1998).

Cyclic loading was observed to improve the ultimate tension capacity in results presented by Buhler and Cerato (2010). The helical anchor named V13 was subjected to a series of two cyclic loadings with 33-39% and 33-65% of the predicted uplift capacity. According to these authors, the densification of the soil above the helices during the cyclic loading is the most likely effect to explain the capacity increase. In addition, the cyclic load amplitude was observed to cause more influence on the anchor response rather than in the maximum load. Degradation of skin friction is believed to occur differently from degradation of base resistance; however, little conclusive data is available for helical anchor foundations.

2.5. Physical modelling in centrifuge

Full scale field tests are expensive and generally provide results with low repeatability. It is difficult to reproduce closely controlled test conditions (Dickin & Leung, 1983). Therefore, parametric analyses of foundations and anchors are often performed by means of reduced scale models. Some experimental techniques used for tests on reduced scale models:

a) experiments under normal gravity (1×*g*) with the simple reduction of the model size;

b) experiments in a calibration chamber;

c) experiments in a geotechnical centrifuge.

According to Hettler (2010), 1×*g* model tests are a useful tool to investigate mechanisms and slip surfaces. However, the 1×*g* scaled models cannot reproduce the behaviour in geotechnical problems that are highly dependent on confining stresses, because the level of geostatic stresses that are reproducible in 1×*g* reduced models are significantly less than the field stress conditions (Kim & Kim, 2011). To overcome this limitation of 1×*g* models, geotechnical centrifuges are commonly used to compensate for the self-weight stress level (Tsuha, Thorel, & Rault, 2013).

A centrifuge is essentially a sophisticated load form on which soil samples can be tested (Taylor, 1995). Experiments with small scale models in centrifuge can use the same material as the prototype and reproduce the same field of forces and mass in a full-scale structure (Garnier, 2001). In centrifuge modelling, the intensity of the gravitational field generated by centrifugal acceleration must be inversely proportional to the reduction scale of the manufactured model (Corté, 1989). According to scaling laws, over a *1/n* scaled model the applied centrifuge acceleration should be *n* times the earth's gravity (Garnier & König, 1998). The scaling factor X^* on a physical parameter X is the ratio of the value X_m in the model to the value X_p in the prototype ($X^* = X_m / X_p$). Physical systems must satisfy fundamental laws of dynamics; thus, the dimensional analysis of physical relationships carries the following similarities:

$$\sigma^* = \rho^* g^* l^* \quad \text{Eq. 7}$$

$$\xi^* = \rho^* t^{*2} \quad \text{Eq. 8}$$

where,

σ^* is the scaling factor for stresses;

ρ^* is the scaling factor for bulk density;

g^* is the scaling factor for mass forces;

l^* is the scaling factor for distance measures;

ξ^* is the scaling factor for displacements;

t^* is the scaling factor for time.

The relationships presented in Eq. 7 and Eq. 8 can be grouped as follows:

$$\frac{\sigma^* t^{*2}}{\rho^* l^{*2}} = 1 \quad \text{Eq. 9}$$

$$\frac{F^{*}t^{*2}}{\rho^{*}l^{*4}}=1 \qquad \text{Eq. 10}$$

As soil behaviour depends on the stress history, which was previously detailed, scaled models must be subjected to the same stress state as the full-scale structure. This assumption leads to the following condition (Taylor, 1995):

$$\sigma^{*}=1 \qquad \text{Eq. 11}$$

Table 2 presents the scaling laws derived from the equation of equilibrium (Eq. 11).

Table 2. Scaling law (Fuglsang & Ovesen, 1988).

Parameter	Notation	Scaling factor
Distance	u^{*}	1/n
Stress	σ^{*}	1
Soil density	ρ^{*}_{soil}	1
Gravity	g^{*}	n
Displacement	ξ^{*}	1/n
Dynamic time	t^{*}_{dyn}	1/n
Strain	ε^{*}	1
Velocity	v^{*}	1
Acceleration	a^{*}	n
Frequency	f^{*}	n
Force	F^{*}	$1/n^{2}$
Unit weight	γ^{*}	n
Mass	m^{*}	$1/n^{3}$

2.5.1. Scale effects

Centrifuge modelling allows for parametric studies with relatively small effort and low-cost compared to full-scale tests. For this reason, this modelling technique has been used successfully to investigate the performance of plate anchors (Ovesen, 1981; Dickin & Leung, 1983; Tagaya *et al*., 1988), and helical anchors (Levesque, 2002; Tsuha *et al*., 2007; Bian *et*

al., 2008; Wang *et al*., 2013). However, the occurrence of scale effects can influence the results of model experiments of geotechnical problems in granular soils.

The reduced scale of models can induce scale effect in relation to the grain-size (Balachowski, 2006). Dilation, roughness, and grain crushing influence the behaviour of granular soils, and the smaller the model is, the greater the effect of these phenomena on the model capacity (Klinkvort, Hededal, & Springman , 2013). Therefore, because the uplift capacity of a deep single-helix anchor is the sum of the shaft skin friction and the helix bearing capacity, for the centrifuge simulation of helical anchors in sand, it is fundamental to verify the occurrence of scale effects on the results of both components of anchor capacity.

2.5.1.1. Particle-size effects on shaft resistance

The particle size effect on the shaft resistance of piles is associated with shear band formation along the shaft. The shear localization in sand in plane strain compression and triaxial tests (Desrues, 1991), and in direct shear apparatus (Boulon, 1998) indicate a mean thickness of the shear band of $10d_{50}$. In the case of sand-pile interfaces, the thickness of the dilatant zone is found as $10d_{50}$, independent of the shaft diameter (Boulon & Foray, 1986). Yoshida and Tatsuoka (1997) observe that the shear band width is proportional to the grain-size and is comprised of between 10 and 20 times the average grain-size. Garnier and König (1998) mention that the shear band thickness is usually assumed to be 10 or $15d_{50}$.

An adequate model simulation of pile-sand interface can be ensured by following a minimum ratio between pile shaft diameter and average grain-size (d/d_{50}). Previous studies on scaling effect on shaft friction have presented different limits of the ratio d/d_{50}. Foray *et al.* (1998) report that particle-size effects are negligible when d/d_{50} is greater than 200. Garnier and König (1998) affirm no significant grain-size effect when d/d_{50} is larger than 100 for pile

models with a rough shaft. Fioravante (2002) comments that scaling effects can be neglected for d/d_{50} greater than 30 to 50, despite the dispersion observed in the results.

The recommendations of the aforementioned studies to prevent scale effects in modelling pile shaft resistance in sand may not be suitable in the case of shaft resistance of helical anchor models due to installation effects. In the case of helical anchor installation, the anchor is penetrated into the soil by rotation, and consequently, significant disturbance occurs within the cylindrical installation zone around the shaft, which could influence the scale effects.

2.5.1.2. Particle-size effects on plate bearing capacity

Since there is no study available on particle size effects on the bearing plate resistance of helical anchor models, the recommendations of previous centrifuge model test investigations on footings and on plate anchors in sand were used by Tsuha *et al.* (2007) to define the minimum ratio D/d_{50} (D is plate diameter) to provide a satisfactory simulation of helical plate bearing resistance.

In the experiments of Yamaguchi *et al.* (1977) no difference was observed in the bearing capacity factor and load-settlement response of shallow foundations with the ratio of foundation width to an average grain size greater than 36. Ovesen (1979) investigated scaling effects in centrifuge tests on footing models in sand, and found that in experiments with a footing model diameter (D) larger than $30d_{50}$ no scale effect was observed. The results presented in Tatsuoka *et al.* (1997a) showed similar results between footing models with D/d_{50} a ratio of 33 and 50. Lau (1988) observed no evidence of serious particle size effects on footing models in sand with B/d_{50} ratios ranging from 165 to 8333.

Three different scales of square plate anchors were tested by Ovesen (1981) in dense sand (*g*-levels ranging from 167*g* to 56*g*). In this cited work, no scale errors were found in models with a ratio between model width (B) and an average grain-size (d_{50}) larger than 25.

From the aforementioned studies, for B/d_{50} ratios greater than 25, no difference in the anchor (or footing) response was observed. However, the minimum B/d_{50} or D/d_{50} ratio to avoid scale effects is still unknown, as there is no available centrifuge investigation on plate anchors using B/d_{50} ratios smaller than 25.

In the case of plate anchor models tested in centrifuge, the sand above the plate is placed in the container after the plate installation. Differently, in the case of centrifuge tests on helical anchors, the helical plate is penetrated into the soil by rotation after sand placement, and consequently, significant disturbance occurs within the cylindrical installation zone of the anchor. Also, the range of the ratio between plate and shaft diameters of helical anchors is usually lower than the ratios used for plate anchors. Therefore, these two differences probably could result in different values of the minimum ratio D/d_{50} necessary to avoid scale effects on helical anchor tests compared to the case of plate anchor and footing models.

2.5.1.3. Scale effects on helical anchor model tests

The values for the ratios D/d_{50} (plate diameter/average grain size) and d/d_{50} (shaft diameter/average grain size) observed in previous studies in order to avoid scale effects on bearing plate resistance and shaft resistance indicates that the shaft diameter should restrict the helical anchor model dimensions (greater d/d_{50} ratios are suggested compared to D/d_{50}). However, the shaft friction resistance corresponds to a very small portion of the total capacity of a helical anchor in sand. Therefore, scale effects on the shaft friction may not be significant compared to the scale effects on the helix bearing resistance.

Centrifuge model investigations on helical anchors in sand can produce reliable simulations of anchor behaviour without influence of scale effects. For this, some relationships between grain and model size should be established in order to provide an accurate reproduction of prototype anchor-soil interaction. In the case of helical anchors, the helix-shaft-soil interaction is influenced by the grain-size in a particular manner.

The scale effects on shaft friction of helical anchors are related to the shaft diameter d similarly to the case of regular piles. However, the relationships between pile shaft diameter and d_{50} recommended to prevent scale effects on model tests may not be suitable for the simulation of shaft resistance of helical anchors, as the soil mass around the shaft (also the dilatant zone) is influenced by the previous installation of the helix.

In the case of helix bearing resistance, it is necessary to establish a helical plate component (such as the helical plate diameter or the effective helical radius) that can be related to particle size effects. In the case of plate anchors, the ratio between plate diameter D and the average grain size d_{50} is usually used to evaluate scale effects. However, the ratio between plate and shaft diameters is much better for plate anchors when compared to helical anchors. In the case of helical anchors, the net projected area of the helix is reduced; therefore, the ratio between helix diameter D and d_{50} cannot be the best parameter to explain the particle size effects on helix bearing resistance.

Therefore, to address the need to examine the scale effects on the results of centrifuge modelling of helical anchors in sand, in the current study a series of tests was conducted to investigate this problem. These tests were performed before the cyclic loading tests to help the decision regarding the optimal dimensions of the instrumented model anchor (shaft and helix diameter) to be fabricated for cyclic tests.

3. MATERIALS AND METHODS

This chapter presents the materials and methods used in this study to evaluate the helical anchor behaviour under cyclic loading. For this evaluation two groups of tests were performed: laboratory model tests in centrifuges and field tests. Additionally, a numerical model was developed in order to simulate the pre-cyclic and post-cyclic uplift capacity of the anchors tested in centrifuges. Therefore, this chapter is divided into three main parts: centrifuge modelling, field tests, and numerical modelling.

3.1. Centrifuge modelling

The centrifuge modelling technique was used to evaluate the effects of cyclic loadings with different amplitudes on the helical anchor performance in sand, and to evaluate the particle-size effects in physical modelling of helical anchors in sand. For these two investigations, the sand sample reconstitution should be closely controlled to minimize the uncertainties related to the sand sample characteristics. Therefore, the samples were reconstituted through the sand raining method to provide repeatability of the characteristics of the various tested samples.

Installation and loading tests on the helical model anchors were performed with a servo-controlled hydraulic actuator that allows carrying out the experiments controlling the loading rate or the displacement rate.

The centrifuge experiments were performed in the IFSTTAR beam centrifuge (Figure 18). This centrifuge has a maximum radius of 5.50 m, and its swinging basket permits the installation of a container with 1.40 m in length, 1.15 m in width and 1.50 m in height, and with payload of 20 kN for experiments at 100×*g*. The experiments for this thesis considered the *n*×*g* centrifuge acceleration applied to the helix of the model anchor, taking into account the distance between the centrifuge spin axis and helix level to determine the application

radius of the centrifuge acceleration, as presented in Figure 19. More details about the IFSTTAR geotechnical centrifuge can be found in Thorel *et al*. (2009).

Figure 18. IFSTTAR geotechnical centrifuge.

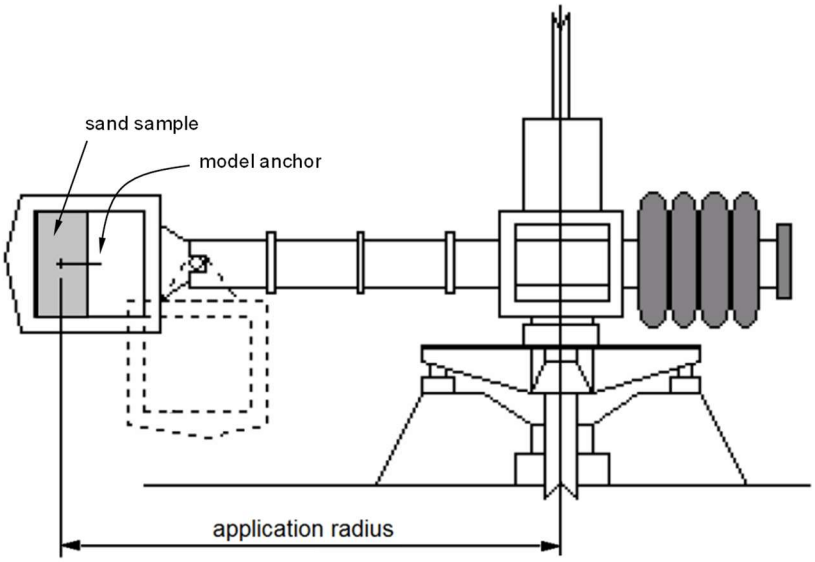

Figure 19. Centrifuge acceleration radius, after Tsuha (2007) adapted.

3.1.1. Sand sample reconstitution

The centrifuge experiments were carried out in reconstituted sand samples prepared through the raining deposition technique inside rectangular steel strongboxes. In this

technique, the sand is placed in an automatic hopper and pours through a slot to produce a uniform sand rain over the strongbox (Figure 20). The hopper moves in round-trips while the sand is deposed in thin layers on the bottom of the strongbox. The hopper horizontal speed is constant while the hopper passes over the strongbox. The sand drop height can be adjusted as well as the rate of flow by setting the horizontal speed and the slot width. The pluviation process is known for providing homogenous specimens and good repeatability (Garnier, 2001; Küs, 1992; Miura & Toki, 1982). The final dimensions of the sand sample are 1200 mm in length, 800 mm in width and 360 mm in depth. To assess the achieved density, at least two calibrated boxes were placed on the bottom of each strongbox.

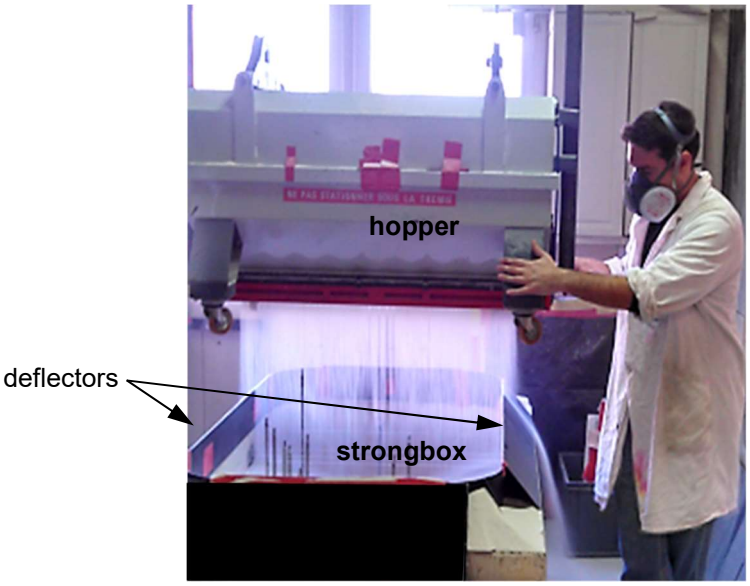

Figure 20. Sample reconstitution.

The centrifuge tests were performed in dry HN38 Hostun dense sand with a density index (I_D) ranging from 94 to 99%. HN38 Hostun sand is a fine silica sand consisting of angular particles (sand extracted in Hostun, France). Hostun sand is used in other laboratory investigations, and its physical properties are well established (Flavigny, Desrues, & Palayer, 1990). Table 3 lists the main characteristics of HN38 Hostun sand. Since the samples are dry,

no distinction will be made between total and effective stresses. The pluviation characteristics used to achieve a sand sample with such relative density were: slot width = 3 mm; drop height = 600 mm; horizontal speed = 18.5 cm/s (corresponding to 50 Hz equipment frequency); round-trip movements = 4. A verification of the sand sample bulk density according to the pluviation parameters are presented in the Appendix D.

Table 3. HN38 Hostun sand main characteristics.

Specific gravity of the sand particles	G_s	2.64
Maximum dry unity weight (kN/m^3)	$\gamma_{d(max)}$	15.24
Minimum dry unity weight (kN/m^3)	$\gamma_{d(min)}$	11.63
Maximum void ratio	e_{max}	1.226
Minimum void ratio	e_{min}	0.699
Average grain size (mm)	d_{50}	0.12
Coefficient of uniformity	C_U	1.97

Ternet (1999) identified inhomogeneous zones in reconstituted sand samples in IFSTTAR caused by boundary effects. The density of the reconstituted sample by sand pluviation is affected by the strongbox walls in a 10 cm wide strip along the longer side and a 20 cm wide strip along the shorter side (Figure 21).

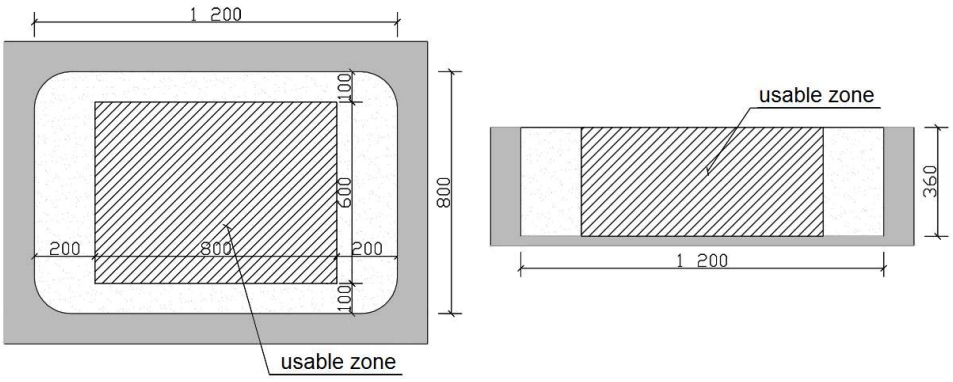

Figure 21. Sand sample usable zone (dimensions in mm), after Rosquët (2004) - modified.

Direct shear and triaxial tests were performed on reconstituted sand samples with I_D = 95%. The sand specimens for the direct shear tests were reconstituted by pluviation, and the sand specimens used in the triaxial tests were reconstituted with sand compaction. The

internal friction angle (ϕ') obtained from direct shear tests was 48º, in terms of peak force values. In the triaxial tests, the internal friction angle obtained was 47º for peak forces values. These tests are discussed in more detail in the Appendix B and C.

3.1.2. Test system

In centrifuge, installation and loading were performed using a servo-controlled system fixed over a sand container. As illustrated in Figure 22, a motor was coupled with the servo-controlled system to rotate the helical anchor model during the installation. In some tests (listed in the Appendix K), a torquemeter was used to measure the installation torque (Figure 22a). The vertical displacement and the vertical force were monitored by displacement and force transducers, respectively. The registration of installation torque, displacement, and force was completed through an automatic data acquisition system installed in the centrifuge swinging basket. The data acquisition frequency was set at 10 Hz. More details concerning the measurement system are provided in Appendix F and in Thorel *et al.* (2009).

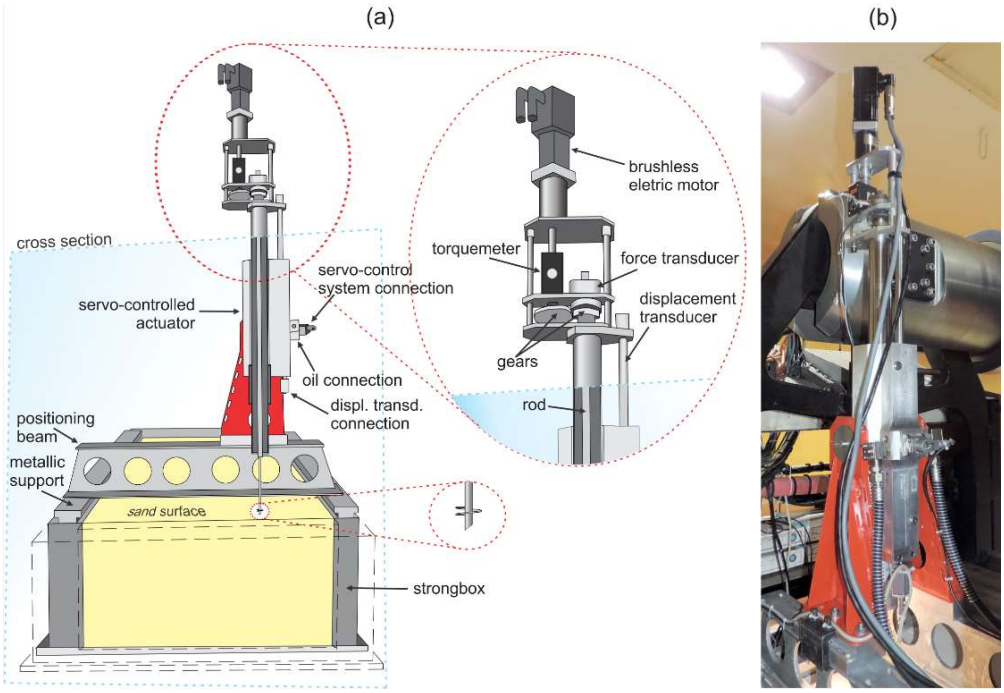

Figure 22. (a) test system; (b) servo-controlled actuator.

The main characteristics of the sensors used in the experiments are listed in Table 4. The measurements of torque, displacement and force were converted into numerical data by an automatic data acquisition system placed in the centrifuge swinging basket.

Table 4. Sensors features.

Feature	Torque Sensor F62	Force sensor F97	Displacement sensor D SV2
Range	50 N·m	1000 N	300 mm stroke
Resolution	0.002 N·m	0.02 N	0.001 mm
Linearity deviation	0.1%	0.15%	0.01%
Hysteresis	0.1%	0.15%	0.004 mm
Manufacturer	FGP	TME	TWK
Model	CD1140-2	F 521 TC	Magnetostrictive displ. transd. MSE

3.1.3. Procedures for installation and monotonic tensile loading tests

The monotonic loading tests of the current research were carried out according to the procedures described in this section.

The installation of the helical anchor models into the sand sample was performed in flight by applying a constant rotation to the model anchor of 5.3 rpm (the field rotation rate normally varies from 5 to 20 rpm). During the model anchor installation, the vertical speed was set to permit the helix installation advances into the soil with a penetration rate of one pitch per revolution. In each container, a minimum axis-to-axis spacing of 10 times the helix diameter was kept between anchors to ensure no influence on the results.

Tensile loading tests were performed 3 minutes after the end of anchor installation. The anchor models were loaded at a vertical displacement rate of 0.3 mm/s. When the pull-out test was completed, the centrifuge was stopped to move the servo-control system over the next anchor model for testing.

The sequence of the test procedure, from sample preparation to anchor testing in flight, is described below:

a) The sand sample is reconstituted by sand pluviation procedure.

b) The sand sample is placed in the centrifuge-swinging basket.

c) The servo-controlled system is installed over the strongbox.

d) Three consecutive stabilization cycles of centrifugation, with a 3 minute duration, with the maximum *g*-level planned for the tests in each container.

e) The model anchor is installed in flight.

f) Three (3) minutes of wait time after model installation (in flight).

g) The anchor pull-out test is carried out with a loading rate of 0.3 mm/s (in flight).

h) The centrifuge is stopped for repositioning the servo-controlled system for the next anchor test.

i) Steps e) through h) are repeated for the next anchor test.

3.1.4. Experiments on particle size effects

For centrifuge modelling studies it is necessary ensure that no scaling issues are influencing the results. An appropriate relationship between sand particle and model size has to be established in order to properly simulate the prototype pile-soil interaction. Previous studies on the soil particle size effect on plate anchors, footings and regular piles have been used as a scale effect reference for modelling helical piles. However, there is no certainty that limiting values of D/d_{50} reported in previous studies are valid for helical model anchors, since footing and plate models experience no reduction in effective diameter because of the shaft. In addition, the installation and the helix-shaft-soil interaction are influenced by soil grain-size differently than the scale effects on the shaft and the plate.

Given the scenario above, an investigation about scale effects on the results of the centrifuge model on helical anchors in sand was carried out for this thesis before the cyclic tests, to assist in the decision about the dimensions of the instrumented anchor model fabricated for the cyclic tests.

The "modelling of models" technique was used in the current study to investigate the scaling effects on helical anchor models. In this technique, a large-scale model is assumed to be practically independent of scale effects. Different sizes of anchor models and *g*-levels were used to simulate the same prototype response. D/d_{50} and d/d_{50} ratios were varied but the D/d ratio was constant. Full similarity between model and prototype is achieved when identical non-dimensional response is observed between them.

Three reconstituted Hostun sand samples, with I_D = 99% (Containers No. 8, 11 and 12), were prepared for these tests under acceleration levels ranging from 8.3 to 16.7×*g*. All models were installed at the same relative embedment depth (z_D) of 6*D*. Since the helical anchor models were fabricated with different helix diameters, the embedment depth of each model was adjusted to provide the same relative embedment depth (6*D*). The sequence of installation and loading tests started from the smallest to the largest scale model.

3.1.4.1. Helical anchor models for experiments on particle size effects

Four single helix anchor models with different sizes were used to provide a helical anchor prototype with 100 mm shaft diameter (full cross-section) and 330 mm helical plate diameter (D/d ratio equals to 3.3). The anchor models were composed of a steel helical plate welded to a round steel shaft, both fabricated with a maximum steel surface roughness R_{max} of 4.87 μm. The results of the steel roughness analysis are presented in the Annex A.

The helical plate embedment depth was equal to 6 times the plate diameter (1.98 m depth in prototype scale). The dimensions of the helical anchor models and their corresponding *g*-levels are presented in Table 5.

Figure 23 shows the four different single-helix anchor models tested in this investigation. The 6FH model differs from the others because this model was fabricated to be used in Tsuha's (2007) research. The other models were fabricated especially for this investigation on particle-size effects.

Table 5. Model piles characteristics.

Model anchor designation	Shaft diameter (d) in mm		Helix diameter (D) in mm		Helix pitch (p) in mm		Helical plate thickness (t_h) in mm		Helix embedment (z_D) in mm		G-level (×g)	d/d_{50}	D/d_{50}	p/D
	Model	Prototype	Model	Prototype	Model	Prototype	Model	Prototype	Model	Prototype				
6FH	6.0	100	20.0	330	1.6	26.7	0.5	8.4	120	1980	16.7	50	167	0.080
8FH	8.0	100	26.6	330	1.4	17.5	0.8	10.0	160	1980	12.5	67	222	0.053
10FH	10.0	100	33.0	330	2.5	25.0	1.8	18.0	198	1980	10.0	83	275	0.076
12FH	12.0	100	40.0	330	3.0	25.0	3.0	25.0	240	1980	8.3	100	333	0.075

Figure 23. Helical model anchors with fixed helix.

Figure 24 illustrates the effective contact area between anchor plate and granular soils, for cases of model anchors with different plate diameter, tested in the same sand sample, used to simulate the same anchor prototype.

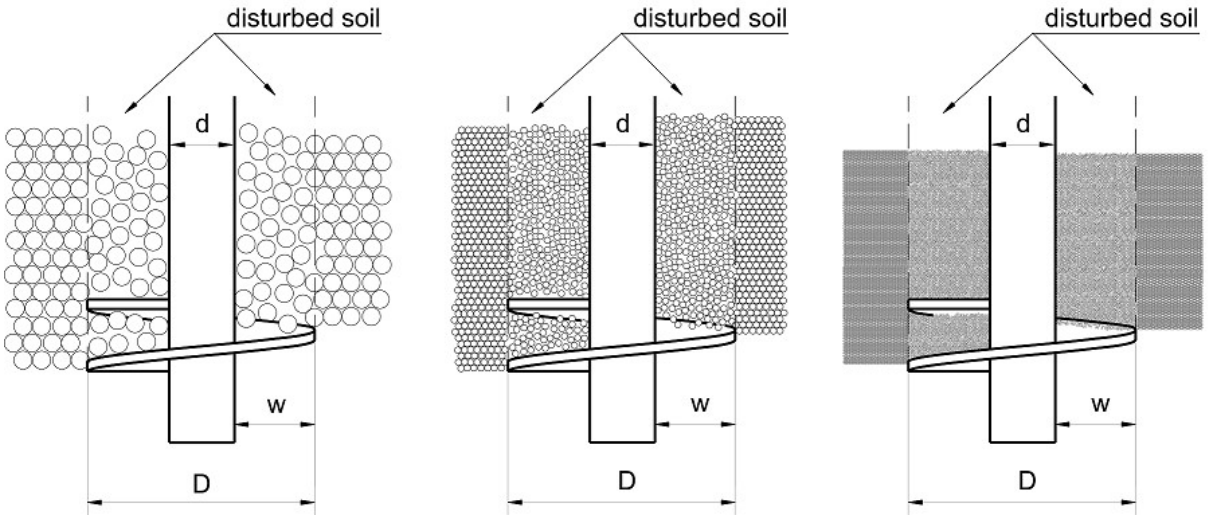

Figure 24. Helical anchor prototype simulated by anchor models of different sizes in the same sand sample.

In the case of anchor models of smaller plate diameter, Figure 24 illustrates that the number of grains at the plate interface is reduced compared to the case of regular plate anchors.

In the current work, the particle size effect on the plate bearing resistance of helical anchors is proposed to be correlated to the helix effective radius *w*:

$$w = 0.5(D - d) \qquad \text{Eq. 12}$$

where,

w is the effective helical radius

D is the helix diameter

d is the shaft diameter

3.1.5. Installation effect

The installation effect on the sand penetrated by the helices influences the uplift behaviour of helical anchors. Therefore, for a better understanding of the cyclic response of helical anchors in this study, different techniques were used to investigate the effect of the anchor installation on the uplift capacity, and to visualise the installation effect and the failure mechanism.

The influence of the installation effect on the helical anchor uplift capacity was investigated by comparing the model anchor response in two situations: a) model anchors were placed during the sand sample reconstitution by pluviation; b) model anchors were installed in flight. The pull-out test procedure was performed as described in section 3.1.3.

Three single-helix anchor models were used in this study: 6FH, 8FH and 10FH. The helix embedded depth for the three anchor models was 8D (see Table 5). The procedure of placing the model anchors during pluviation was intended to avoid any sand disturbance.

The sand pluviation in the strongbox was stopped when the sand level reached the helix embedment level. After that, the model anchor was placed on the sand sample and the sand deposition continued. Two parallel nylon lines were fixed on the top of the strongbox to maintain the anchor models in a vertical position. Figure 10 shows the nylon lines, four calibrated boxes and two helical anchor models already placed during the sand sample reconstitution. Figure 26 shows the sand sample with the anchor models after the pluviation.

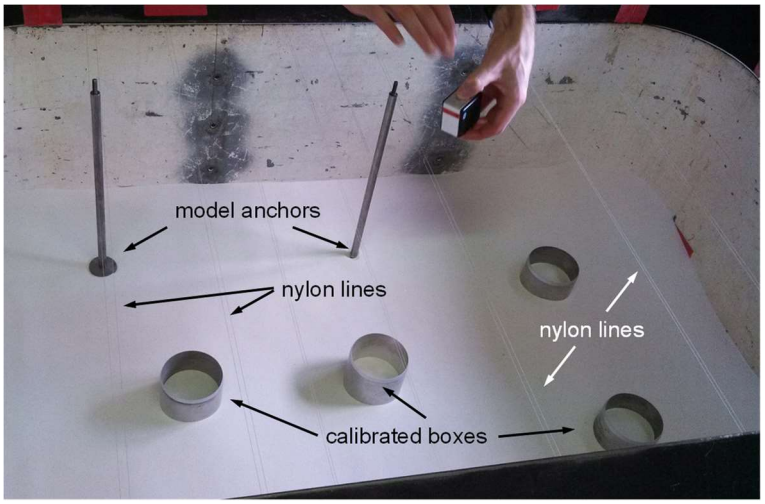

Figure 25. Installation of the helical anchor models during pluviation.

Figure 26. Sand sample reconstituted with helical anchor models placed during pluviation.

3.1.5.1. Sand sample excavation

Two sand samples were excavated after anchor installation in flight to evaluate the sand disturbance caused by the anchor model installation. For visualization of sand disturbance, thin layers of artificially coloured dark sand were prepared each at 40 mm depth, where the helical anchor models would be installed. The following sand samples with $I_D = 95\%$ were used in this investigation:

a) Container No. 5: the model 12FH was installed in flight until a helix embedment depth equalled to 255 mm (6.4*D*). After the installation, this anchor model was disconnected from the servo-controlling system. No pull-out test was performed (only installation).

b) Container No. 7: models 8FH and 12FH were installed in flight and then pulled up to a vertical displacement of the anchor head of 0.2*D*.

A special device (Figure 27) was fabricated to unpin model 12HF from the servo-controlled system to prevent any anchor movement after the test in Container No. 7. Model 12FH can move freely within this device, thus a pin is used to lock the model in place during the installation and pulling. After stopping the centrifuge, the pin is removed and the servo-controlled actuator can be elevated without moving the model anchor. The model 8FH was simply unscrewed from the hydraulic actuator after the end of the test by making the servo-controlled system rotates in the opposite direction of installation.

Figure 27. Device for 12HF connection.

For the sample excavation after the anchor installation and pull-out test, it is necessary to moisten the sand sample. The water content was controlled by adding water over the strongbox to provide some temporary cohesion due to matric suction. The sand surface was protected by a geotextile to avoid erosion of the sample surface. The sample excavation (Figure 28) was done at least 6 hours after the addition of water.

Figure 28. Sample excavation for the visualisation of installation and failure mechanisms.

3.1.5.2. Tomography

A helical anchor model fabricated in plastic (6HFp) was used to investigate the density changes in a sand sample after the installation (Figure 29). As the dimensions limits of the (X-ray) CT scanner are 60 mm in the three axes, the helical anchor model was fabricated with the size corresponding to the 6FH model.

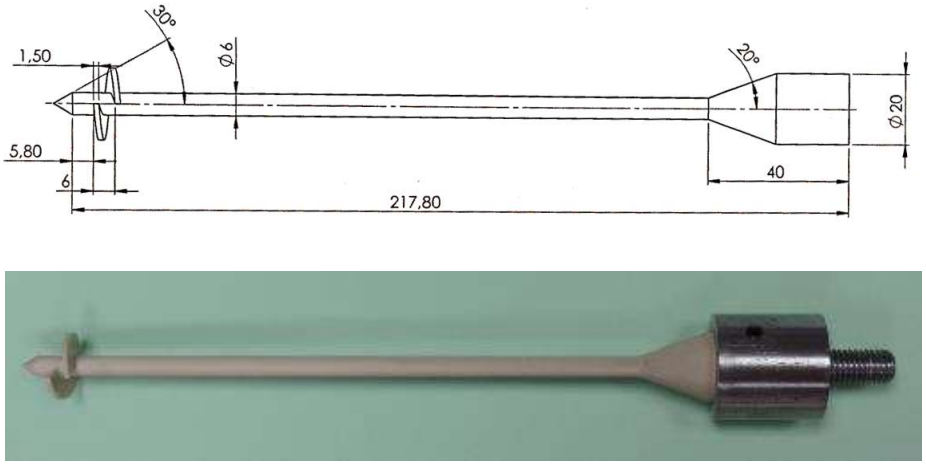

Figure 29. 6FHp plastic model (dimensions in mm).

The 6HFp was installed in flight with the helix at a 150 mm depth (7.5*D*). After installation, the plastic anchor model was pulled up 10 mm (0.5*D*), and then the centrifuge was stopped to disconnect the model. A steel coupling device was fabricated to permit an easy disconnection between the model and the servo-controlled system (Figure 30).

Figure 30. Coupling device.

The sand sample was moistened (as described in 3.1.5.1) to insert of two PVC tubes (external diameter = 55 mm and length = 170 mm) to extract the specimens for analysis (Figure 31). One PVC tube was used to recover the plastic model anchor + sand, and the other PVC tube was used to extract a non-disturbed sand specimen.

Figure 31. Extraction of specimens (with and without a model anchor).

The X-ray micro-tomography analysis was kindly performed by Dr. Christophe Dano with the micro-tomography apparatus of the Ecole Centrale de Nantes. The digital image processing was also performed by Dr. Dano.

3.1.6. Evaluation of shaft and helix bearing resistances

The evaluation of the individual contribution of shaft resistance and helix bearing resistance to the total helical anchor uplift capacity was done using two different methods: a) comparison between the uplift capacity results of the fixed and removable helix model anchors; b) uplift tests on an instrumented helical anchor model.

The removable helix models (Figure 32) were constructed with a male-female connection with a square cross-section designed to transfer torque during installation and allow the separation of the anchor shaft from the helix during the shaft pull-out tests.

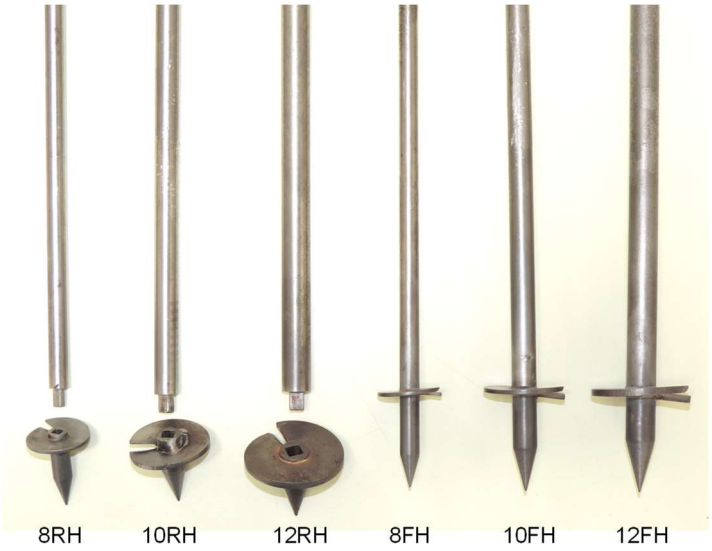

Figure 32. Removable (RH) and fixed (FH) helix model anchors.

The instrumented anchor model 10HFi was fabricated with one force gauge positioned just above the helix and other at the top shaft. A rotary switch was coupled to the anchor top to permit the data acquisition of both strain gauges while the anchor turned during the installation. Figure 33 shows the instrumented 10FHi model. The characteristics of the force gauge are presented in Annex B.

Figure 33. 10FHi instrumented model.

Table 6 presents the model anchor characteristics used for both analyses. The tests on the removable helix models were carried out in containers No. 2, 3 and 4. Tests on the instrumented anchor model 10FHi were carried out in container No. 9. The installation and loading test procedures were conducted as described in 3.1.3.

Table 6. Models characteristics (model values).

Model	Type	d (mm)	D (mm)	Pitch (mm)	Helical plate thickness (mm)	z_D/D	g-level
Prototype	fixed helix	100	330	41.2	25	various	-
8RH	removable helix	8	26	3.3	0.8	8	12.5
10RH	removable helix	10	33	4.1	1.8	7.4	10.0
12RH	removable helix	12	40	5	3	6	8.3
8FH	fixed helix	8	26	1.4	0.8	8	12.5
10FH	fixed helix	10	33	2.5	1.8	7.4	10.0
12FH	fixed helix	12	40	3	3	6	8.3
10FHi	instrumented	10	33	9.7	2.5	7.4	10.0

3.1.7. Cyclic loading tests on single-helix anchor models in centrifuge

Cyclic tensile loading tests were conducted in this study to evaluate the effect of the combination of mean load and load amplitude, and of the number of loading cycles on the helical anchor response.

Cyclic loading tests with different combinations of load amplitude, mean load and number of cycles were performed in eight sand samples reconstituted with dry HN38 Hostun sand with a density index (I_D) ranging from 94 to 99%.

Model 10FH, previously described in section 3.1.4.1, was cyclically tested in Containers No. 4, 5, 6 and 7. Model 10FHi, previously described in section 3.1.6, was tested in Containers No. 9, 10, 13 and 14. Both models had helix diameters equal to 33 mm and shaft diameters equal to 10 mm.

3.1.7.1. Cyclic loadings

One of the objectives of the cyclic loading tests was to evaluate the cyclic stability of single-helix anchors in sand using Interaction Diagrams. Therefore, the cyclic tests were performed in a range of pre-tensile load (Q_{pre}) to reproduce the common range in the practice. The application of a pre-tensile load intends to simulate the pre-tensile load of a helical anchor used to support guyed anchor towers, even in the absence of cyclic loadings. This pre-tensile load is equivalent to the minimum cyclic load (Q_{min}).

The cyclic loading characteristics Q_{mean} and Q_{cyclic}, normalized by the anchor uplift capacity before cycling (Q_T), are plotted in Figure 34, which presents all the cyclic tests performed for this research. The number of cycles to failure in each test can be marked in the plot. The contours of the number of cycles to failure (100 and 1000) define three stability zones. In the current research, the number of cycles of the cyclic tests ranged between 1000 and 3000. For cyclic loadings with greater maximum load (Q_{max}), a lower number of cycles were performed. Table 7 presents the main characteristics of the cyclic loadings.

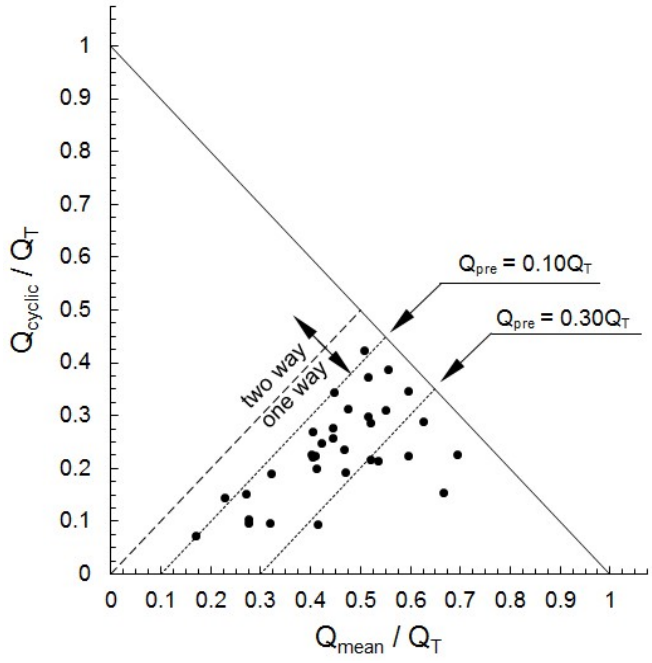

Figure 34. Points of experiments on the Interaction Diagram.

The installation of the helical anchor model was carried out to the maximum stroke of the servo-controlled system, which provided a helix embedment depth (z_D) of 7.4D (244 mm in model scale). After the installation, the system was maintained standing at a minimum of 3 minutes and then, the pre-tensile loading (Q_{pre}) was applied.

The pre-tensile load ranged from 10% to 50% of the anchor uplift capacity; however the majority of the tests were performed with pre-tensile loads between 10 and 30% (as showed in Table 7). After the application of the pre-tensile load and before starting the cyclic loadings, another three minute pause was taken. After the cyclic loading, a monotonic pull-out test was performed 3 minutes (or more) after the end of the cyclic test. Figure 35 illustrates the complete procedure of the cyclic load tests.

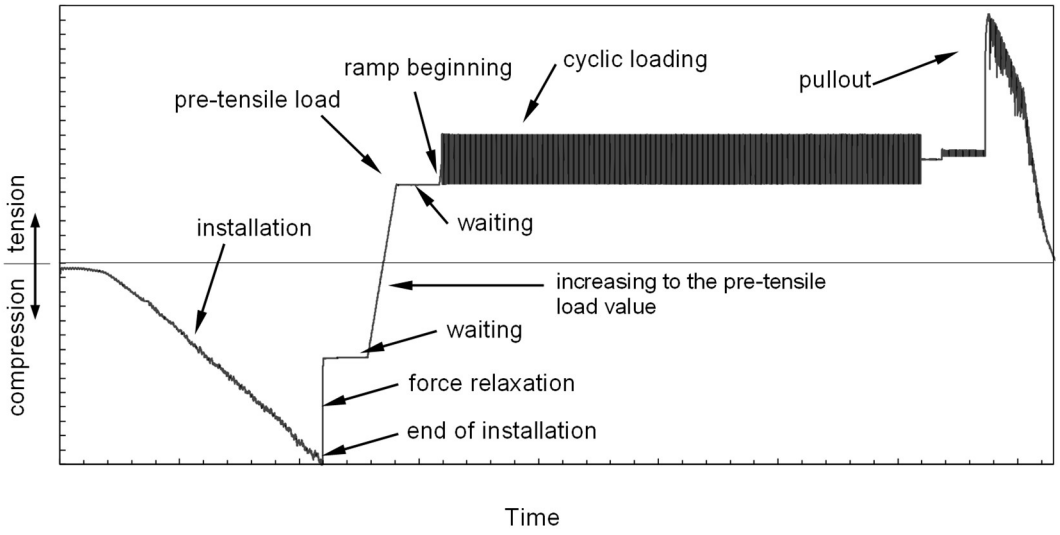

Figure 35. Description of the cyclic loading test procedure (model scale).

Table 7. Characteristics of the cyclic load tests carried out.

Sample	Model nº	Q_{mean}/Q_T	Q_{cyc}/Q_T	Pre-load/Q_T	Cycles
4	10HF-3	0.17	0.07	0.10	1500
4	10HF-4	0.23	0.14	0.09	1000
4	10HF-5*	0.32	0.23	0.10	1000
4	10HF-6*	0.42	0.32	0.10	63
5	10HF-2*	0.53	0.21	0.32	520
5	10HF-3	0.32	0.10	0.22	2000
5	10HF-4*	0.41	0.14	0.27	500
5	10HF-5	0.41	0.09	0.32	2000
5	10HF-6*	0.33	0.16	0.18	2000
6	10HF-1	0.32	0.19	0.13	2000
6	10HF-2	0.41	0.22	0.18	2000
6	10HF-3	0.47	0.19	0.28	2000
6	10HF-4	0.47	0.23	0.23	1000
6	10HF-5	0.28	0.10	0.18 0.19	3000 1000
6	10HF-6	0.45	0.26	0.19 0.18	1000 3000
7	10HF-1	0.45	0.26	0.32	2000
7	10HF-2	0.28	0.10	0.18	2000
7	10HF-5	0.54	0.21	0.23	1000
7	10HF-6	0.40	0.23	0.14	700
9	10HFi-3	0.52	0.29	0.12	1000
9	10HFi-4	0.41	0.27	0.18	1000
9	10HFi-5	0.27	0.15	0.17 0.18	3000 1000
9	10HFi-6	0.41	0.22	0.17 0.17	1000 3000
10	10HFi-1	0.28	0.10	0.30	1000
10	10HFi-2	0.45	0.28	0.22	1000
10	10HFi-3	0.45	0.28	0.21	1000
10	10HFi-4	0.27	0.10	0.37	1000
10	10HFi-6	0.52	0.22	0.51	1000
10	10HFi-7	0.52	0.30	0.47	1000
13	10HFi-1	0.41	0.20	0.16	1000
13	10HFi-2	0.60	0.22	0.24	1000
13	10HFi-3	0.67	0.16	0.14	1000
13	10HFi-4	0.69	0.23	0.25	1000
14	10HFi-1	0.48	0.31	0.08	1000
14	10HFi-2	0.55	0.31	0.10	1000
14	10HFi-3	0.51	0.37	0.18 0.17	1000 300
14	10HFi-4	0.60	0.35	0.17 0.17	1000 300
14	10HFi-5	0.51	0.42	0.34	1000

* test results not considered in the analysis because of problems in the servo-controlled system configuration

A software produced by Moog Inc. is used in the IFSTTAR centrifuge to control the servo-controlled actuator in force or in displacement. All the cyclic tests performed in the current research were force-controlled to satisfy the cyclic loading parameters (Q_{mean} and Q_{cyclic}) specified for each test. In some cyclic loadings, the servo-controlled system could not properly follow the set point due to a bad configuration of the P.I.D. Moog parameters (servo-control parameters in force). For a good agreement with the setpoint, the P.I.D. settings were adjusted to: P = 0.1, I = 0.1 and D = 0. Figure 36 illustrates the difference between cyclic loadings with coarse and fine P.I.D. adjustments.

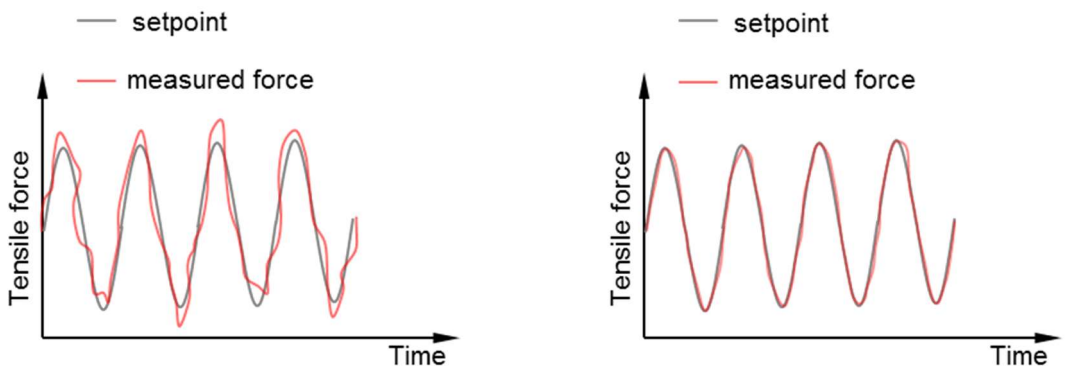

Figure 36. Cyclic loading with (a) coarse and (b) fine P.I.D. configuration.

3.1.8. Tests with two consecutive cyclic loadings

Test series of two consecutive cyclic loadings with different Q_{mean} and Q_{cyclic} and a different number of cycles were performed to evaluate the influence of a previous cyclic loading on the anchor cyclic performance. In addition, the post-cyclic responses were compared to evaluate which sequence of cyclic loadings causes greater post-cyclic capacity degradation.

For the first test, a cyclic loading with a large amount of cycles (from 1000 to 3000 cycles) of small amplitude was performed on the anchor model. After that, still in flight, a

cyclic loading with a larger amplitude and fewer cycles (from 300 to 1000 cycles) was carried out. After the second cyclic loading, a monotonic tensile load test was performed (Figure 37).

For a second test, the inverse sequence of cyclic loadings was conducted: (a) the first, a few load cycles with large amplitudes were carried out; (b) next, a greater amount of cycles with smaller amplitudes was applied, and then; (c) a monotonic tensile load test was conducted on the anchor model. The installation, cyclic loading and pull-out tests were performed in the same manner as for the single cyclic loadings tests (see section 3.1.7).

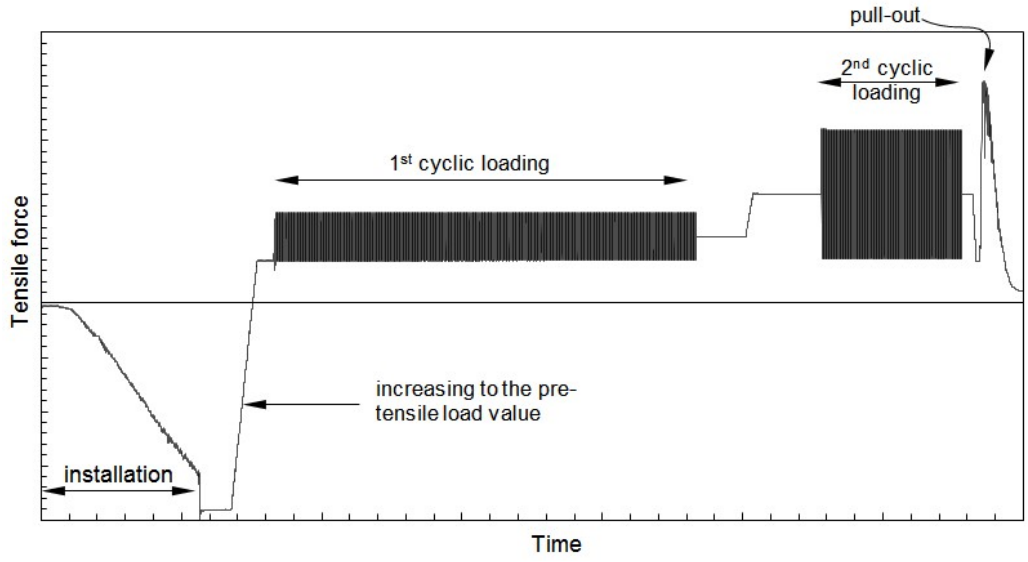

Figure 37. Two different cyclic loadings on the same helical anchor model.

3.2. Field tests

Two single-helix anchors with an instrumented section above the helix were used to carry out monotonic and cyclic tests at the Experimental Foundations Site of the University of São Paulo at São Carlos. These anchors were manufactured by Vercon Industrial and were termed as 1MHA (monotonically tested helical anchor) and 1CHA (cyclically tested helical anchor - monotonic tests were also performed after each series of cyclic loading).

The lead section of these single-helix anchors was composed of a cylindrical steel shaft with a 101.6 mm external diameter and a 7.1 mm wall thickness, and a helical bearing plate with a 305 mm diameter, a 12.5 mm plate thickness and a 75 mm pitch (Figure 38).

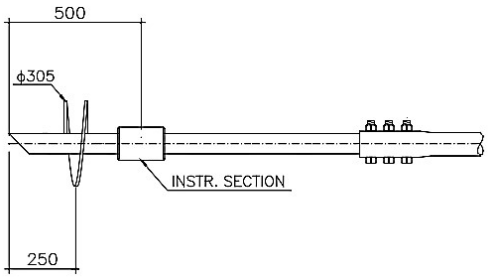

Figure 38. Instrumented lead section of the helical anchors tested (dimensions in mm).

The helical anchors were instrumented with strain gauges oriented in Wheatstone full bridge to measure the axial force in a shaft section 250 mm above the helix. Split steel sleeves covered the instrumentation to prevent damage during transportation and installation.

The strain gauges used were the PA-06-125BA-350-LEN simple unidirectional model polyamide based, designed steel, bondable type with a nominal resistance of 350 Ω. The strain gauges were bonded in pairs at opposite quadrants of the shaft cross section. In each pair, the strain gauges were bonded perpendicular to each other, one parallel and other perpendicular to the shaft's longitudinal axis.

The circuit was connected using a three-wire cable model 326-DFV manufactured by Vishay Precision Group. The cable comprises three twisted copper wires coated with tin with 0.404 mm diameter each wire (AWG 26).

The steel surface preparation for the strain gauges bonding was executed through the following process: i) solvent cleaning; ii) sanding (with sandpaper P60 and P120 grits); iii) cleaning with isopropanol; iv) application of conditioner and neutralizer; v) strain gauges fixing with cyanoacrylate adhesive.

The cables connecting the instrumented section to the data acquisition system were placed inside the anchor shaft. The hole to pass the cables was sealed with adhesive joints and the external protection of the circuit was assured with a split steel sleeve.

The instrumented sections of both anchors were calibrated using a 500 kN capacity load cell with 0.5 kN resolution, a hydraulic actuator attached to a manual hydraulic pump, and a steel reaction frame (Figure 39). Data acquisition was performed using a P3 Vishay Micro-Measurements data acquisition system (Vishay Precision Group, 2011), registering the electrical signals of the load cell and of the strain gauges.

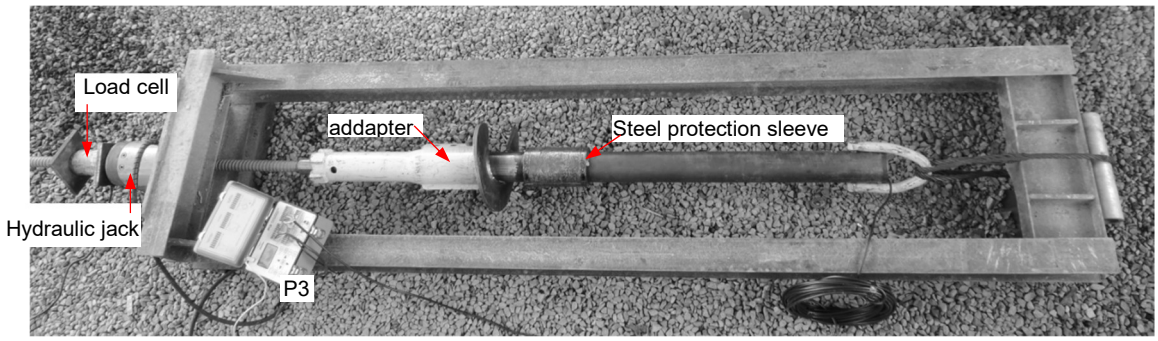

Figure 39. Calibration of the instrumented sections.

3.2.1. Experimental site at EESC-USP

The full-scale loading tests were conducted at the Experimental Site of the University of São Paulo at São Carlos. This site is located in the central region of the state of São Paulo in south-eastern Brazil. São Carlos is approximately 231 km from the city of São Paulo (Figure 40).

According to the Research Center for Applied Weather and Climate in Agriculture (CEPAGRI-UNICAMP), the Köppen Climate Classification for São Carlos is Cwa, presenting a tropical high-altitude climate with dry winter, with a minimum average temperature of 15.3 °C and a maximum of 27.0 °C (Cepeagri, 2016). Table 8 presents some data on the climate of São Carlos.

Figure 40. São Paulo state, by de Abreu (2006) - adapted.

Table 8. Climate of São Carlos (Cepeagri, 2016).

Month	Jan	Feb	Mar	Apr	May	Jun	Jul	Aug	Sep	Oct	Nov	Dec	Year
Avg. Max. Temp. (º C)	28.0	28.0	28.0	28.0	25.0	24.0	24.0	27.0	28.0	28.0	28.0	25.0	27.0
Avg. Min. Temp. (° C)	18.0	18.0	17.0	16.0	13.0	12.0	12.0	13.0	15.0	16.0	16.0	18.0	15.3
Rainfall (mm)	268.7	227.4	136.7	59.4	49.7	32.1	15.5	26.6	58.9	132.8	164.9	240.1	1422.8

The city of São Carlos is based on rocks of the “São Bento Group”, constituted of sandstones of the “Botucatu Formation” and migmatites of the “Serra Geral Formation”. Above these rocks, conglomerates and sandstones of the “Bauru Group” and, then, Cenozoic Sediments appear covering the whole region.

The typical geotechnical-geologic profile of the EESC-USP Experimental Site comprises a superficial layer of Cenozoic sediment composed of brown clayey sand (6 m thick), overlying a reddish clayey sand, originated from sandstone of the “Bauru Group” (Figure 41). The action of weathering under local conditions causes a laterization process, which results in a very porous and collapsible material that is the superficial layer. A line of quartz pebbles and limonite separates the two soil layers. Figure 42 and Table 9 present the soil’s granulometric characteristics at 3 different depths of the Experimental Site (3, 5 and 8 m depth).

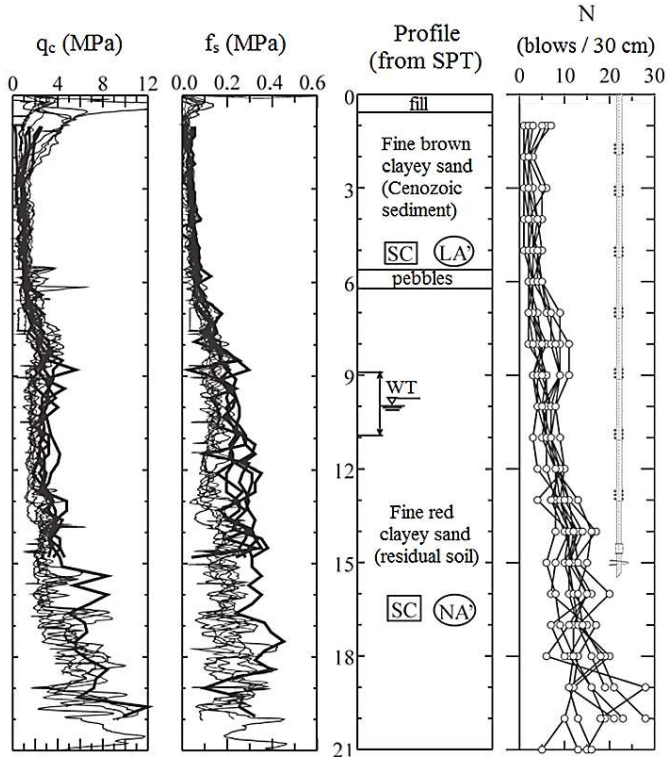

Figure 41. Soil profile at experimental site of the University of São Paulo at São Carlos, Brazil, after Giachetti *et al.* (2004) and Machado (1998).

The level of the groundwater table varies from 9 and 12 m depth, depending on the season of the year. Figure 41 illustrates the horizontal variability of this tropical soil site, observed in the results of CPT and SPT (N_{60}) tests presented in Giachetti *et al.* (2004) and in Machado (1998). The helical plates of both anchors were installed at a depth of 15 m to be embedded in the residual soil layer below the water table.

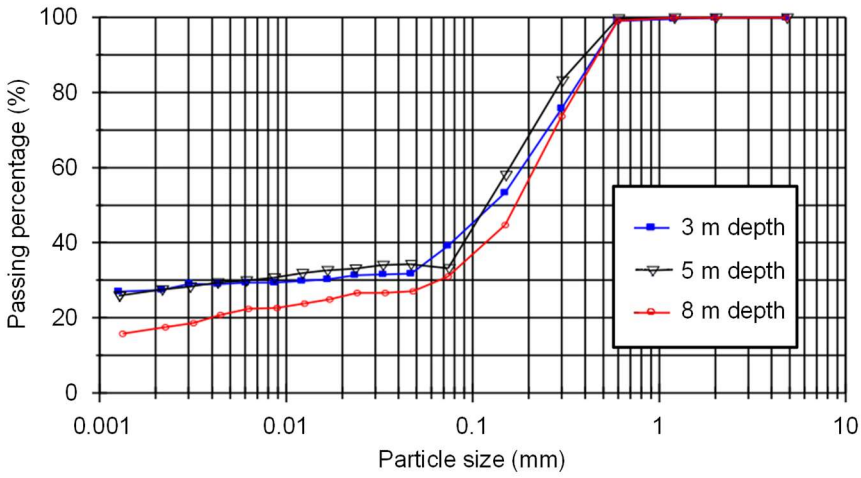

Figure 42. Soil granulometric distribution of the EESC-USP Experimental Site, after Machado (1998).

Table 9. Granulometric fractions of soils according to NBR 6502 (ABNT, 1995) , after Machado (1998).

Depth (m)	Sand (%)	Silt (%)	Clay (%)
3.0	60.8	11.9	27.3
5.0	66.7	5.90	27.4
8.0	68.9	13.7	17.4

Table 10. Soil characteristics obtained with undisturbed specimens, after Machado (1998).

Prof. (m)	1	2	3	4	5	6	7	8	9
Water content (%)	13.7	14.6	15.8	16.8	16.4	17.2	19.1	16.7	18.3
γ_d (kN/m^3)	12.5	13.6	13.8	14.3	14.4	14.7	15.2	16.1	16.6
γ (kN/m^3)	14.2	15.6	16.0	16.7	14.8	17.1	18.1	18.8	19.6
Void ratio	1.17	0.99	0.96	0.90	0.88	0.84	0.78	0.68	0.63
ϕ (º)[1]	-	29.0	-	-	31.2	-	-	26.4	-
c (kPa) [1]	-	0	-	-	10.5	-	-	26.9	-

[1] obtained from saturated triaxial tests

3.2.2. Helical anchor installation and load test procedure

The helical anchors were installed on May 16th, 2014. Each anchor was screwed into the ground with a hydraulic torque motor mounted on a backhoe loader, equipped with a digital torque indicator. The installation torque values were manually annotated every 0.5 m of penetration through the observation of the torquemeter display. Figure 43 shows the equipment used for the helical anchor installation and the torquemeter in detail.

The anchor 1CHA was tested monotonically and cyclically. Firstly, the 1CHA anchor was submitted to a monotonic tensile load test, and then, 4 cyclic and 4 monotonic tests were performed in an alternate fashion. Five monotonic tensile load tests were performed on reference anchor 1MHA, after the monotonic tests on anchor 1CHA were finished. Table 11 summarizes the loading tests carried out with both helical anchors.

Figure 43. Installation of an instrumented helical anchor at the test site.

Table 11. Field tests on MHA1 and CHA1 anchors.

Tested anchor	1MHA	1CHA
1st test	1st monotonic	1st monotonic
2nd test	2nd monotonic	1st cyclic
3rd test	3rd monotonic	2nd monotonic
4th test	4th monotonic	2nd cyclic
5th test	5th monotonic	3rd monotonic
6th test	-	3rd cyclic
7th test	-	4th monotonic
8th test	-	4th cyclic
9th test	-	5th monotonic

The monotonic and cyclic tensile load tests were performed using a hollow hydraulic jack with 450 kN capacity, and a reaction beam (composed of two 2.7 m long steel I-beams W530×92) centred over the anchor and resting on wood cribbing. A threaded rod was used to connect the hydraulic jack to the anchor. The applied load was measured using a 500 kN capacity load cell. The P3 Vishay Micro-Measurements data acquisition system was used to

register the applied load. The anchor head displacements were monitored using four dial-gauges with a resolution of 0.01 mm attached to two independent reference beams. Figure 44 shows the load test setup.

The axial load tests were conducted according to the Brazilian Standard ABNT-NBR 12131 (ABNT, 2006). The load was applied in increments of 5% of the estimated anchor uplift capacity, with 5 minutes of maintained load for each load step. The loading was applied until an anchor head displacement equal or higher than 10%D was reached. The unloading was performed in 5 steps of 5 min until a load of 10% of the ultimate tension capacity was reached. The last unload step was maintained for 60 minutes.

Figure 44. Load test setup.

The ultimate tension capacity was estimated in 100 kN, based on the results of a tensile load test presented in Tsuha (2007) on a double-helix anchor installed at the same EESC-USP Experimental Site ($D_{lower\ helix}$ = 254 mm, $D_{upper\ helix}$ = 304.8 mm and d = 73 mm). This helical anchor was installed with the lower helix at 14.4 m depth and presented an ultimate tension capacity of 170 kN.

A preload of 4 kN was applied to the anchors to eliminate gaps in the connections of the shaft extension segments. After this procedure, the acquisition system was zeroed and the load test commenced.

The cyclic load tests were carried out with the same pre-tensile load (Q_{pre}) in all of the tests, corresponding to 10% of the ultimate tension capacity obtained in the 1st monotonic test on the anchor 1CHA (Q_{T1}). The characteristics of the cyclic load tests are presented in Table 12. The applied loading was registered every 25 seconds, and the anchor head displacements were registered 2 times per cycle, when the applied load reached the Q_{max} and Q_{min} values.

Table 12. Characteristics of the cyclic load tests on anchor 1CHA.

Cyclic test	Q_{mean}/Q_{T1}	Q_{cyclic}/Q_{T1}	Number of cycles	Period (s)
1st test	0.15	0.05	50	60
2nd test	0.25	0.15	50	60
3rd test	0.35	0.25	50	60
4th test	0.58	0.48	50	60

3.3. Numerical modelling

Numerical analyses using the finite element method (FEM) were carried out with Abaqus/Explicit FEM suite to simulate the pre- and post-cyclic uplift response of the helical anchor tested in centrifuge.

Parametric analyses of different properties of the soil disturbed by the anchor installation were carried out to evaluate the model response sensitivity of each parameter. The helical anchor prototype simulated in the numerical modelling presented the same geometrical characteristics as the prototype simulated in the centrifuge modelling. The measured and numerical results are compareble in this study.

3.3.1. Explicit and implicit (Abaqus/Standard) analysis

An explicit FEM analysis performs the incremental procedure and at the end of each of the increment updates the stiffness matrix changes based on the geometric and material changes. Then a new stiffness matrix is constructed and the following increment is carried out. In this type of analysis the increments are small enough to produce accurate results. One problem lies in the need for a large number of very small increments for accuracy, which causes a large computational cost along with it being time consuming. If the number of increments is not sufficient, the calculations tend to deviate from the correct solution. This is due to the fact that force balance is not strictly enforced, i.e., this method does not enforce force balance of the internal structure reaction forces with the externally applied loads.

An explicit analysis is a function of time. Thus, the velocity and acceleration, as well as the mass and damping, have to be considered. In an explicit method, Central Difference Time Integration (CDTI) is used to calculate field variables at respective nodal points. Since only a numerical solution is possible for a non-linear ordinary differential equation, the explicit method is particularly suited for non-linear problems (CAE ANALYSIS, 2011). It requires the inversion of the lumped mass matrix as opposed to that of the global stiffness matrix in the implicit methods. In the CDTI, the equation of motion is evaluated at the previous time step (t_n-1, where t_n is the current time-step).

An implicit FEM analysis is analogous to the explicit analysis with the addition that, after each increment, Newton-Raphson iterations are carried out to ensure the force balance of the internal structure forces with the externally applied loads. Force balance is enforced to a specified tolerance. One drawback of the method is that during the Newton-Raphson iterations one must update and reconstruct the stiffness matrix for each iteration, and this can be computationally costly. However, larger increments are possible and the accuracy is typically higher than in the explicit case.

In an implicit scheme, displacement is not a function of time. Hence the velocities and accelerations which are time derivatives of displacement turn out to be zero and the mass and damping factors can be neglected. In order to solve a FEM problem using the implicit method, inversion of stiffness matrix is required. Very large deformation problems, such as crash analysis, can result in millions of degrees of freedom which effectively increase the size of the stiffness matrix. The larger the stiffness matrix, the longer the required computational time for its inversion. Hence, there is a need for an explicit method that would prevent the inversion of the stiffness matrix.

According to Helwany (2007), implicit (static) analysis is the evident option for numerical simulations of footings since the load application is static, inducing no dynamic effects in the model. However, in situations with expected severe distortions, a static analysis may terminate when a few soil elements near a geometric singularity are excessively distorted. For this type of situation, progressive failure and post-failure conditions are able to be analyzed if explicit/dynamic formulations are used with caution. If the explicit/dynamic scheme is employed, the velocity of loading application must be very low to avoid “exciting” the finite element model.

In the current research, the Standard/Implicit analysis was chosen primarily for modelling the helical anchor response. However, excessive distortion of the soil elements

caused the termination of the analysis after a few millimeters of anchor displacement (around 5 mm). Therefore, explicit/dynamic analysis was chosen to simulate the quasi-static problem of the helical anchor model under tensile loading.

3.3.2. Model geometry, boundary conditions, finite elements and mesh characteristics

The numerical model was constructed with similar geometrical characteristics to the prototype simulated by the centrifuge modelling: a single-helix anchor with a helix diameter of $D = 330$ mm and a full cross-section shaft diameter of $d = 100$ mm. The numerical simulations comprised a unique helix embedment depth of $z_D = 7.4D$, that is the helix depth adopted for the cyclic tests and some monotonic tests with models 10FH and 10FHi in centrifuge.

In the current investigation, the installation effect on the soil mass was considered in a simplified manner, assuming a cylinder of disturbed soil with different characteristics (compared with the undisturbed soil) around the anchor shaft. Therefore, the model geometry was constructed considering that the helical anchor was already installed into the ground. The geometrical characteristics and the model mesh are shown in Figure 45.

A distinct cylindrical zone of disturbed soil by the anchor installation was established according to experimental observations about the installation effects. The cylindrical zone of disturbed soil was considered with a radius 3 cm larger than the helix radius because the Abaqus software requires that any model part must have its left boundary over the axis of symmetry. Therefore, the disturbed soil above the helix and the soil below the helix were considered as the same material and therefore appropriate to be combined. Then a 3 cm × 3 cm zone was created to the right of the helix to join the soil above with the soil below the helix.

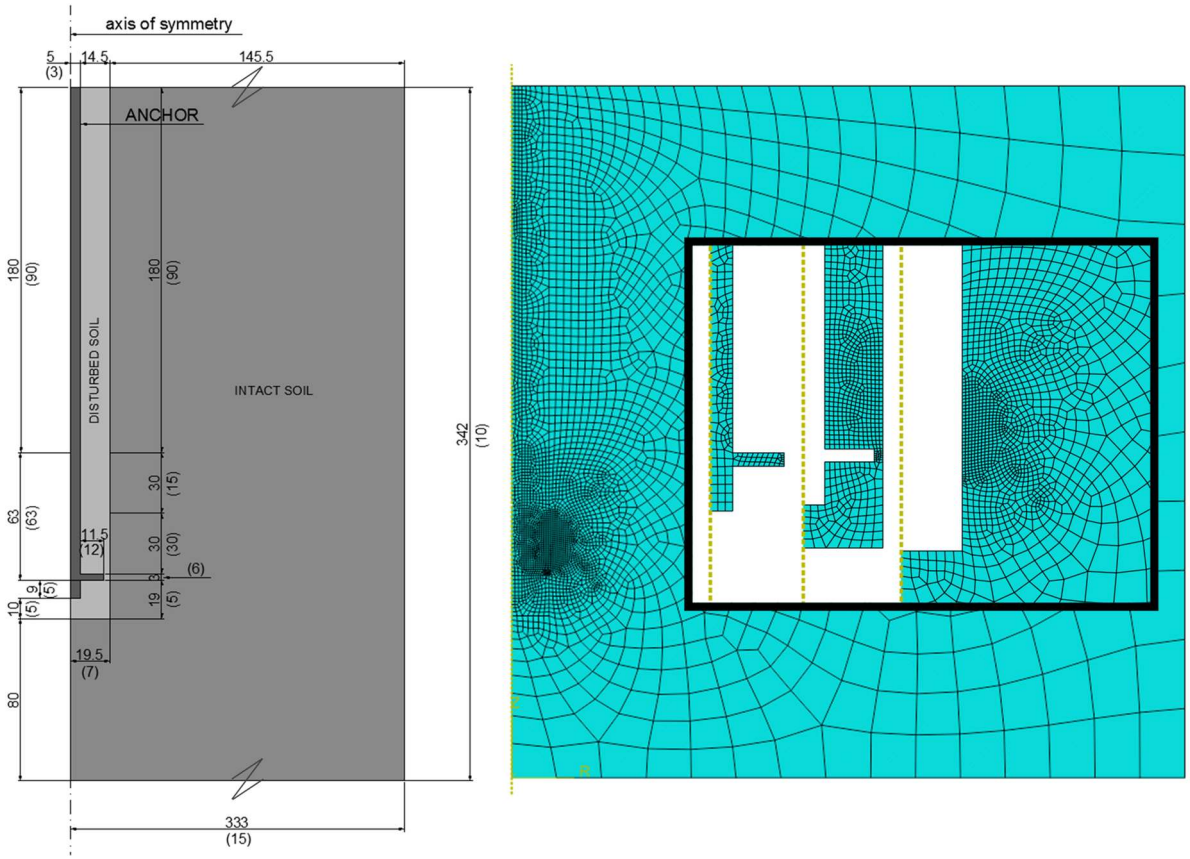

Figure 45. Geometric and mesh characteristics, distances in centimetres (the numbers in parenthesis indicates the number of elements the line was divided).

In the Abaqus software, the axis of symmetry is established on the left boundary of the model. Vertical and horizontal displacements were restrained at the model base, and the right boundary had the displacements restrained in the horizontal direction.

The model included three principal zones. The undisturbed soil mass was modelled with 2105 elements and 2192 nodes using CAX4R elements, which are 4-node bilinear axisymmetric quadrilateral elements with reduced integration (with second-order accuracy). The disturbed soil cylinder was modelled with 1101 elements and 1249 nodes and the anchor was modelled with 478 elements and 629 nodes, both using CAX4R elements. The whole model was comprised of 3684 elements and 4070 nodes. Due to the large deformations caused during the loading stage, model re-meshing was adopted to prevent excessive mesh distortion in the disturbed soil zone. The arbitraty Lagrangian-Eulerian (ALE) technique was used in the

analyses. This technique combines the features of the Lagrangian and Eulerian analyses, as illustrated in Figure 46.

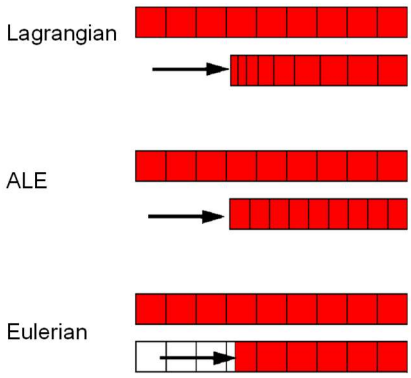

Figure 46. Motion of mesh and material with Lagrangian, ALE and Eulerian methods (Abaqus, 2005).

3.3.3. Constitutive models

The numerical model basically involves two materials: i) steel for the anchor; ii) sand for the soil. The material behaviour for the helical anchor (steel) is assumed as linear-elastic with no material yielding given the low stresses generated by the applied loading. The material properties used in the helical anchor are shown in Table 13. The density material for the anchor was chosen equals to the soil density to avoid convergence issues during the gravity loading step.

Table 13. Material properties considered for the helical anchor.

Young modulus	E = 200000 MPa
Poisson ratio	ν = 0.3
Density	ρ = 1555 kg/m³

For modelling the soil material (sand), the Abaqus software provides the following plastic constitutive models suitable for modelling problems involving soils: Mohr-Coulomb plasticity, extended Drucker-Prager, modified Drucker-Prager/Cap model and the Critical

state (clay) plasticity model. In addition, the software allows the implementation of different constitutive models.

The soil material (sand) was modelled with the Mohr-Coulomb plasticity associated with linear elasticity. The Mohr-Coulomb criterion assumes that yield occurs when the shear stress on any point in a material reaches a value that depends linearly on the normal stress on the same plane. The flow potential for the Mohr-Coulomb yield surface is chosen as a hyperbolic function on the meridional stress plane and the smooth elliptic function proposed by Menétrey and Willam (1995) on the deviatoric stress plane (Abaqus, 2014).

The mechanical properties of the undisturbed soil were obtained through triaxial tests (see Appendix C), and the bulk density was obtained with density boxes placed on the bottom of the strongboxes (Table 14). In addition, a numerical analysis of the triaxial tests with 3 confining stresses was carried out to compare the results.

A parametric analysis was carried out for the soil disturbed by the passage of the helix and shaft by varying the Young modulus and the internal friction angle of the soil. Thus, the agreement between the numerical and experimental results pre- and post-cycles was evaluated. These results are presented in section 6.

Table 14. Material properties considered for the undisturbed sand.

Young modulus	$E = 50$ MPa
Poisson ratio	$\nu = 0.3$
Angle of internal friction	$\phi = 47^o$
Cohesion	$c = 0$
Meridional eccentricity	$\epsilon = 0.1$ (software default)
Deviatoric eccentricity	$e = (3 - \sin\phi) / (3 + \sin\phi)$
Coefficient of lateral pressure	$K_s = \nu / (1 - \nu)$
Bulk density	$\rho = 1555$ kg/m³

3.3.3.1. Numerical modelling of triaxial compression tests

The triaxial compression tests on HN38 Hostun sand specimens were also numerically simulated with Abaqus/Explicit. The cylindrical sand specimen with a 100 mm diameter and 200 mm high was modelled in the axisymmetric condition. The vertical and horizontal displacements were restrained at the base and the left-hand boundary was the axis of symmetry. A confining stress was applied at the top and right-hand boundaries of the specimen and the deviatoric stress was applied to the top of the specimen by an axial displacement with a 0.05 mm/s displacement rate. The previously described elements CAX4R were used to compose the finite element mesh with 216 elements, each with approximately 1 mm side.

Figure 47 presents the numerical modelling results of the three triaxial tests. A slightly greater angle of internal friction was found for the test with the lowest confining pressure (σ_3 = 50 kPa – Figure 47a) in comparison to the other two tests (Figure 47b and c).

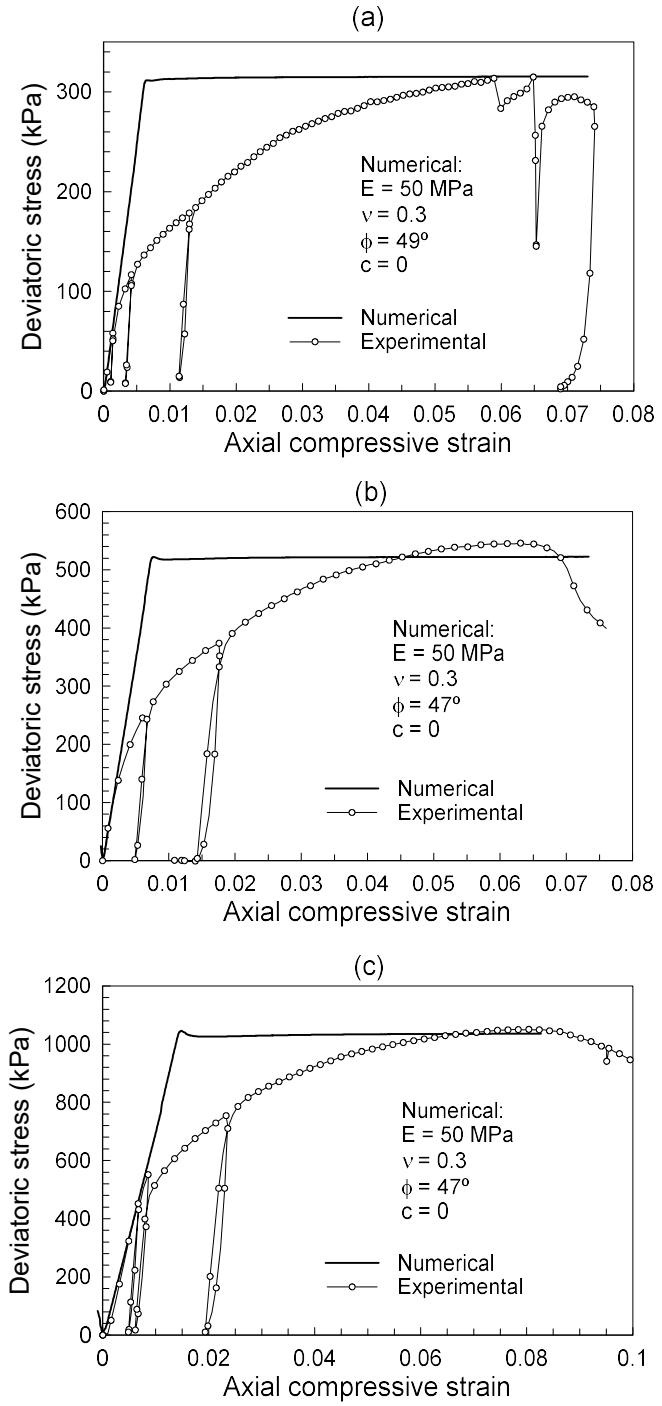

Figure 47. Experimental and numerical results of triaxial compression tests: (a) σ_3 = 50 kPa; (b) σ_3 = 100 kPa; (c) σ_3 = 200 kPa.

3.3.4. Interfaces

The consideration of 3 different zones in the numerical model required the use of interaction models for the anchor-disturbed soil interface and for the boundary between the

disturbed soil and the undisturbed soil. The interface between the anchor (helix and shaft) and the disturbed soil was modelled as a surface-to-surface contact with normal and tangential mechanical behaviours attributed. Normal surface behaviour was established as a "hard" pressure-overclosure relationship (no contact pressure until nodes are in contact; unlimited contact pressure once contact has been established), and the tangential surface behaviour was defined using the penalty friction formulation with an interface friction angle δ =15º.

The nodes in the disturbed soil-undisturbed soil boundary were coupled using the tie interaction. This option imposes coupled interaction between pairs of surfaces. An additional verification was performed using the surface-to-surface contact option instead of the tie interaction. In this verification, the attributed interface normal stiffness was 1×10^{10} N/m and the tangential behaviour considered an interface friction angle equalled to the disturbed soil's angle of friction. No difference was noticed comparing the results of both considerations for the disturbed soil-undisturbed soil interface.

3.3.5. Numerical analyses parameters

The analysis of the numerical model was comprised of 3 steps: i) initial (software default); ii) gravity loading; iii) tensile loading. In the initial step, a geostatic stress pre-defined field was attributed to eliminate material strain caused by the application of the gravity load in the subsequent step. This pre-defined field establishes the geostatic stress and the coefficient of lateral pressure before the application of gravity as a load in the second step. The gravity was applied uniformly on the whole model.

The third step involved the application of the tensile loading as vertical upward velocity acting on the shaft top surface. After testing different velocity values, no influence on the results was observed for velocities less than or equal to 2 mm/s.

4. RESULTS OF PHYSICAL MODELLING OF SINGLE-HELIX ANCHORS IN SAND

4.1. Particle-size effects

For the verification of scale effects for modelling helical anchors in sand, the value of uplift capacity (Q_T) of the anchor models was assumed to be the peak tensile force measured during the pull-out tests (Figure 48). The peak uplift capacity ($Q_{T\ (peak)}$), is very close to the tensile load related to a displacement of 10% of the plate diameter, ($Q_{T\ (0.1D)}$), as shown in Table 15. This table shows that the Q_T results are similar in the range of models tested. The variability in the results of container No. 11 is probably due to the sample heterogeneity, as the other two samples provided uniform results for all models tested.

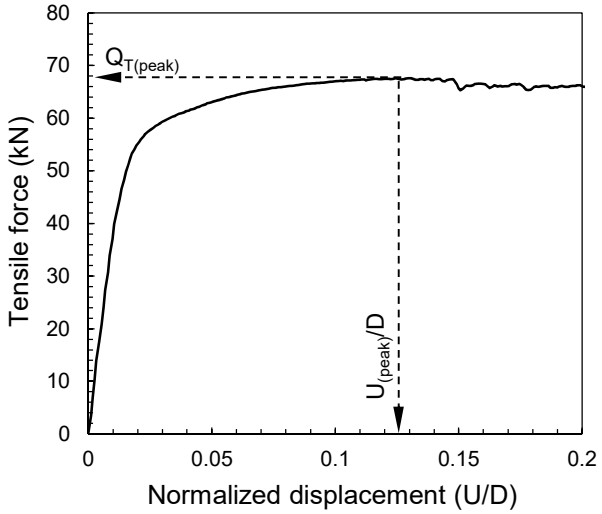

Figure 48. Identification of the peak tensile force for the monotonic test on model 10FH in Container No. 12.

Table 15 shows that the ultimate load was reached at a vertical displacement ranging from 10% to 16% of the helical plate diameter. The larger anchor models required slightly smaller displacements to attain the ultimate load; however, no clear trend was observed.

Table 15. Results of the investigation on the particle-scale effects.

Sand sample	Model	d/d_{50}	D/d_{50}	w/d_{50}	T_f (kN·m)	T_{avg-3D} (kN·m)	K_t (m^{-1})	$Q_{T\ (0.1D)}$ (kN)	$Q_{T\ (peak)}$ (kN)	$U_{(peak)}$ (mm)	U/D
Container No. 8	8FHa	67	220	77	-	-	-	54	55	52.9	0.16
	8FHb	67	220	77	-	-	-	51	53	48.3	0.15
	12FHa	100	333	117	-	-	-	57	57	36.6	0.11
	12FHb	100	333	117	-	-	-	56	57	42.7	0.13
Container No. 11	6FHa	50	167	58	6.9	3.7	17	62	63	46.5	0.14
	6FHb	50	167	58	5.1	2.9	17	49	50	38.5	0.12
	10FHa	83	275	96	6.5	3.8	18	67	67	36.5	0.11
	10FHb	83	275	96	6.8	4.3	16	67	68	40.4	0.12
	12FH	100	333	117	8.9	8.9	6	55	55	32.7	0.1
Container No. 12	6FH	50	167	58	6.9	4.3	16	65	67	53	0.16
	8FH	67	220	77	7.1	4.7	15	66	69	47.4	0.14
	10FH	83	275	96	7.8	5.0	14	67	68	38.3	0.12
	12FH	100	333	117	10.2	6.9	10	65	66	38	0.12
				Mean	7.4	4.9	14	60	61	42.4	
				Standard deviation	1.5	1.9	3.9	7	7	6.6	
				Coefficient of variation	20%	37%	27%	12%	11%	16%	

Figure 49 compares the ultimate uplift capacity according to the w/d_{50} ratio (effective helical radius$/d_{50}$) of the model anchors with different sizes. The average ultimate load of the 13 tests is 61 kN, with an 11% coefficient of variation (COV). The variation in the Q_T results probably occurred due to the variability in the sand samples and may not be attributed to particle size effects.

Previous studies on scale effects indicate that the values of bearing capacity and shaft resistance increase as the model size decreases (e.g. Ovesen, 1979 and 1981; Foray *et al.*, 1998; Garnier & König, 1998). The particle size investigation comprised monotonic tests on model anchors with w/d_{50} ratios ranging from 58 to 333. In this range of models assessed in this investigation, the almost horizontal trend line shown in Figure 49 suggests that no particle-size effect was observed for $w/d_{50} \geq 58$.

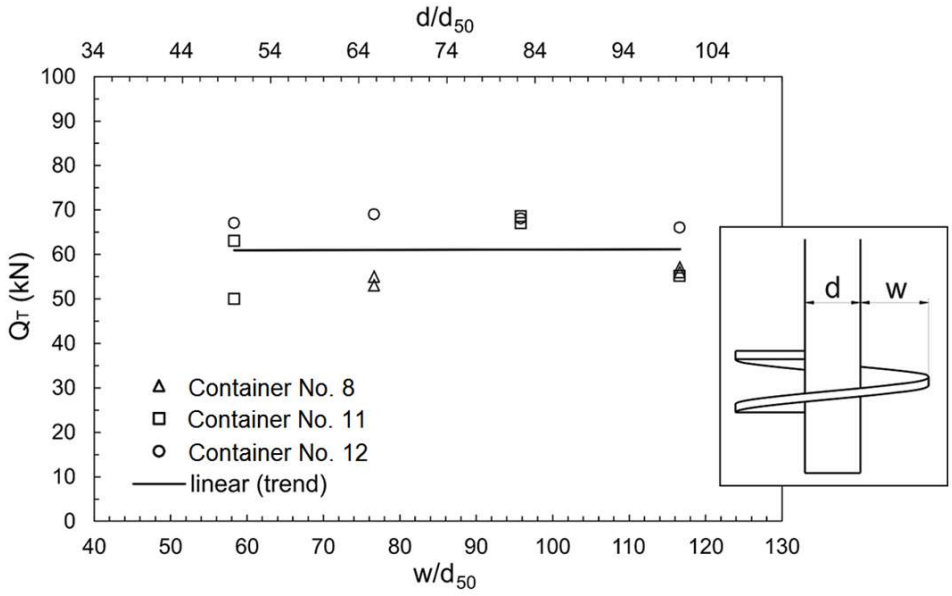

Figure 49. Ultimate tensile load of helical anchor models of different sizes (in prototype values).

The uplift capacity of the prototype simulated for this verification of scale effects was calculated by using Terzaghi's equation, as proposed in Adams and Klym (1972) for single-helix anchors, and using bearing factor N_{qu} presented in Mitsch and Clemence (1985) for single-helix anchors in sand. The predicted value was 120 kN, which is approximately twice the measured mean value of uplift capacity (61 kN).

Gavin *et al.* (2014) observed a similar difference between the results of numerical simulation and field experiments on a single-helix anchor in dense sand. These significant differences between the estimates and the measurements suggest that an important effect of the anchor installation is not considered in the prediction methods.

The results of installation torque necessary to install the anchor models tested in containers No. 11 and 12 are shown in Figure 50.

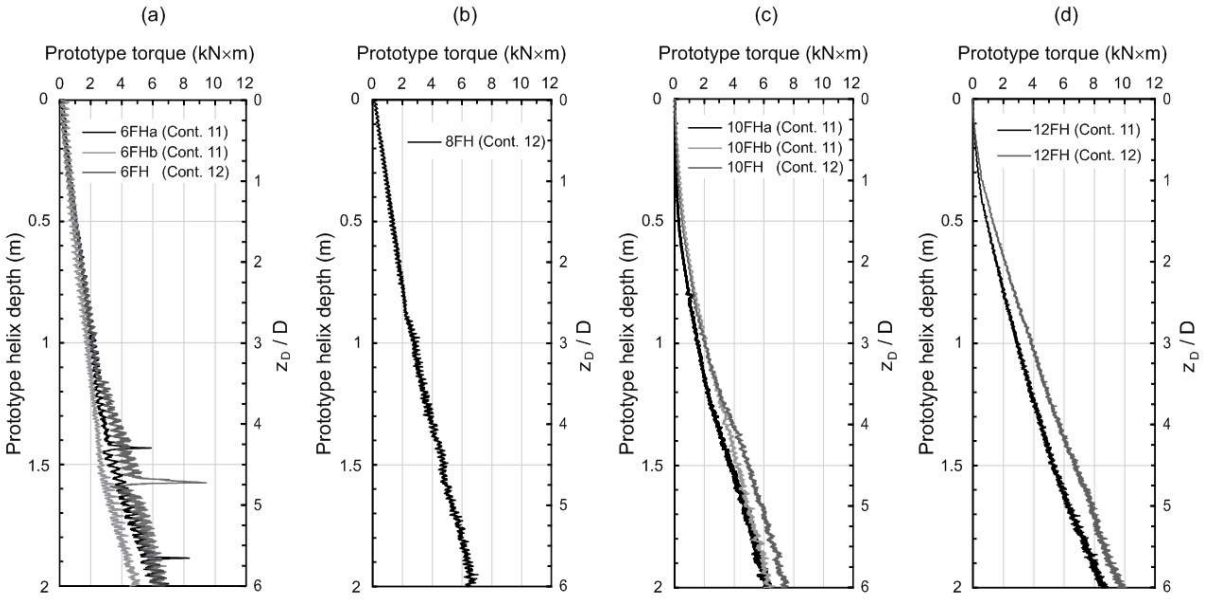

Figure 50. Torque readings during the installation: (a) model 6FH, (b) model 8FH, (c) model 10FH and (d) model 12FH, in prototype values.

Figure 51 shows that the final installation torque for models 10FH and 12FH is slightly greater than the results found for the other models. Models 10FH and 12FH were fabricated with a thicker helical plate (18.0 and 25.0 mm thickness in prototype scale, respectively) compared to models 6FH and 8FH (8.4 and 8.8 mm thickness in prototype scale) to avoid plate bending during installation. According to Sakr (2014), installation torque increases with helix thickness, since one of the torsional moment components acting on the helix is caused by the moment acting on side surface of outer perimeter of the helix. In addition, the thicker the helical plate, the greater the volume of the displacement soil by the passage of the helix. Thus, the torque gain observed in models 10FH and 12FH is not evidence of a scale effect on the results of torque measurements. Accordingly, Figure 51 suggests that the installation torque was not influenced by scale effects. This verification highlights that the centrifuge modelling technique can be used successfully for investigations on the installation torque of helical foundations using anchor models with a ratio w/d_{50} greater than 58.

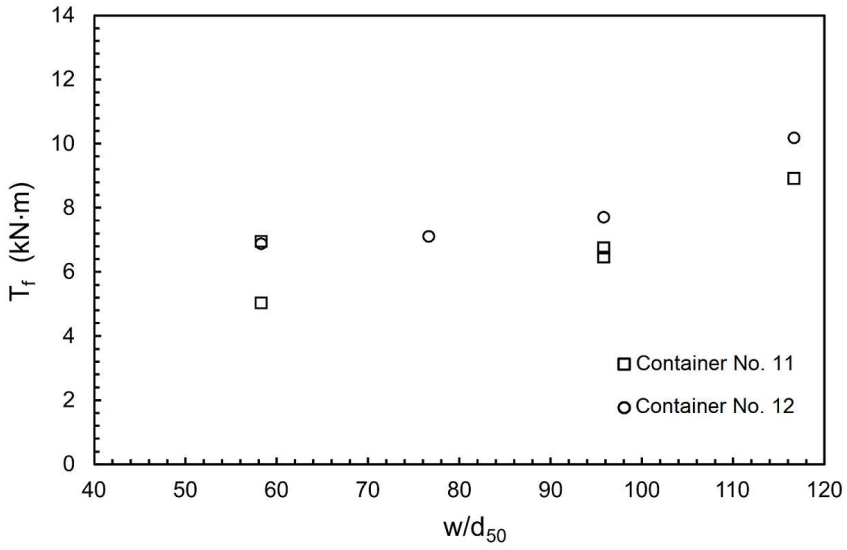

Figure 51. Final installation torque, in prototype values.

Hoyt and Clemence (1989) proposed an empirical relationship between the installation torque and the axial uplift capacity of helical piles, given by Eq. 13:

$$Q_T = K_t \times T_{avg-3D} \qquad \text{Eq. 13}$$

where,

$T_{avg\text{-}3D}$ = average of the torque measured along the final distance corresponding to 3 times the helix diameter;

K_t = torque correlation factor that varies with the shaft diameter.

To verify if the physical modelling well reproduced the field behaviour of helical anchors during installation and under tensile loading, K_t values were determined in this investigation, as presented in Table 15. The centrifuge tests provided K_t values of similar magnitude to the field measured value presented in Gavin *et al.* (2014) for a single-helix anchor with similar dimensions installed in dense sand. These authors found a K_t value of 13 m^{-1}, and the current centrifuge tests provided a mean K_t value of 15 m^{-1}. Therefore, no scale effect was observed in the simulation of a prototype K_t factor in the range of model sizes

tested. On the other hand, the coefficients of variation of of installation torque and K_t factor indicate that the resisting forces acting on the helical anchor during installation are more variable than the forces acting on the anchor under tensile loading.

4.2. Evaluation of installation effect

The evaluation of the installation effects on the uplift capacity of helical anchors in dry sand was done in this study using the three different techniques described below.

4.2.1. Comparison between anchors in disturbed and undisturbed sand

For a comparison between helical anchors in disturbed and undisturbed sand, pull-out tests were carried out on helical anchor models with a helix embedment depth of 8*D*, under two different conditions:

a) model anchors placed in the sand sample during the pluviation to eliminate the soil disturbance caused by anchor installation;

b) model anchors installed in flight to simulate the soil disturbance that occurs in field installation.

The results of the six uplift tests conducted with the anchors in both conditions of sand disturbance are presented in Table 16 and in Figure 52.

Table 16. Results of the uplift tests with model anchors in two different conditions.

Test	Condition	z_D/D	Q_T (kN)	$U_{(peak)}$ (mm)	$U_{(peak)}/D$
6FH Cont. No. 1	Placed before	8.0	38.5	45.9	0.14
6FH-2 Cont. No. 11	Installed in flight	8.0	104.5	49.7	0.15
8FH-1 Cont. No. 1	Placed before	8.0	31.4	51.2	0.16
8FH-1 Cont. No. 2	Installed in flight	8.0	89.3	77.6	0.23
10FH-1 Cont. No. 1	Placed before	8.0	55.8	52.6	0.16
10FH-1 Cont. No. 2	Installed in flight	8.0	88.0	63.9	0.19

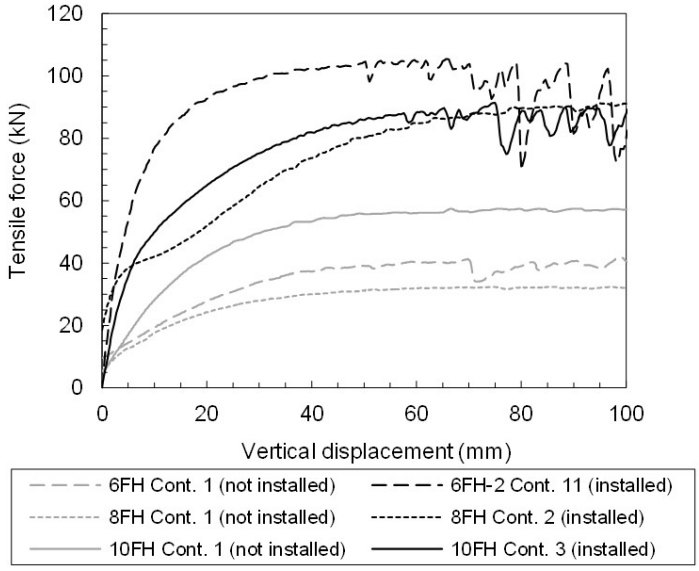

Figure 52. Results of the pull-out tests with anchor models placed during the sand pluviation (not installed) and installed in flight, in prototype scale.

The uplift capacity was lower for the anchor models placed during pluviation (with supposedly no sand disturbance). This observation contradicts Zhang (1999) that, after performing compression and tension loading tests on helical foundations, concluded that the installation effect causes soil loosening within the disturbed zone, reducing the helix bearing capacity. In the present investigation, the lower uplift capacity for the tests on model anchors in undisturbed sand may be related to a limitation in sample preparation. Since the model anchors were placed during sample preparation, the anchor models represented an obstacle for the sand pluviation process. The collision of the falling sand particles with the model anchors may have caused reduction of the kinetic energy of the sand particles, affecting the sample reconstitution around the model anchor. The zone of sand around the model anchors might be less dense than the rest of the sample, and consequently the uplift capacity of the anchors is reduced.

4.2.2. Images of sand movement during installation and after loading

For this thesis another verification of the installation disturbance effect was performed by excavating two sand samples: the first excavation was conducted in container No. 4 around the model anchor after the model installation in centrifuge; the second excavation was done in container No. 7 were models 8FH and 12FH were installed and tested in flight until the vertical displacement of the anchor model head attained 20%*D*. The objectives of these tests were: (i) understand sand movement during the helical anchor installation and (ii) visualize the failure zone after tensile loading.

During the sample reconstitution in both containers, a specific zone was prepared with horizontal thin layers of dyed dark sand (spacing ≈ 40 mm) for the installation of anchor model 12FH in said zone in flight.

Figure 53a shows a photograph of the sand sample after the anchor installation. In this figure, the disturbed sand around the anchor is clearly observed. The sand is dragged down near the shaft and the soil above the helix rises upwards (as observed in Komatsu, 2007). Figure 54 illustrates the movement of the sand grains due to the helical anchor installation.

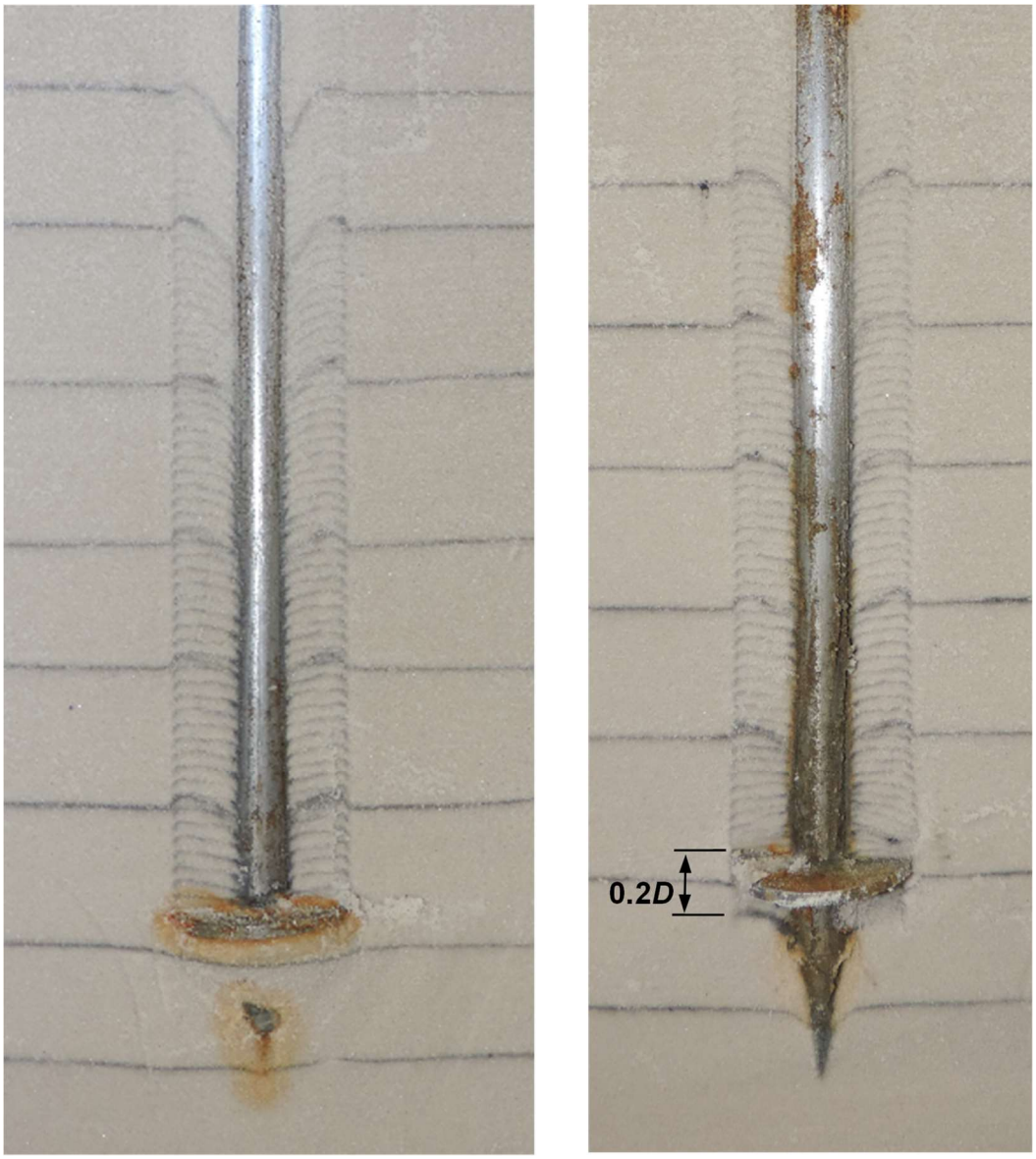

Figure 53. Photographs of the sand sample after excavation around the 12FH model: (a) after model installation, and (b) after uplift loading.

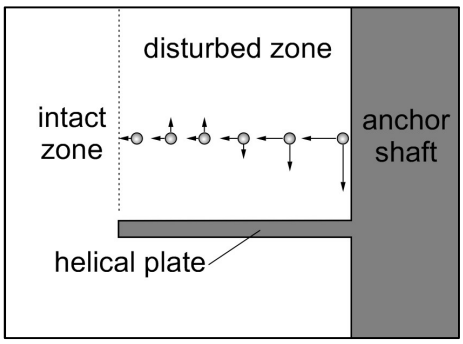

Figure 54. Installation effect: vertical and horizontal movement of sand grains that were aligned horizontally before the installation.

Figure 53b shows the sand sample after the model anchor displacement of 20%*D*. This figure indicates the soil directly above the helix controls the anchor performance. In this case, the anchor load-displacement response is controlled by the properties of the disturbed soil because the shear surface was located within the cylindrical installation zone. Additional photographs are presented in Appendix P.

4.2.3. Micro-tomographic analysis

Additionally, for the investigation of installation effects on the sand penetrated by a helical anchor in sand, micro-tomographic analyses were conducted in two samples: one with a plastic anchor model installed inside the sand, and the other with undisturbed sand prepared by the pluviation technique.

The plastic model anchor was installed in container No. 14 at an embedment depth of 7.5*D*, and submitted to an uplift loading with a maximum vertical displacement of 165 mm (0.5*D*) in prototype scale. The two samples were obtained by driving PVC tubes into the sand (disturbed and undisturbed). A verticality deviation of the tubes was observed due to the difficulty in maintaining a vertical guide during the driving.

Figure 55 shows the micro-tomographic images of the intact sand sample. Different shades of grey indicate horizontal thin layers with different densities than that is inherent to the sand sample reconstitution by pluviation. As the sand colour changes from light to dark grey, the sand becomes less dense. Nevertheless, the arrangement and thickness of the sand layers indicate uniform deposition of sand; and therefore, the sand mass characteristics can be assumed as uniform in the scale of the current experiments, despite the vertical heterogeneity if the sand is analysed with greater detail.

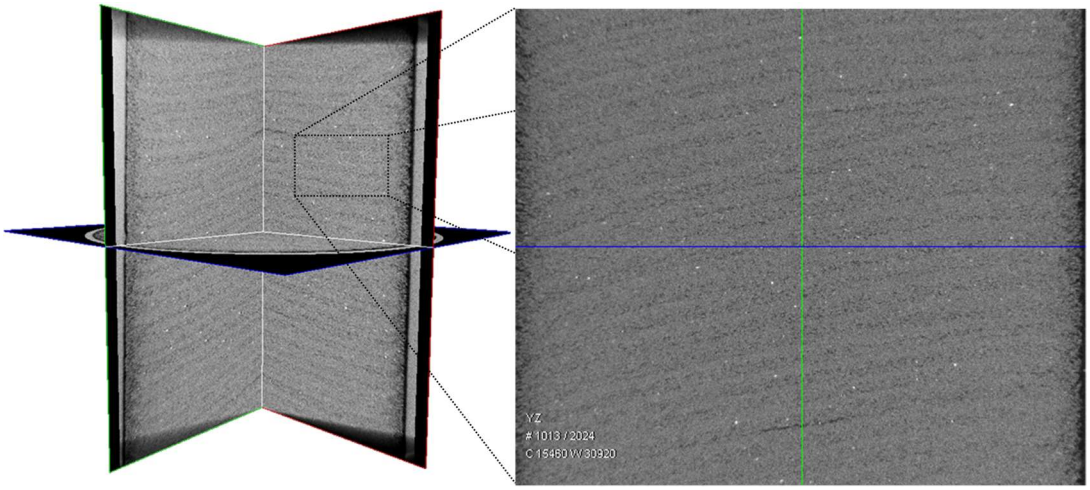

Figure 55. Micro-tomographic images of the intact sand specimen collected from container No. 14.

The micro-tomographic image of the sand specimen with the plastic model anchor inside, shown in Figure 56, illustrates darker shades of grey that correspond to the cylindrical zone of disturbed sand around the shaft penetrated by the helix. In addition, a gap and a less dense sand zone are noted below the helix, caused by the uplift movement of the model anchor. As the model moved up, the sand particles around and below the helix moved toward the gap.

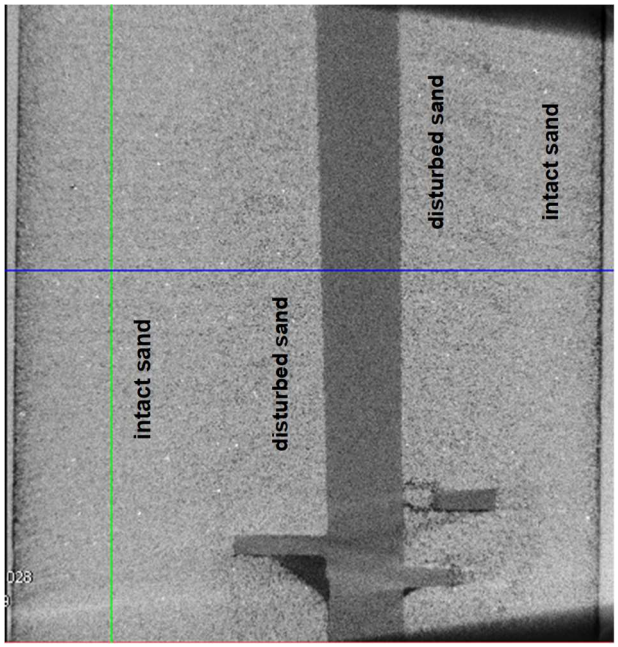

Figure 56. Micro-tomographic longitudinal section of the sand specimen with the plastic model anchor inside after a vertical uplift of 0.5*D*.

Figures 57a and b show that the sand around the helix and around the shaft present different densities compared to the rest of the sand specimen. Close to the shaft, there are zones of both light and dark grey corresponding to dense and less dense sand, respectively (Figure 57a). This observation suggests that the sand disturbance is not uniform along the cylindrical zone above the helix, and that the configuration of dense and less dense zones depends on the patch followed by the helix. The same observation can be used for the zone around the helix illustrated in Figure 57b. This figure shows that the concentration of dark grey colour is more noticeable in one quadrant of the helix circumference. These observations support the hypothesis that during the model anchor installation, the traversed and displaced sand by shaft and helix during installation experiences different degrees of disturbance. Possibly during the installation, the helix pushes up the undisturbed sand, and after the helix passage, the sand moves down to fill the gap created when the helix leaves this region. These sand layers are only slightly affected by the helix movement and, therefore, these layers of sand remain dense.

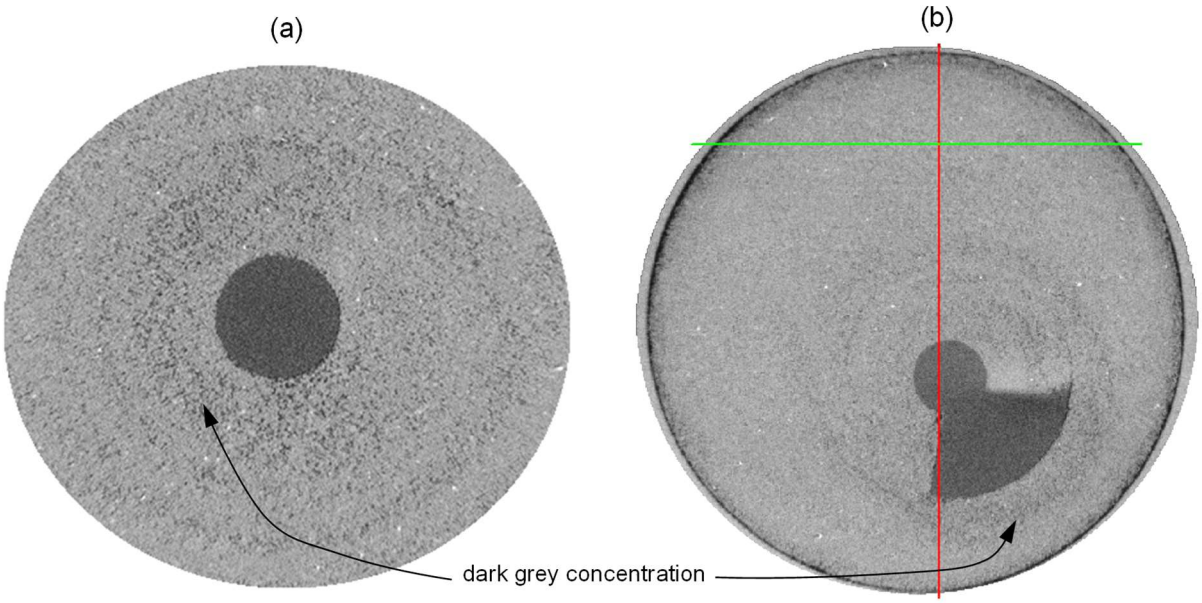

Figure 57. Micro-tomographic images of the sand specimen with the plastic model anchor inside: (a) cross section at the shaft level; (b) cross section at helix level.

4.3. Monotonic behaviour of the single-helix anchor under tensile loading

4.3.1. Comparison between centrifuge simulation and field test response

Figure 58 compares the results of uplift load tests performed on anchor 10FH and 10FHi, with the results of the field test of the helix bearing resistance mobilized during a tension loading test on a single-helix anchor installed in dense sand (possibly I_D = 100%)[1]. Both anchor models had a helix embedment depth of 7.4*D* and the full-scale field test had a helix embedment depth of 6.1*D* (Gavin *et al*. 2014). Although the mean fraction of shaft resistance (obtained from tests on the instrumented piles of this study) is 18% of the total capacity (Figure 60), the results show that the centrifuge and field tests are comparable.

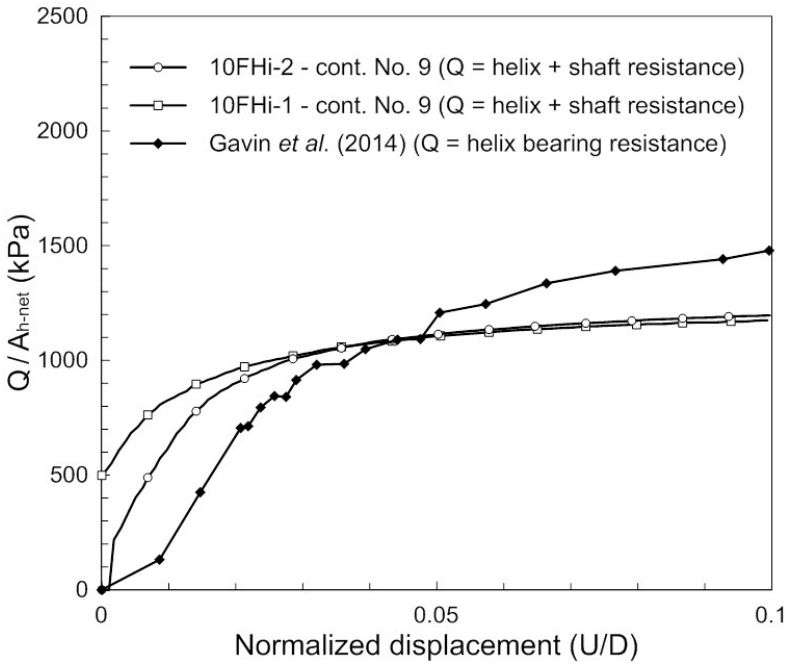

Figure 58. Comparison between the results of Gavin *et al*. (2014) and tests performed on 10FH and 10FHi in z_D = 7.4*D* (container No. 4, 5 and 9).

[1] The sand density index in the site is not clearly reported in Gavin *et al*. (2014), in Gavin and Lehane (2007), in Igoe *et al.* (2010) and in Doherty *et al.* (2012). A I_D = 100% is reported for reconstituted sand samples for triaxial tests for the site characterization, however there is no clearly indication of the site I_D. Estimations performed by the present author using the correlation proposed by Jamiolkowsky *et al.* (2003) with the CPT results presented by Gavin *et al.* (2014) have indicated a I_D value around 95%.

4.3.2. Helical anchor response under reloading

Two loading-unloading-reloading tests on anchor model 10FH were carried out to evaluate the monotonic anchor response after different levels of vertical displacement. For test 10FH-2 in container No. 4, the anchor model was loaded in tension to a vertical displacement of around 10%*D*. The second tensile loading test (10FH-1 in container No. 5) was conducted to a vertical displacement of the anchor head of approximately 1.2*D*. Figure 59 shows that the load-displacement responses of both tests are similar during the first loading stage. However, during the reloading stage, the anchor model that experienced a larger vertical displacement during the first loading exhibited a substantial reduction in the ultimate load. This occurred because the large displacement of the helix after the end of the first loading caused a gap below the helix, and a portion of sand moved to the gap, causing a decrease in sand density around the helix, and a consequent reduction in uplift capacity.

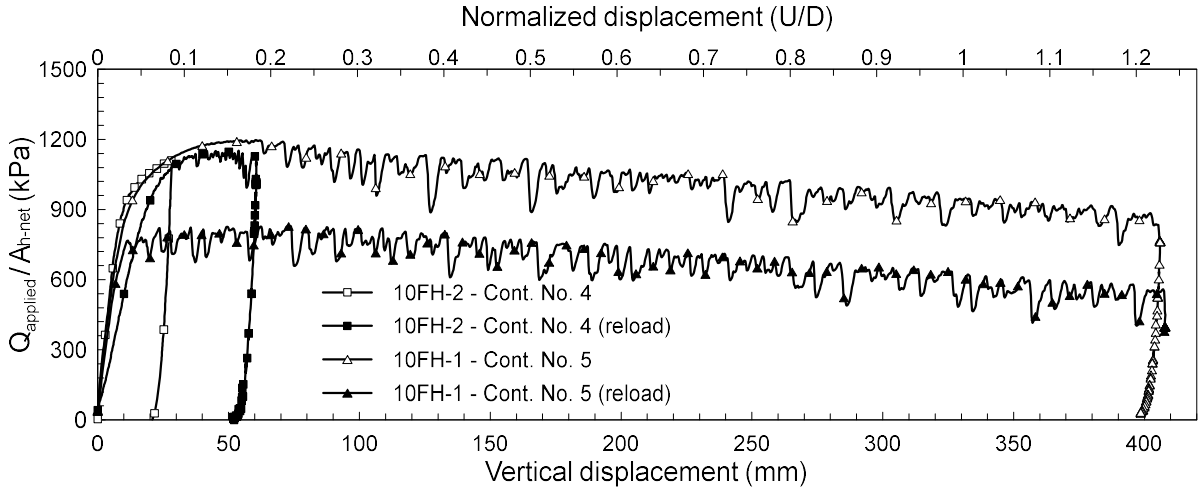

Figure 59. Results in prototype values of the pull-out tests 10FH-2 in container No. 4 and 10FH-1 in container No. 5.

4.4. Load distribution along the single-helix anchor under monotonic tensile loading

4.4.1. Tests on an instrumented model anchor

Two monotonic pull-out tests were performed on the anchor model 10FHi installed in container No. 9. However, the loads registered in the force gauge above the helix was influenced by the torque, as explained in Appendix H. Since no supplementary pre-cyclic monotonic tests were conducted after correcting the measures of the force gauge in the subsequent containers, the pre-cyclic load-displacement response was analysed during the test stage after the model installation and before the cyclic loading. During this period, the applied force passes from compression (measured forces at the end of anchor installation) to tension (the Q_{pre} value), and then to the mean cyclic load in tension (Q_{mean}). As this procedure of increasing force in tension is monitored, the percentage of load resisted by the helix and by the shaft can be quantified.

From the results of the tests on the 10FHi model, the portion of load resisted by helix bearing corresponded to a mean value of 82% of the applied load, with a coefficient of variation of 12%. Figure 60 shows the ratio of the load on the helix to the maximum applied load ($Q_{helix}/Q_{applied}$) within the analysed test period.

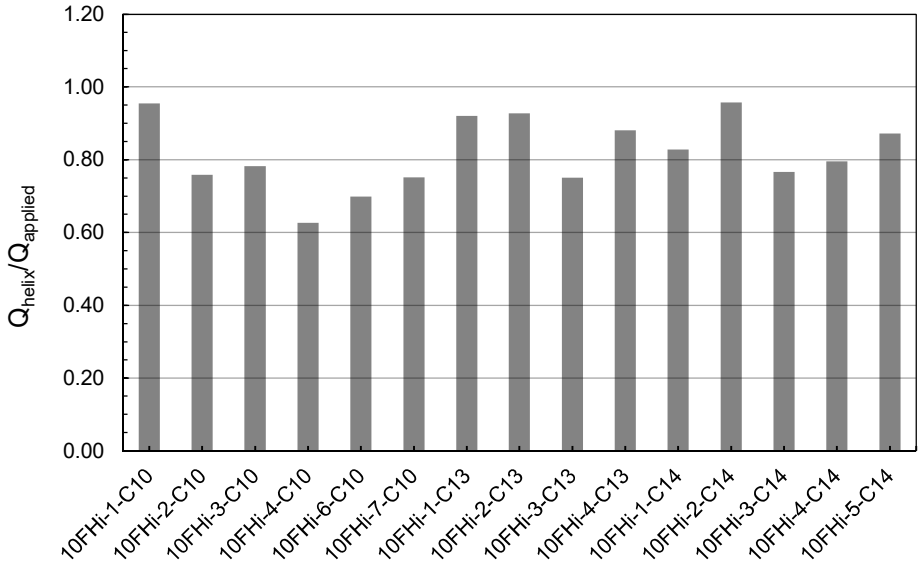

Figure 60. Registered load in the shaft section just above the helix compared with the applied load on the anchor head.

4.4.2. Tests on models with removable helix

Three helical anchor models (8RH, 10RH and 12RH) were fabricated with a removable helix to measure only the shaft resistance (when the anchor rod is pulled-out the helix remains embedded in the sand sample). The experiments were carried out in container No. 2 with a helix embedment depth $z_D = 8D$ for models 8RH and 10RH, and in container No. 3 with $z_D = 6D$ for model 12RH.

Figure 61 shows the results of the uplift tests on the anchor models with a removable helix. The three curves exhibit a peak followed by a sharp decrease in tensile force. Peak and reduction constitute an un-expected behaviour which does not reproduce a typical load-displacement response of regular piles subjected to uplift. The perturbation in the initial portion of the curves was caused by an additional friction in the helix-shaft connection. This behaviour occured because the applied torque at the end of the model installation was not completely dissipated, consequently, the anchor model was maintained under torsion in its longitudinal axis. This torque caused an additional normal stress on the contact surface

between the pin and the hole of the helix-shaft connection. Consequently, an additional resistance to the rod pull-out was generated, causing the helix to partially resist the tensile loading until the disconnection occurred. After 6.8 to 7.3 mm of vertical displacement in model values, when the helix was completely disconnected from the rod, the load-displacement curves indicated a stabilization of the tensile force (see Figure 61) indicating a value of residual shaft resistance of around 10 kN for models 8RH and 10RH.

Figure 62 presents a scheme of the helix-rod connection of the model anchors with a removable helix when there is a remaining torque after the anchor installation.

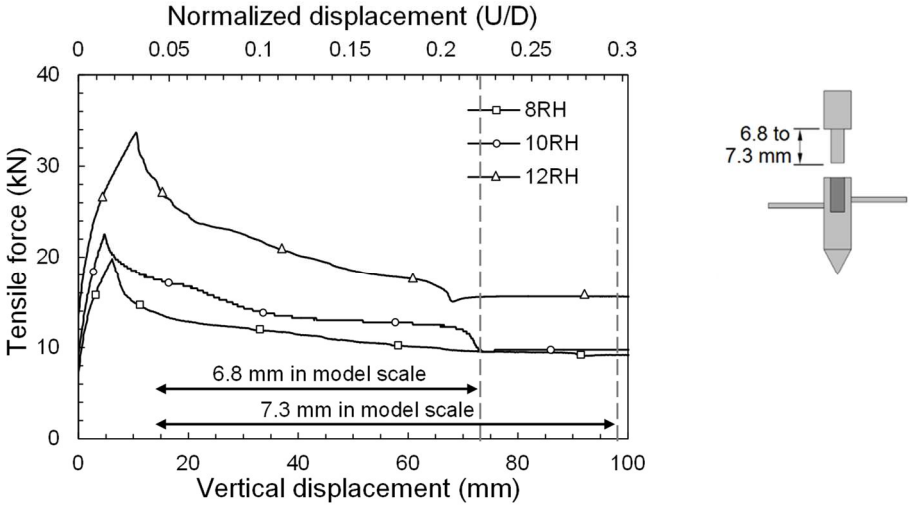

Figure 61. Load-displacement responses of the model anchors with removable helix (in prototype values).

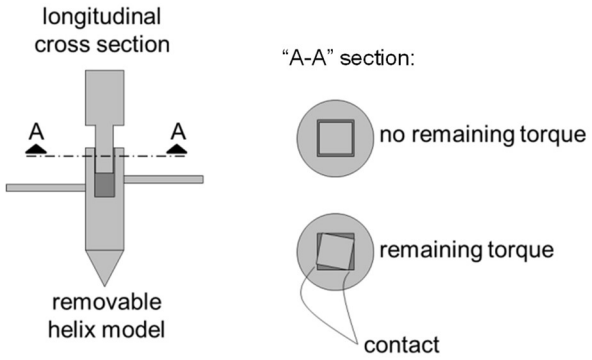

Figure 62. Scheme of the additional contact in the helix-shaft connection due to torque.

4.5. Cyclic loading tests with 10FH and 10FHi

The cyclic loading investigation was conducted with the instrumented 10FHi and non-instrumented 10FH single-helix models with a helix diameter of 33 mm and a shaft diameter of 10 mm. The cyclic loading tests were carried out with different loading amplitudes (Q_{cyclic}) and different pre-tensile loads (Q_{pre}). The cyclic parameters are illustrated in Figure 11 of section 2.2.

The basic parameters required to describe a cyclic loading are: mean load (Q_{mean}), cyclic load (Q_{cyclic}), frequency and number of cycles. Usually, Q_{mean} and Q_{cyclic} are normalized through the monotonic capacity in tension or compression. Therefore, before the series of cyclic tests, monotonic uplift tests were conducted on model anchors 10FH and 10FHi installed at the same embedment depth as the cyclic tests (z_D = 7.4D). The load-displacement responses of the monotonic loading tests for models 10FH and 10FHi are presented in Figure 63. These results are utilized to define the ultimate load to be used for the determination of Q_{mean} and Q_{cyclic} values for the cyclic loading tests.

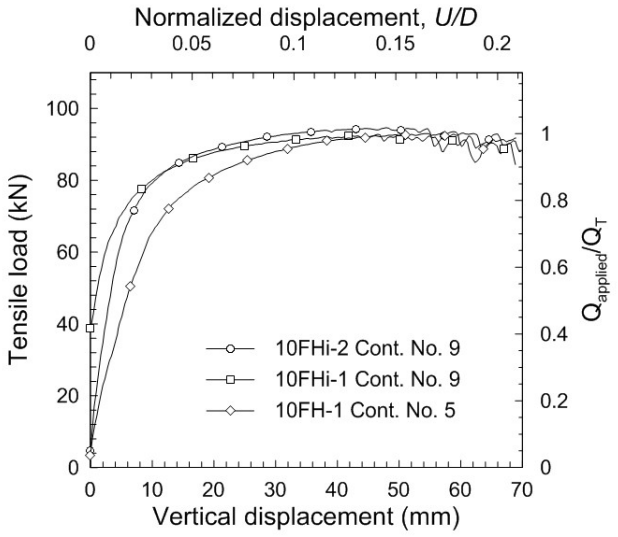

Figure 63. Monotonic load-displacement responses of uplift tests with 10FH and 10FHi models (prototype values).

The monotonic capacity in tension (Q_T) was established as the peak tensile load independent of displacement. The ultimate load was found equal to 93.0 kN, in prototype value, for the 10FH model tested in container No. 5 (I_D = 95%). About the same value was found in the pull-out tests of the 10FHi model: 92.7 kN for the first test and 94.5 kN for the second test, both carried out in container No. 9 (I_D = 99%). Therefore, the monotonic capacity in tension (Q_T) was adopted as the average value of the three results, Q_T = 93.4 kN.

4.5.1. Helical anchor behaviour under cyclic tensile loading

After installation, the model anchors were cyclically tested in tension with values of Q_{pre} varying from 0.08Q_T to 0.51Q_T (see Table 5, Chapter 3) to simulate the field minimum service load.

From a total of 38 cyclic tests, only 33 tests have been analysed: 14 tests with anchor model 10FH and 19 tests with anchor model 10FHi. Results of 5 tests with 10FH model have not been used due to problems in maintaining the cyclic loading controlled in force in the appropriate range of load variation. In addition, due to a configuration error in programming the servo-controlling system, some tests initiated the cyclic loading before the pre-load being completely applied. Nevertheless, the results of these tests with cyclic loading starting prematurely were used in the analyses.

Figure 64a presents the pile head responses to axial cyclic loading in tension with a similar pre-tensile load value (Q_{pre}) and three different load amplitudes: small (Q_{cyclic} = 0.10Q_T), medium (Q_{cyclic} = 0.23Q_T) and large (Q_{cyclic} = 0.29Q_T). This figure shows that the accumulated displacement after 1000 cycles surpassed 10%D for the cyclic test with the larger amplitude (35.3 mm or 0.11D). For the case of intermediate cyclic amplitude, the accumulated displacement was 25.3 mm (0.08D), and for the lower amplitude case it was 8.7 mm (0.03D) (in prototype values).

In one-way cyclic loadings on regular piles (with no helices or wings), displacements greater than 0.1D have been commonly observed for Q_{cyclic} lower than 0.3Q_T after 1000 cycles (Tsuha *et al.,* 2012b; Puech *et al*., 2013). In the present research, the tests have shown the helical anchor model experiences 0.1D of accumulated displacement after 1000 cycles for cyclic loadings with Q_{cyclic} from 0.2Q_T to 0.3Q_T, depending on the combination with Q_{mean}. However, the cyclic response of a helical anchor is not comparable to the response of conventional piles under cyclic tensile loading, as the role of the bearing helix controls the cyclic behaviour of this type of foundation.

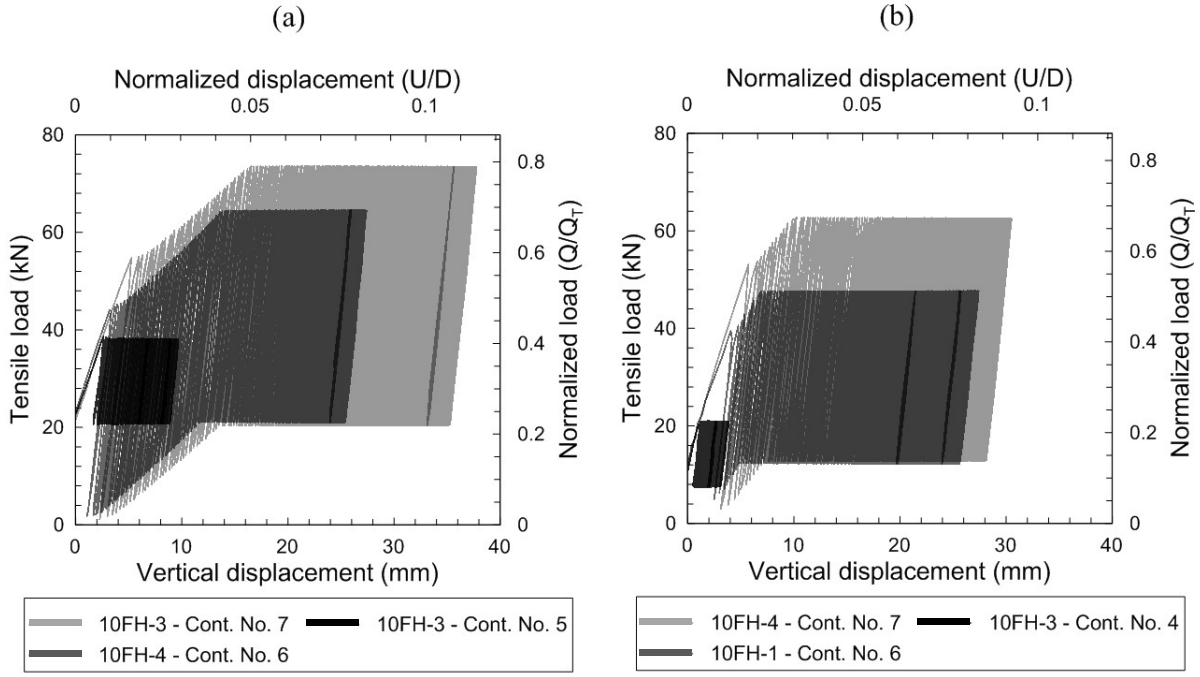

Figure 64. Load-displacement behaviour of cyclic tests with 10FH model: (a) $Q_{pre} \cong 0.23Q_T$; and (b) $0.09Q_T \leq Q_{pre} \leq 0.14Q_T$.

The results presented in Figure 64b were obtained with cyclic tests with a Q_{pre} between 9% and 14%Q_T. In this figure, the cyclic tests with a larger load amplitude ($Q_{cyclic} = 0.29Q_T$) resulted in 28.1 mm (0.08D) of accumulated displacement after 600 cycles (the end of the test). An estimate using a logarithmic function fit allowed inferring the accumulated displacement of 31.4 mm (~0.1D) for load cycle No. 1000.

Figures 64a and b show that the first load cycle is observed to differ significantly from the following ones. The permanent displacement at the end of the first cycle was much larger compared to the subsequent cycles. The first cycle corresponds to the first loading on the disturbed sand above the helix; therefore, the subsequent cycle starts after a sand densification above the helix.

Wichtmann and Triantafyllidis (2004) did not consider the deformations during the first cycle in the analysis of accumulation of deformations under cyclic loading since the analysis performed by these authors intended to investigate rules of cyclic displacement accumulation in sand specimens. Concerning the unloading branch of the first cycle, Wichtmann and Triantafyllidis (2004) argues that the strain generated in the three following quarters of the first cycle is negligible in comparison with the strain accumulated during the large number of subsequent cycles. In cyclic stability analysis, however, the displacements of the first cycles may be considered, since the initial conditions of the studied prototype does not involve the application of a pre-cyclic load greater than the maximum cyclic load (Q_{max}).

The results of the 5th cyclic test carried out in container No. 9 (10FHi-5 – Cont. No. 9), presented in Figure 65, illustrate the effect of the application of a previous pre-tensile loading greater than the cyclic test Q_{max} (test 10FH-5 Cont. No. 4). For this case, at the end of the installation, a delay between stopping the vertical advance and stopping the helix rotation was observed. This mismatch caused an additional tensile force at the anchor head of about 64 kN, which pre-loaded the anchor with a greater value than the Q_{max} of this cyclic test. The occurrence of a large tensile load before the cycles increased the initial anchor stiffness and reduced the displacements of the first cycle. However, the results with no previous application of tensile loading (tests 10FHi-1 and 10FHi-2 in container No. 14) exhibit large displacements during the first cycle (Figure 65).

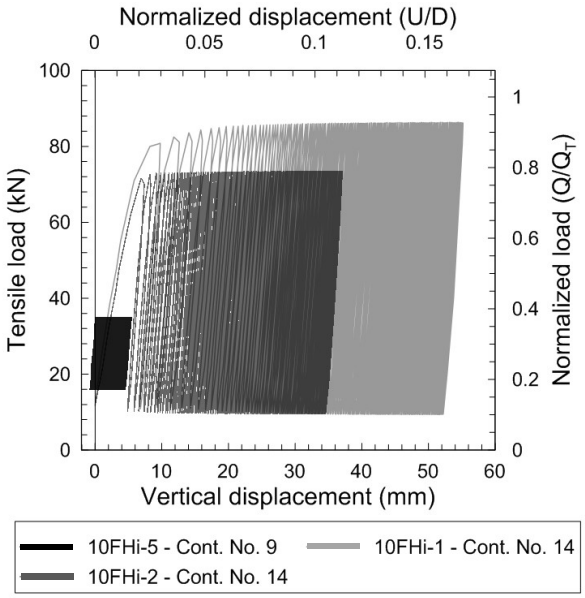

Figure 65. Load-displacement behaviour of cyclic tests with 10FHi model with $0.08Q_T \leq Q_{pre} \leq 0.17Q_T$.

The measurements of the applied load on the anchor head and the registered load in the force gauge above the helix are presented in Figure 66 for tests 10FHi-2 and 10FHi-3 in container No. 10 and for test 10FHi-4 in container No. 13. The results presented in Figure 66a (with a lower mean load and a lower cyclic amplitude condition) show that the anchor head displacement was 4.5%D after 1000 cycles, and 5.7%D after 2000 cycles. In the test with an intermediate condition of mean load and cyclic amplitude (Figure 66b), the maximum displacement achieved was 9.0%D after 1000 load cycles. The results of the test with a greater mean load and cyclic amplitude (Figure 66c) indicate a maximum anchor head displacement of 10.9%D at the last cycle (N = 300).

In Figure 66, the permanent displacement was much larger at the end of the first cycle than in the following cycles of the three tests. As mentioned before in this text, the first cycle includes the first loading on the sand above the helical plate, which is in a disturbed condition due to the anchor installation; therefore, the subsequent cycle starts after the sand densification above the helix.

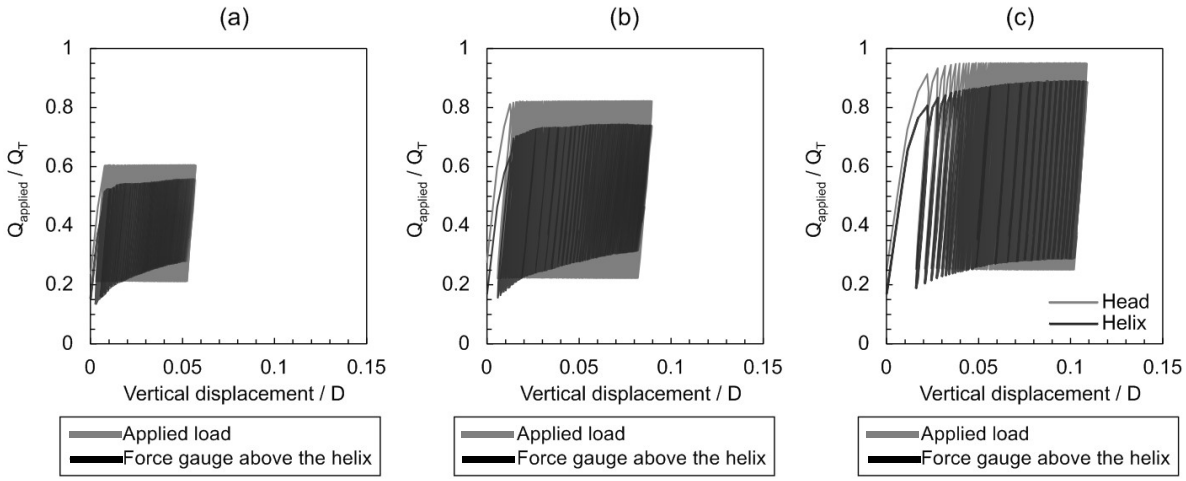

Figure 66. Normalized load-displacement cyclic responses: (a) $Q_{mean} = 0.41Q_T$ and $Q_{cyclic} = 0.20Q_T$; (b) $Q_{mean} = 0.51Q_T$ and $Q_{cyclic} = 0.29Q_T$; (c) $Q_{mean} = 0.59Q_T$ and $Q_{cyclic} = 0.34Q_T$.

After a few cycles, during the unloading stages of each cycle, the results presented in Figure 66 indicate that the force registered by the force gauge above the helix becomes greater than the applied force Also, the minimum tension force registered by the force gauge at the end of the unloading stage increases with the number of cycles. This occurs because at the beginning of the unloading stages the anchor movement alternates, and the anchor starts to move down. Consequently, at the end of the unloading stage a force below the anchor tip pushes up the helical anchor. When the applied tension load increases, the contact between the anchor tip/helix and the soil below the tip/helix is reduced and this force disappears. At the same time the sand grains move toward the "gap" formed beneath the anchor helix/tip. After that, in the next unloading stage, the soil that fills the gap below the helix/tip will cause the registered pushing up force when the anchor moves down, as explained in Figure 67, and as discussed in section 4.2. This pushing-up force observed at the end of the unloading stage increased over the cycles and was greater tests of smaller cyclic amplitudes (Figure 66a), probably because the gap formed beneath the helix/tip is greater in larger cyclic amplitudes.

The assumptions illustrated in Figure 67 are corroborated by previous findings about the installation effects in section 4.2, and from Figure 56.

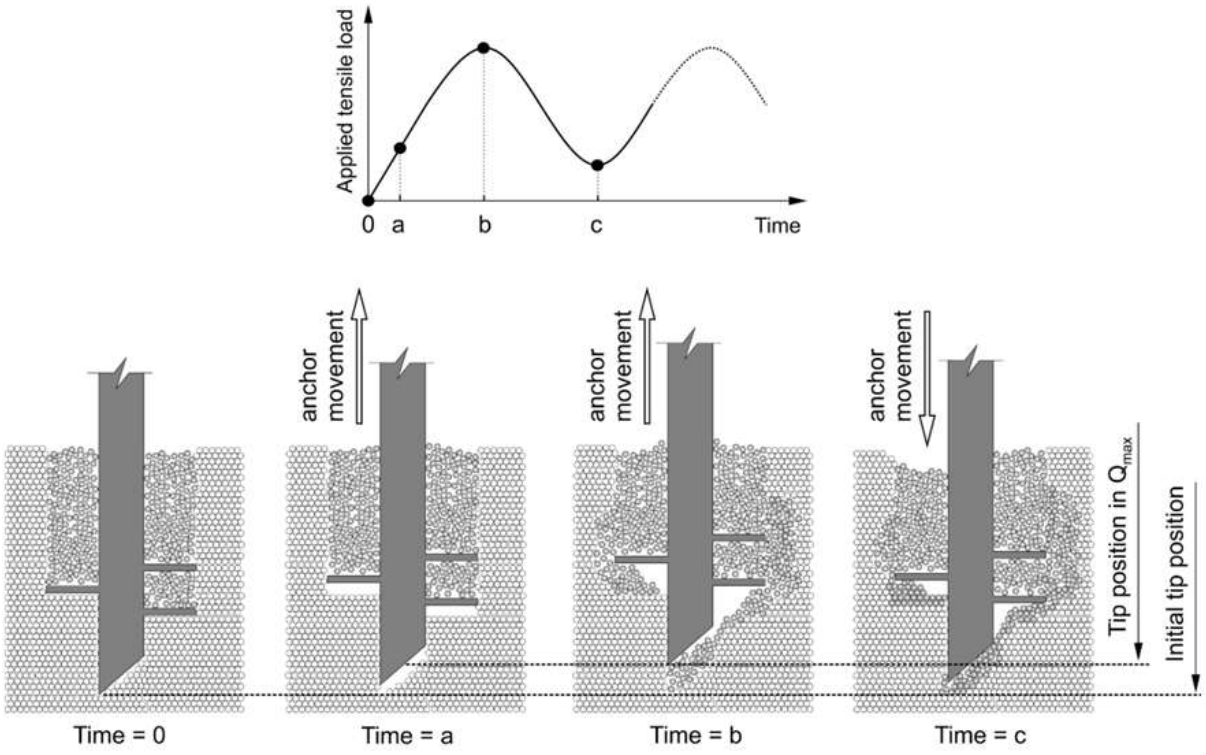

Figure 67. Gap formation and sand particles movement during the cyclic loading.

4.5.2. Cyclic accumulated displacement

Figure 68 presents the accumulated displacements of cyclic tests with different combinations of Q_{mean} and Q_{cyclic}. The displacements accumulated faster for cycles with a higher cyclic amplitude (Q_{cyclic}.). Figures 68a and b show that the displacement accumulation is more noticeable in the initial 50-200 cycles. For large load amplitudes, a significant reduction in the strain amplitude with N is typically noticed in the course of the first 100 cycles, which coincides with observations reported by Wichtmann *et al.* (2005). Plotting the accumulated displacements with the log of cycles an approximately bi-linear trend is observed in Figures 68c and d. These figures show that for higher cyclic amplitudes, a smaller amount of cycles is necessary to change the slope of the curve.

Figure 69 presents the accumulated displacements plotted with the square of the logarithm of N. An inflection point can be observed in all results of this figure. Between the

beginning of the test and the inflection point, a non-linear trend is observed, which means the displacement accumulation rule follows a different function of the $(\log N)^2$. In this figure, a straight line can be fitted after the inflection point.

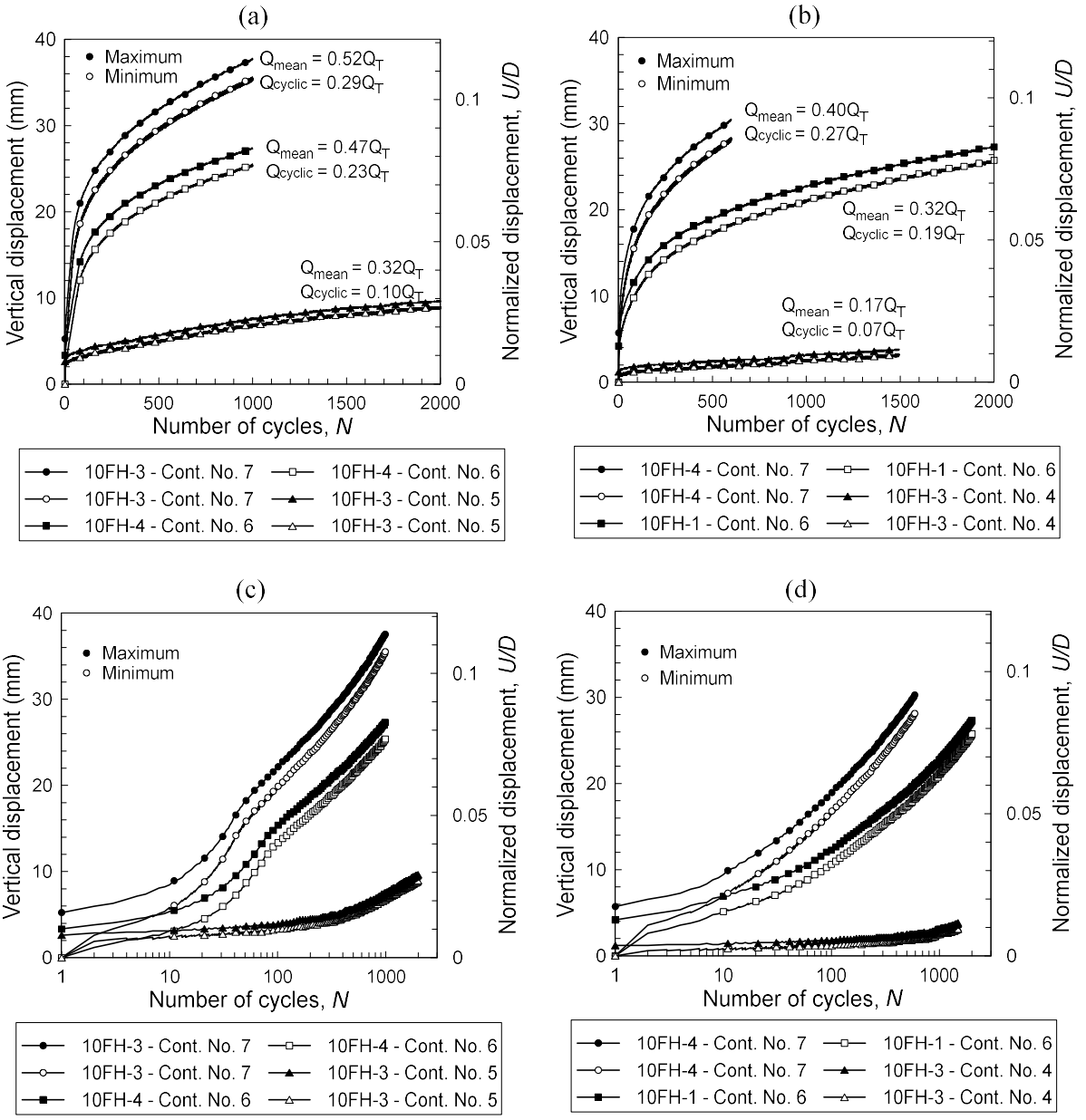

Figure 68. Maximum and minimum values of vertical displacements with number of cycles in (a) and (b) linear scale; and (c) and (d) log scale.

The results of various tests in Figure 69, indicate that all the inflection points are placed along a straight line (separating non-linear from linear trends). This observation suggests that, after a number of cycles, the accumulated displacement can be predicted by a

(log*N*)² function according to the combination of cyclic parameters as a mean load and a load amplitude.

Figure 70 presents typical curves of the displacement accumulation rate (the increment of accumulated displacement per cycle). The displacement rate is greater for higher values of cyclic amplitude and mean load. However, after a dozen cycles, the displacement rate drops to about 5% of the initial rate.

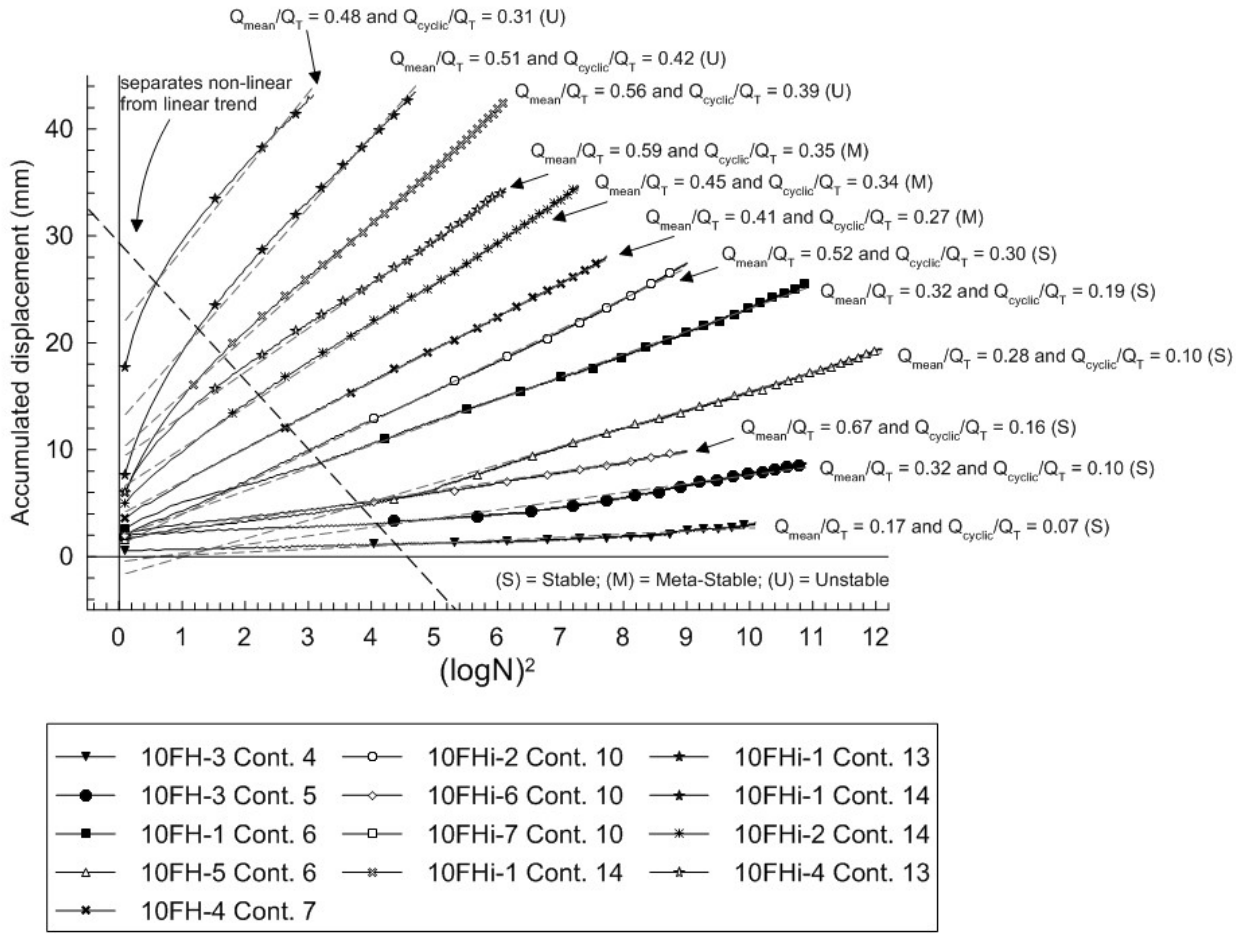

Figure 69. Accumulated displacements analysed in function of the logarithm of the number of cycles squared.

The cyclic results in Figure 70a indicate that the displacement accumulation rate passes from 1.2 mm/10cycles in cycle No. 10 to about 1 mm/150cycles after 100 cycles in test 10FH-3 Cont. No. 5 (the case of low cyclic amplitude presented in the figure). For the tests with higher amplitude presented in Figure 70 (10FH-1 Cont. No. 7), the displacement

accumulation rate decreased from 3 mm/cycle to around 1 mm/10cycles after 100 cycles, and after 200 cycles passed to 1 mm/40 cycles.

Large displacement accumulation rates are observed during the first cycles due to the sand densification above the helix throughout the cycles, and because of shaft resistance degradation. However, no sudden cyclic failure was observed. Axial anchor stiffness increases over the loading cycles due to the densification of the disturbed soil above the helix.

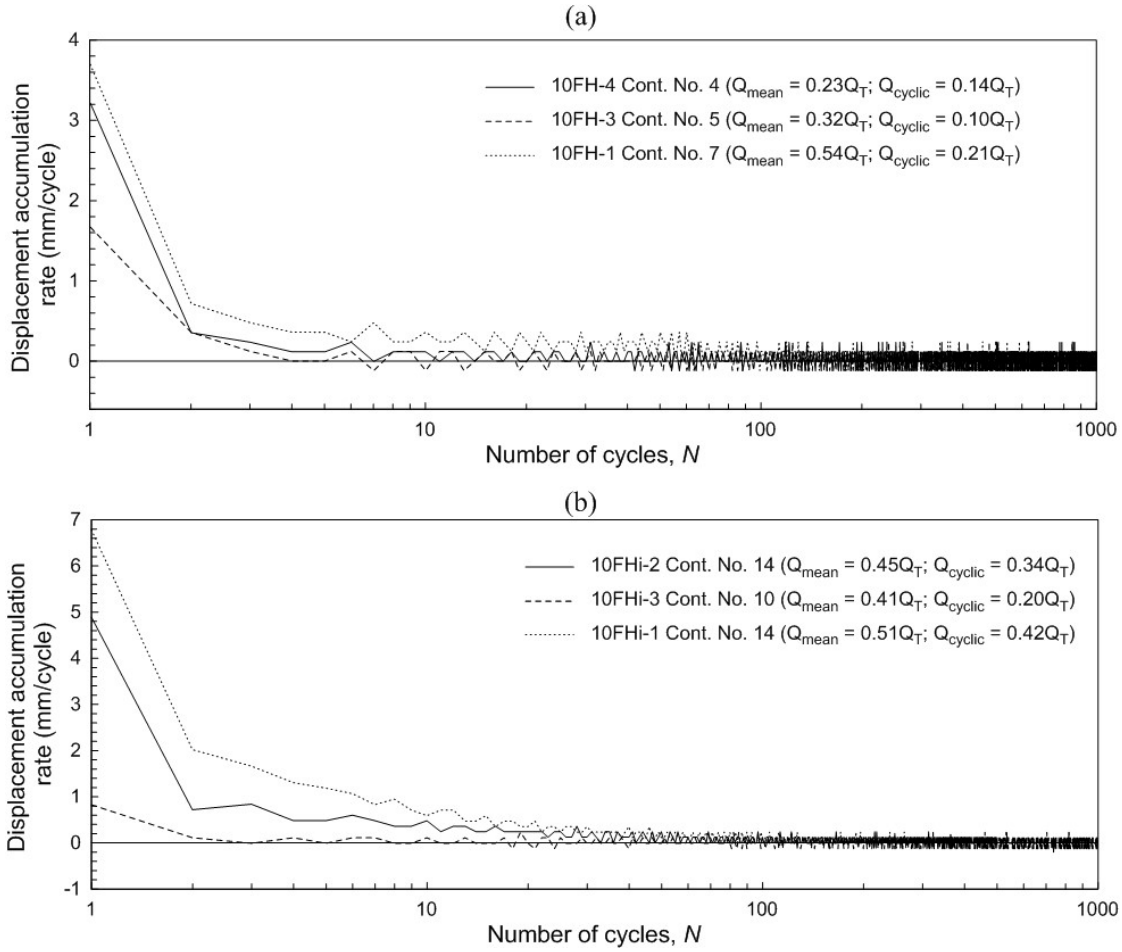

Figure 70. Displacement accumulation rates in cyclic tests performed on the models: (a) 10FH; (b) 10FHi, in prototype values.

Figure 70b presents the displacement accumulation rate of the cyclic tests on instrumented model anchor 10FHi with higher cyclic amplitudes compared to the tests on the 10FH model (Figure 70a). The results of the three tests on 10FHi indicate a stabilization of the displacement rate between 20 (for Q_{max} = 0.61Q_T) and 200 cycles (for Q_{max} = 0.93Q_T).

Even at large cyclic loads (Q_{max} = 0.93Q_T) a significant decrease of the displacement accumulation rate is observed after a number of cycles.

For guyed tower anchors, a few cycles of cyclic loading with such intensity (0.93Q_T) would cause the anchor to fail cyclically due to excessive displacements. However, as the helix bearing resistance increased due to the soil densification above the helix during the cyclic loading, little or no loss in uplift capacity was observed in the post-cyclic monotonic test results. Therefore, the adjustment of the pre-stressed tower cables may be a repairing solution for excessive cyclic displacements of the anchor with no loss of capacity.

Figure 71 shows that no indication of displacement increase is observed after cyclic displacements of about 10%*D*. The displacement accumulation tends to decrease and stabilize at a given rate value depending on the cyclic loading intensity. Table 17 presents values of displacement accumulation rates of the three tests shown in Figure 71.

Table 17. Displacement accumulation rates in tests with the 10FHi model (prototype values).

				Displacement accumulation rate (mm/10cycles)		
Test	Q_{max}/Q_T	Cycles	N_f	Initial	N = 100 cycles	Final
10FHi-3 Cont. No. 10	0.61	1000	-	4 (U_{acc} = 0.01D)	3 (U_{acc} = 0.01D)	0 (U_{acc} = 0.05D)
10FHi-1 Cont. No. 14	0.93	300	47	74 (U_{acc} = 0.06D)	10 (U_{acc} = 0.12D)	5 (U_{acc} = 0.16D)
10FHi-2 Cont. No. 14	0.79	500	377	36 (U_{acc} = 0.03D)	5 (U_{acc} = 0.07D)	2 (U_{acc} = 0.10D)

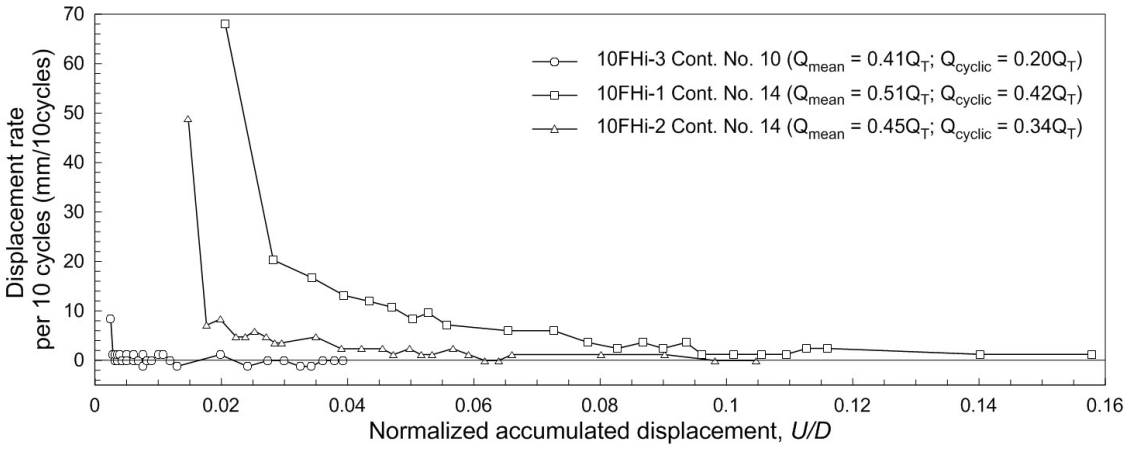

Figure 71. Displacement accumulation rates *versus* accumulated vertical displacements in cyclic tests performed with 10FHi model, in prototype values.

4.5.3. Cyclic axial stiffness

The cyclic stiffness response is evaluated in this study using the parameters described in Figure 72 based on the work of Rimoy *et al.* (2013).

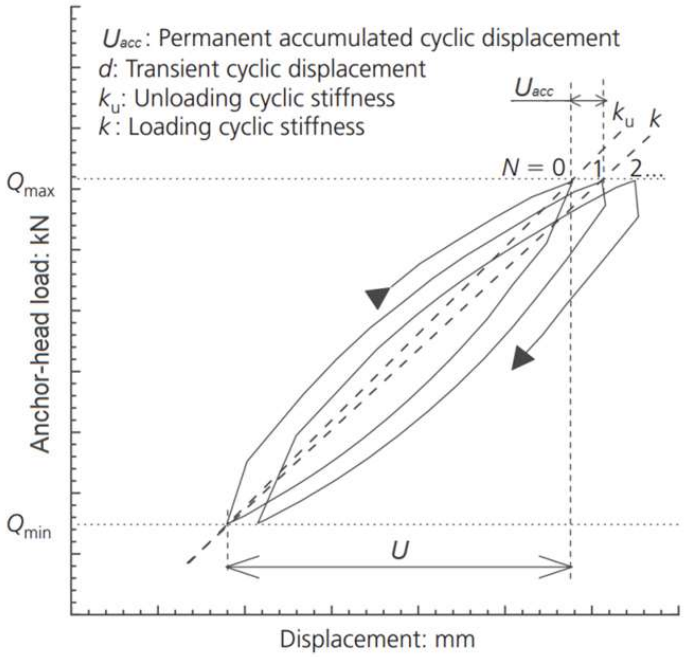

Figure 72. Stiffness and displacement cyclic parameters (adapted from Rimoy *et al*., 2013).

Figure 73 shows that the anchor axial stiffness enhances up to 4 times the initial stiffness, with more significant growth in the first 10 cycles for the tests on the 10FH model (Figure 73a). For the tests carried out on 10FHi model, the gain of anchor axial stiffness achieves a value from 1.7 to 3.6 times the initial stiffness, with more significant growth in the first 100 cycles (Figure 73b).

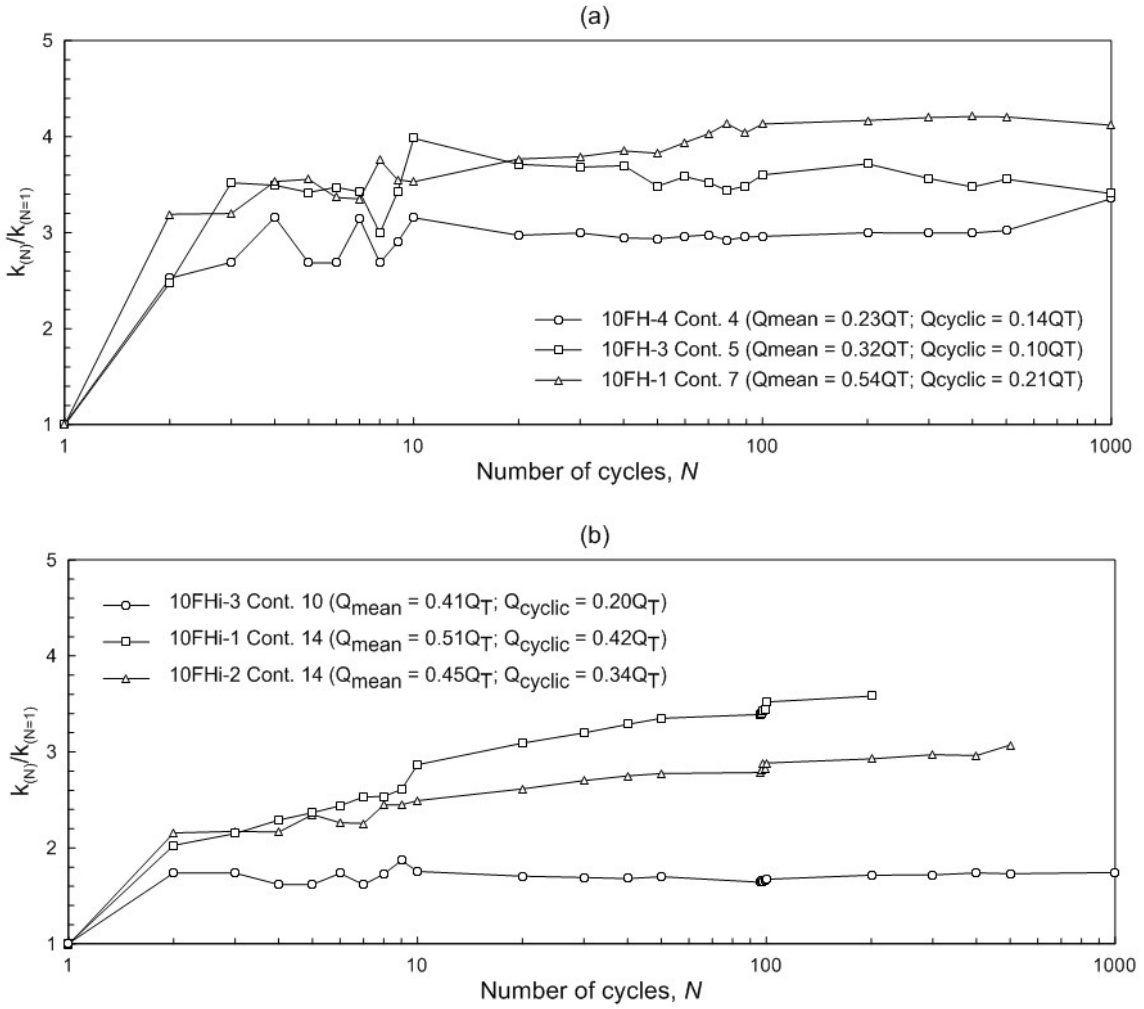

Figure 73. Typical results of normalized axial cyclic stiffness (loading cyclic stiffness) for tests conducted on models: (a) 10FH and (b) 10FHi.

Table 18 presents the results of the anchor's cyclic axial stiffness at the 1st, 100th and 1000th cycle (or for a final cycle if N<1000). This table indicates that the stiffness increase is dependent on the cyclic loading amplitude and on the maximum cyclic loading. Similar observations were made by Rimoy (2013) that reported cyclic stiffness patterns varying mainly based on the cyclic amplitude in cyclic tests on conventional piles.

For cyclic tests with Q_{cyclic} varying from 10% to 15%Q_T the stiffness gain was less than in the cyclic tests with a Q_{cyclic} of 34% and 42%Q_T. However, two cyclic tests with Q_{cyclic} at about 20%Q_T showed significant difference in stiffness gain, being 15.1 kN/mm for the 10FH test against 9.1 kN/mm for the test on model 10FHi, in prototype values. The difference is

probably due to the different in the mean load (Q_{mean}) of these tests (greater mean load for the test on the model 10FH). Comparing only the results obtained from the tests on model 10FHi, the influence of the cyclic amplitude is clear. For these cases, the cyclic tests with higher Q_{cyclic} (34% and 42%Q_T) exhibited a stiffness increase 50% greater than the tests with lower cyclic amplitude (Q_{cyclic} = 20%Q_T).

Table 18. Axial anchor stiffness in cyclic tests on models 10FH and 10FHi (prototype values).

Test	Q_{mean}/Q_T	Q_{cyclic}/Q_T	Q_{max}/Q_T	Cycles	Axial anchor stiffness (kN/mm)			
					Initial	N = 100 cycles	Final	Difference $k_{(N=last)} - k_{(N=1)}$
10FH-4 Cont. No. 4	0.23	0.14	0.37	1000	5.9	17.4	18.1	12.2
10FH-3 Cont. No. 5	0.32	0.10	0.42	1000	6.1	21.9	21.3	15.2
10FH-1 Cont. No. 7	0.54	0.21	0.75	1000	4.8	19.9	19.9	15.1
10FHi-3 Cont. No. 10	0.41	0.20	0.61	1000	12.8	21.3	21.9	9.1
10FHi-1 Cont. No. 14	0.51	0.42	0.93	300	7.1	24.3	25.2	18.1
10FHi-2 Cont. No. 14	0.45	0.34	0.79	500	8.6	24.7	25.8	17.2

Figure 74 compares the anchors' axial stiffness of the cyclic tests performed on models 10FH and 10FHi. This figure demonstrates that for all tests the axial stiffness tends to stabilize after around 10 cycles. Also, at between 10 and 1000 cycles, the values of axial stiffness are comparable for all cyclic tests presented in this figure, with different values of Q_{mean} and Q_{cyclic}.

For the first 10 cycles, the stiffness increase rate is higher in the tests on model 10FH (Figure 74a) than in tests on model 10FHi (Figure 74b). During the three cyclic tests on 10FH, with cyclic amplitudes up to 20%Q_T, the sand above the helix is densified and passes to an overconsolidated state. For the tests with higher cyclic amplitudes (34% and 42%Q_T), after a dozen cycles, a larger zone of sand above the helix is affected by the helix

displacement and the sand densification continues. This effect can be verified by the late stiffness gain in the tests on the 10FHi model in container No. 14 (Figure 74b).

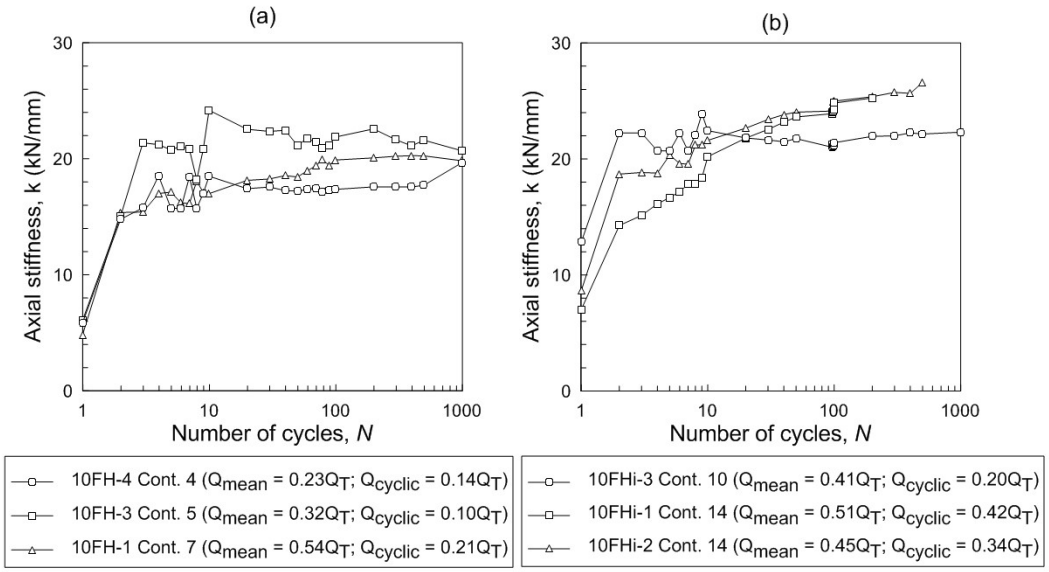

Figure 74. Typical results of axial cyclic stiffness for tests conducted on models: (a) 10FH and (b) 10FHi.

4.5.4. Shaft resistance degradation

Figure 75 presents the shaft resistance mobilized during the cyclic tests performed on the instrumented anchor model (10FHi). The initial value of the shaft resistance (Q_{shaft}) varied from 2.8 kN to 28 kN in prototype values, which corresponds to 3% to 30% of the anchor uplift capacity (Q_T), respectively. Tests presenting greater values of skin friction (f_s) were typically conducted with a larger Q_{mean}. This observation indicates that a larger applied load induces a greater mobilization of the shaft resistance. Thus, in a one-way tensile cyclic loading with low values of Q_{mean} and Q_{cyclic}, the shaft resistance cannot be fully mobilized. On the other hand, in the cyclic loadings with higher cyclic amplitudes the shaft resistance is completely mobilized, and also exhibits the degradation of shaft resistance in early cycles.

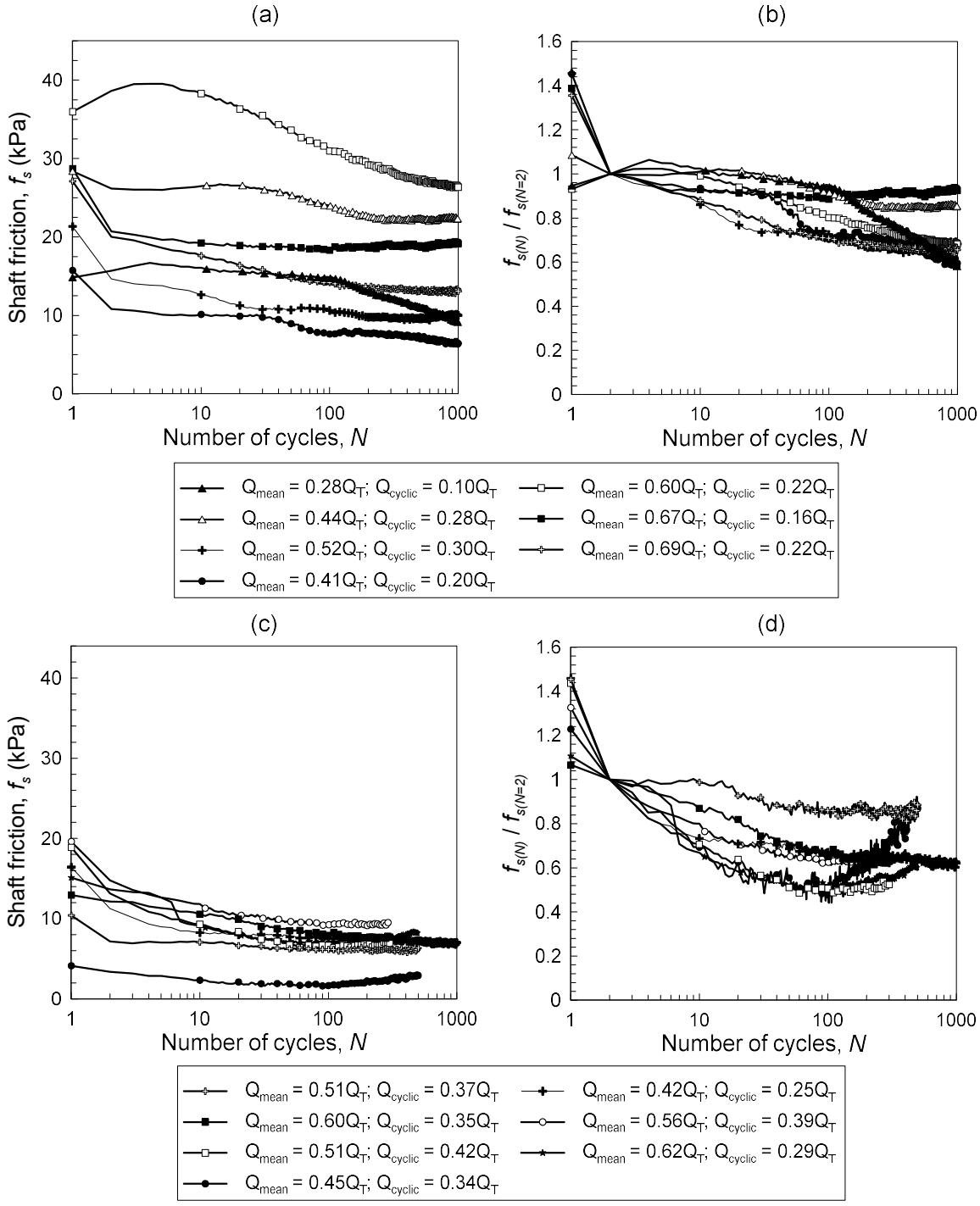

Figure 75. Skin friction degradation: (a) and (b) cyclic tests in containers No. 9 and 10; (c) and (d) cyclic tests in containers No. 13 and 14.

Skin friction degradation occurred in all cyclic loading tests, noticeably in the first 100 cycles. In contrast, some tests exhibited a significant reduction in skin friction after 100 cycles. During the first cycles, the reduction of skin friction corresponds to 50% of the skin friction degradation observed for the entire test.

At the end of the cyclic test, the reduction in skin friction varies from 22% to 60% of the initial skin friction (N = 1), corresponding to a shaft load (Q_{shaft}) ranging from 3% to 8% of the maximum applied load in the last performed cycle. Therefore, at the end of cyclic loading the shaft resistance is reduced to a very low value (almost nil), and the helix bearing resistance controls the anchor uplift capacity.

The results of this investigation showed that skin friction degradation is dependent on the cyclic loading magnitude and on the initial value of the shaft load (Q_{shaft}). Figures 75a and b present the results of cyclic tests with $U < 10\%D$ after 1000 cycles for most cases (tests conducted in containers No. 9 and 10). In these figures, the skin friction degradation is observed over the entire test, indicating no stabilization. On the other hand, for cyclic tests with $U \geq 10\%D$ the most significant degradation occurred before 100 or 200 cycles (Figures 75c and d).

Figure 76 illustrates the level degradation of skin friction observed for the performed cyclic tests with different combinations of Q_{mean} and Q_{cyclic}.

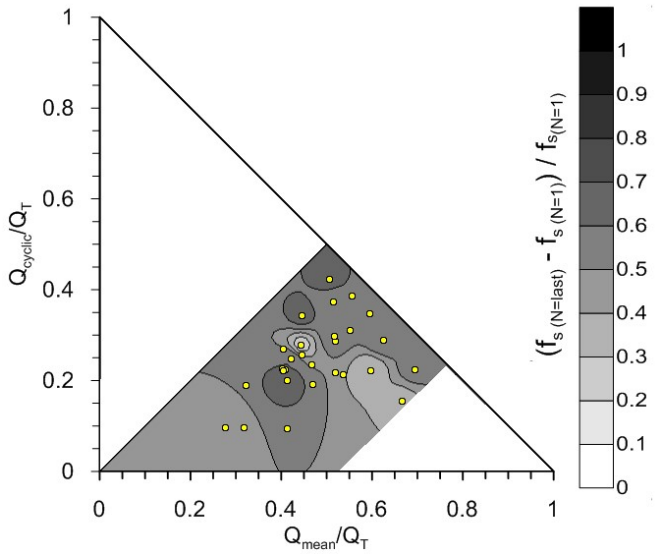

Figure 76. Maximum skin friction degradation observed in the cyclic tests.

The evolution of skin friction degradation along the loading cycles is presented in Figure 77 for cases of degradation levels of 15, 30, 40 and 55% of the maximum skin friction at the first cycle. From 15 to 40% of skin friction degradation, the most tests is in the white zone, indicating that few cycles (less than 100) are required to cause degradation up to 40% of the maximum skin friction in the first cycle.

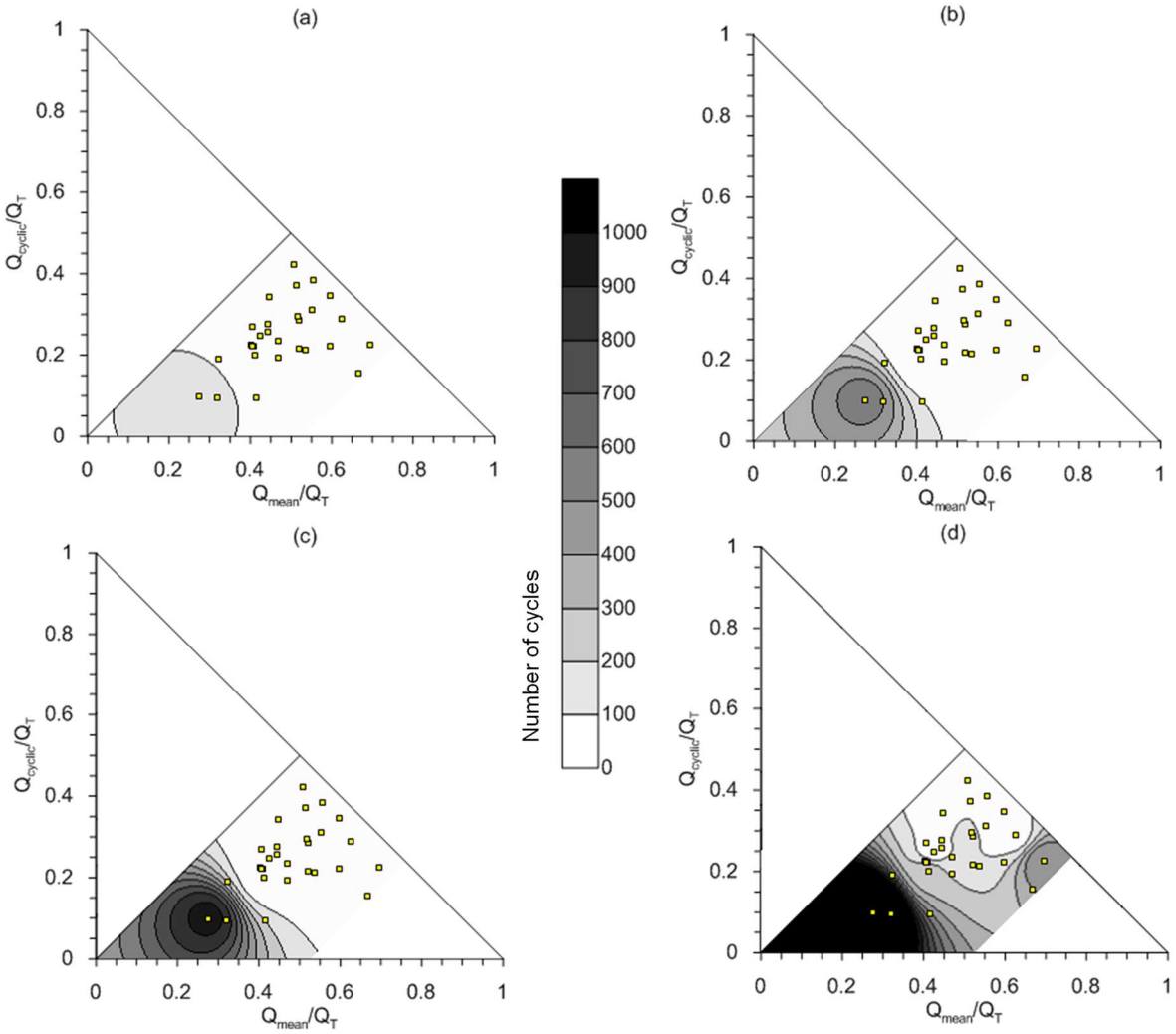

Figure 77. Contours of percentages of skin friction degradation: (a) $f_{s\,(N)}/f_{s\,(N=1)}$ = 0.85; (b) $f_{s\,(N)}/f_{s\,(N=1)}$ = 0.7; (c) $f_{s\,(N)}/f_{s\,(N=1)}$ = 0.6; (d) $f_{s\,(N)}/f_{s\,(N=1)}$ = 0.45.

4.5.5. Cyclic response of the helix beating resistance

The helix bearing resistance controlled the behaviour of the model anchor since 70% to 97% of the applied load during the first cycles was resisted by the helix. In the last cycle, the portion of the applied load resisted by the helix was found to be from 92% to 97% of the maximum applied load. Figures 78a and c present the helix bearing mobilization during the cycles.

Greater shaft resistance was observed in the cyclic tests in container No. 9 and 10 in comparison with containers No. 13 and 14. In these cases, a smaller load was resisted by the helix (Figures 78a and c). However, as the skin friction degradation increases, the helix bearing also increases.

Figures 79b and d show the applied load resisted by the helix during the cycles normalized by the load resisted by the helix during the second cycle ($N = 2$).The majority of the cyclic tests performed on anchor model 10FHi showed a helix bearing resistance increase of up to 20% in relation to the value obtained in the first cycle (Figures 79b and d). This gain in helix bearing provided cyclic stability to the helical anchor, which resulted in a wide zone of Stable response in the interaction diagram is shown in section 4.5.7 (displacement limit criteria). Consequently, a narrow zone of Unstable response is noticed.

An increase in the helix bearing resistance of around 10% was observed after the first cycle of all tests. In the following cycles, an increase of helix resistance is observed up to 100 cycles for cyclic tests with higher cyclic amplitudes (Q_{cyclic} ranging from 25 to 42%Q_T). However, for cyclic loadings with smaller cyclic amplitudes (up to Q_{cyclic} of around 20%Q_T) the helix bearing exhibits increase after 100 cycles. Figure 79 shows the contours of percentages of the helix bearing resistance increase during cyclic tests.

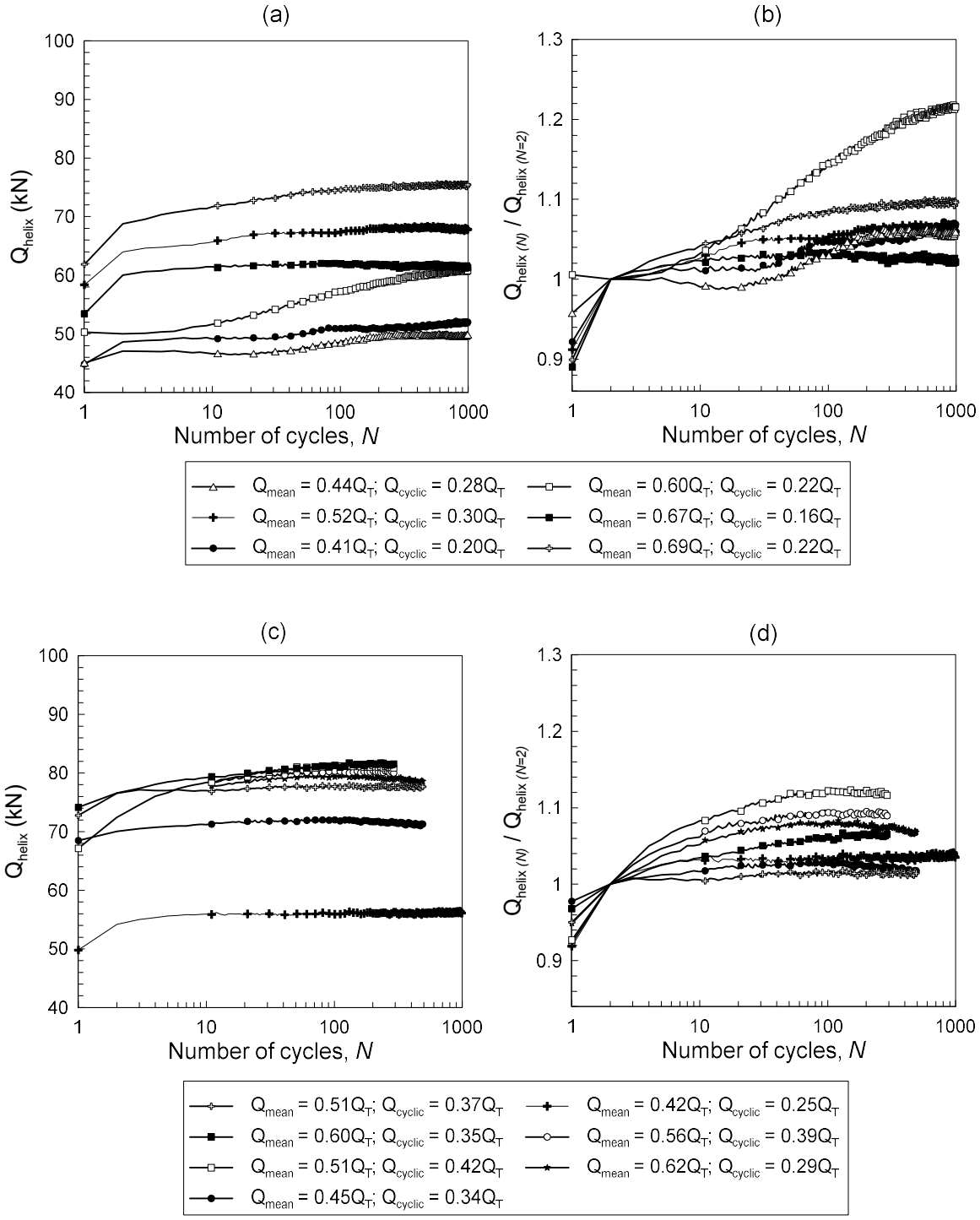

Figure 78. Helix bearing resistance: (a) and (b) cyclic tests in containers No. 9 and 10; (c) and (d) cyclic tests in containers No. 13 and 14.

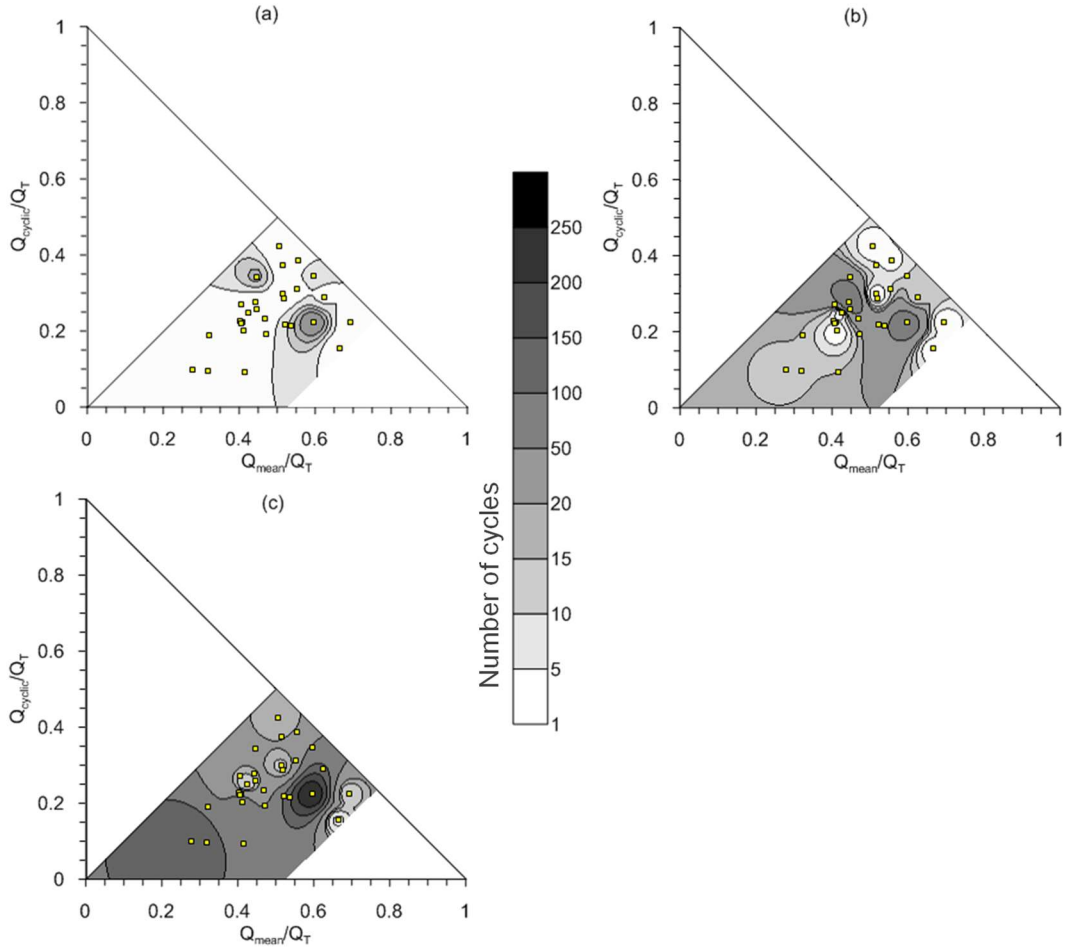

Figure 79. Contours of the increase of the maximum cyclic load registered in the force gauge above the helix: (a) $Q_{helix\ (N)}/Q_{helix\ (N=1)}$ = 1.05; (b) $Q_{helix\ (N)}/Q_{helix\ (N=1)}$ = 1.10; (c) $Q_{helix\ (N)}/Q_{helix\ (N=1)}$ = 1.15.

4.5.6. Post-cyclic monotonic response

After the cyclic tests, monotonic uplift tests were performed to evaluate the influence of the cyclic loading on the post-cyclic response of the anchor.

No clear relationship was found between any cyclic loading parameter and the post-cyclic capacity ($Q_{T\text{-}pc}$) variation. Generally, the post-cyclic uplift capacity was greater than the pre-cyclic monotonic capacity when the applied cyclic loading caused accumulated displacements greater than 10%D and up to 400 cycles (Figure 80a). Still, some cyclic tests with accumulated displacements smaller than 10%D exhibited a $Q_{T\text{-}pc}$ greater than Q_T. Figure

80b indicates the model anchors exhibited post-cyclic capacity greater than the pre-cyclic capacity for values of $Q_{max} > 82\%Q_T$.

(a)

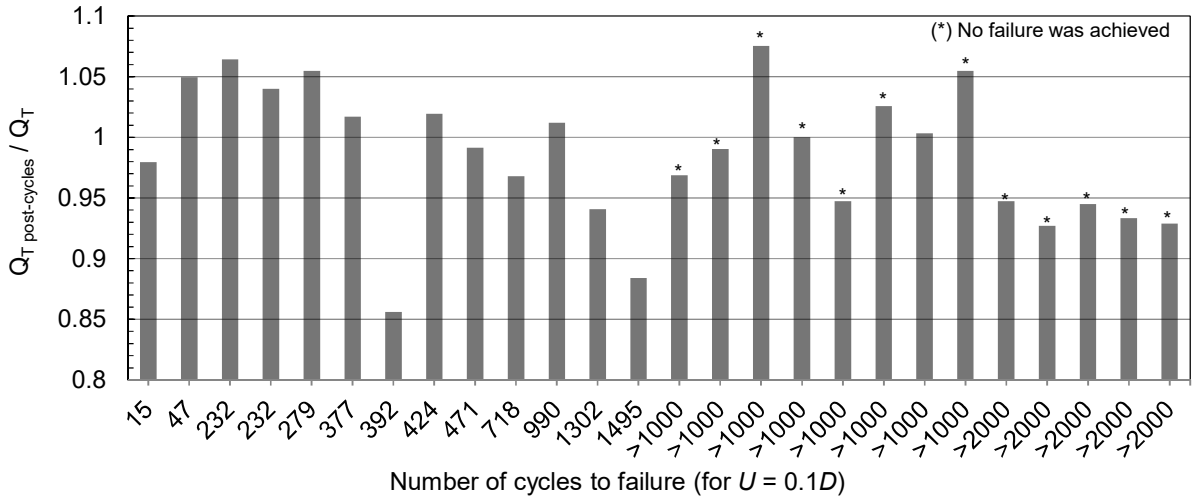

(b)

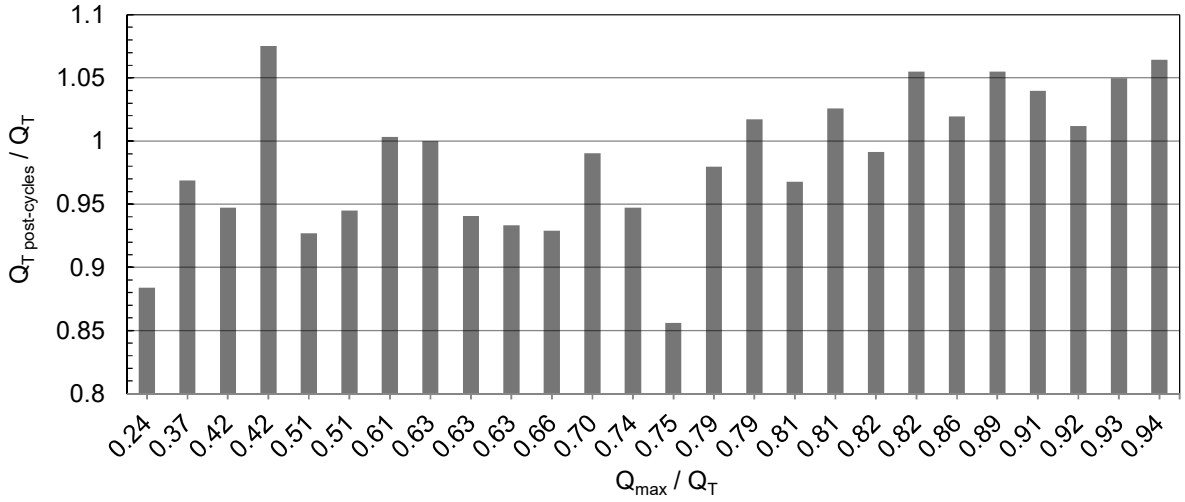

Figure 80. Post-cyclic ultimate tension load: (a) according to the number of cycles to failure; (b) according to the maximum cyclic load experienced during the cyclic loading carried.

Table 19 summarizes the results of the post-cyclic monotonic uplift tests. The post-cyclic capacity gain seems to be related to the minimum value of the mean cyclic load (Q_{mean}). The majority of the post-cyclic monotonic tests with a post-cyclic capacity greater than the pre-cyclic capacity were performed with Q_{mean} between 45 and 67%Q_T. However, the

maintenance of the Q_{mean} between these values was not the single cause of the capacity gain. The tests that exhibited a post-cyclic capacity increase also had a maximum cyclic load (Q_{max}) with values greater than 80%Q_T. Therefore, the gain in post-cyclic capacity occurred when the cyclic loading was performed with the Q_{mean} maintained around 50%Q_T, and reaching to values of Q_{max} greater of 80%Q_T or more. A cyclic loading with such conditions of Q_{mean} and Q_{max} induces important densification of the sand above the helix, resulting in an increase in the helix bearing capacity.

Table 19. Summary of results of the post-cyclic monotonic tests.

Cont. No.	Test No.	Q_{mean}/Q_T	Q_{cyclic}/Q_T	Q_{pre}/Q_T	N (cycle)	$Q_{T\text{-}pc}$ (kN)	$Q_{T\ post\text{-}cycles}/Q_T$	$Q_{helix\ post\text{-}cycles}$ (kN)	$N_{q\text{-}pc}$
4	10FH-3	0.17	0.07	0.10	1500	82.2	0.88	-	28.5
4	10FH-4	0.23	0.14	0.09	1000	90.1	0.97	-	31.2
5	10FH-3	0.32	0.10	0.22	2000	88.1	0.95	-	30.5
5	10FH-5	0.41	0.09	0.32	2000	89.0	0.96	-	30.8
6	10FH-1	0.32	0.19	0.13	2000	87.9	0.94	-	30.4
6	10FH-2	0.41	0.22	0.19	2000	86.8	0.93	-	30.1
6	10FH-3	0.47	0.19	0.28	2000	86.4	0.93	-	29.9
6	10FH-4	0.47	0.23	0.23	1000	92.1	0.99	-	31.9
7	10FH-1	0.54	0.21	0.32	2000	79.6	0.86	-	27.6
7	10FH-2	0.40	0.23	0.18	2000	87.5	0.94	-	30.3
7	10FH-3	0.52	0.29	0.23	2000	90.0	0.97	-	31.2
9	10FHi-3	0.27	0.15	0.12	1000	100.0	1.08	-	34.6
9	10FHi-4	0.41	0.22	0.18	1000	93.0	1.00	-	32.2
10	10FHi-1	0.52	0.22	0.30	1000	88.1	0.95	93.3	32.3
10	10FHi-2	0.52	0.30	0.22	1000	95.4	1.03	87.5	30.3
10	10FHi-3	0.41	0.20	0.21	1000	93.3	1.00	86.8	30.1
10	10FHi-4	0.60	0.22	0.37	1000	92.2	0.99	87.3	30.2
10	10FHi-6	0.67	0.15	0.51	1000	98.1	1.06	82.4	28.5
10	10FHi-7	0.69	0.22	0.47	1000	94.1	1.01	85.6	29.6
13	10FHi-1	0.48	0.31	0.16	1000	91.1	0.98	89.4	31.0
13	10FHi-2	0.55	0.31	0.24	1000	94.8	1.02	94.8	32.8
13	10FHi-3	0.51	0.37	0.14	500	98.1	1.05	94.6	32.8
13	10FHi-4	0.59	0.35	0.25	300	99.0	1.06	94.8	32.8
14	10FHi-1	0.51	0.42	0.08	300	97.6	1.05	93.3	32.3
14	10FHi-2	0.45	0.34	0.10	500	94.6	1.02	90.8	31.4
14	10FHi-5	0.63	0.29	0.34	500	96.7	1.04	91.4	31.6

The cyclic loading also caused degradation of the anchor's post-cyclic uplift capacity in 15 of the 26 pull-out tests performed after cycling. In most of the cyclic tests that caused accumulated displacements (U_{acc}) smaller than 0.1D after 1000 cycles, a post-cyclic capacity reduction was noticed. In tests reaching $U_{acc} \geq 0.1D$ before 1000 cycles, although the limit displacement condition had not been attained, no capacity degradation was noticed for most tests except an increase of up to 8% of the post-cyclic capacity.

Table 19 also shows values of calculated post-cyclic bearing factors $N_{q\text{-}pc}$ using the measured results of pots-cyclic uplift capacity. For the calculation of $N_{q\text{-}pc}$ values obtained from the tests on model 10FH (non-instrumented anchor model), the value of total uplift capacity was used (without subtracting the shaft resistance). For the tests on model 10FHi, the value of the measured helix bearing resistance was used for these estimates. However, as shown in this table, the $N_{q\text{-}pc}$ values for all tests are very similar, as the portion of shaft resistance after the cyclic loadings are almost insignificant. The measured values of $N_{q\text{-}pc}$ for all different types of cyclic tests are very similar (mean value of 31 with a coefficient of variation of 5%).

Figure 81 shows the load-displacement response obtained for the three post-cyclic monotonic tests carried out on model 10FHi. This figure demonstrates that no loss in uplift capacity occurred after the cyclic tests. The cyclic loading caused densification of the disturbed soil above the helix, improving the helix bearing response. For cyclic tests of greater cyclic load amplitudes, the gain observed was higher. Figure 81 indicates that after cycles of higher load amplitude (10FHi-4 – Cont. No. 13), a stiffer response of the anchor was observed (smaller displacements of the anchor head compared to the other post-cyclic tests).

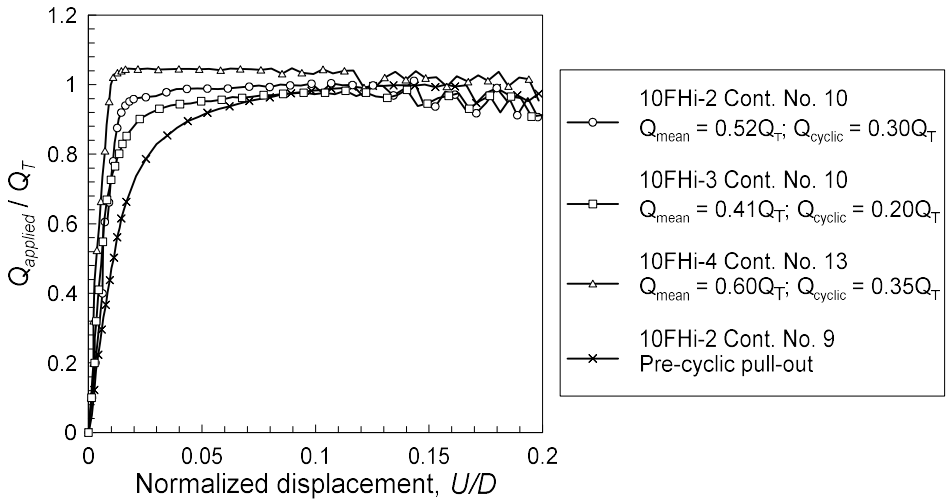

Figure 81. Post-cyclic monotonic responses.

Figure 82 compares the load registered in the force gauge above the helix (Q_{helix}) before and after the cyclic loadings. In all tests, the percentage of load resisted by the helix increased after the cyclic loading. The helix bearing resistance (Q_{helix}) after the cycles was around 93% of the total applied load, while before the cycles the portion of Q_{helix} was around 82% of the applied load.

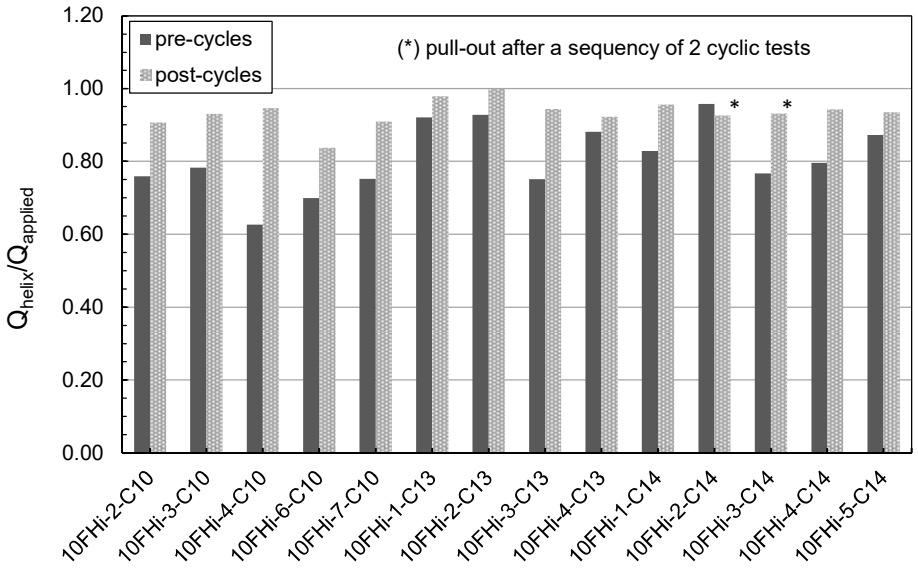

Figure 82. Comparison between the load registered in the force gauge above the helix before and after the cyclic loading.

4.5.7. Cyclic interaction diagram

Three categories of cyclic responses were used to classify the cyclic loadings of this study: Stable, Meta-Stable and Unstable, in accordance to Karlsrud *et al.* (1986) and Poulos (1988). This categorization was applied to previous studies on the degradation of shaft resistance, e.g, Jardine & Standing (2012), Tsuha *et al.* (2012b) and Rimoy *et al.* (2013). Nevertheless, studies on the pile response to cyclic compressive loading have been performed considering both base resistance and the skin friction responses to construct cyclic interaction diagrams (Karlsrud *et al.*, 1986; Poulos, 1988; Al-Douri & Poulos; 1995; Puech *et al.* 2013).

The helical anchor behaviour under cyclic tensile loadings is dependent on the joined responses of the shaft resistance and the helix bearing resistances. Therefore, the cyclic interaction diagrams in this study consider the set of helix bearing and shaft resistances in the analysis.

A Stable (S) response is defined for the cases in which the displacements of the anchor head accumulate slowly and do not reach values of 10% of the helix diameter (0.1*D*), during 1000 cycles or more. The Unstable (U) response is characterised by a rapid increase of the anchor head accumulated displacement reaching a limiting value of 0.1*D* during the first 100 cycles. For intermediate situations in which the anchor head reaches an accumulated displacement of 0.1*D* after 100 and before 1000 cycles, and the cumulative displacements increases at a moderate rate without stabilising, the cyclic response is classified as Meta-Stable (MS).

Based on these categories of cyclic response, Figure 83 presents an interaction diagram only taking into account the limit accumulated displacement condition (10%*D*), indicating the zones of Stable, Meta-Stable and Unstable responses.

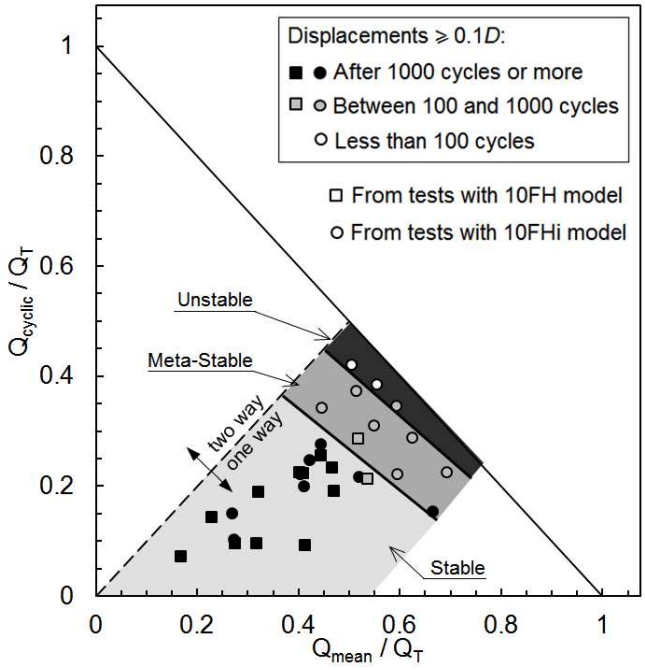

Figure 83. Cyclic interaction diagram classifying cyclic responses only into account the limit displacement condition (10%*D*).

Figure 83 illustrates a thin zone of unstable response. The lower limit line of the unstable group varies through Q_{mean} and Q_{cyclic} values, which correspond to values of maximum cyclic loads (Q_{max}) between 0.9 and 0.95Q_T. For the Meta-Stable zone, the lower limit line passes over the points that correspond to Q_{max} values between 73% (for the lower Q_{pre} values) and 80%Q_T (for the higher Q_{pre} values). These observations indicate that the limit of each zone is related to Q_{max}, which is the sum of Q_{mean} and Q_{cyclic}.

The effects of the cyclic loading parameters Q_{cyclic} and Q_{mean} are demonstrated by considering the accumulated cyclic displacements developed after a particular number of cycles as shown in Figure 84. In this figure, the contours are drawn according to the number of cycles to generate a given value of accumulated displacement. The points drawn in the graphic correspond to the performed cyclic tests.

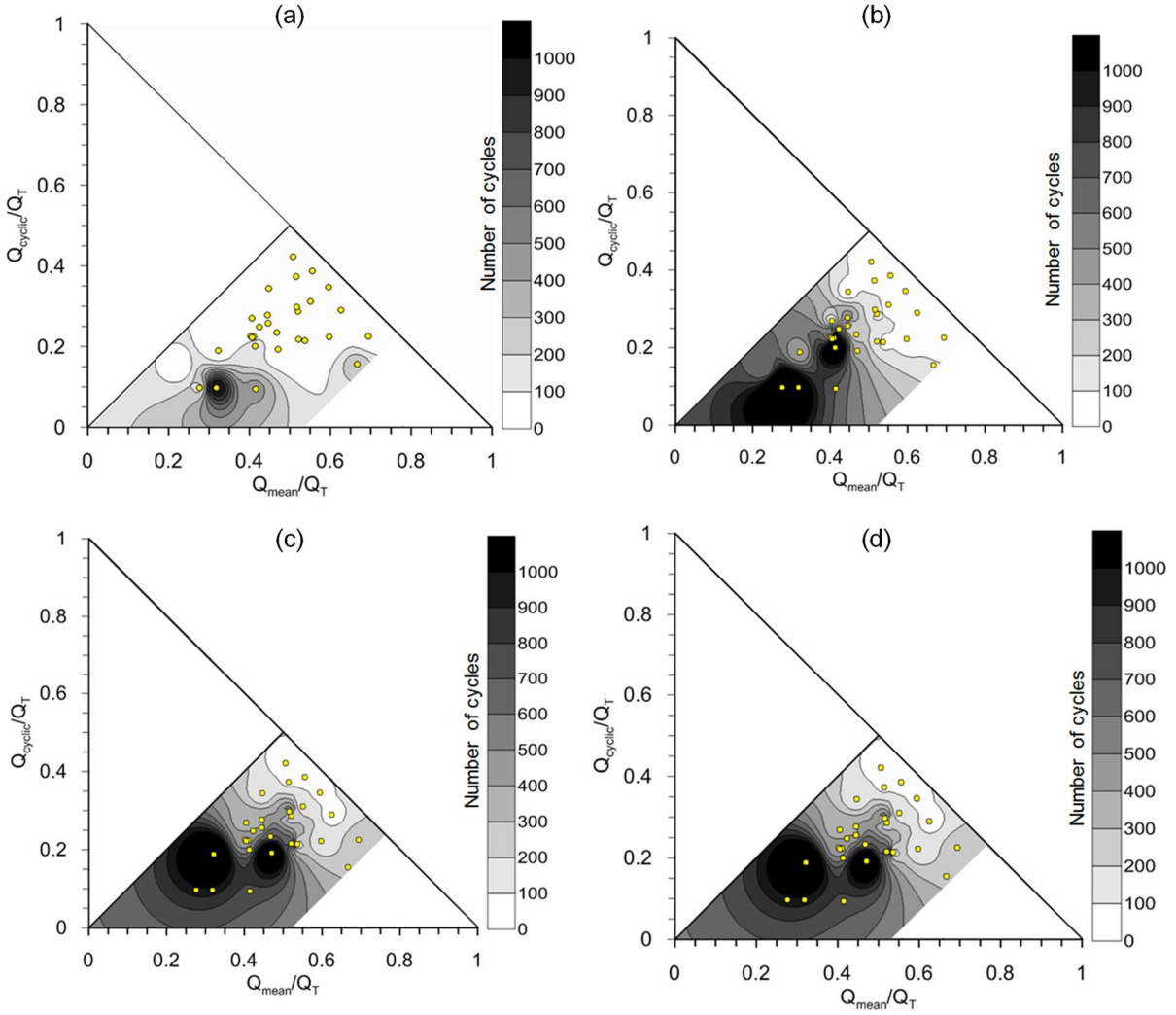

Figure 84. Contours for accumulated cyclic displacements equivalent to (a) 2%D, (b) 5%D, (c) 7%D and (d) 10%D.

Although the analysis of displacement accumulation is necessary, the anchor performance is also dependent on the effect of the cyclic loading on the post-cyclic response. This effect must not be neglected since the degradation and consequent reduction of the post-cyclic anchor uplift capacity implies in a reduction in the foundation safety factor.

The results presented in section 4.5.6 show that the degradation of the post-cyclic uplift capacity occurred in cyclic loadings with accumulated displacements smaller than 10%*D* up to 1000 cycles.

On the other hand, for some cyclic tests with values of accumulated displacements larger than 10%*D* with less than 1000 cycles (sometimes less than 100 cycles), the post-cyclic monotonic capacity increased in relation to the pre-cyclic capacity. This fact is explained by the greater densification of the soil above the helix, causing the increase of helix bearing capacity.

Figure 85 presents the contours of the normalized post-cyclic uplift capacity varying with the cyclic parameters Q_{mean} and Q_{cyclic}.

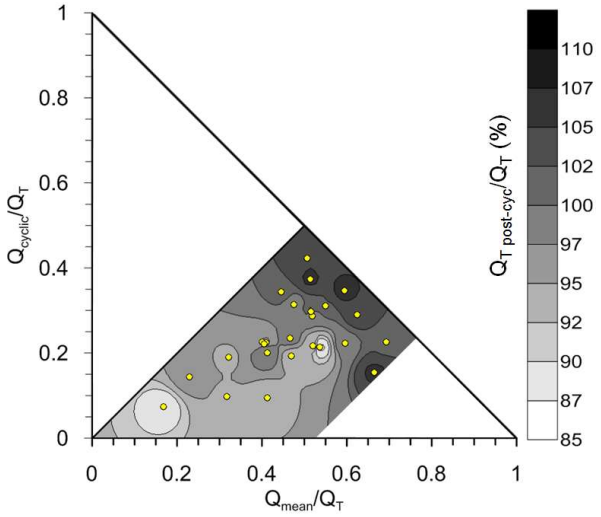

Figure 85. Contours of the normalized post-cyclic uplift capacity.

During low amplitude cyclic loadings, the sand densification is lower compared to the cases of higher cyclic amplitudes, and the accumulated displacements after 1000 cycles did not reach 10%*D*. In this case, the displacements are insufficient to compact a significant zone of sand above the helix. Thus, the loss in post-cyclic uplift capacity compared to the pre-cyclic capacity is caused by the skin friction degradation.

In the case of high-amplitude cyclic loadings, the anchor displacement during the cyclic loadings re-arrange and compact the sand mass of a wide zone above the helix. This effect is responsible for avoiding reductions in the post-cyclic uplift capacity, although the shaft resistance is reduced after the loading cycles.

In some cyclic loading tests, despite the anchor accumulated displacement is greater than 10%*D* after a few cycles, no degradation of the post-cyclic uplift capacity was observed. Therefore, a cyclic stability classification using the interaction diagram has proven un-suitable if only the displacement limit is the only criterion used to distinguish the cyclic responses.

Instead of evaluating the cyclic response merely based on the accumulated displacement, the cyclic behaviour of helical anchors should also be evaluated for the effects of the cyclic loading on the degradation of the anchor uplift capacity. Thereby, appropriate safety factors have to be used in the cyclic and post-cyclic stages of the helical anchor in service. Thus, two interaction diagrams are constructed in this study to separately evaluate the cyclic accumulated displacements and the post-cyclic capacity.

The first diagram (shown in Figure 83) provides information about the accumulated displacements during the cycles in order to guide the estimation of helical anchors displacement response under cyclic tensile loadings. The second diagram (Figure 86) provides the uplift capacity degradation.

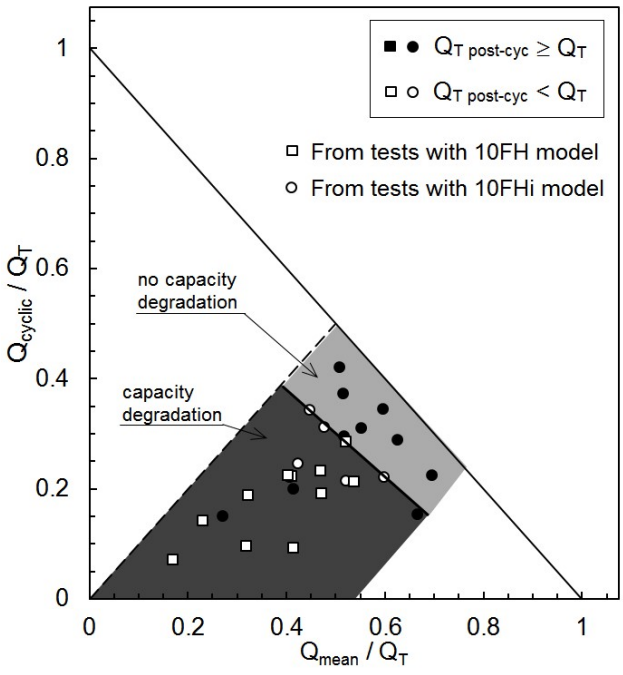

Figure 86. Post-cyclic capacity interaction diagram.

4.5.8. Sequences of cyclic loadings

In field conditions, the intensity of the cyclic loadings varies according to the intensity of the acting forces on the structure. For guyed towers, as the main acting forces are due to wind action, the helical anchors can be subjected to sequences of cyclic loading of different amplitudes. Depending on the combinations of amplitudes, the helical anchor performance can be affected in different manners. Therefore, the effect of combining two successive and different cyclic loadings of different cyclic amplitude was also evaluated in this study, following a similar procedure shown in Blanc and Thorel (2016).

Firstly, a cyclic loading test with 3000 cycles of low-amplitude (Stable) was carried out on model anchor 10FH, followed by 1000 cycles of a medium-amplitude cyclic loading, which lies at the limit between Stable and Meta-Stable, according to the limit displacement criteria of 10%*D*. After that, a second cyclic test was performed in an inversion of the order used for the first test. Both tests were conducted in container No. 6.

Figure 87a presents the load-displacement response of the first cyclic test (low amplitude followed by medium-amplitude cyclic loading) on anchor model 10FH (test 10FH-5). Both parts of the cyclic loading were carried out with the same pre-tensile load (Q_{pre} or Q_{min}) of 17%Q_T, but with $Q_{cyclic} = 0.10Q_T$ for the first part of the test and $Q_{cyclic} = 0.28Q_T$ for the second part. The load-displacement response of the second cyclic test (10FH-6), which was carried out with the inverse sequence used for the first test is presented in Figure 87b.

Figure 87 shows that when a medium-amplitude cyclic loading ($Q_{cyclic} = 0.28Q_T$) is performed before a low-amplitude cyclic loading, the accumulated displacements at the end of the cyclic loading is 42% smaller compared to the case in which a low-amplitude cyclic loading of $Q_{cyclic} = 0.10Q_T$ is applied first. The accumulated displacements at the end of test 10FH-6 corresponded to 9%*D* (Figure 87b), while in test 10FH-5 the accumulated displacements reached 15%*D* (Figure 87a).

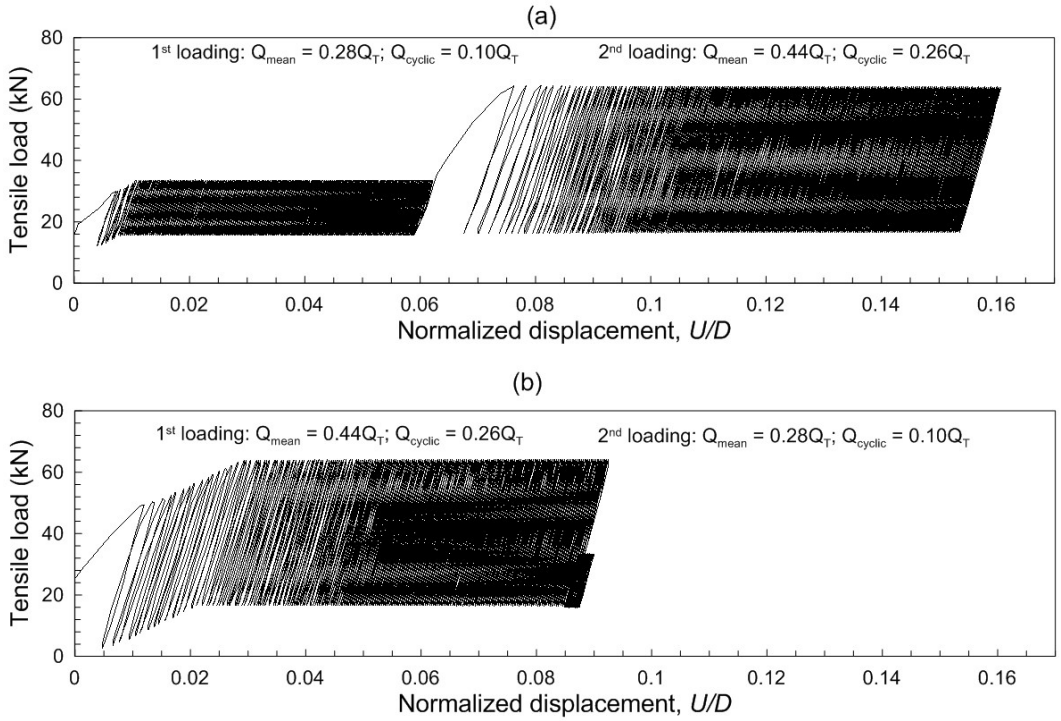

Figure 87. Load-displacement responses of tests with sequence of different cyclic loadings: (a) test 10FH-5 and (b) test 10FH-6, both in Cont. No. 6 (prototype values).

Cyclic tests with a sequence of 2 different cyclic loading amplitudes were also conducted on instrumented model anchor 10FHi. Two tests were carried out in container No. 9: 10FHi-5 and 10FHi-6. The first cyclic test (10FHi-5) was performed with the same characteristics as the first test conducted on the model anchor 10FH, presented previously in this section in Figure 88a. The second cyclic test was carried out with the inverse sequence of cyclic loadings of the first.

Because tests 10FHi-5 and 10FHi-6 in container No. 9 were carried out with the same characteristics of the cyclic loading tests performed on model 10FH, the influence of the size of the helix pitch could be evaluated, considering the helix pitch is 2.5 mm in model 10FH and 9.7 mm in model 10FHi (both dimensions in model scale). The load-displacement responses of cyclic tests 10FHi-5 and 10FHi-6 are shown in Figure 88.

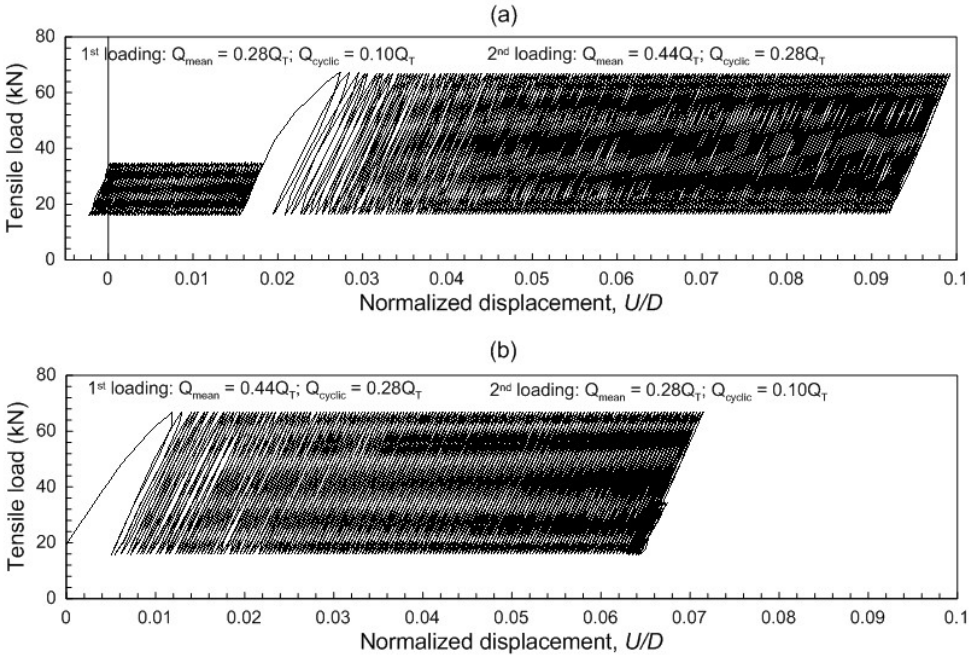

Figure 88. Load-displacement responses of tests with different cyclic loadings sequences: (a) test 10FHi-5 and (b) test 10FHi-6, both in Cont. No. 9 (prototype values).

Figure 88 indicates that during the initial cycles of the first cyclic loading, test 10FHi-5 exhibited a stiffer behaviour compared to test 10FH-5 in Cont. No. 6. Negative displacements can also be noted at the minimum applied load in 10FHi-5. This stiffer behaviour was caused by an accidental pre-loading at the end of the model installation, reducing the displacement rate at the initial cycles.

Both tests performed with model 10FHi (Figure 88) showed smaller accumulated displacements compared to the tests on 10FH (Figure 87). The larger displacements observed during the tests on model 10FH probably occurred due to the lower stiffness of the disturbed soil above the helix. This lower stiffness could be caused by two different circumstances: (1) the accidental pre-loading at the end of the model installation compacted the sand above the helix, (2) during the installation of the anchor with smaller helix-pitch the soil above the helix is traversed more times compared to the model of the larger helix-pitch (10FHi), and as a consequence the level of sand disturbance is greater. However, no conclusions could be drawn about these observations.

A 3rd and a 4th cyclic test on model 10FHi were performed with sequences of cyclic loading with different combinations of cyclic loading amplitudes, but with approximately the same Q_{pre} value.

In the 3rd cyclic test (10FHi-3 Cont. No. 14), for the first part of the cyclic loading a similar medium-amplitude to the first and second tests on 10FHi ($Q_{cyclic} = 0.28Q_T$) was used (with a limit of stable and meta-stable cyclic responses using 10%D displacement criteria). The second part of the 3rd cyclic test consisted of 300 cycles with a high load amplitude, capable of causing accumulated displacements larger than 10%D before 100 cycles ($Q_{cyclic} = 0.39Q_T$). The 4th cyclic test was conducted using the inverse sequence of cyclic loadings (test 10FHi-4 Cont. No. 14).

Figure 89 presents the results of the 3rd and 4th cyclic tests conducted on model 10FHi. The cyclic test with the higher amplitude applied first caused larger accumulated displacements, differently than that observed for the tests with sequences of medium and low amplitudes (Figure 88).

The medium-amplitude loading of tests 10FHi-6 and 10FHi-3, respectively in containers 9 (Figure 88b) and 14 (Figure 89a), caused a reduction in the displacement accumulation rate in both tests. When high-amplitude cyclic loading was carried out first, the accumulated displacement reached 13%D at the end of this cyclic loading part (Figure 89b). When the medium-amplitude loading was applied first (Figure 89a), the accumulated displacement during the following cyclic loading (the high-amplitude loading) was 7%D.

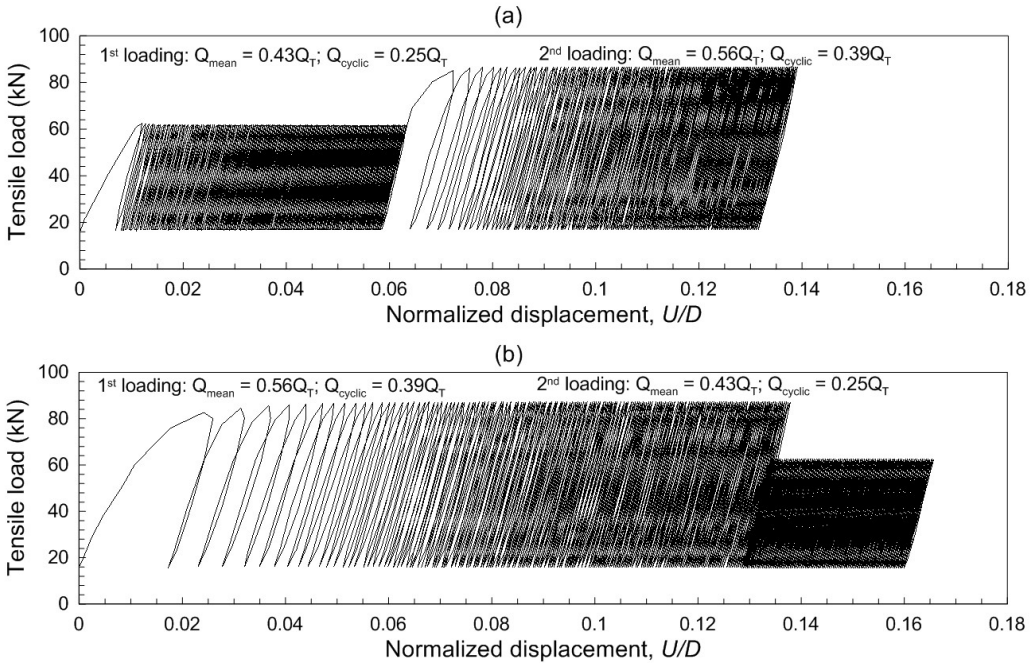

Figure 89. Load-displacement responses of tests with different sequences of cyclic loadings: (a) test 10FHi-3 and (b) test 10FHi-4, both in Cont. No. 14 (prototype values).

Figure 90a shows the vertical cyclic displacements for the four cyclic loading tests (with two different parts) on instrumented anchor model 10FHi. In this figure, the smallest cyclic load amplitude ($Q_{cyclic} = 0.10Q_T$) causes no significant increase in the helix bearing resistance (anchor axial stiffness) that could reduce the accumulated displacements of subsequent load cycles. On the other hand, the medium-amplitude cyclic loading ($Q_{cyclic} \approx 0.28Q_T$) applied first was responsible for the increase in the anchor axial stiffness, reducing the anchor accumulated displacement from 43.9 mm to 23.7 mm in the high-amplitude cyclic loading.

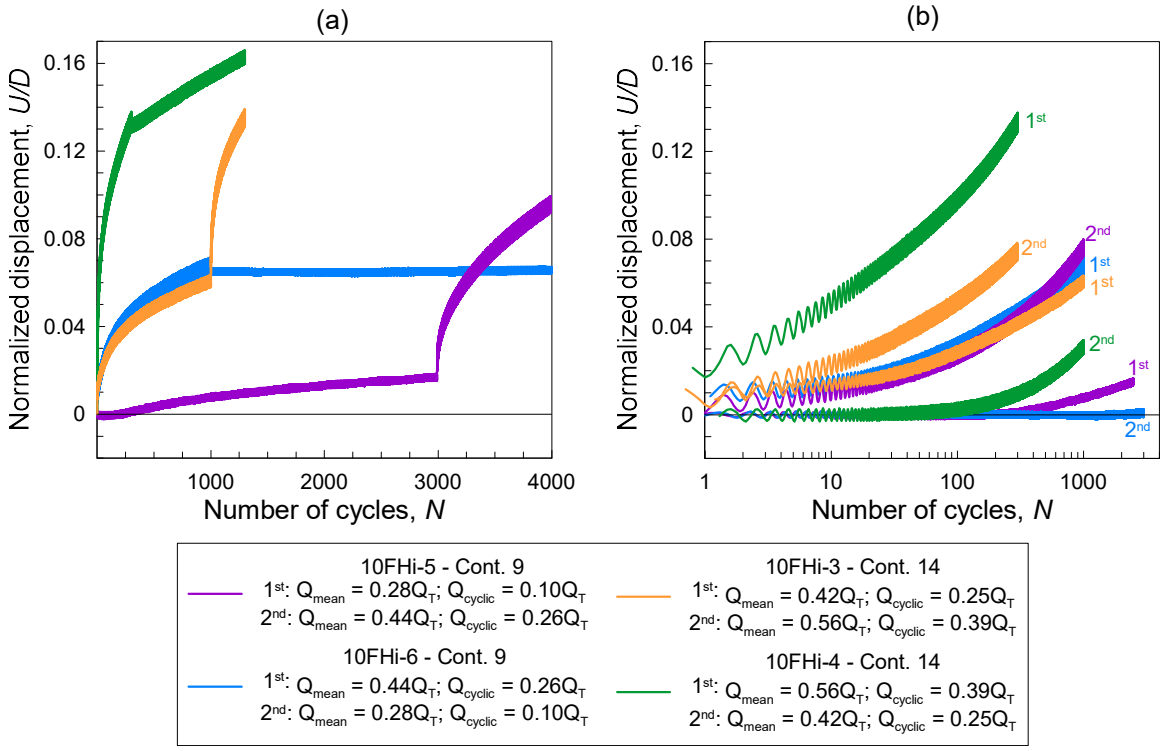

Figure 90. Anchor head vertical displacements of tests with sequence of cyclic loadings: (a) cycles in linear scale and (b) cycles in log scale.

In the first part of the cyclic loading, an increase in the anchor axial stiffness was observed in three of the four tests on 10FHi (Figures 91a and c). The only case of stiffness decrease observed was in the first loading, because the anchor initial stiffness was higher than the other three tests, caused by an accidental pre-loading as explained previously.

On the other hand, two cyclic tests presented a stiffness decrease in the second part of the cyclic loading. The similarity between these two tests is in the smaller amplitude compared to the first part of the cyclic loading (Figures 91b and d).

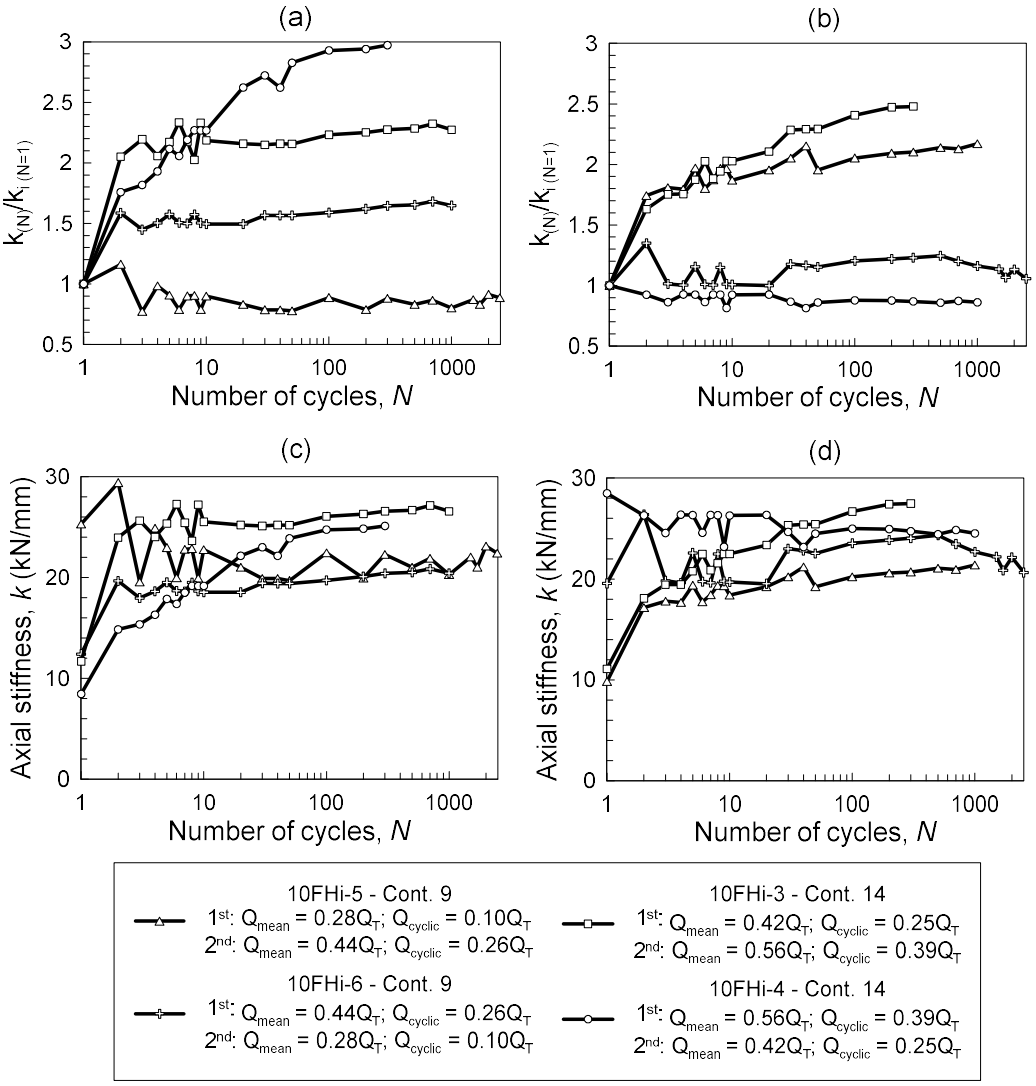

Figure 91. Normalized stiffness of the (a) first loading and (b) second loading of the test sequence; Anchor axial cyclic stiffness (in prototype scale) of the (c) first loading and (d) second loading of the test sequence.

The post-cyclic response was also evaluated for 6 tests with two different cyclic loading sequences. Figure 92 shows that the greater pull-out capacities were observed after the two high-amplitude cyclic tests (10FHi-3 and 4, both in Cont. No. 14). For these cases, the post-cyclic values of pull-out capacity are greater than the pre-cyclic (Q_T). All the cyclic tests using higher-lower loading amplitudes exhibited post-cyclic capacities greater than the tests with sequences of lower-higher loading amplitudes.

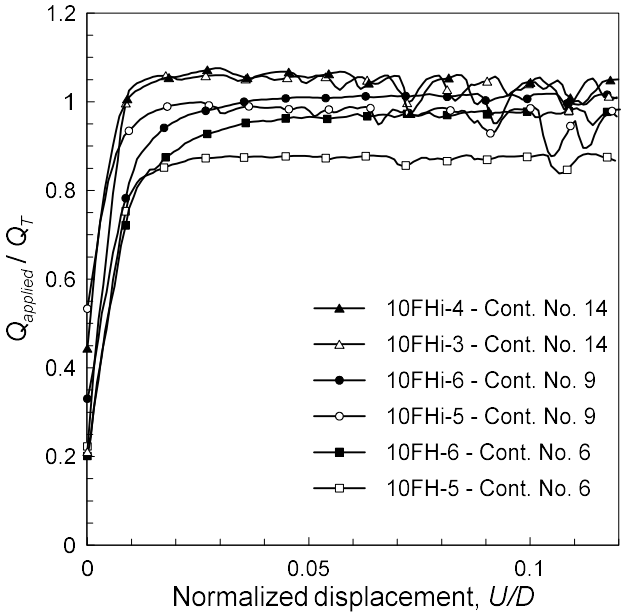

Figure 92. Post-cyclic monotonic tensile responses.

4.6. Summary and conclusions

From the centrifuge testing programme carried out during this study, the following main observations were made about the behaviour of the helical model anchors under monotonic and cyclic loading:

a) Comparable monotonic uplift capacity was found for anchor models with w/d_{50} ratio ranging from 58 to 117. For the same range of w/d_{50}, the results of installation torque and torque correlation factor K_t were not affected by scale effects. In addition, the K_t values were found to be comparable to field measurements. These findings are valid for a D/d ratio equals to 3.3.

b) The sand disturbance in the cylindrical zone above the helix was not uniform with the depth. Contrast between less dense and denser sand was observed at a given cross-section of the cylinder of disturbed soil, indicating that the sand undergoes greater disturbance in the path the helix goes through.

c) Under monotonic tensile loading, the portion of the applied load resisted by helix bearing was found to be, on average, 82% of the applied load. After cycling, the portion resistance by helix bearing increased to 93% of the applied load, on average. This increase is mainly due to the degradation of the shaft friction resistance.

d) During the unloading stages (minimum applied load) of the cyclic tests, the tension force registered by the load cell above the helix was observed to become greater than the tension force applied to the anchor head. This minimum tension force registered by the load cell at the end of the unloading stage increases with the number of cycles. This phenomenon is related to the presence of the sand grains below the anchor does not allow the anchor to return to its initial starting elevation, thus with successive load cycles, the sand grains slowly creep underneath the anchor helix.

e) This study is focused on the cyclic behaviour of helical anchors used to support guyed tower under high wind speeds (low probability occurrence and low number of loading cycles). For this type of structure, the failure is associated with a specific displacement that will cause the slack of the cable. For this reason, this study is focused on the cyclic displacement response. For the cyclic loading conditions and numbers of cycles performed in the current study, no catastrophic anchor failure was observed.

f) Two different displacement accumulation trends were observed during the cyclic tests. These two trends were found to follow different functions. The transition from one trend to another was found to occur at specific values of cycle number (N) and accumulated displacement (U_{acc}). These specific values of N and U_{acc} were found to align in a straight line when the displacement accumulation response is analysed in a graphic of $(\log N)^2$ *versus* U_{acc} for cyclic tests varying Q_{mean} and Q_{cyclic}.

g) The cyclic stability of helical anchors was suggested to be evaluated from the accumulation of displacements and from the degradation of the post-cyclic capacity. Thus, two interaction diagrams were constructed.

5. RESULTS OF FIELD LOAD TESTS

5.1. Installation torque

The installation torque of both single-helix anchors tested at the Experimental Site of the University of São Paulo at São Carlos was registered every 0.5 m for the 15 m of anchor installation. The installation torque results are presented in Figure 93 and compared with the values reported by Tsuha (2007). This author tested two double-helix anchors installed at the same site with 14.4 m depth.

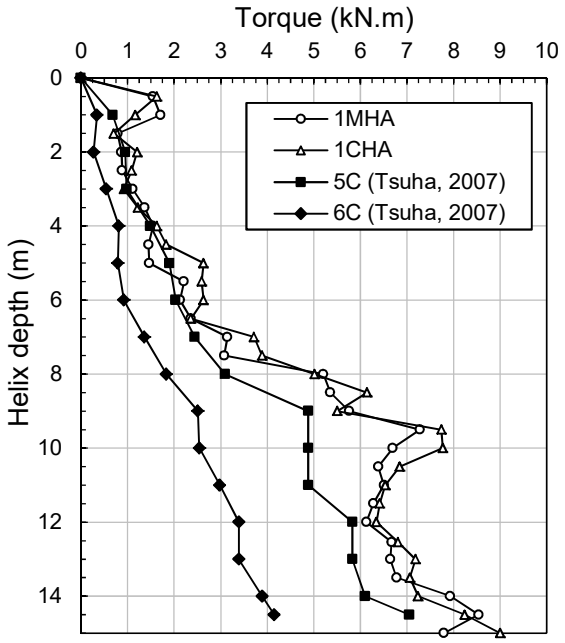

Anchor	Number of helices	$D_{lower\ helix}$ (mm)	$D_{upper\ helix}$ (mm)	d (mm)	$z_{D\ lower}$ (m)
1MHA	1	305	-	101.6	15
1CHA	1	305	-	101.6	15
5C	2	254	304.8	73	14.4
6C	2	254	304.8	73	14.4

Figure 93. Comparison of the installation torque of Tsuha's (2007) experiments with the current research.

The installation torque in the current study was greater than those presented by Tsuha (2007) for two primary reasons:

a) a larger shaft diameter was used for the current study: 101.6 mm against 73 mm in Tsuha (2007).

b) a different number of helices and different helix diameter were used for the current study. For the work of Tsuha (2007) the helices diameters of double-helix anchor 5C were 254.0 mm and 304.8 mm, and for anchor 6C were 127.0 mm and 152.4 mm. Although the helix diameter of top helix of the anchor 5C (Tsuha 2007) is equal to the helix diameter of the current study, in the current study the helix of 305 mm was installed deeper. Also, during the installation of top helix of the anchor 5C, the penetrated soil was already disturbed by the installation of the bottom helix, facilitating the penetration of the top helix, and reducing the installation torque.

5.2. Initial monotonic tension load test

The field experiments comprised: cyclic tensile loading tests on anchor 1CHA, and monotonic tensile loading tests on anchors 1MHA and 1CHA. Both anchors were instrumented to separate shaft and helix bearing resistances.

The anchor uplift capacity was established as the applied load to cause an anchor head displacement equals to 10%D (33 mm). This criterion is commonly adopted for helical anchors.

Figure 94 presents the load-displacement response for the uplift load tests on both 1MHA and 1CHA helical anchors. According to a limiting displacement criterion of 10%D, the uplift capacities of the first load test (Q_{T1}[2]) were 89.1 and 97.6 kN respectively for 1MHA and 1CHA anchors.

The helix responses in both tests were identical in most load steps. During the last load step, the load registered in the shaft section above the helix was 77.2 kN for 1MHA and

[2] Q_{T1} is the reference uplift capacity obtained from the 1st monotonic test for the calculation of the cyclic loading parameters.

60.3 kN for 1CHA (respectively, 87 and 62%Q_T). The shaft resistance ($Q_{applied}$ - Q_{helix}) exhibited a peak approximately in the middle of the test (at a displacement of around 6%D or 18%d, where D and d were the helix and shaft diameters, respectively), followed by a decrease, which was more pronounced for anchor 1MHA.

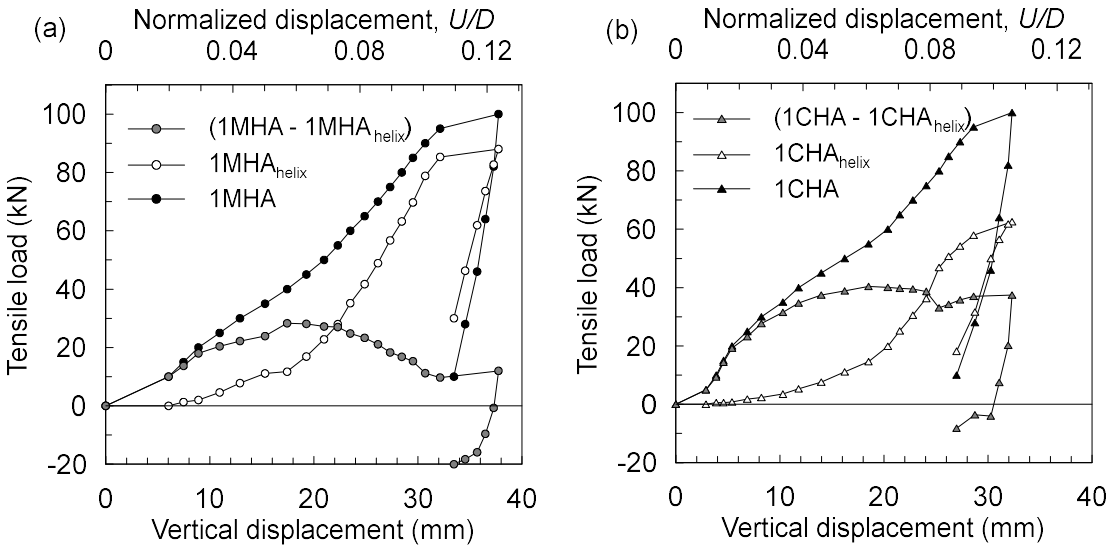

Figure 94. Results of the 1st monotonic load tension tests performed on anchors (a) 1MHA and (b) 1CHA.

At the end of the load test, a negative skin friction and, consequently, a residual load at the helix was observed in both tests. The observed residual load was greater for the anchor 1MHA (Figure 94). Figure 95 presents a scheme of the reacting forces on the helical anchor during the first load tests. At the end of the unloading stage with no applied load on the anchor head, the skin friction prevents the rebound of the helix which causes the application of compressive forces on the soil above the helix. Therefore, to equilibrate the reacting forces on the helix caused by the compressed soil, the skin friction is reversed and becomes negative.

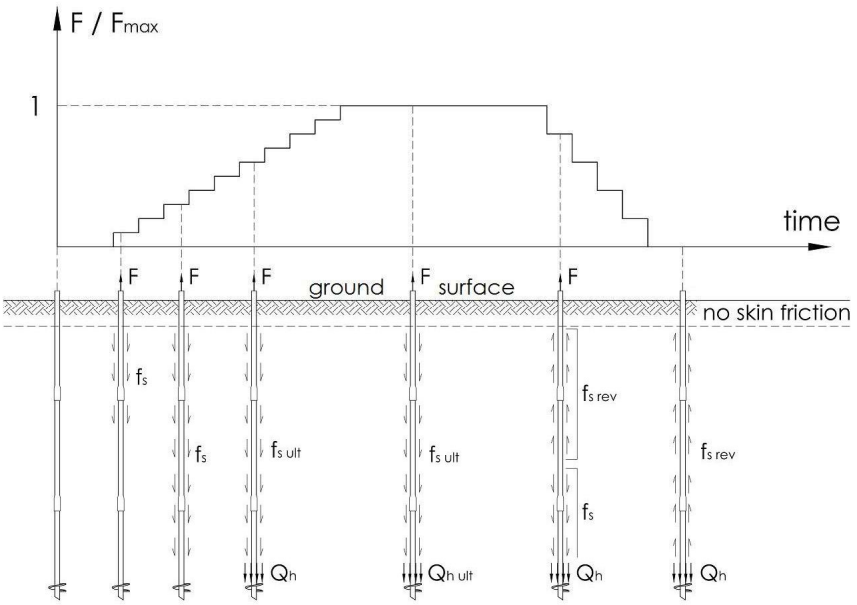

Figure 95. Reacting forces on the helical anchor during the first tension load test.

5.3. Cyclic loading tests on 1CHA anchor

In this section, the results of the cyclic tests and the subsequent monotonic load tests are presented and discussed in the same order in which the tests were performed (chronological order). In addition, the results of the monotonic tension load tests on 1CHA are compared with the results of the monotonic load tests on the reference anchor (1MHA), which did not experience cyclic loadings. Table 20 recapitulates the characteristics of the cyclic loadings carried out on anchor 1CHA.

Table 20. Characteristics of the cyclic load tests on anchor 1CHA.

Cyclic test	Q_{mean}/Q_{T1}	Q_{cyclic}/Q_{T1}	Number of cycles	Period (s)
1st test	0.15	0.05	50	60
2nd test	0.25	0.15	50	60
3rd test	0.35	0.25	50	60
4th test	0.58	0.48	50	60

The four cyclic loading tests performed on anchor 1CHA are presented in Figure 96. Monotonic tensile loading tests were conducted on this anchor before and after all cyclic

loading tests. In parallel to the monotonic tests on anchor 1CHA, monotonic tests were also conducted on reference anchor (1MHA).

The first cyclic test was carried out after the 1st monotonic uplift test on 1CHA (Figure 96a). This first cyclic test was performed with cyclic parameters of $Q_{mean} = 0.15Q_{T1}$ and $Q_{cyclic} = 0.05Q_{T1}$ to evaluate the possible increase in the anchor's capacity due to low-amplitude cyclic loadings, typical in service conditions of guyed tower anchors. Due to the previous ultimate load applied on anchor 1CHA, Figure 96a shows that the cyclic loading caused very small displacements (around 0.1%D) during each cycle, with a negative accumulated displacement of the same magnitude. Despite causing large displacements that reached a limit condition of 10%D, the application of a single load cycle with a large amplitude of $Q_{max} = Q_{T1}$ (1st monotonic load test) caused an improvement in the soil above the helix resulting in increased and the elimination of the accumulated cyclic displacements. Negative accumulated displacements were observed during the cycles (Figure 96a) and can be explained by the negative skin friction on the shaft and the effects of the previous monotonic loading test on the soil above the helix.

Figure 96b shows that the registered load in the instrumented section (just above the helix) was virtually constant during the cycles. This constant load value during the cycles indicates that the shaft skin friction fluctuates between upward and downward sense depending on the magnitude of the applied force. Also in this figure, a decrease of the maximum load in the instrumented section helix occurred during the cycles (around 17%). Since no helix bearing degradation is expected due to the helix bearing capacity increase after each monotonic tension load test, the decrease in the registered load in the instrumented section is probably due to the positive friction gain caused by the reversion of the negative skin friction.

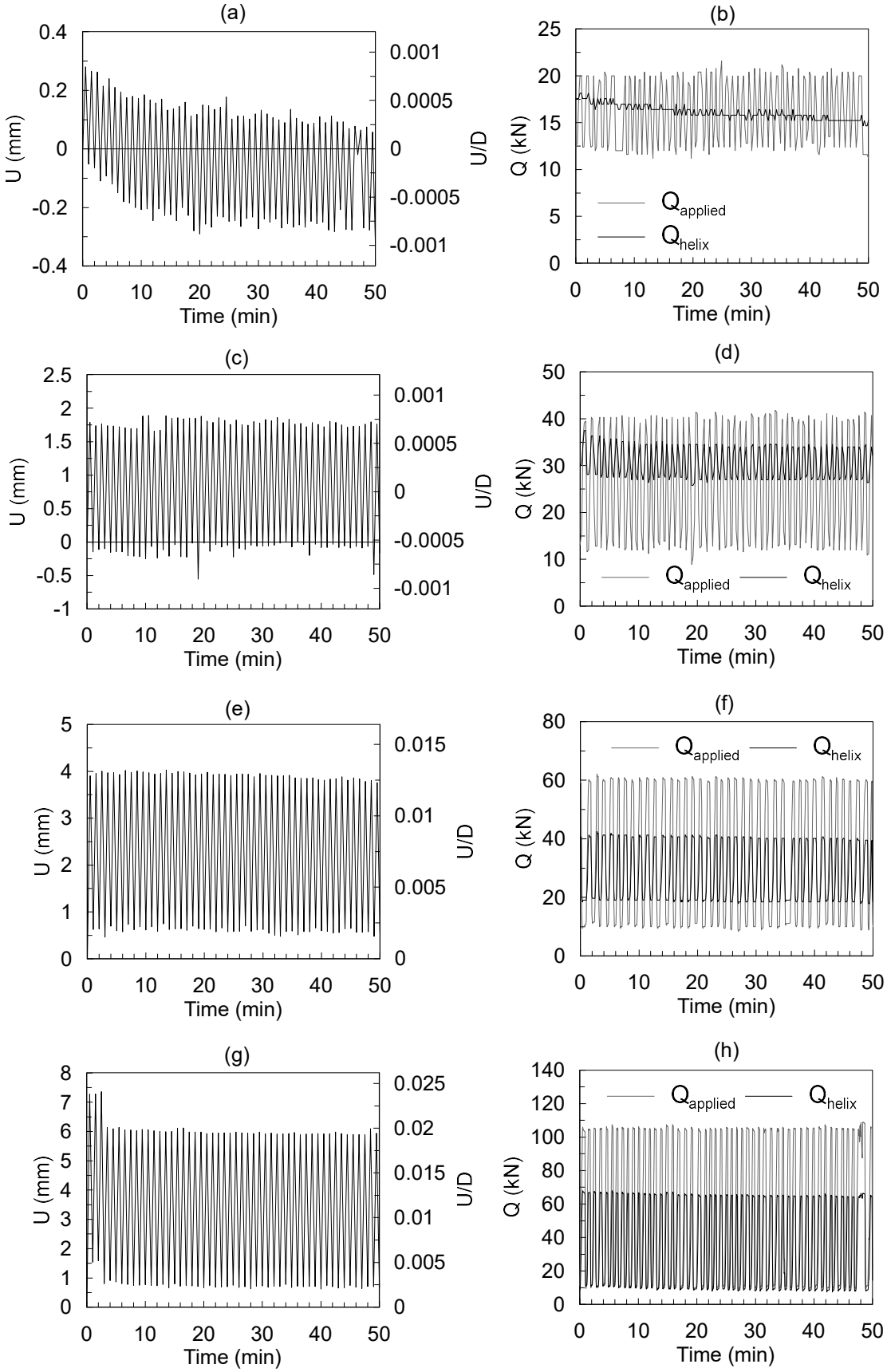

Figure 96. Results of the cyclic tests on 1CHA: (a) and (b) 1st test $Q_{mean} = 0.15Q_{T1}$ and $Q_{cyclic} = 0.05Q_{T1}$; (c) and (d) 2nd test $Q_{mean} = 0.25Q_{T1}$ and $Q_{cyclic} = 0.15Q_{T1}$; (e) and (f) 3rd test $Q_{mean} = 0.35Q_{T1}$ and $Q_{cyclic} = 0.25Q_{T1}$; (g) and (h) 4th test $Q_{mean} = 0.58Q_{T1}$ and $Q_{cyclic} = 0.48Q_{T1}$.

The results of the 2nd monotonic load test conducted on anchors 1CHA (after the 1st cyclic loading) and 1MHA are presented in Figure 97b. The ultimate applied load in this 2nd monotonic loading test increased in around 55% in comparison with the 1st load test. At the last load step of the 2nd monotonic test, the applied tension load was equal to 154.0 kN and caused vertical displacements of 32.55 and 33.41 mm, respectively for 1MHA and 1CHA. Therefore, no influence of the 1st cyclic loading was observed on the post-cyclic response of anchor 1CHA. Both anchors exhibited a similar load-displacement response registered at the anchor head. However, differences were observed in the registered force in the instrumented section above the helix. In the instrumented section, a greater load (91%$Q_{applied}$) was observed for 1MHA anchor in the last load step in comparison with 1CHA (72%$Q_{applied}$).

Observing the shaft resistance ($Q_{applied}$ - Q_{helix}), an increase was noticed at an anchor vertical displacement of around 5%d (or 1.6%D). After this peak, the shaft resistance decreased for 1MHA and slightly increase for 1CHA. Therefore, at the last load step, the shaft resistance achieved values of 13.9 and 44.2 kN respectively for 1MHA and 1CHA.

The 2nd cyclic test was carried out after the 2nd monotonic uplift test on 1CHA with $Q_{mean} = 0.25Q_{T1}$ and $Q_{cyclic} = 0.15Q_{T1}$. The maximum applied cyclic load (Q_{max}) corresponds to 26% of the ultimate load obtained during the 2nd monotonic test on 1CHA. Figure 96c shows that no displacement increase occurred during the cycles and also no accumulated displacement was observed at the end of the cyclic test. Figure 96d shows a slight decrease of the maximum load measured in the shaft section just above the helix compared to the 1st cyclic test (12% in the 2nd cyclic test and 17% in the 1st cyclic test). Also in Figure 96d, as in the 1st cyclic test, the force registered in the instrumented section was greater than the applied load on the anchor head during the minimum cyclic load (Q_{min} or Q_{pre}), indicating that reversion of shaft friction still occurs.

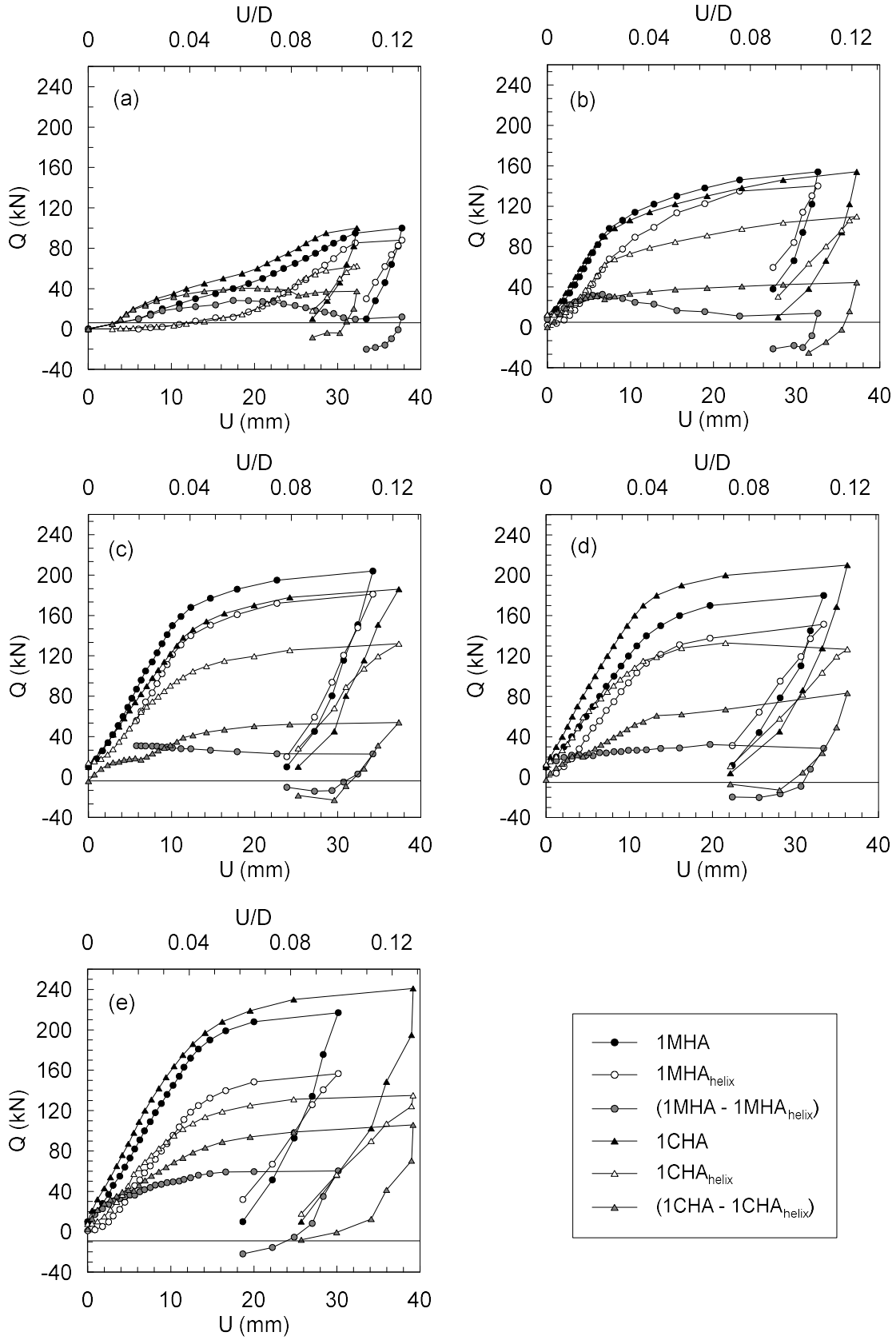

Figure 97. Results of the monotonic tension load tests: (a) 1st load test; (b) 2nd load test; (c) 3rd load test; (d) 4th load test and (e) 5th load test.

The 3rd series of monotonic tension load tests was performed on anchor 1CHA (after the 2nd cyclic test) and 1MCA (reference). The uplift capacities of the anchors increased compared to the previous test. Also, an asymptotic trend (more clear failure indication) of the applied load began to be observed for vertical displacements of around 6%D in both 1CHA and 1MHA[3] tests (Figure 97c). The maximum applied load attained greater values for the load test on 1MHA (204 kN) than for 1CHA (186 kN).

Comparing the shaft resistance values ($Q_{applied}$ - Q_{helix}) obtained in the 2nd and 3rd monotonic loading tests, increases of 9.0 and 11.4 kN (64% and 27%) were observed for 1MHA and 1CHA, respectively.

The application of a single load cycle with a large amplitude of $Q_{max} = Q_{T(N)}$ (in a monotonic loading test) has been shown to cause no damage to the anchor behaviour in both 1MHA and 1CHA anchors. At least, in the results of the first three monotonic tests, each time the anchors were re-tested monotonically, the ultimate load increased.

The results of the 3rd cyclic test (Figures 96e and f) also illustrate the anchor performance improvement due to the previous application of a single cycle with large amplitude (during the monotonic loading test). In this cyclic test, cyclic loading with $Q_{mean} = 0.35Q_{TI}$ and $Q_{mean} = 0.25Q_{TI}$ caused an accumulated displacement of 0.60mm after 50 cycles; however, this accumulated displacement was generated in the first load cycle, and no further increase of accumulated displacement was noticed for the following 49 cycles.

During the 3rd cyclic test, the $Q_{helix}/Q_{applied}$ ratio decreased in comparison to the 2nd cyclic load test (Figure 96d and f). While in the 2nd cyclic test the maximum registered load in the instrumented section was $Q_{helix} = 0.94Q_{applied}$, in the 3rd test the maximum load was $Q_{helix} = 0.71Q_{applied}$, indicating an increase in shaft resistance mobilization.

[3] The load in the instrumented section above the helix was not recorded at the 8 first load steps.

After the 3rd cyclic test, the 4th monotonic tension load test performed on anchor 1CHA exhibited an ultimate load 17% greater than anchor 1MHA (Figure 97d), which had presented the greater ultimate load value in the previous (3rd) monotonic load test (Figure 97c). Besides the ultimate load increase of anchor 1CHA, the registered load in the last load step indicated no load increase in comparison with the previous monotonic test (3rd). The ultimate registered load in the instrumented section of this anchor was 129.0 kN in the 4th monotonic tests. Meanwhile, for the 3rd test, the load in this section was 131.9 kN, which may indicate the ultimate helix bearing capacity was attained. In consequence, a shaft resistance increase was observed in anchor 1CHA. Identical behaviour was observed for the 4th monotonic load test on anchor 1MHA; however, a lower shaft load was observed for this anchor.

Due to the observed increase of the ultimate load with the monotonic tension load tests, the last cyclic test (4th) was conducted with a higher cyclic load amplitude resulting in Q_{max} = 1.05Q_{T1} and Q_{pre} = 0.10Q_{T1} to evaluate the anchor response to a large amplitude cyclic loading. Comparing with the results of the last monotonic test (4th) on anchor 1CHA, the maximum applied cyclic load (Q_{max}) corresponded to 50% of the ultimate load.

Figure 96g and h present the results of the 4th cyclic test on anchor 1CHA. Similar displacement accumulation behaviour was observed during the 3rd cyclic test. An initial accumulated displacement of around 0.7 mm was maintained until the end of the 4th cyclic test with no increase during the cycles. Figure 96h shows that, for this 4th cyclic test, the force registered in the instrumented section during the minimum cyclic load (Q_{min}) is inferior to the force applied on the anchor head, indicating no more signal of negative shaft friction, as observed in previous cyclic tests.

Figure 97e shows that the load-displacement response is similar for both anchors, with an ultimate load of anchor 1CHA slightly greater than that of anchor MHA1 (around 7% greater). Therefore, no degradation of the uplift capacity was noticed due to the application of

the previous cyclic loading with a higher load amplitude (4th cyclic test). The registered load in the instrumented section indicated similarities between the ultimate values of the last three monotonic tests (3rd, 4th and 5th). On the other hand, the shaft load increased by 27% in comparison to the previous monotonic test (4th). For the 5th monotonic load test on anchor 1MHA, the increase in the shaft load was 111% in comparison to the 4th monotonic test on this anchor.

Table 1 summarizes the results of the monotonic tensile load tests on both 1MHA and 1CHA anchors.

Table 21. Summary of the results of the monotonic tensile load tests.

Test No.	1MHA			1CHA		
	Q_{ult} (kN)	Q_{helix} (kN)	Q_s (kN)	Q_{ult} (kN)	Q_{helix} (kN)	Q_s (kN)
1	89.1	77.2	11.9	97.6	60.3	37.3
2	154.0	140.0	14.0	154.0	111.3	42.7
3	204.0	181.0	23.0	186.0	131.9	54.1
4	180.0	151.5	28.5	210.0	129.0	81.0
5	217.0	156.7	60.3	241.0	131.1	109.9

Generally, the cyclic performance of the 1CHA helical anchor was affected by the monotonic load test performed before each cyclic test to simulate the ultimate loading of a blast of wind. In contrast, the cyclic load tests seem to not affect the monotonic behaviour of the helical anchor.

The load-displacement response of the first monotonic test on both 1MHA and 1CHA differed significantly from the results of the following monotonic tests (Figure 49). In addition, when the load-displacement responses are plotted according to the displacement history, each monotonic test appears to continue where the preceding test finished, perhaps with some capacity increase for anchor 1CHA.

Figure 49 shows clearly the improvement in the anchor response after each monotonic test on both anchors. The soil above the helices (described in Figure 41 of section 3.2.1) is a

tropical residual soil, with a N_{SPT} varying from 5 to 15 blows/30cm at the depth of the helix, with the bearing capacity disturbed by the helix penetration. Therefore, the monotonic tests improved the soil with low bearing capacity. If the helical anchors were installed in different soil, the improvement would probably be different. Figure 99 presents the registered load in the instrumented section in all monotonic tests according to the anchor's history of displacements. Both helix bearing and shaft resistance increased after the monotonic tests, however a greater increase of shaft resistance was observed for the anchor that experienced cyclic loadings. On the other hand, a slightly greater increase of helix bearing resistance was observed for the anchor that did not suffer cyclic loadings.

Additionally, Figures 96b, d, f, h and Figure 100 indicate that the negative skin friction (residual load) is reduced after a series of cyclic loadings.

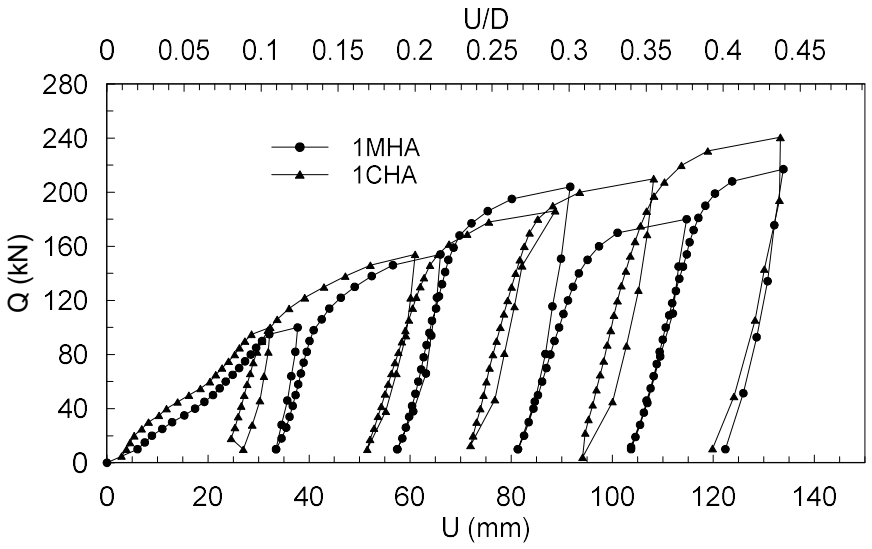

Figure 98. Monotonic load-displacement responses plotted according to the displacement history of each tested anchor.

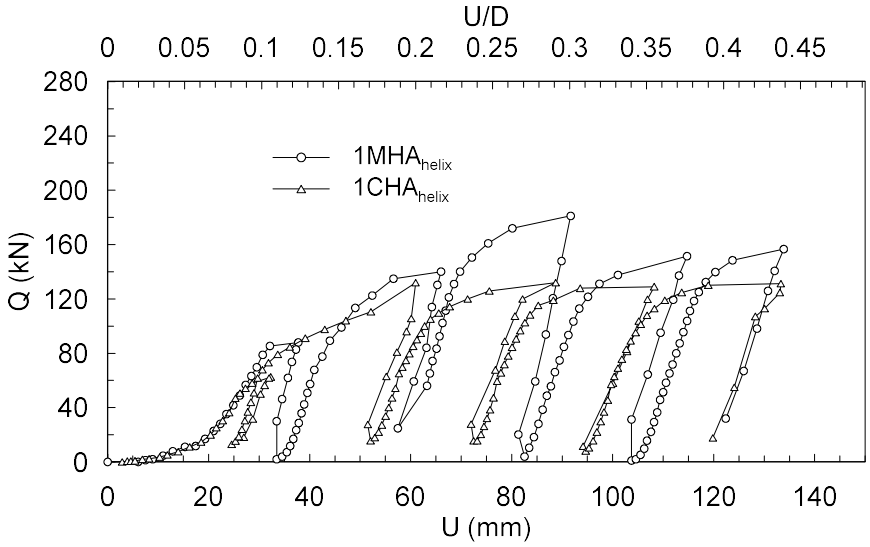

Figure 99. Registered load in the instrumented section above the helix plotted according to the displacement history of each tested anchor.

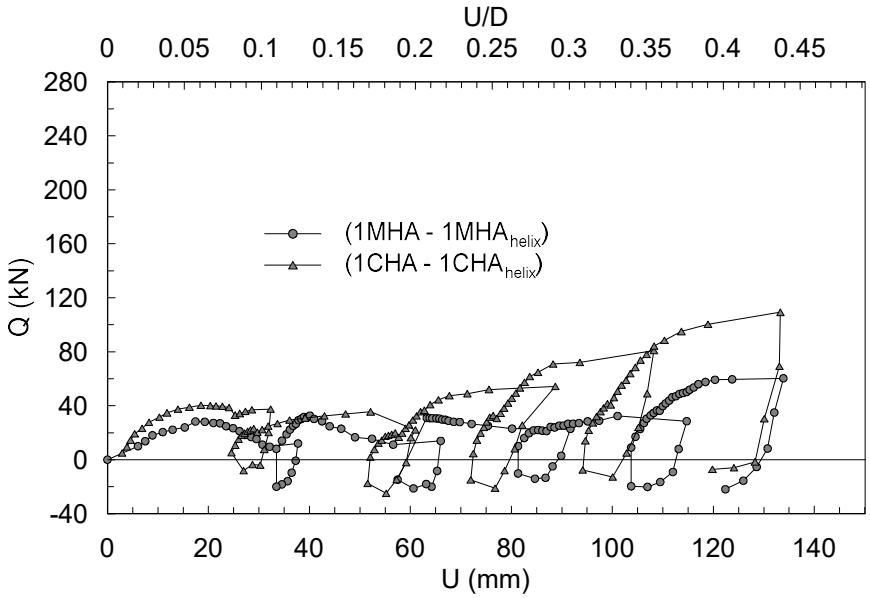

Figure 100. Shaft friction plotted according to the displacement history of each tested anchor.

6. RESULTS OF NUMERICAL MODELLING

In the present study, the numerical modelling was carried out to simulate the pre- and post-cyclic uplift response of the helical anchor tested in centrifuge. The numerical model was constructed with the helical anchor installed into the sand mass.

Several preliminary numerical simulations were carried out to optimize the numerical model and the input parameters. When the Young modulus of the triaxial tests was considered for the undisturbed soil, the load-displacement responses of the preliminary numerical simulations resulted in poor agreement with the experimental results of the pre-cyclic monotonic tests. For these preliminary simulations, the numerical simulation resulted in a significantly less stiff load-displacement response compared to the measured response. Therefore, increase values of Young modulus were used in the subsequent simulations. The parameters considered in the concluding analyses are shown in Table 22.

Table 22. Parameters of the concluding numerical simulations.

Parameter		Test 1	Test 2	Test 3	Test 4	Test 5	Test 6	Test 7	Test 8
Undisturbed soil	E (MPa)	75	75	75	70	80	120	90	80
	ν	0.3	0.3	0.3	0.3	0.3	0.3	0.3	0.3
	ϕ (º)	47	42	42	42	47	48	48	42
	ψ (º)	6	6	6	6	6	6	6	6
Disturbed soil	E (MPa)	50	50	50	50	70	90	90	45
	ν	0.3	0.3	0.48	0.48	0.3	0.3	0.3	0.3
	ϕ (º)	37	33	33	33	33	37	42	33
	ψ (º)	1	1	1	1	1	1	1	1
Interface shaft-soil	δ (º)	15	15	15	20	15	15	15	15

6.1. Overall pre-cyclic monotonic response

Figure 101 shows the monotonic load-displacement responses of the numerical simulations compared to the experimental pre-cyclic load-displacement response of the test

10FHi-2 carried out in the Container No. 9. Typically, the initial branch of the load-displacement curve of the numerical results showed agreement with the experimental curve for Young modulus between 80 and 90 MPa for the undisturbed soil and between 70 and 80 MPa for the disturbed soil (respectively in Tests 5 and 6). When the Poisson's ratio was increased from 0.3 (Test 2) to 0.48 (Test 3), the anchor stiffness also increased, without changing the Young modulus.

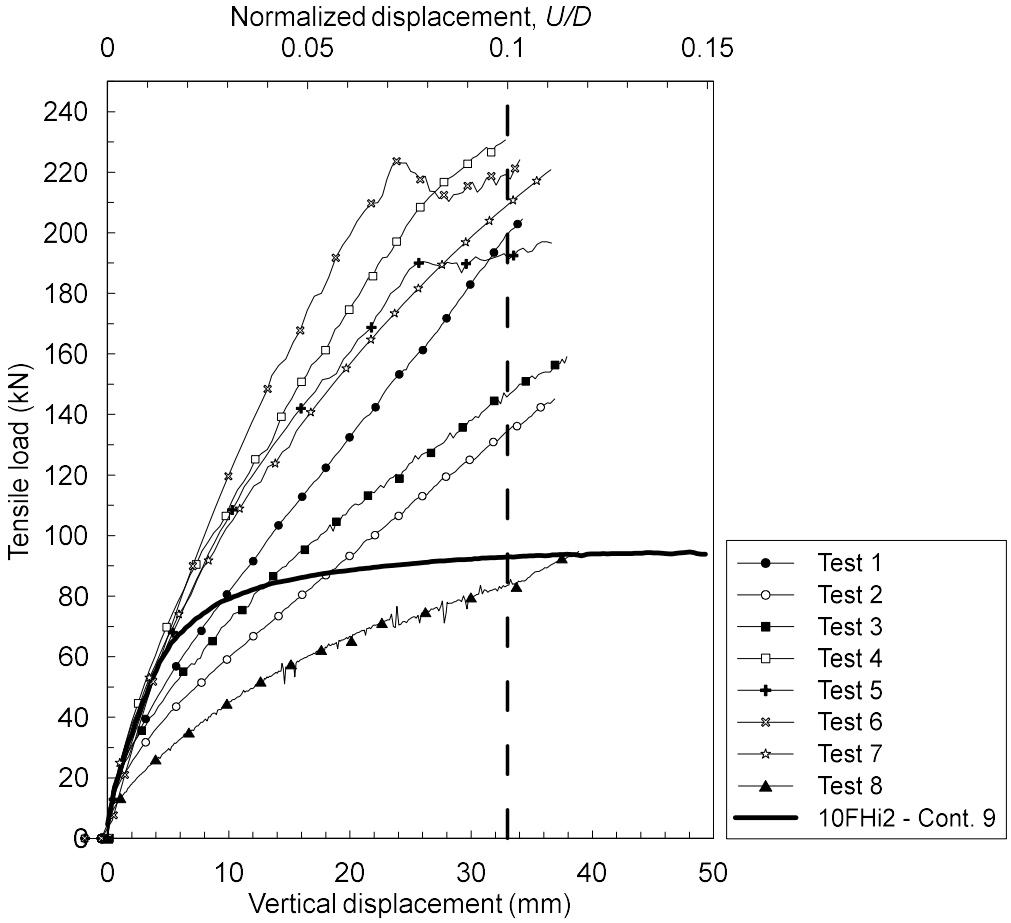

Figure 101. Comparison between numerical and experimental pre-cyclic monotonic responses.

Although the initial branch of some numerical load-displacement responses showed agreement with the experimental data, most numerical analyses overpredicted the anchor's ultimate tensile capacity from 45% to 147% in all the numerical simulations (considering that failure occurs for an uplift displacement of 10%*D*). Most of numerical simulations have not

shown an asymptotic trend as exhibited in the experimental tests. The only two numerical tests that showed an asymptotic trend were the tests with greater Young modulus for both undisturbed and disturbed soils (Tests 5 and 6), leading to believe that the asymptotic trend can be obtained only for Young modulus greater than 70 MPa for the disturbed soil. On the other hand, tests with low values of both E and ϕ may yield ultimate load values close to the experimental results, but with poor agreement with the initial branch of the experimental load-displacement response (e.g. Test 8).

Gavin *et al.* (Field investigation of the axial resistance of helical piles in dense sand, 2014) also performed numerical simulations of a monotonic full-scale tensile test on a single-helix anchor installed in dense sand with $z_D = 6.1D$. The numerical result presented by these cited authors showed an overprediction in the ultimate uplift capacity of 120% more than the field result. Gavin *et al.* (Field investigation of the axial resistance of helical piles in dense sand, 2014) argues that their relatively poor prediction is related to significantly different strength and stiffness properties, and stress paths during loading of the numerical model (based on triaxial tests) compared with the field conditions. In addition, these cited authors mention that the anchor was modelled as a wished-in-place element, disregarding the effects of the installation procedure. Therefore, for the present numerical simulation, the effects of the anchor installation were simplistically simulated by a cylinder of disturbed soil above the helix, as recommended in Mosquera *et al*. (Discussion of "Field investigation of the axial resistance of helical piles in dense sand", 2015).

6.2. Failure mechanisms

From the observations of the results of preliminary and subsequent simulations, the difficulties in modelling helical anchors are recognized mainly in the reproduction of the ground conditions at the vicinity of the helical anchor.

Two different movements occur during the anchor installation: i) displacement of the soil due to shaft advancement; ii) soil shearing and displacement due to the rotational and downward movements of the helix. The first action could resemble a jacked pile installation (cylindrical cavity expansion theory), leading the lateral earth pressure coefficient to increase at the vicinity of the shaft and densifying the surrounding sand; however, the helix movement during the anchor penetration would cause a decrease in soil shear strength and stiffness.

Few experimental data are available about the soil stress condition after the anchor installation. An example is the investigation with 1*g* model tests reported by Mitsch and Clemence (1985) in which they observed an increase in the lateral stresses during the helical anchor installation and during the anchor uplift loading. Nevertheless, the increase in the lateral stresses around the anchor would not be a trivial procedure for a numerical model with anchor as a wished-in-place element. Therefore, an alternative is to vary the parameters of stiffness and resistance of the soil around the anchor to try to reproduce the behaviour of the helical anchor.

Figure 102 compares the contours of vertical stress and vertical displacement of Tests 1 and 4 under a displacement of 0.1*D*. These contours highlight the differences in the failure mechanisms in models with different material stiffness. The simulation of Test 1 was performed with smaller values of Young modulus (Figures 102a and c) than of the Test 4 (Figures 102b and d). Thus, the vertical stresses in the Test 1 concentrated inside the cylinder of disturbed soil. In contrast, for the Test 4, higher levels of vertical stress can be visualized outside the cylinder. The same trend can be observed in the contours of displacement (Figures 102c and d). If no distinction of material would be made, the stresses and displacements outside the cylinder would be even larger.

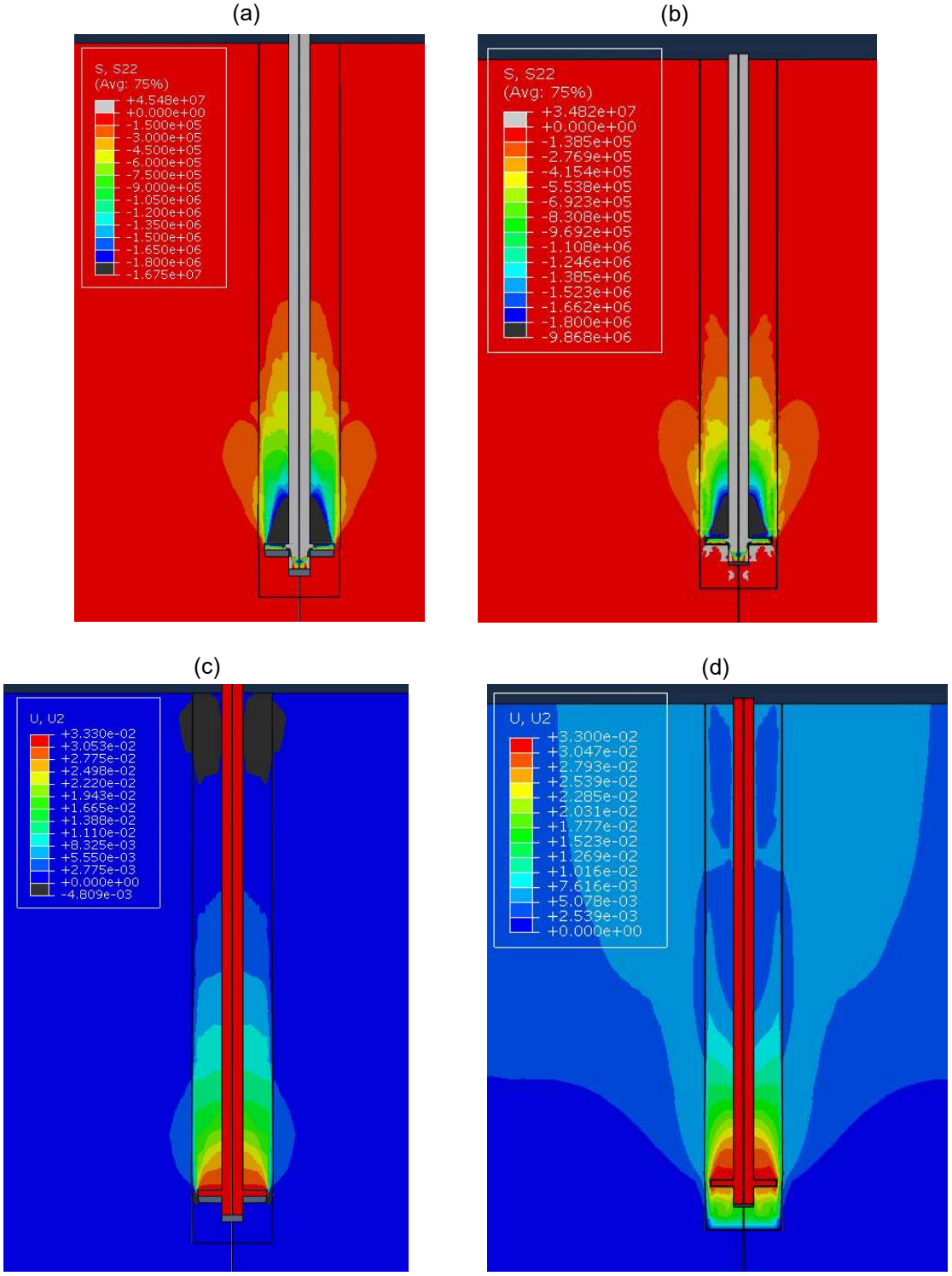

Figure 102. Contours of vertical normal stress (values in Pa) for (a) Test 1 and (b) Test 4, and contours of vertical displacement (values in metres) of (c) Test 1 and (d) Test 4 for a vertical displacement of 10%*D*.

Figure 103 shows the contours of plastic equivalent strain (PEEQ) for Test 1 and Test 4. Larger values of PEEQ are observed for the model with lower values of Young modulus (Test 1 - Figure 103a). Also, the plastic zone is larger for the Test 1 (Figure 103a). By using the

feature of dividing the soil mass into two zones (undisturbed and disturbed), the formation of the failure surface can be observed between undisturbed and disturbed soil. This failure mechanism is more realistic and agrees with the experimental results (see section 4.2.2).

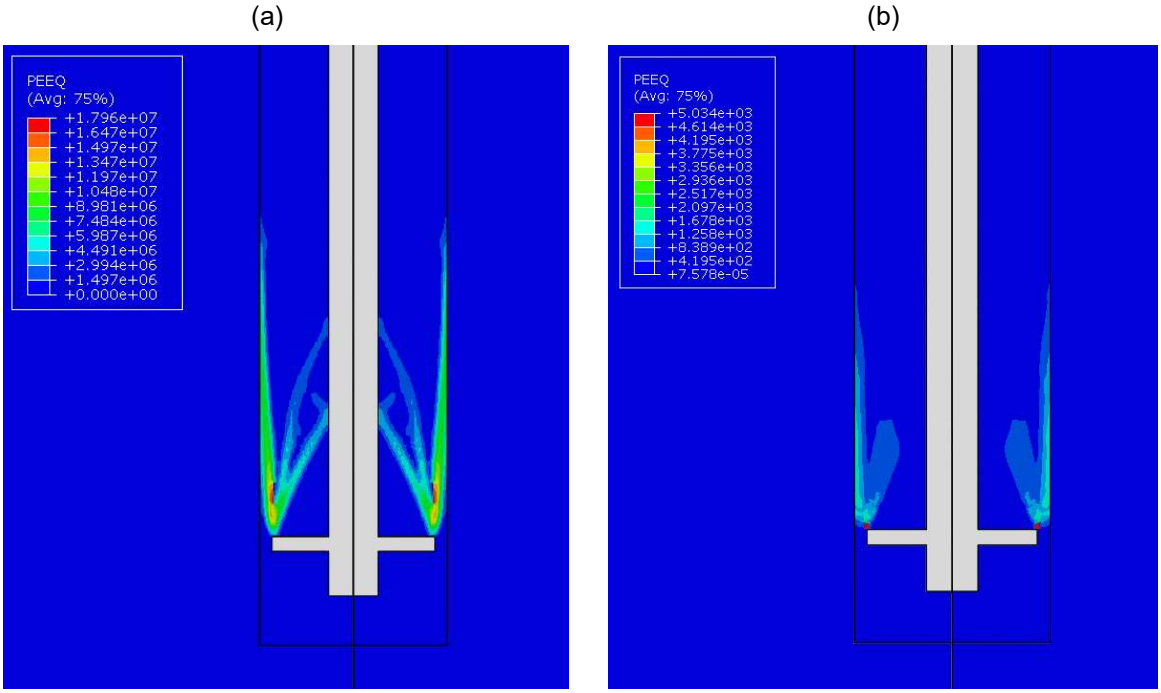

Figure 103. Contours of plastic equivalent strain for (a) Test 1 and (b) Test 4.

6.3. Overall post-cyclic monotonic response

The post-cyclic load-displacement response has been observed to exhibit a stiffness increase with a brittle behaviour (the anchor failure can be clearly identified with around 5 mm of anchor uplift displacement). Figure 104 presents two post-cyclic load-displacement responses that were typically observed in the centrifuge tests. Comparing the experimental results with the results of the numerical simulations, we observe that all numerical simulations provided a less stiff response. However, the ultimate uplift capacity was overpredicted by the numerical analyses, as occurred with the pre-cyclic response simulation. Figure 105 compares the helix bearing pressure obtained in the centrifuge tests and in the numerical analyses (the two numerical load-displacement responses that resulted closer to the experimental results).

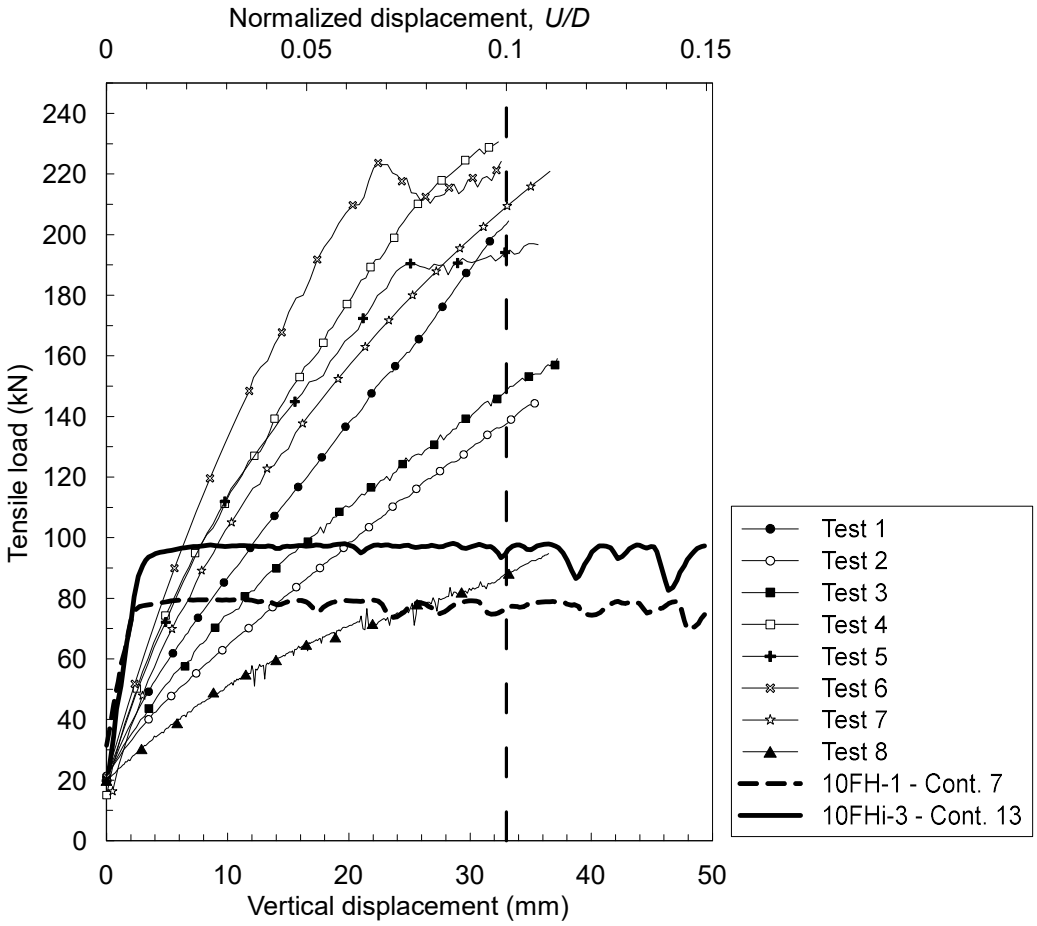

Figure 104. Comparison between numerical and experimental post-cyclic monotonic responses.

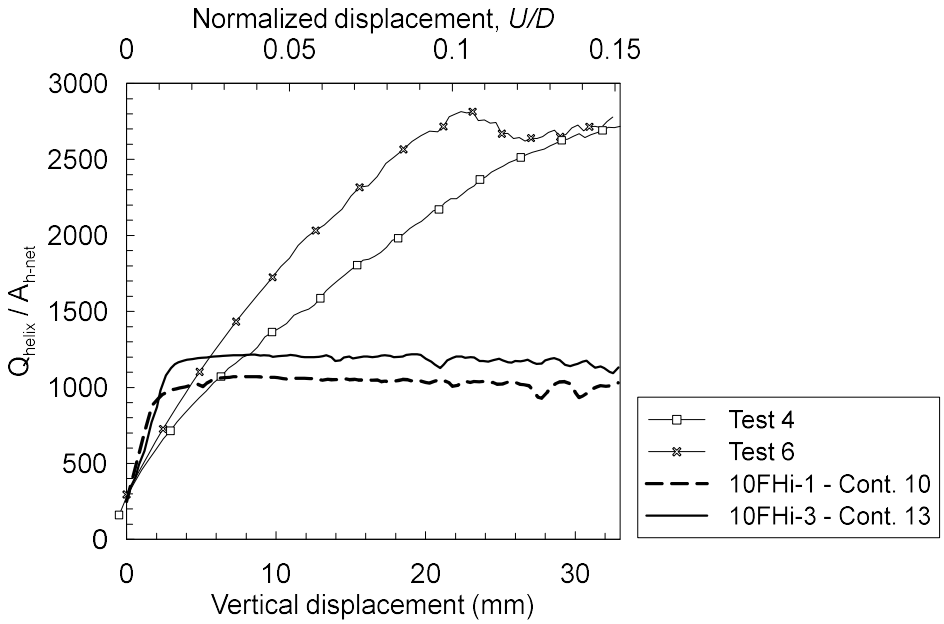

Figure 105. Helix bearing resistance mobilized during experimental and numerical post-cyclic uplift load tests.

7. PROPOSITIONS FOR THE DESIGN OF SINGLE-HELIX ANCHORS UNDER CYCLIC LOADING IN SAND

The results presented in the current study highlight the need to establish some guidelines for the design of helical anchors under cyclic loadings.

The observations from the cyclic tests reveal three topics of major significance:

- The effect of pre-failure and pre-loading on the anchor uplift behaviour: the reloading of a helical anchor that experienced failure during a previous loading test can cause excessive accumulated displacement and reduction of ultimate load of helical anchors in dense sand. However, for helical anchors with the helices installed in residual tropical soils of low to medium bearing capacity, the anchor response during reloading is improved compared to the first test, due to the compaction of the disturbed soil (destruction of soil structure of the residual soil during installation) above the helix.
- Displacement accumulation during cyclic loading: although the results of the present study have shown that no complete anchor pull-out occurs during the cyclic loading, the accumulated displacements generated during the cycles may reach the serviceability limit state.
- Increase or reduction of post-cyclic tensile capacity due to cyclic loadings: in addition to the analysis of displacement accumulation, the monotonic post-cyclic anchor performance should not be neglected, since degradation and consequent reduction of the post-cyclic anchor uplift capacity imply in reduction of the foundation safety factor.

For the first topic, concerning the effect of pre-failure and preloading on the helical anchor response, it is difficult to propose some design guideline, since this effect is dependent

on to soil type, and more tests are needed to confirm the trends observed in centrifuge and field tests. However, in some cases of helical anchors in tropical soils, conducting a pre-loading can improve the anchor response.

The other two topics have been rarely addressed and little information has been available to provide support for decisions in design of helical anchors.

Therefore, the following sections in this chapter offer some suggestions to guide the prediction of the cyclic loading response of single-helix anchors in sand. These recommendations are based on the results of the cyclic tests carried out on anchor models 10FH and 10FHi (in centrifuge) that represent a prototype of a single-helix anchor with $D = 330$ mm and $d = 100$ mm, and with helix embedment depth of $7.4D$ (at 2.44m depth). However, for cyclic conditions different of the conditions tested in this study, the applicability of such recommendations should be verified by further studies.

7.1. Estimation of the cyclic accumulated displacements

A proposition to describe the displacement accumulation of a single-helix anchor in dense sand during cyclic loading is presented in this chapter. Simple equations have been developed based on the results of cyclic tests on models 10FH and 10FHi. These proposed equations relate the accumulated displacement with number of cycles and cyclic amplitude.

According to Buhler and Cerato (Design of dynamically wind-loaded helical piers for small wind turbines, 2010), the cyclic amplitude (Q_{cyclic}) has greater influence on the anchor response than the maximum cyclic loading (Q_{max}). In the current study, the mean cyclic load (Q_{mean}) was found to have minor influence on the model anchor behaviour than the cyclic amplitude. Therefore, the proposed expression to estimate the accumulated displacement at a given cycle ($U_{acc\ (N)}$) includes only the cyclic amplitude (Q_{cyclic}).

As previously discussed in section 4.5, the displacements generated by the first load cycle differ significantly from the following ones. According to Wichtmann (Explicit accumulation model for non-cohesive soils under cyclic loading, 2005), the deformations in the first cycle can differ materially from those in the following cycles, and therefore the first cycle is not suitable for the determination of the total strain amplitude. By the observation of Figure 69, the greater the cyclic amplitude (Q_{cyclic}), the earlier is the transition point of displacement accumulation following the $(\log N)^2$ rule. For the first cycles (before the transition point) the accumulated displacements are not properly estimated by a function type $(\log N)^2$. Therefore, the procedure presented here proposes the use of two expressions to determinate the accumulated displacements. These two expressions were obtained by custom equation fitting, observing the correspondence between calculated and registered displacements in the test of mathematic functions and constants.

The application of one or other expression depends on the cycle number on which the accumulated displacement is required to be estimated. Figure 106 illustrates the situations in which both expressions are applied.

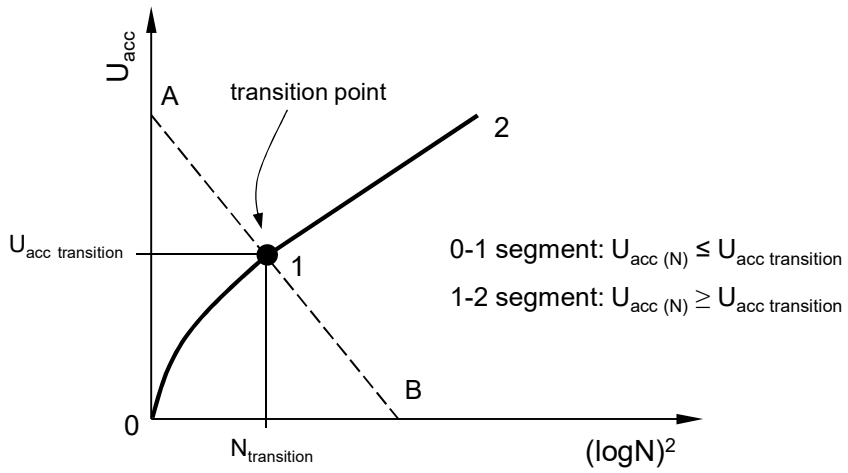

Figure 106. Two different trends in displacement accumulation.

At the initial cycles, when the number of cycles is less than the amount required to change the displacement accumulation trend, and is below and in the left side of the A-B line in Figure 106, Eq. 14 can be used to estimate the accumulated displacements. If the load cycle number N is greater, and is above and at the right side of the A-B line in Figure 106, Eq. 15 can be used. The load cycle number that corresponds to the transition point (Figure 106) between the two different displacement accumulation responses is called here $N_{transition}$.

$$U_{acc(N)} = \frac{10 \times \frac{Q_{cyclic}}{Q_T} \times (log\, N)^{2.5}}{2 + \frac{Q_{max}}{Q_T}} + U_{acc(N=1)} \quad \text{for } U_{acc\,(N)} \leq U_{acc\ transition} \qquad \text{Eq. 14}$$

$$U_{acc(N)} = \frac{20 \times \frac{Q_{cyclic}}{Q_T} \times [log(N - N_{transition})]^{1.5}}{2 - \frac{Q_{max}}{Q_T}} + U_{acc\ onset} \quad \text{for } U_{acc\,(N)} > U_{acc\ transition} \qquad \text{Eq. 15}$$

The calculation of the $N_{transition}$ value for a given cyclic loading is proposed to be done through the Eq. 16. This equation corresponds to the A-B line equation in Figure 106, and has been determined by multiple linear regression considering the accumulated displacement at the $N_{transition}$ cycle number ($U_{acc\ onset}$) as a function of number of cycles (N), cyclic amplitude (Q_{cyclic}) and mean cyclic load (Q_{mean}). Since both $U_{acc\ transition}$ and $N_{transition}$ are unknown, a system of equations with Eq. 14 and Eq. 16 should be solved considering $N = N_{transition}$ in Eq. 14 to determine the value of $N_{transition}$ and $U_{acc\ transition}$. Figure 107 illustrates the determination of both $U_{acc\ transition}$ and $N_{transition}$ for a cyclic loading with $Q_{cyclic} = 0.2Q_T$ and $Q_{mean} = 0.3Q_T$.

$$U_{acc\ transition} = \frac{1.29Q_{mean} - 3.67Q_{cyclic}}{Q_T} - 6.78(log\, N_{transition})^2 + 30.36 \qquad \text{Eq. 16}$$

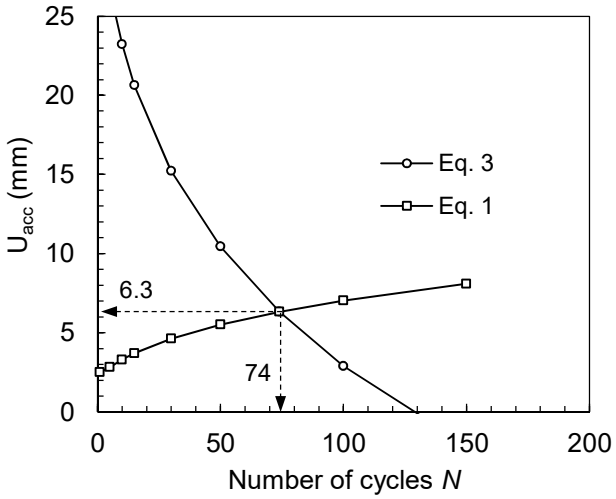

Figure 107. Resolution of the system of equations with Eq. 14 and Eq. 16 through iteration procedure for a cyclic loading with $Q_{cyclic} = 0.2Q_T$ and $Q_{mean} = 0.3Q_T$ (prototype values).

The agreement between experimental and calculated values of U_{acc} is illustrated in Figure 108. Although a dispersion of 50% around the experimental values is observed, the difference between experimental and calculated values tends to decrease for values of accumulated displacement greater than 20 mm (6%*D*) in prototype values. A comparison between calculated and experimental values is presented in the Appendix Q for 300, 500 and 1000 cycles.

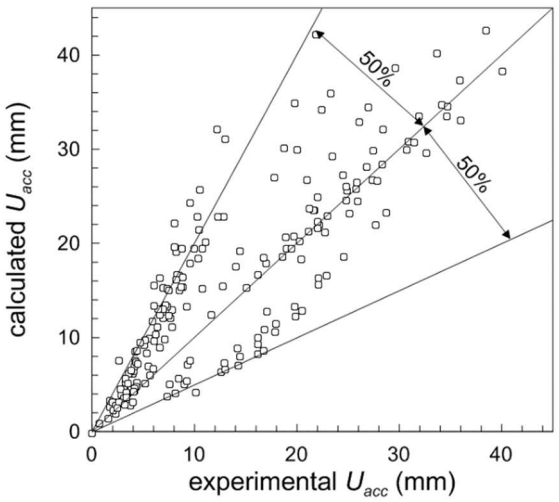

Figure 108. Comparison between calculated and experimental values of the cyclic accumulated displacements (in prototype values).

7.2. Evaluation of the cyclic stability using the Interaction Cyclic Diagram

Based on the equations proposed in the previous section 7.1, Interaction Diagrams were constructed to provide estimations of the anchor's cyclic behaviour in relation to the accumulated displacement regime.

Figure 109 permits to estimate the number of cycles (N_f) required to cause a limiting displacement of 10%D for a single-helix anchor in sand under cyclic loading characterized by Q_{mean} and Q_{cyclic} parameters. In this figure, the dashed lines indicate the values of a constant minimum load (Q_{pre}).

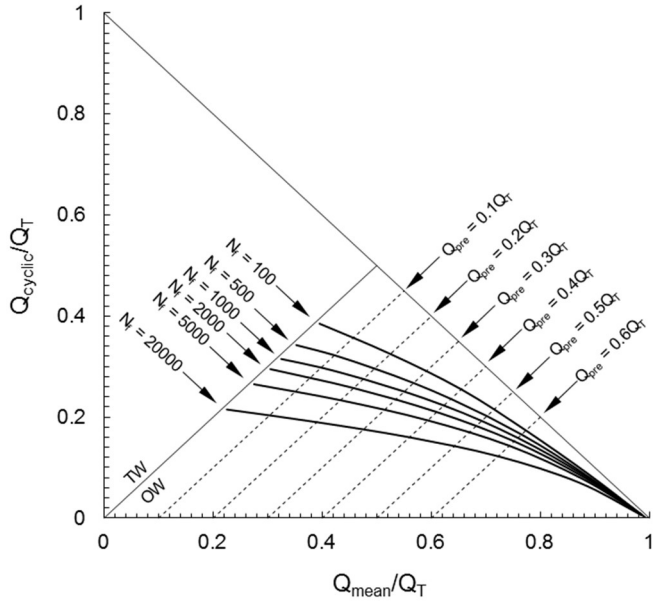

Figure 109. Isovalues lines of cycles to cause a limiting accumulated displacement of 10%D.

The accumulated displacements of 2.5%D, 5%D and 10%D, depending on the cyclic parameters Q_{cyclic} and Q_{mean}, can be estimated using Figures 110a and b, for 100 and 1000 cycles, respectively.

The estimation of the number of cycles required to cause a certain anchor accumulated displacement is important to establish a service life period after which an adjustment of the pre-stressing load in the guy cable is necessary. Therefore, Figure 110 presents iso-values

lines of accumulated displacements for 100, 500, 1000 and 2000 cycles that permits to estimate the number of cycles and consequently the service life duration in function of the cyclic parameters Q_{cyclic} and Q_{mean}.

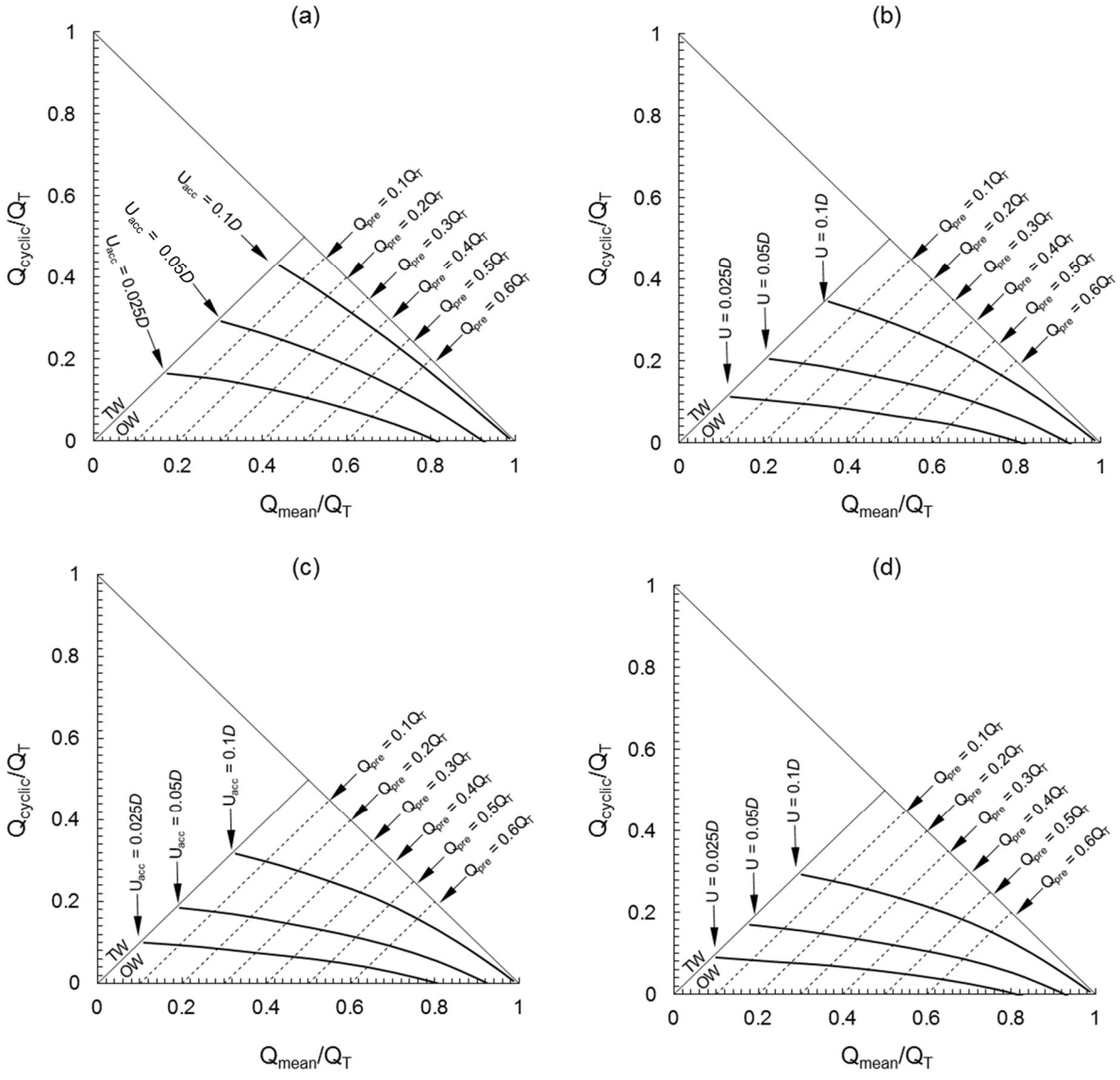

Figure 110. Isovalues lines of accumulated displacement (U_{acc}) after (a) 100 cycles, (b) 500 cycles, (c) 1000 cycles and (d) 2000 cycles.

7.3. Estimation of the post-cyclic capacity

The results of the cyclic load tests in centrifuge have shown that the post-cyclic tensile capacity was mainly affected by the mean cyclic load (Q_{mean}) and by the number of cycles (N). Generally, for higher values of Q_{mean} (50%Q_T or more), the cyclic loading caused a gain in post-cyclic uplift capacity. However, it is important to emphasize that the majority of the tests that exhibited gain in post-cyclic capacity was performed with less than 1000 cycles (the model anchor showed $U_{acc} \geq 10\%D$ before 1000 cycles). In cyclic tests with 1000 cycles or more, the post-cyclic capacity typically showed a reduction up to 15% of the pre-cyclic capacity.

The pre-cyclic monotonic loadings in centrifuge have shown that the shaft resistance of the helical anchors was around 18% of the applied load, under loadings up to 65% of the anchor tensile capacity. On the other hand, in post-cyclic monotonic tests, the shaft resistance was around 7% of the anchor tensile capacity (with a maximum of 16%). Therefore, the post-cyclic shaft resistance is suggested to be not considered for the prediction of the post-cyclic uplift capacity of helical anchors due to the small contribution to the post-cyclic capacity observed in the experiments.

A multiple regression was used to correlate the variation in the post-cyclic helix bearing capacity factor ($N_{q\text{-}pc}$) with N (number of cycles), Q_{mean} and Q_{cyclic}, resulting in the Eq. 17. For this regression, only the measured results of $N_{q\text{-}pc}$ obtained from the tests on the instrumented pile were used, because in this case it was possible to separate the shaft resistance from the helix bearing resistance.

A comparison between the measured and calculated values of post-cyclic uplift capacity using Eq.4 is presented in Figure 111. For the calculated value of uplift capacity, the shaft friction resistance is not considered, in this post-cyclic helix bearing.

$$N_{q-pc}/N_q = -0.433\left(\frac{N}{100}\right) - 0.236\left(\frac{1}{Q_{mean}}\right)^2 + 0.285\left(\frac{1}{Q_{cyclic}}\right)^2 + 98 \qquad \text{Eq. 17}$$

(valid for the tested interval of $0.4 < Q_{mean}/Q_T < 0.7$)

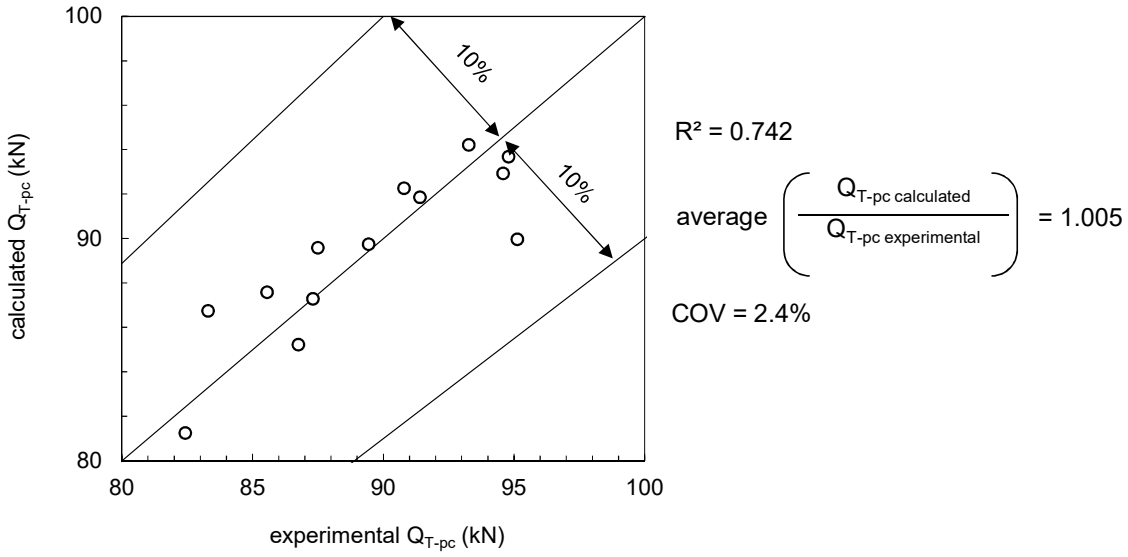

Figure 111. Comparison between measured and calculated results of post-cyclic helix bearing capacity.

The post-cyclic capacity ($Q_{T\text{-}pc}$) was found to be more dependent of N and Q_{mean}, and less dependent on Q_{cyclic}. Figure 112 illustrates the variation of the post-cyclic uplift capacity calculated using the Eq. 17. The reduction of the post-cyclic capacity seems to be more important when the helical anchors are subjected to a greater number of cycles, as shown in the comparison between Figure 112a and b.

Figure 112b illustrates that after 2000 cycles almost all of the tests showed uplift capacity decrease.

After 1000 cycles no capacity decrease was observed for Q_{mean}/Q_T greater than around 0.40 in the centrifuge tests. This feature could be reproduced using Eq. 17 (Figures 112a and b). Although the cyclic tests with 1000 cycles and larger amplitudes have caused no reduction

in post-cyclic uplift capacity, cyclic loadings with larger Q_{max} would reach first the limiting condition in terms of displacement, unlike the case of small amplitude cyclic loadings.

The post-cyclic response after cyclic loadings with Q_{mean} /Q_T lower than 0.40 varies widely, and the variability is greater for smaller values of Q_{mean} /Q_T. This observation indicates a more uniform post-cyclic response is expected for cyclic loadings with higher Q_{mean}, and the level of capacity reduction should vary only with the number of cycles.

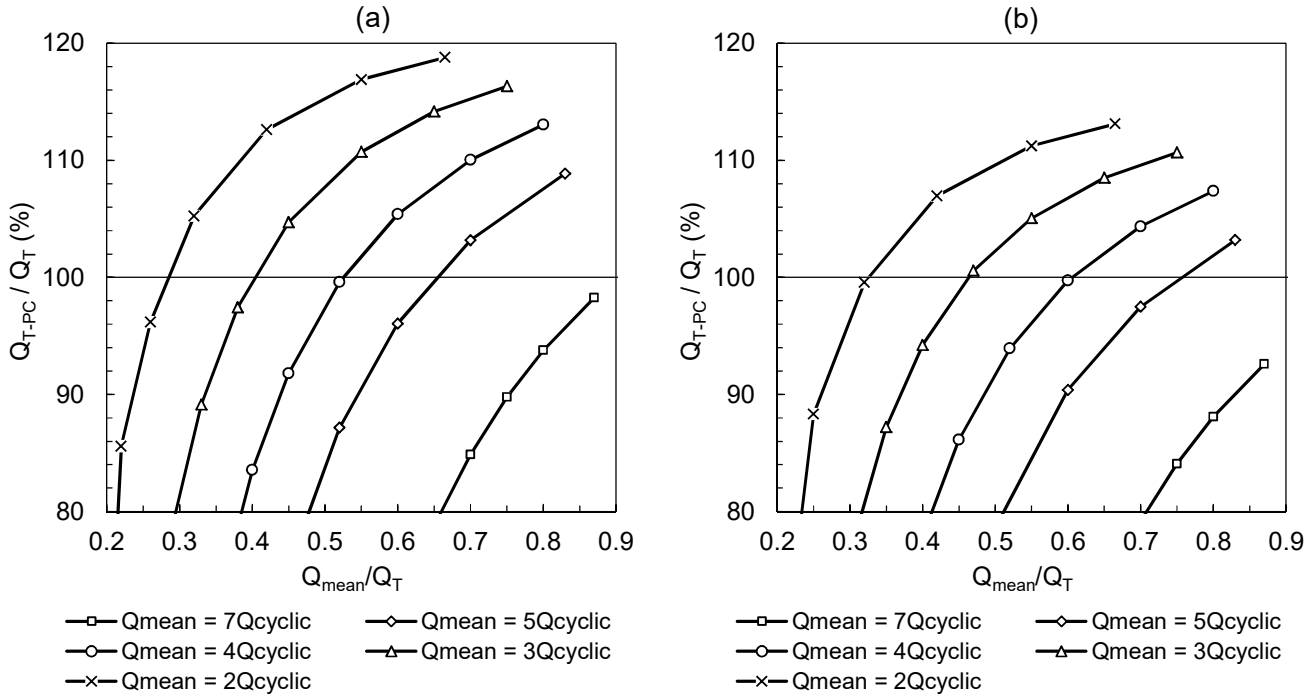

Figure 112. Variation of the post-cyclic capacity ($Q_{T\text{-}pc}$) for (a) N = 1000 cycles and (b) N = 2000 cycles.

8. CONCLUSIONS

The current thesis evaluated the behaviour of helical anchors subjected to tensile cyclic loadings in very dense sand, through centrifuge model tests and full-scale field tests in a tropical residual soil site. Therefore, the conclusions are divided into main two parts: centrifuge modelling and field tests.

PART 1 – Centrifuge modelling

a) Scale effects

The use of a geotechnical centrifuge to investigate helical anchor behaviour has shown to be advantageous because field tests are time consuming, expensive, and difficult to be repeated or compared due to the natural soil variability. However, scaling issues in modelling helical anchors have not been investigated previously. To address this problem, in the current study, pull-out tests on different reduced models of helical anchor in sand were performed in centrifuge previously to help the decision about the most suitable anchor model to be used for the cyclic tests.

The finding concerning scale effects presented here is valid for helical anchor models with D/d (helix/shaft diameters) ratios similar or greater than the one tested in this study. The performance of helical anchor models with different D/d ratios may be affected by scaling effect in a different manner due to the increase of the shaft resistance contribution to the total capacity. The main conclusion of the verification of scale effects is that prototype results of uplift capacity are comparable when anchor models with the ratio w/d_{50} (ratio of the effective helical radius to the average grain size) greater than 58.

b) Anchor installation effects in dry sand

The installation effect on the soil traversed by the helices influences directly the uplift behaviour of helical anchors. Therefore, for a better understanding of the cyclic response of helical anchors in this investigation, different techniques were used to verify the effect of the anchor installation on the sand penetrated, and to visualise the failure mechanism.

The main conclusions of this investigation are: (i) the anchor load-displacement response and failure mechanism are controlled by the disturbed soil within the cylindrical installation zone; and (ii) the sand disturbance is not uniform along the cylindrical zone above the helix.

c) Monotonic response of a single helix-anchor in very dense dry sand

The main observations about the monotonic response of helical anchors tested in centrifuge are: (i) a comparison between the load-displacement curves obtained in uplift tests on helical anchors in centrifuge is comparable to results found in field tests under similar conditions of soil; (ii) the helix bearing resistance correspond to a mean value of 82% of the total applied load during a pre-loading performed before cyclic tests; and (iii) a pre-failed anchor, that experienced large vertical displacement, presents a reduction in ultimate load compared to the first loading.

d) Cyclic and post cyclic behaviour of single-helix anchors in very dense dry sand

The physical modelling in centrifuge was carried out on helical anchor models installed in dry sand to evaluate the influence of the combination of cyclic amplitude and mean load, the number of cycles, and the sequence of different cyclic loadings.

The results of this investigation showed that the helical anchor behaviour was governed by helix bearing, with no loss of helix bearing capacity during the cyclic loadings. In contrast, the shaft resistance degradation was noticed mainly during the first 100 cycles, when the

accumulation of permanent displacements was more significant. A cyclic stability classification according to the interaction diagram has shown not suitable because:

i) Despite the helical anchor exhibited vertical displacements larger than 10% of the helix diameter (*D*) after 1000 cycles (failure criteria), the post-cyclic uplift capacity did not show degradation (the post-cyclic capacity even increased in some tests). However, after 2000 cycles, almost all of the cyclically tested anchors presented reduction on the post-cyclic uplift capacity compared to the pre-cyclic capacity.

ii) In some cases with low mean load, the accumulated displacements did not reach 10%*D* after 1000 cycles; however, the post-cyclic uplift capacity presented some degree of degradation.

Therefore, this thesis proposed the use of an Interaction Diagram to evaluate the cyclic performance of helical anchors based only on the accumulated displacement response. Simple expressions have been presented to aid the preliminary evaluation of the cyclic behaviour of helical anchors in dense sand with helix embedment depth of around 7*D*. For different embedment depths, the application of these expressions should be verified. Based on these expressions, Interaction Diagrams have been drawn to assist the evaluation of the cyclic stability.

The study on the post-cyclic behaviour of helical anchors also provided insights and allowed the construction of a curve fitting to estimate the variation of post-cyclic uplift capacity due to the cyclic loadings.

The cyclic response of the single-helix anchor after a sequence of two different cyclic loadings was also evaluated in this research. In general, when cycles of intermediate amplitude are performed first, a reduction in the vertical displacements of the following cyclic loading is observed. On the other hand, when a sequence of cyclic loadings with intermediate and high amplitudes is carried out, the magnitude of the accumulated displacement is weakly

dependent on the loading order. Different stability criteria were proposed in this thesis from experimental data. The results and analyses presented here complement the database for the study of helical anchors under cyclic loadings and also provide guidelines for the design.

PART 2 – Field tests

The number of field cyclic tests on helical anchors is reduced compared to the number of cyclic tests performed in centrifuge for this investigation. As mentioned before in this text, cyclic loading tests on piles (or anchors) are much less time consuming and expensive using centrifuge compared to field tests. For this reason, the most part of this thesis is dedicated to centrifuge model tests.

For the field experiments cyclic tensile loading tests were performed on an instrumented single-helix anchor (instrumentation to distinguish shaft and helix bearing responses). This anchor was installed in a site of residual tropical soil (sandstone) at São Carlos, in Brazil.

Four series of cyclic loading tests were performed on this anchor, intercalated with monotonic tensile loading tests (after and before every cyclic test). The results of post-cyclic monotonic tensile load tests on this anchor were compared with the results of monotonic tensile load tests on an identical reference anchor which did not experienced cyclic loadings.

The main findings from these tests are: (i) occurrence of negative skin friction and consequent residual loads after anchor installation and uplift tests; however, for the anchor that experienced cyclic loadings, the negative friction decreased at the end of the unloading stage compared to the anchor that did not experience cyclic loadings; (ii) the effect of negative skin friction influences the cyclic response of the helical anchor; (iii) anchor response improvement was observed after every monotonic test on both anchors; this improvement was caused by soil compaction above the helices (the monotonic tests improved this disturbed soil which has low bearing capacity); (iv) the anchor's cyclic performance was

influenced by the preceding monotonic test; (v) cyclic load tests performed in this field investigation did not affect the monotonic behaviour of the helical anchor; (vi) both helix bearing and shaft resistances increased after the monotonic tests; however, a greater increase of shaft resistance was observed for the cyclically tested anchor. On the other hand, a slightly greater increase of helix bearing resistance was observed for the anchor that did not experienced cyclic loadings.

8.1. Recommendations for future work

- Future numerical studies to simulate the behaviour of helical anchors under monotonic and cyclic loading should consider constitutive models that can reproduce hardening and cyclic degradation of soils. For modelling with wished-in-place element, the initial condition of the soil should be improved in order to better reproduce the lateral stresses around the anchor, and then, investigate the influence of the variation of lateral stresses on the anchor behaviour;
- Physical modelling of helical anchors in calibration chamber to better investigate the modifications on the soil lateral stresses around the anchor after anchor installation.
- Centrifuge model tests to investigate the behaviour of single-helix anchors under two-way cyclic loadings.
- Centrifuge investigations on the effect of the number of helix on the cyclic response of helical anchors.
- Centrifuge model tests to investigate the cyclic behaviour of helical anchors in loose sand and in cohesive soils.
- Centrifuge model tests to investigate the behaviour of helical anchors under cyclic horizontal loadings.

REFERENCES

AB Chance Co. (2013). *Dial torque indicator.* Acesso em 29 de april de 2014, disponível em http://www.abchance.com/products/tools/digital-torque-indicator

Abaqus. (2005). *Lecture 6 - Adaptive meshing and distortion.* Acesso em 14th de July de 2016, disponível em Dassault systèmes.

Abaqus. (2014). *User Manual: Abaqus Theory Guide* (Version 6.14 ed.). USA: Dassault Systèmes Simulia Corp.

ABNT. (1995). *Rocks and soils - Terminology.* Rio de Janeiro: Brazilian Technical Standards Association (ABNT).

ABNT. (2006). *ABNT NBR-12131: Piles - static load test - test method.* Rio de Janeiro: Brazilian Technical Standards Association (ABNT).

Adams, J. I., & Klym, T. W. (1972). A study of anchorages for transmission tower foundations. *Canadian Geotechnical Journal, 9*(1), pp. 89-104.

AFNOR. (1991). *NF P94-054 Détermination de la masse volumique de particules solides des sols.* Technical standard, French national organization for standardization, France.

AFNOR. (1996). *Sols: reconnaissances et essais, Analyse granulométrique, méthode de tamisage à sec après lavage.* Technical standard, French national organization for standardization, France.

Airey, D., Poulos, H., & Al-Douri, R. (1992). Estimation of pile friction degradation from shearbox tests. *Geotechnical Testing Journal, 15*(4), pp. 388-392.

Al-Dhouri, R., & Poulos, H. (1995). Predicted and observed cyclic performance of piles in calcareous sand. *Journal of geotechnical engineering, 121*(1), pp. 1-16.

Andreadis, A., & Harvey, R. (1981). A design procedure for embedded anchors. *Applied Ocean Research, 3*(4), pp. 177-182.

Andreadis, A., Harvey, R., & Burley, E. (1981). Embedded anchor response to uplift loading. *Journal of the geotechnical engineering division, 107*(1), pp. 59-78.

Ansell, P., & Brown, S. (1978). A Cyclic Simple Shear Apparatus for Dry Granular Materials. *Geotechnical Testing Journal, 1*(2), pp. 82-92.

ASTM. (2014). *ASTM D4253 - Standard Test Methods for Maximum Index Density and Unit Weight of Soils Using a Vibratory Table.* Technical standard, ASTM, West Conshohocken.

ASTM. (2014). *ASTM D4254 - Standard Test Methods for Minimum Index Density and Unit Weight of Soils and Calculation of Relative Density.* Technical standard, ASTM, West Conshohocken.

Balachowski, L. (2006). Scale effect in shaft friction from the direct shear interface tests. *Archives of civil and mechanical engineering, 6*(3).

Beard, R. (1980). *Holding capacity of plate anchors.* Technical repport Civil Engineering Laboratory, Naval Facilities Engineering Command, Port Hueneme.

Benzaria, O. (2013). *Contribution à l'étude du comportement des pieux isolés sous chargements cycliques axiaux.* University Paris-Est. Paris: Champs-sur-Marne.

Benzaria, O., Puech, A., & Le Kouby, A. (2013). Cyclic axial load tests on bored piles in dense sands. *Proceedings of the 18th International Conference on Soil Mechanics and Geotechnical Engineering*, (pp. 2323-2326). Paris.

Bian, Y., Hutchinson, T., Wilson, D., Laefer, D., & Brandenberg, S. (2008). Experimental investigation of grouted helical piers for use in foundation rehabilitation. *Journal of Geotechnical and Geoenvironmental Engineering, 134*(9), pp. 1280-1289.

Blanc, M., & Thorel, L. (2016). Effects of cyclic axial loading sequences on piles in sand. *Géotechnique Letters, 6*(2), pp. 163-167.

Boulon, M. (1998). Numerical and physical behaviour under monotonous and cyclic loading. Em K. e. (ed), *Modelling Soil-Water-Structure Interactions* (pp. 285-293). Rotterdam: Balkema.

Boulon, M., & Foray, P. (1986). Physical and numerical simulation of lateral shaft friction along offshore piles in sand. *Third International Conference on Numerical Methods in Offshore Piling*, (pp. 127-147). Nantes.

Bowman, E., & Soga, K. (2005). Mechanisms of set-up of displcaement piles in sand: laboratory creep tests. *Canadian Geotechnical Journal, 42*(5), pp. 1391-1407.

Buhler, R., & Cerato, A. (2010). Design of dynamically wind-loaded helical piers for small wind turbines. *Journal of Performance of Constructed Facilities, 24*(4), pp. 417-426.

CAE ANALYSIS. (2011). *CAE analysis - just another Finite Element Analysis blog*. Acesso em 13th de July de 2016, disponível em https://caeanalysis.wordpress.com/2011/04/03/implicit-explicit-finite-element-analysis/

Cepeagri. (2016). *Climate of São Paulo state Municipalities*. Acesso em 12th de July de 2016, disponível em http://www.cpa.unicamp.br/outras-informacoes/clima_muni_549.html

Cerato, A., & Victor, R. (2009). Effects of long-term dynamic loading and fluctuating water table on helical anchor performance for small wind tower foundations. *Journal of performance of constructed facilities*, pp. 251-261.

Chan, S., & Hanna, T. (1980). Repeated loading on single piles in sand. *Journal of the geotechnical engineering division, 102*(2), pp. 171-180.

Chow, S., O'Loughlin, C., Corti, R., Gaudin, C., & Diambra, A. (2015). Drained cyclic capacity of plate anchors in dense sand: experimental and theoretical observations. *Géotechnique Letters, 5*(2), pp. 80-85.

Clemence, S., & Pepe, F. (1984). Measurement of lateral stress around multihelix anchors in sand. *Geotechnical Testing Journal, 7*(3), pp. 145-152.

Clemence, S., & Smithling, A. (1984). Dynamic Uplift Capacity of Helical Anchors in Sand. *4th Australia-New Zealand Conference on Geomechanics*, (pp. 88-93). Perth.

Clemence, S., Crouch, L., & Stephenson, R. (1994). Prediction of uplift capacity for helical anchors in sand. *Proceedings of the 2nd Geotechnical Engineering Conference.* Cairo, Egypt.

Corté, J. (1989). L'essor de la modélisation en centrifugeuse en géotechnique. *Revue Française de Géotechnique, 48*, pp. 7-13.

Cremer, C., Pecker, A., & Davenne, L. (2001). Cyclic macro-element for soil-structure interaction: material and geometrical non-linearities. *International Journal for Numerical and Analytical Methods in Geomechanics, 25*(13), pp. 1257-1284.

D'Aguiar, S., Lopez-Caballero, F., Modaressi-Farahmand-Razavi, A., & Santos, J. (2009). Piles under cyclic loading: study of the friction fatigue and its importance in piles behaviour. *Proceedings of the 17th International Conference on Soil Mechanics and Geotechnical Engineering*, (pp. 1313-1316). Alexandria.

D'Aguiar, S., Modaressi, A., Santos, J., & Lopez-Caballero, F. (2011). Piles under cyclic axial loading: study of the friction fatigue and its importance in pile behavior. *Canadian Geotechnical Journal, 48*(10), pp. 1537-1550.

Das, B. (1990). *Earth anchors* (1st ed. ed.). Amsterdam: Elsevier Science.

de Abreu, R. (2006). *Map of São Paulo state*. Acesso em 12th de July de 2016, disponível em Wikipedia: https://commons.wikimedia.org/wiki/File:SaoPaulo_MesoMicroMunicip.svg

DeJong, J., Randolph, M., & White, D. (2003). Interface load transfer degradation during cyclic loading: a microscale investigation. *Soils and Foundations, 43*(4), pp. 81-93.

Desrues, J. (1991). An introduction to strain localisation in granular media. *Physics of Granular Media, Proceedings of Winter School les Houches* (pp. 127-142). Nova Sciences Publications.

Dickin, E., & Leung, C. (1983). Centrifugal model tests on vertical anchor plates. *Journal of Geotechnical Engineering*, pp. 1503-1525.

Doherty, P., Kirwan, L., Gavin, K., Igoe, D., Tyrrell, S., Ward, D., & O'Kelly, B. (2012). Soil properties at the UCD geotechnical research site at Blessington. Em C. C. O'Connor (Ed.), *National Bridge and Concrete Research in Ireland Conference* (pp. 499-504). Dublin, Ireland: Bridge and Concrete Research in Ireland (BCRI).

El Sharnouby, M., & El Naggar, M. (2011). Monotonic and cyclic axial full-scale testing of reinforced helical pulldown micropiles. *Proceedings of the 14th Pan-American Conference on Soil Mechanics and Geotechnical Engineering*, (p. 6). Toronto.

Fioravante, V. (2002). On the shaft friction modelling of non-displacement piles in sand. *Soils and Foundations, 42*(2), pp. 23-33.

Flavigny, E., Desrues, J., & Palayer, B. (1990). Le sable d'Hostun RF. *Revue française de géotechnique, 53*(67-70 (in French)).

Foray, P. (1991). Scale and boundary effects on calibration chamber pile tests. *First International Symposium on Calibration Chamber Testing/ISOCCTl* (pp. 147-160). Potsdam: New York.

Foray, P., Balachowski, L., & Rault, G. (1998). Scale effect in shaft friction due to the localisation of deformations. *International Conference Centrifuge 98*, (pp. 211-216). Tokyo.

Fuglsang, L., & Ovesen, N. (1988). The application of the theory of modelling to centrifuge studies. Em W. J. Craig, *Centrifuges in Soil Mechanics* (1 ed.). Rotterdam: A. A. Balkema.

Garnier, J. (2001). Physical modelling in geotechnics: state of the art and recent advantages. 1st Coulomb Lecture. *Caquot Conference*, (pp. 405-414).

Garnier, J., & König, D. (1998). Scale effects in piles and nails loading tests in sand. *International Conference Centrifuge 98* (pp. 205-210). Tokyo: A.A. Balkema.

Gavin, K., & Lehane, B. (2007). Base load - displacement response of piles in sand. *Canadian Geotechnical Journal, 44*(9), pp. 1053-1063.

Gavin, K., & O'Kelly, B. (2007). Effect of friction fatigue on pile capacity in dense sand. *Journal of Geotechnical and Geoenvironmental Engineering, 133*(1), pp. 63-71.

Gavin, K., Doherty, P., & Tolooiyan, A. (2014). Field investigation of the axial resistance of helical piles in dense sand. *Canadian Geotechnical Journal, 51*(11), 1343-1354.

Ghaly, A. M., Hanna, A. M., & Hanna, M. S. (1991). Uplift behavior of screw anchors in sand - Part I: dry sand. *Journal of Geotechnical Engineering, 117*(5).

Ghaly, A., & Clemence, S. (1998). Pullout performance of inclined helical screw anchors in sand. *Journal of Geotechnical and Geoenvironmental Engineering, 124*(7), pp. 617-627.

Ghaly, A., & Hanna, A. (1991). Experimental and theoretical studies on installation torque of screw anchors. *Canadian Geotechnical Journal, 28*(3), pp. 353-364.

Giachetti, H., Peixoto, A., & Mondelli, G. (2004). Comparison between mechanical and electrical cone penetration testing results in tropical soils. *Solos e Rochas, 27*(2), pp. 191-200.

Gudehus, G., & Hettler, A. (1981). Cyclic and monotonous model tests in sand. *Proceedings of the 10th International Conference on Soil Mechanics and Foundation Engineering*, *2*, pp. 211-214. Stockholm.

Hanna, A., Ayadat, T., & Sabry, M. (2007). Pullout resistance of single vertical shallow helical and plate anchors in sand. *Geotechnical and geological engineering, 25*(5), pp. 559-573.

Hanna, T., & Al-Mosawe, M. (1981). Performance of prestressed anchors under slow repeated loadings. *Proceedings of the 10th International Conference on Soil Mechanics and Foundation Engineering*, *2*, pp. 127-133. Stockholm.

Hanna, T., Sivapalan, E., & Senturk, A. (1978). Behaviour of dead anchors subjected to repeated and alternating loads. *Ground Engineering, 11*(3), pp. 28-34, 40.

Healy, K. (1971). Pullout resistance of anchors buried in sand. *Journal of the soil mechanics and foundations division, 97*(11), pp. 1615-1622.

Heerema, E. (1978). Predicting pile drivability: heather as an illustration of the "friction fatigue" theory. *Proceedings of the European Offshore and Petroleum Conference and Exhibition* (pp. 413-423). London: Society of Petroleum Engineers.

Helwany, S. (2007). *Applied soil mechanics with ABAQUS applications.* Hoboken: John Wiley & Sons Inc.

Hettler, A. (2010). Possibilities and limitations of 1-g model techniques. Em L. Seward (Ed.), *Physical Modelling in Geotechnics. 1*, pp. 135-140. Zurich: CRC Press.

Houlsby, G. (1991). How the dilatancy of soils affects their behaviour. *Proceedings of the 10th European Conference on Soil Mechanics and Foundation Engineering* (pp. 1189-1202). London: Taylor & Francis.

Hoyt, R., & Clemence, S. (1989). Uplift capacity of helical anchors in soil. Em P. C. ICSMFE (Ed.), *Proceedings of the 12th International Conference on Soil Mechanics and Foundation Engineering* (pp. 13-18). Rio de Janeiro: CRC Press .

Igoe, D., Doherty, P., & Gavin, K. (2010). The development and testing of an instrumented open-ended model pile. *Geotechnical Testing Journal, 33*(1), pp. 1-12.

Ishihara, K., Tatsuoka, F., & Yasua, S. (1975). Undrained deformation and liquefaction of sand under cyclic stresses. *Soils and Foundations, 15*(1), pp. 29-44.

Jamiolkowski, M., Lo Presti, D., & Manassero, M. (2003). Evaluation of relative density and shear strength of sands from CPT and DMT. *Soil behavior and soft ground construction, 7*(119), 201-238.

Jardine, R. (1992). Some observations on the kinematic nature of soil stiffness. *Soils and Foundations, 32*(2), pp. 111-124.

Jardine, R., & Standing, J. (2012). Field axial cyclic loading experiments on piles driven in sand. *soils and foundations, 52*(4), pp. 723-736.

Jardine, R., & Standing, R. (2000). *Pile load testing performed for HSE cyclic loading study at Dunkirk, France. Two Volumes.* Offshore Technology Report, Health and Safety Executive, London.

Kanai, S. (2007). A seismic retrofitting application by means of multihelix micropiles. *23th U.S.–Japan Bridge Engineering Workshop.* Tsukuba.

Karlsrud, K., Nadim, F., & Haugen, T. (1986). Piles in clay under cyclic axial loading: field tests and computational modeling. Em I. F. Chaissées (Ed.), *Proceedings of the 3rd International Conference of Numerical Methods in Offshore Piling* (pp. 165-190). Nantes: Technip.

Kim, N., & Kim, D. (2011). The role of the physical modeling in the design of geotechnical systems. Em M. K. Thompson (Ed.), *Proceedings of the 1st International Workshop on Design in Civil and Environmental Engineering*, (pp. 11-18). Daejeon.

Klinkvort, R., Hededal, O., & Springman , S. (2013). Scaling issues in centrifuge modelling of monopiles. *International Journal of Physical Modelling in Geotechnics, 13*(2), pp. 38-49.

Komatsu, A. (2007). Development on battered pile with screw pile method (NS-ECO pile). *International Workshop on Recent Advances of Deep Foundations* (pp. 253-257). Yokosuka: Taylor & Francis.

Kulhawi, F. (1985). Uplift behavior of shallow soil anchors – an overview: uplift behavior of anchor foundations in soil. *Session sponsored by the Geotechnical Engineering Division of the American Society of Civil Engineers in conjunction with the ASCE Convention* (pp. 1-25). Detroit: ASCE.

Küs, B. (1992). *Pluviation des sables, DEA report.* Université de Nantes, Nantes.

Lau, C. (1988). *Scale effects in tests on footings.* PhD Thesis, University of Cambridge, Cambridge.

Le Kouby, A., Canou, J., & Dupla, J. (2004). Behaviour of model piles subjected to cyclic axial loading. Em T. Triantafyllidis (Ed.), *Proceedings of the International Conference on Cyclic Behaviour of Soils and Liquefaction Phenomena* (pp. 159-166). Bochum: A.A. Balkema.

Lehane, B., Gaudin, C., & Schneider, J. (2005). Scale effects on tension capacity for rough piles buried in dense sand. *Géotechnique, 55*(10), pp. 709-719.

Lehane, B., Jardine, R., Bond, A., & Frank, R. (1993). Mechanism of shaft friction in sand from instrumented pile test. *Journal of Geotechnical Engineering, 119*(1), pp. 19-35.

Levesque, C. (2002). *Centrifuge modelling of helical anchors in sand.* MSc thesis, University of New Brunswick, Fredericton.

Li, Z., Bolton, M., & Haigh, S. (2012). Cyclic axial behaviour of piles and pile groups in sand. *Canadian Geotechnical Journal, 49*(9), pp. 1074-1087.

Machado, S. (1998). *Application of elastoplasticity concepts to non-saturated soils.* DSc thesis, University of São Paulo, São Carlos.

Menétrey, P., & Willam, K. (1995). Triaxial failure criterion for concrete and its generalization. *ACI structural Journal, 92*(3), pp. 311-318.

Merifield, R. (2011). Ultimate uplift capacity of multiplate helical type anchors in clay. *Journal of geotechnical and geoenvironmental engineering, 137*(7), pp. 704-716.

Mitsch, M. P., & Clemence, S. P. (1985). The uplift capacity of helical anchors in sand. *Uplift behavior of anchor foundations in soil* (pp. 26-47). Michigan: ASCE.

Miura, S., & Toki, S. (1982). A sample preparation method and its effect on static and cyclic deformation-strength properties of sand. *Soils and Foundations, 22*(1), pp. 61-77.

Mortara, G., Mangiola, A., & Ghionna, V. (2007). Cyclic shear stress degradation and post-cyclic behaviour from sand-steel interface direct shear tests. *Canadian Geotechnical Journal, 44*(7), pp. 739-752.

Mosquera, Z., Tsuha, C., Schiavon, J., & Thorel, L. (2015). Discussion of "Field investigation of the axial resistance of helical piles in dense sand". *Canadian Geotechnical Journal, 52*(8), pp. 1190-1194.

Narasimha Rao, S., Prassad, M., Shetty, M., & Joshi, V. (1989). Uplift capacity of screw pile anchor. *Geotechnical Engineering, 20*(2), pp. 35-50.

Ovesen, N. (1979). The scaling law relationship. Panel discussion. *7th European Conference on Soil Mechanics and Foundaton Engineering*, *4*, pp. 319-323. Brighton.

Ovesen, N. (1981). Centrifuge tests of the uplift capacity of anchors. *10th International Conference on Soil Mechanics and Foundation Engineering*, (pp. 717-722). Stockholm.

Perko, H. (2000). Energy method for predicting the installation torque of helical foundations and anchors. *ASCE Geotechnical Special Publication*(100).

Perko, H. (2009). *Helical piles: a practical guide to design and installation.* (J. W. Sons, Ed.)

Perko, H., Stan, J., & Rupiper, P. (2000). *Helix pier engineering handbook 2000.* INC. Worldwide Helix Pier Distributors.

Petereit, R. (1987). *The static and cyclic pullout behavior of plate anchors in fine saturated sand.* MSC thesis, Oregon State University, Corvallis.

Poulos, H. (1982). Influence of cyclic loading on axial pile response. *Proceedings of the 2nd International Conference on Numerical Methods in Offshore Piling*, *1*, pp. 419-440. Austin.

Poulos, H. (1988). Cyclic stability diagram for axially loaded piles. *Journal of Geotechnical Engineering, 114*(8), pp. 877-895.

Poulos, H. (1989). Cyclic axial loading analysis of piles in sand. *Journal of Geotechnical Engineering, 115*(6), pp. 839-852.

Poulos, H., & Chua, E. (1985). Bearing capacity of foundations on calcareous sand. Em P. C. ICSMFE (Ed.), *Proceedings of the 11th International Conference on Soil Mechanics and Foundation Engineering*, *3*, pp. 1619-1622. San Francisco.

Puech, A., Benzaria, O., Thorel, L., Garnier, J., Foray, P., Silva, M., & Jardine, R. (2013). Cyclic stability diagrams for piles in sands. Em A. Puech (Ed.), *Proceedings of TC 209 Workshop 18th ICSMGE. Design for cyclic loading: piles and other foundations.* (pp. 85-88). Paris: Presses des Ponts.

Rimoy, S. (2013). *Ageing and axial cyclic loading studies of displacement piles in sands.* PhD Thesis, Imperial College London, Department of Civil and Environmental Engineering, London.

Rimoy, S., & Jardine, R. (2011). On strain accumulation in a silica sand under creep and low level cyclic loading. Em C.-K. C. al. (Ed.), *Proceedings of the Fifth International Symposium on Deformation Characteristics of Geomaterials*, (pp. 463-470). Seoul.

Rimoy, S., Jardine, R., & Standing, J. (2013). Displacement response to axial cycling of piles driven in sand. *Proceedings of the Institution of Civil Engineers-Geotechnical Engineering, 166*(2), pp. 131-146.

Rosquët, F. (2004). *Pieux sous charge latérale cyclique.* PhD thesis, Université de Nantes, Nantes.

Sakr, M. (2014). Relationship between installation torque and axial capacities of helical piles in cohesionless soils. *Canadian Geotechnical Journal, 52*(6), pp. 747-759.

Santos Filho, J. (2014). *Effects of installation of helical piles in tropical soils.* MSc dissertation, University of São Paulo, São Carlos.

Schiavon, J., Santos Filho, J., Tsuha, C., & Thorel, L. (2015). The occurrence of residual stresses in helical piles. Em D. S. Manzanal (Ed.), *From Fundamentals to Applications in Geotechnics: Proceedings of the 15th Pan-American Conference on Soil Mechanics and Geotechnical Engineering* (p. 8p). Buenos Aires: Millpress.

Stuyts, B., Cathie, D., Falepin, H., & Burgraeve, A. (2012). Axial pile capacity of wind turbine foundations subject to cyclic loading. Em S. o. Technology (Ed.), *Offshore Site Investigation and Geotechnics: Integrated Technologies-Present and Future*, (pp. 315-322). London.

Tagaya, K., Scott, R., & Aboshi, H. (1988). Pullout resistance of buried anchor in sand. *Soils and Foundations, 28*(3), pp. 114-130.

Tatsuoka, F., Goto, S., Tanaka, T., Tani, K., & Kimura, Y. (1997a). Particle size effects on bearing capacity of footing on granular material. Em T. A. Akira Asaoka (Ed.), *Deformation and Progressive Failure in Geomechanics*, (pp. 133-138). Tokyo.

Tatsuoka, F., Jardine, R., Lo Presti, D., Di Bennedetto, H., & Kodaka, T. (1997b). Characterising the pre-failure deformation properties of geomaterials: theme lecture for plenary session no. 1. *Proceedings of the 14th International Conference on Soil Mechanics and Geotechnical Engineering*, *4*, pp. 2129-2164. Hamburg.

Taylor, R. (1995). Centrifuges in modeling: principles and scale effects. Em *Geotechnical centrifuge technology* (1 ed.). New York: Chapman & Hall.

Ternet, O. (1999). *Reconstitution et caractérisation des massifs de sable. Application aux essais en centrifugeuse et en chambre de calibration.* PhD thesis, Univsersity of Caen Normandy, Caen.

Thomassen, K. (2016). *Experimental Investigations of Tension Piles in Sand Subjected to Static and Cyclic Loading.* PhD thesis, Aalborg University, Aalborg, Denmark.

Thorel, L., Rault, G., Garnier, J., Carol, M., Gaudicheau, P., Neel, A., & Favraud, C. (2009). *Mesures en macrogravité sur modèles réduits d'ouvrages géotechniques.* https://hal.archives-ouvertes.fr/hal-00376812: Hal archives-ouvertes.

Tomlinson, M. (1971). Some effects of pile driving on skin friction. *Proceedings of the Conference on Behaviour of Piles* (pp. 107-114). London: ICE Publishing.

Trofimenkov, Y., & Mariupolskii, L. (1964). Screw piles as foundations of supports and towers of transmission lines. *Soil Mechanics and Foundation Engineering, 1*(4), pp. 232-239.

Tsuha, C. (2007). *Theoretical model to control on site the uplift capacit of helical screw piles embedded in sandy soil.* DSc thesis, University of São Paulo, Department of Geotechnical Engineering, São Carlos.

Tsuha, C., & Aoki, N. (2010). Relationship between installation torque and uplift capacity of deep helical piles in sand. *Canadian Geotechnical Journal, 47*(6), pp. 635-647.

Tsuha, C., Aoki, N., Rault, G., Thorel, L., & Garnier, J. (2012a). Evaluation of the efficiencies of helical anchor plates in sand by centrifuge model tests. *Canadian Geotechnical Journal, 46*(9), pp. 1102-1114.

Tsuha, C., Aoki, N., Rault, G., Thorel, L., & Garnier, L. (2007). Physical Modelling of Helical Pile Anchors. *International Journal of Physical Modelling in Geotechnics, 7*(4), pp. 1-12.

Tsuha, C., Foray, P., Jardine, R., Yang, Z., Silva, M., & Rimoy, S. (2012b). Behaviour of displacement piles in sand under cyclic axial loading. *Soils and foundations, 52*(3), pp. 393-410.

Tsuha, C., Thorel, L., & Rault, G. (2013). A review of centrifuge model tests of helical foundations. Em A. Lutenegger (Ed.), *1st International Geotechnical Symposium on Helical Foundations*, (pp. 1-23). Amherst.

Turner, J., & Kulhawy, F. (1990). Drained uplift capacity of drilled shafts under repeated axial loading. *Journal of geotechnical engineering, 116*(3), pp. 470-491.

Uesugi, M., Kishida, H., & Tsubakihara, Y. (1989). Friction between sand and steel under repeated loading. *Soils and Foundations, 29*(3), pp. 127-137.

Urabe, K., Tokimatsu, K., Suzuki, H., & Asaka, Y. (2015). Bearing capacity and pull-out resistance of wing piles during cyclic vertical loading. *Proceedings of the 6th International Conference on Earthquake Geotechnical Engineering*, (p. 9). Christchurch.

Van Weele, A. (1979). Pile bearing capacity under cyclic loading compared with that under static loading. *Proceedings of the 2nd International Conference on the Behaviour of Off-Shore Structures*, *1*, pp. 475-488. Bedford.

Vesic, A. (1970). Tests on instrumented piles, Ogeechee River site. *Journal of Soil Mechanics & Foundations Division, 96*(2), pp. 561-584.

Vishay Precision Group. (2011). *P3 Strain Indicator and Recorder - Document No.: 11102.* Acesso em 12th de july de 2016, disponível em Micro Measurements: www.vishaypg.com/docs/11102/p3.pdf

Vucetic, M. (1994). Cyclic threshold shear strains in soils. *Journal of Geotechnical Engineering, 120*(12), pp. 2208-2228.

Wang, D., Merifield, R., & Gaudin, C. (2013). Uplift behaviour of helical anchors in clay. *Canadian Geotechnical Journal, 50*(6), pp. 575-584.

White, D., & Bolton, M. (2004). Displacement and strain paths during plane-strain model pile installation in sand. *Géotechnique, 54*(6), pp. 375-397.

White, D., & Lehane, B. (2004). Friction fatigue on displacement piles in sand. *Géotechnique, 54*(10), pp. 645-658.

Wichtmann, T. (2005). *Explicit accumulation model for non-cohesive soils under cyclic loading.* PhD thesis, Ruhr University Bochum, Bochum.

Wichtmann, T., & Triantafyllidis, T. (2004). Influence of a cyclic and dynamic loading history on dynamic properties of dry sand, part II: cyclic axial preloading. *Soil Dynamics and Earthquake Engineering, 24*(11), 789-803.

Wichtmann, T., Niemunis, A., & Triantafyllidis, T. (2005). Strain accumulation in sand due to cyclic loading: drained triaxial tests. *Soil Dynamics and Earthquake Engineering, 25*(12), pp. 967-979.

Yamaguchi, H., Kimura, T., & Fujii, N. (1977). On the scale effect of footings in dense sand. *Proceedings of the 9th International Conference on Soil Mechanics and Foundation Engineering*, (pp. 795-798). Tokyo.

Yoshida, T., & Tatsuoka, F. (1997). Deformation property of shear band in sand subjeted to plane strain compression and its relation to particle characteristics. Em P. C. ICSMFE (Ed.), *14th International Conference on Soil Mechanics and Foundation Engineering. 1*, pp. 237-240. Hamburg: A.A. Balkema.

Yoshimi, T., & Kishida, T. (1981). A ring torsion apparatus for evaluating friction between soil and metal surfaces. *Geotechnical Testing Journal, 4*(4), pp. 145-152.

Youd, T. (1972). Compaction of sands by repeated shear straining. *Journal of the Soil Mechanics and Foundations Division, 98*(SM7), pp. 709-725.

Zhang, D. (1999). *Predicting capacity of helical screw piles in Alberta soils.* MSc Thesis, University of Alberta, Edmonton.

APPENDIX

Appendix A. Characteristics of the HN38 Hostun sand

HN38 Hostun sand is a fine silica sand consisting of angular particles is extracted in Hostun village, 66 km far from Grenoble, France. The characterization tests conducted with the HN38 Hostun sand were:

- Test for determination of the Specific Gravity of the sand particles (G_s);
- Test for determination of the Particle-Size Distribution;
- Test for determination of the maximum and minimum dry density;

The specific gravity of sand particles (G_s) was obtained from tests carried out by Unisol Laboratories following the French Standard NF P94-054 (AFNOR, 1991). The specific gravity of the HN38 Hostun sand was $G_s = 2.64$.

The particle-size distribution of the HN38 Hostun sand was carried out according to the French Standard NF P94-056 (AFNOR, 1996) at the IFSTTAR laboratory. Figure 113 shows the equipment used in the tests.

Figure 113. Sieve analysis apparatus

The variation in the granulometric distribution due to reuse of the same batch of sand to reconstitute multiple samples was also investigated. Another sieve analysis was conducted on with the same sand batch after using this sand five times to reconstitute sand samples to carry out tests in centrifuge. In this second test, additional sieves were used to detail specific ranges of particle size.

A third sieve analysis was performed at the laboratory of soil mechanics of the Department of Geotechnical Engineering at EESC-USP. This sieve analysis used a sand sample from a new batch of HN38 Hostun sand, brought from France, to compare the resulting granulometric curves of the three sieve analysis. This third analysis was conducted using a different set of sieves of the two previous tests, with slightly different sieve openings. Table 24 presents the percentage of cumulated passing material of the three tests. Figure 114 shows the three granulometric curves obtained from the three sieve analysis. In these three curves, the average grain size (d_{50}) was found around 0.12 mm. No significant dispersion was observed among the resulting curves.

Table 23. Sieve analysis results

Sieve opening	Passing material (%)		
(mm)	First test	Second test	Third test
1.000	100.0	Not used	Not used
0.595	Not used	Not used	100.0
0.500	100.0	Not used	Not used
0.400	Not used	100.0	Not used
0.315	Not used	100.0	Not used
0.297	Not used	Not used	99.9
0.210	Not used	Not used	98.7
0.200	96.1	96.4	Not used
0.160	Not used	72.4	Not used
0.149	Not used	Not used	74.1
0.125	Not used	52.9	Not used
0.105	Not used	Not used	41.1
0.100	Not used	32.1	Not used
0.080	17.8	15.7	Not used
0.075	Not used	Not used	17.1
0.063	6.2	6.0	Not used
0.040	0.9	0.1	0.0

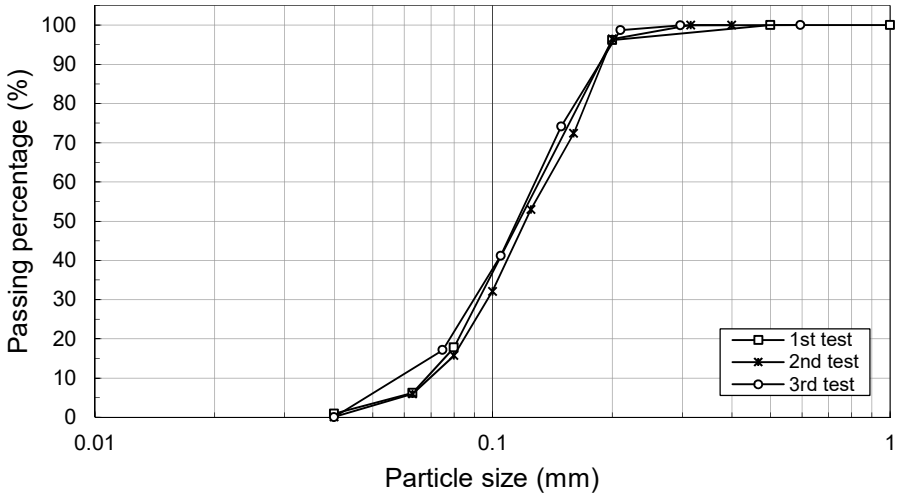

Figure 114. Granulometric distributions of HN38 Hostun sand.

The tests for determination of the maximum and minimum dry density were carried out according to the ASTM Standards D4253 (ASTM, 2014) and D4254 (ASTM, 2014), respectively. The maximum and minimum dry density were found, respectively, equals to 1554 kg/m³ and 1186 kg/m³, with a minimum void ratio of 0.70 and a maximum void ratio of 1.23.

Additional tests on sand specimens prepared according to the procedure described in Miura and Toki (1982) were carried out to verify the value obtained for the maximum dry density ($\rho_{d(max)}$). The sand specimen preparation consisted in using a multiple sieving pluviation apparatus. Various densities of sand specimens can be achieved when the rate of sand discharge is controlled. According to Miura and Toki (1982), when this procedure is performed with granular materials with relatively small uniformity coefficient, a very high density can be achieved without vibrating or impacting the specimen. In contrast with the results presented by Miura and Toki (1982) with Toyura sand (C_U = 1.5 and d_{50} = 0.18 mm), the maximum dry density obtained with this procedure using the HN38 Hostun sand was only 3% greater than the result achieved with the test conducted according to the ASTM Standard

D4253 (ASTM, 2014). Table 24 presents a summary of the characteristics of the HN38 Hostun used in centrifuge tests of this investigation.

Table 24. HN38 Hostun sand characteristics

Specific gravity of the sand particles	G_s	2.64[a]
Maximum dry density (kg/m^3)	$\rho_{d(max)}$	1554
Minimum dry density (kg/m^3)	$\rho_{d(min)}$	1186
Maximum void ratio	e_{max}	1.226
Minimum void ratio	e_{min}	0.699
Average grain-size (mm)	d_{50}	0.12
Coefficient of uniformity	C_U	1.97
Coefficient of curvature	C_C	0.99

[a] Provided from tests carried out by Unisol Laboratories

Appendix B. Direct shear tests with HN38 Hostun sand

A series of three direct shear tests was carried out with dry HN38 Hostun sand with 98% mean density. Cylindrical samples with 59.92 mm diameter and 26.80 mm high were reconstituted by pluviation using the equipment showed in Figure 115a. During the direct shear tests, the vertical load was maintained constant and the horizontal load was monitored with a force transducer. The horizontal rate of displacement was set in 0.02 mm/s and the vertical displacement was monitored using a displacement transducer. The equipment for the direct shear tests is showed in Figure 115b.

Figure 115. (a) pluviation equipment; (b) direct shear test equipment.

Three tests were carried out with different normal stress: 50, 100 and 200 kPa. Figure 116a presents the shear stress-strain curves of the three tests. The ultimate shear stress was 64.4, 118.3 and 223.0 kPa for normal stress of 50, 100 and 200 kPa, respectively. At the peak stress, the measured horizontal displacement (*dH*) was around 2.5% of the specimen

diameter (59.92 mm). The measures of vertical displacement were not reliable due to the low resolution of the available transducer in comparison to the range of the vertical displacements. Figure 116 presents the vertical and horizontal displacement for the three tests. The Mohr-Coulomb envelope (Figure 117) determined for the peak values of shear stress yielded an effective friction angle ϕ' = 48º and a friction angle ϕ' = 42º for a horizontal displacement (*dH*) of 10% of the sand specimen diameter.

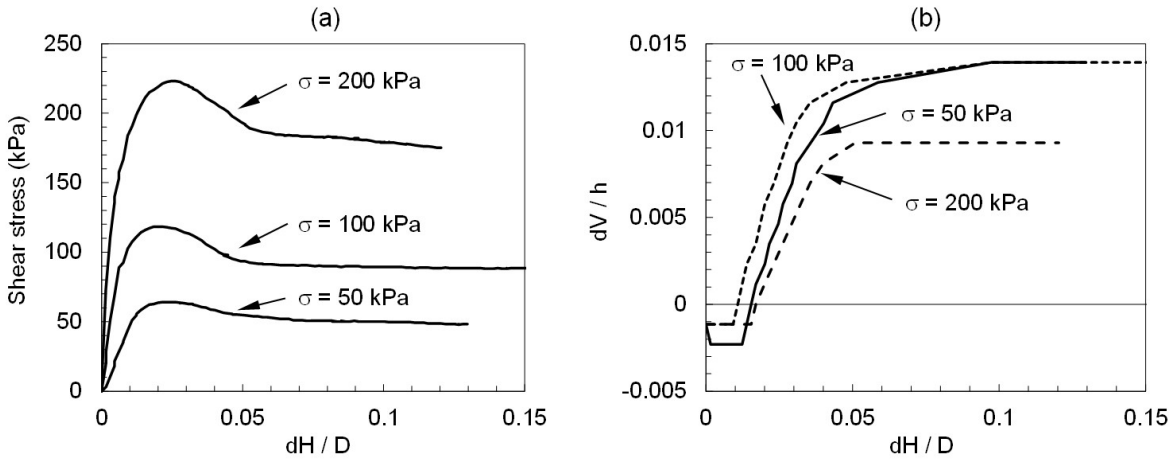

Figure 116. Results of the direct shear tests on HN38 Hostun sand (I_D = 98%): (a) horizontal displacement *vs* shear stress; (b) horizontal displacement *vs* vertical displacement.

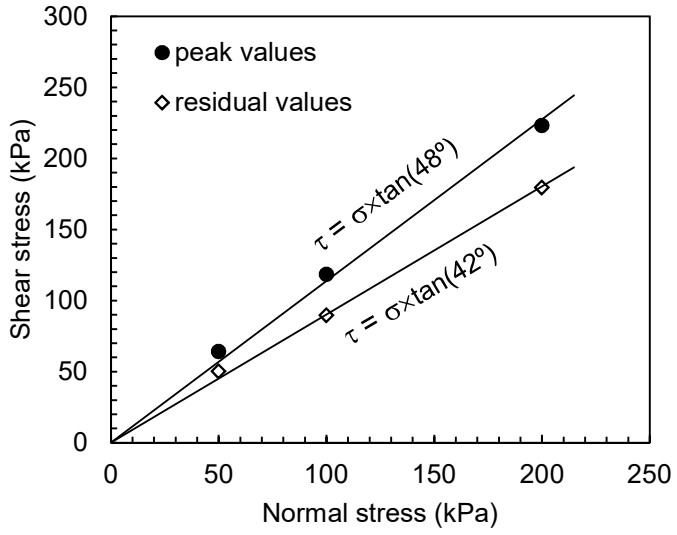

Figure 117. Mohr-Coulomb envelope with peak values (c' = 0 and ϕ' = 48°) and post-peak values at dH/D = 0.10 (c' = 0 and ϕ' = 42°).

Appendix C. Triaxial compression tests with HN38 Hostun sand

A series of three triaxial compression tests was carried out in the laboratory of soil mechanics at the Ecole Centrale de Nantes. Sand specimens were reconstituted with dry HN38 Hostun sand in order to achieve a density index (I_D) between 90 and 95% (the specimen reconstitution is difficult when a specimen of very dense sand is intended). The sand specimens with 100 mm diameter and 200 mm high were reconstituted by vibration and compaction of 5 layers using a two-part mould. The stability of the sand specimen during the mould removal was ensured by applying a negative pressure (suction) to the specimen.

The confining pressure was applied one hour before initiating the shearing stage, but no data was recorded during the application of the confining pressure. For the shearing stage, the axial displacement rate was set in 0.003 mm/s with data acquisition of the vertical displacement, axial load, confining pressure and volume variation of the water inside the cylindrical chamber. Figure 118a presents the sand specimen after reconstitution using the two-part mould. The sand specimen sealed and subjected to negative pressure is presented in Figure 118b. Figure 118c shows the triaxial test apparatus.

Figure 119a presents the stress-strain response of HN38 Hostun sand for three levels of confining stress. A volumetric expansion, typical behaviour of dense sands, is observed in Figure 119b. Table 25 presents some results of the triaxial tests. The Mohr-Coulomb envelope with the resulting strength parameters is presented in Figure 120.

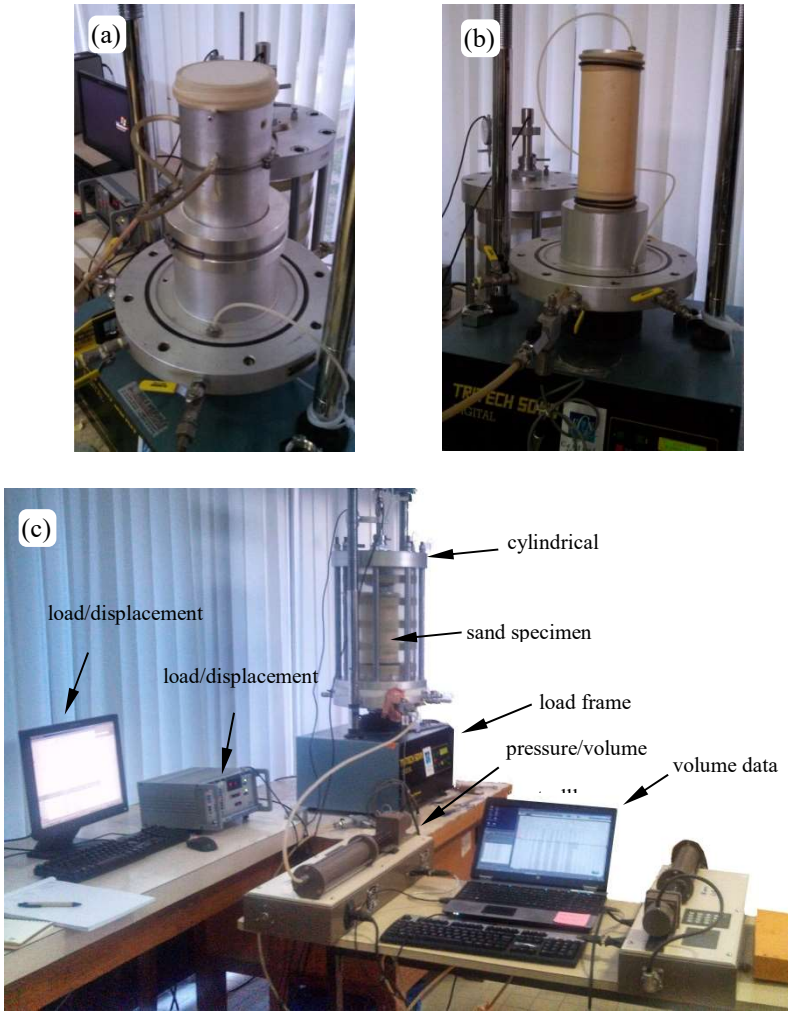

Figure 118. (a) sample with two-part mould and (b) under suction.

Table 25. Summary of results of the triaxial tests

σ_3 (kPa)	$\sigma_{1\ max}$ (kPa)	$(\sigma_1 - \sigma_3)_{max}$ (kPa)	E_i (kPa)	E_{50} (MPa)	$E_{50\text{-reload}}$ (MPa)	ν	ϕ' (º)	$\phi'_{test\ end}$ (º)
50	374.9	324.9	42100	17500	97000	0.20		
100	652.8	552.8	64700	35700	92700	0.24	47	42
200	1255.9	1055.9	62400	64400	127800	0.24		

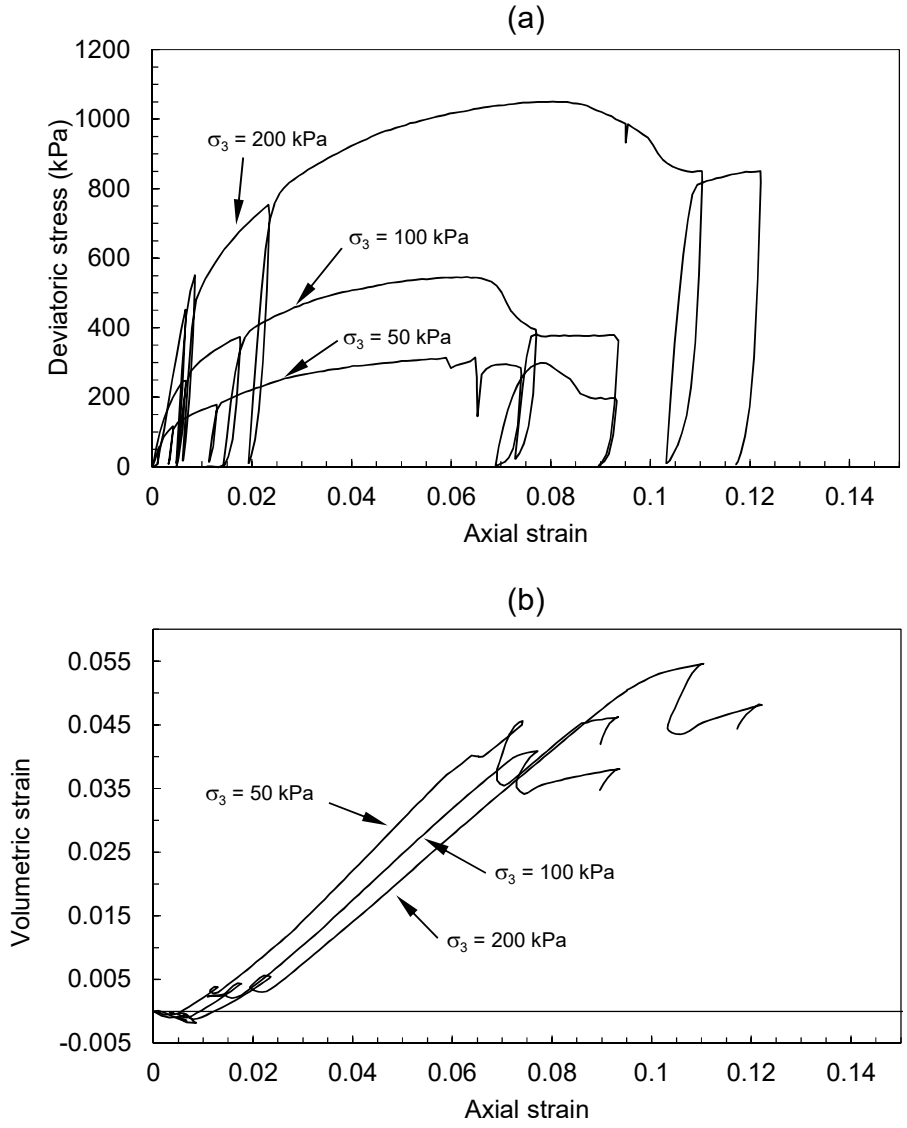

Figure 119. Triaxial test results: (a) stress-strain curves; (b) strain responses.

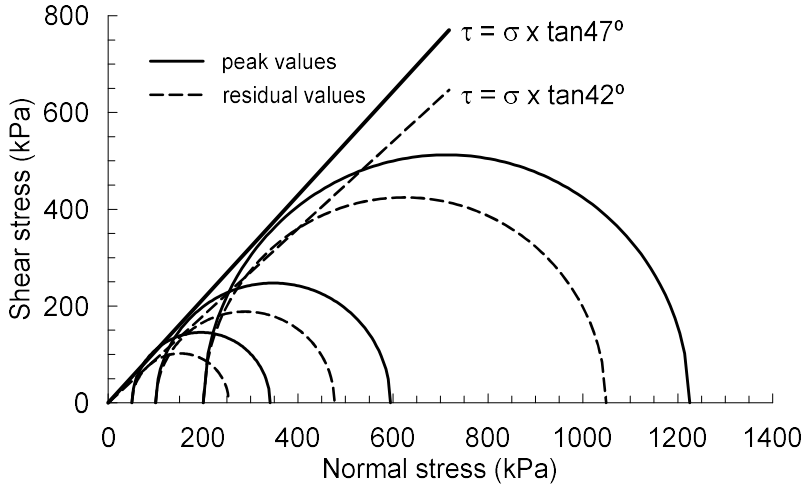

Figure 120. Mohr-Coulomb envelope of HN38 Hostun sand (c' = 0 and ϕ' = 47º).

Appendix D. Tests of sample reconstitution by the pluviation technique

The density of a reconstituted sample by pluviation depends on the following parameters: hopper horizontal speedy, hopper slot opening and sand drop height. By varying these three parameters different sample densities can be obtained. Thus, the tests were performed to optimize the sample reconstitution varying the three parameters according to aimed density.

Five calibrated boxes were positioned at the bottom of the rectangular strongbox to determine the relative density of the sand sample reconstituted with HN38 Hostun sand. To maintain the same particle drop height during the tests, the hopper was stopped after a certain number of round-trip movements, depending on the slot opening: after 4 round-trip movements for 2 mm of slot opening; for 3 mm and 2 mm of slot opening, the hopper the drop height was verified after 3 and 1 round-trip movements, respectively.

Figure 121 shows the configuration of the calibration boxes inside the strongbox.

Table 26 lists the variation of the pluviation parameters and the results.

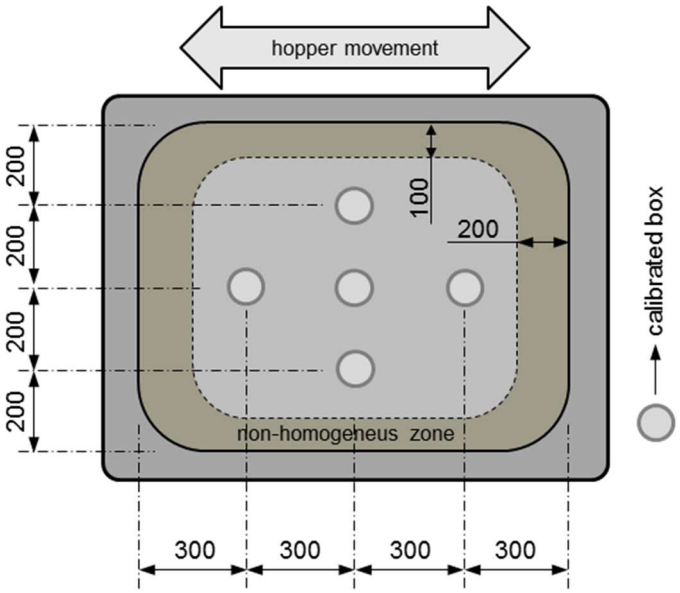

Figure 121. Position of calibration boxes (dimensions in mm).

Table 26. Summary of the parameters and results.

Parameter	Test 1	Test 2	Test 3	Test 4	Test 5	Test 6
Drop height (mm)	60	60	60	60	57.5	115
Horizontal speed (cm / s)	7.7	11.9	11.9	18.5	18.5	18.5
Slot opening (mm)	3	4	3	3	2	2
Mean dry bulk density (kg/m^3)	1500	1480	1518	1525	1542	1532
Relative density (%)	85%	80%	90%	92%	97%	94%
Coefficient of variation (%)	0.74	0.86	0.75	0.81	0.39	0.76

Appendix E. Penetrometric tests on sand sample

Five penetrometric tests (mini-CPT) were carried out in container 3 at 10*g* and at a constant penetration rate of 10 mm/s. Figure 122 shows the IFSTTAR mini-CPT equipment. These tests intended to evaluate the vertical and horizontal homogeneity of the sand sample tested. The results of the five mini-CPT tests are presented in Figure 123.

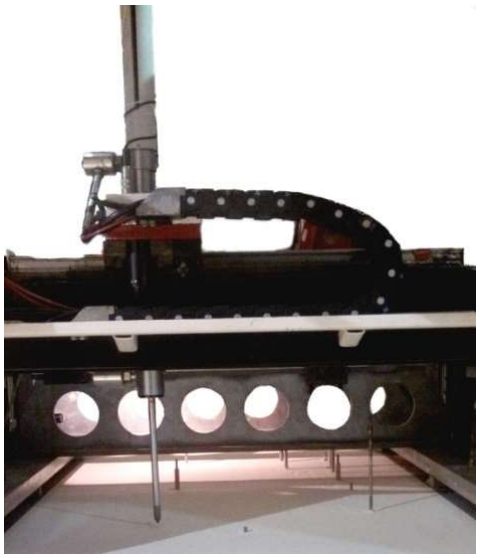

Figure 122. IFSTTAR mini-CPT equipment

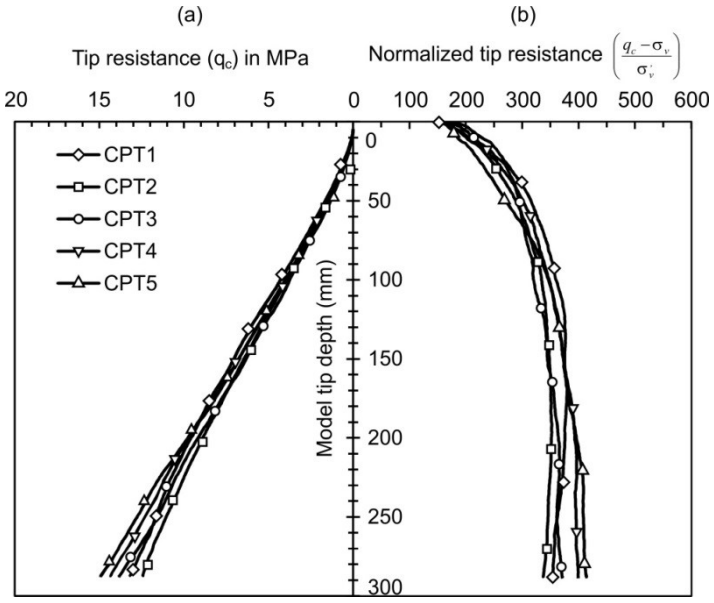

Figure 123. Mini-CPT results, in model values.

Appendix F. Data acquisition system and servo-controlled hydraulic actuator

In the IFSTTAR Centrifuge, the on-board measurements during the tests are performed with the Spider8 (8-channel modules) data acquisition modules manufactured by HBM. The control of the data acquisition system is done with the DASYLab software via a graphical programming interface that enables to register the data on an external hard drive backup and facilitates the data duplication on a dedicated network space. Any type of sensor can be conditioned (full bridge, half-bridge, voltage source, temperature probe) with a sampling frequency up to 1200 Hz. Positioned in the centrifuge basket, Spider modules are then connected via a parallel link to a central processing unit at the centrifuge swing (Thorel, et al., 2009).

Figure 124. Spider data acquisition modules (Thorel, et al., 2009).

The hydraulic servo-actuator is equipped with a Moog electro-hydraulic servo-valve which is capable of operating up to 100*g*. The oil supply is provided by a stationary hydraulic power unity on the stator side (flow rate of 6.8 litres/minute at 50 °C under 15 MPa).

Appendix G. Characteristics of the helical anchor models

Table 27. Characteristics of the model anchors.

Model anchor designation	Shaft diameter (d) in mm	Helix diameter (D) in mm	Helix pitch (p) in mm	Helical plate thickness (t_h) in mm	p / D
6H	6	20	1.6	0.5	0.08
8H	8	26.6	1.4	0.8	0.053
10H	10	33	2.5	1.8	0.076
12H	12	40	3	3	0.075
10FHi	10	33	9.7	1.5	0.294

Appendix H. Calibration of the 10FHi force gauge

The force gauge of the model anchor 10FHi was calibrated in tension with a universal press (Figure 125a). A support base was used to attach the pile head to the press base (Figure 125b). Figure 126 presents the calibration curve of the force gauge at the shaft section above the helix of the model 10FHi.

During the first experiments with the model 10FHi (tests 10FHi-1 and 10FHi-2 in Container No. 9) we observed that the readings of this force gauge were being affected by the installation torque. Thus, a preliminary verification was done with the model anchor out of the sand sample and with no axial loading. The top of the model anchor was maintained attached to the servo-controlled actuator and a torque was applied to the anchor tip using a manual torque wrench. The axial force was observed to increase as the applied torque increased. This occurred because the force gauge has screws on both sides to attach both helix and shaft to the force gauge. Thus, as the torque increases, the shaft and the helix tend to be screwed even more into the screws of the force gauge. Figure 127 illustrates this mechanism. As consequence, the data registered with the force gauge above the helix are required to be corrected as a function of the applied torque. This correction was done by calibrating the arisen load in the force gauge due to the torque application.

The calibration was performed using the same servo-controlled system and the torquemeter used in the model anchor installation in centrifuge. As performed in the preliminary verification aforementioned, the top of the model anchor was maintained attached to the servo-controled actuator and a torque was applied to the anchor tip using a manual torque wrench. The applied torque was registered by the torquimeter attached to the servo-controlled system, and the load in the force gauge was monitored. As the torque increased, the force gauge indicated a compressive force in a linear correlation. Figure 128 presents the curve for the correction of force gauge readings with the applied torque.

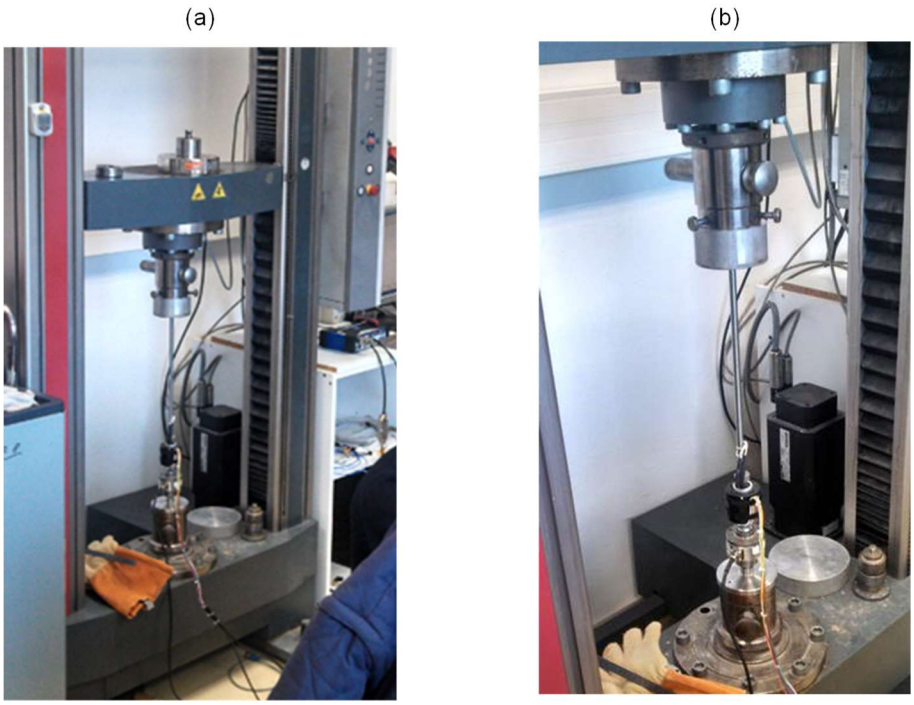

Figure 125. (a) calibration of the force gauge of the model 10FHi; (b) support base.

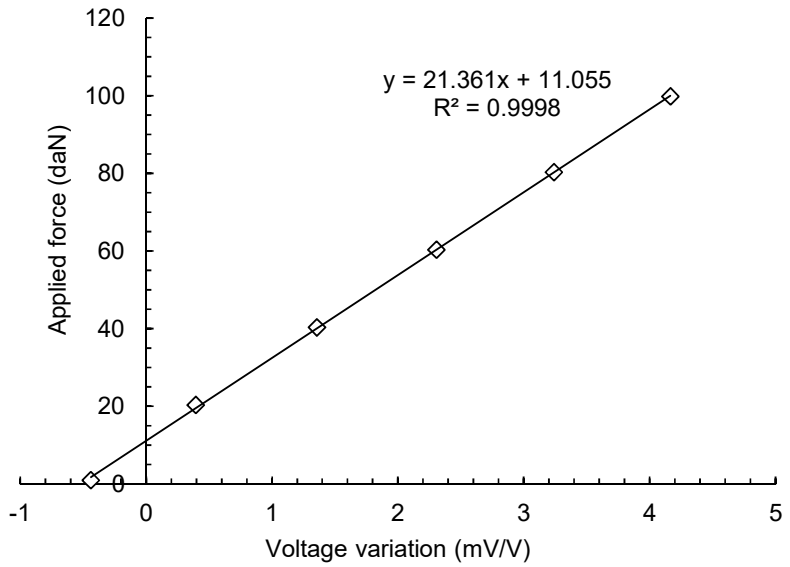

Figure 126. Calibration of the force gauge of the model 10FHi in tension.

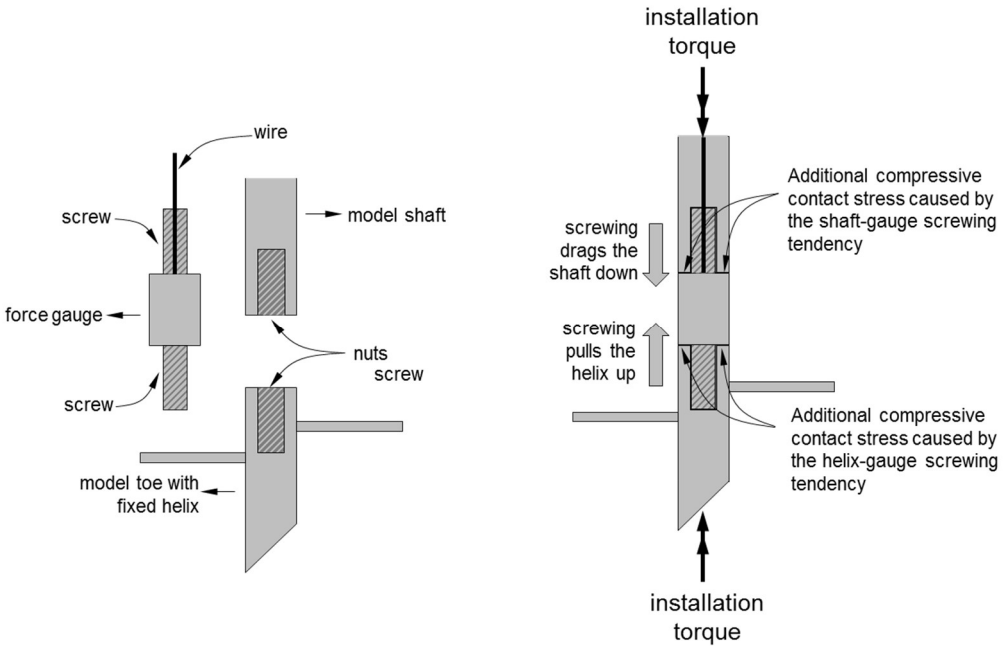

Figure 127. Additional efforts arisen on the force gauge due to model screwing.

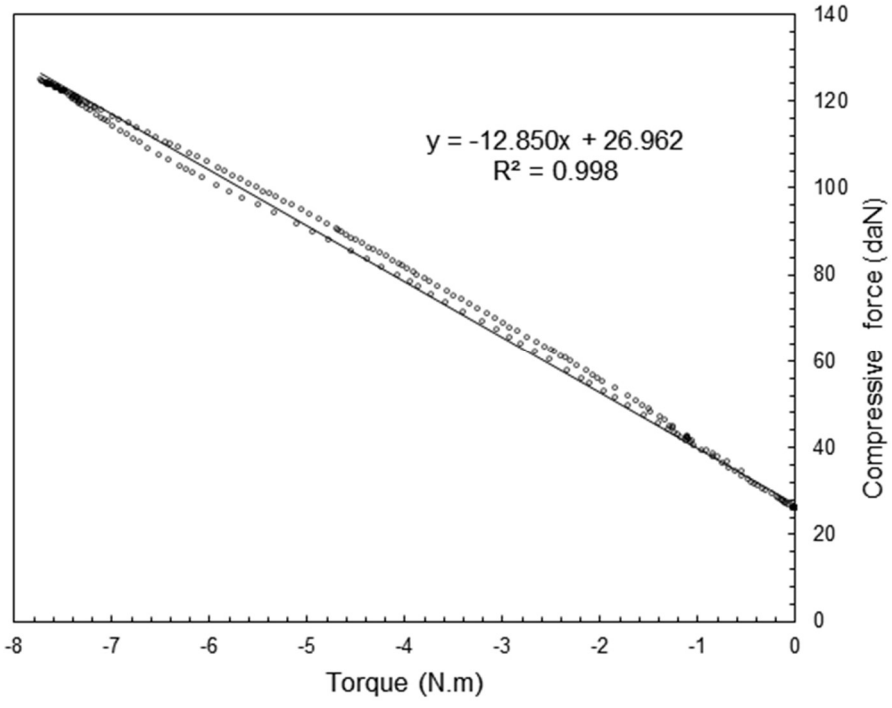

Figure 128. Torque applied *vs* measured force (compression is positive) in the force gauge above 10FHi helix.

Appendix I. Calibration curve of the load cell used in the Field tests

The calibration of the load cell was carried out in a hydraulic servo-controlled press MTS 815 with a 500 kN capacity load cell. The results are presented in Figure 129.

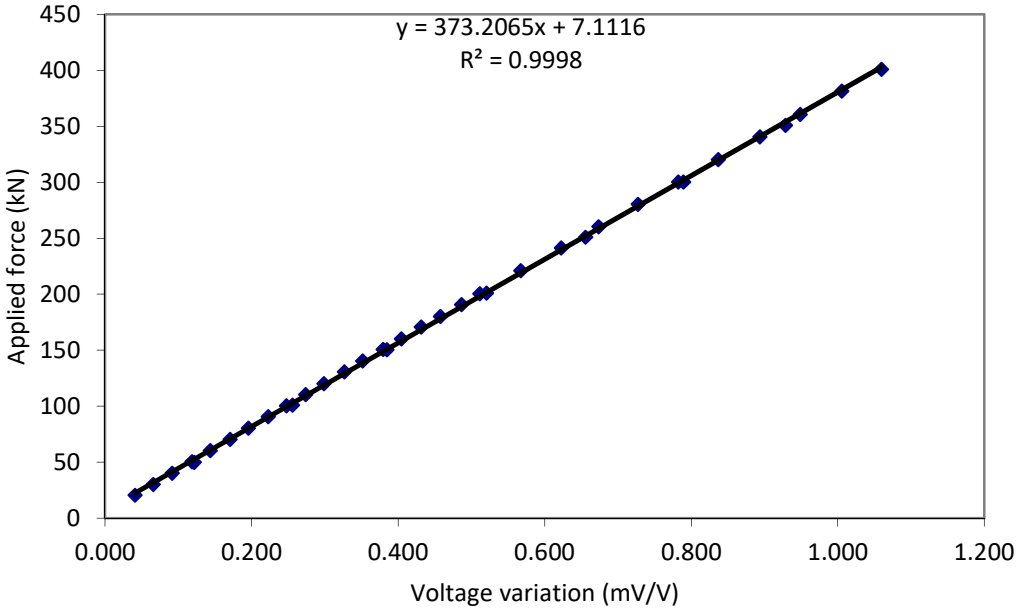

Figure 129. Calibration of the load cell with loading and unloading data.

Appendix J. Calibration curves of the instrumented section of 1MHA and 1CHA helical anchors

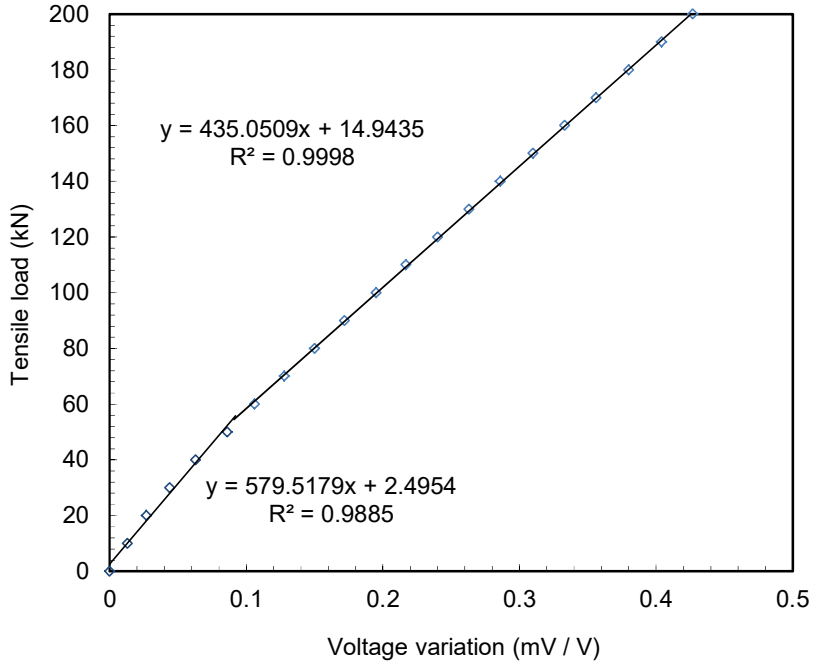

Figure 130. Calibration of the instrumented section of 1MHA anchor.

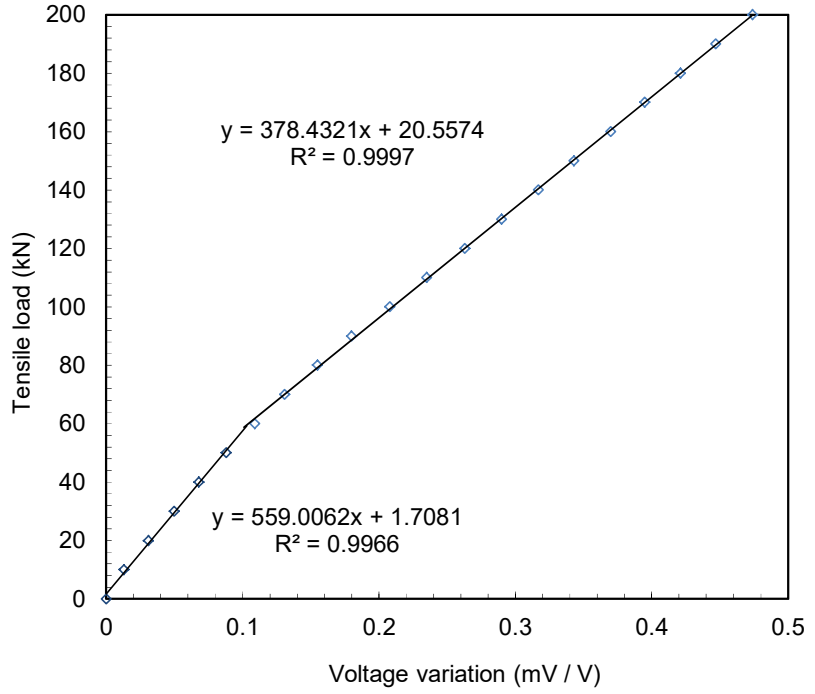

Figure 131. Calibration of the instrumented section of 1CHA anchor.

Appendix K. Summary of centrifuge tests with helical pile models

Table 28. Summary of centrifuge tests with helical pile models

Cont. No.	Model	Test No.	D_r (%)	G-level (×g)	z_D/D	Study	Installation	Type of load	Obtained measures
1	6FH	6FH-1	95	16.7	8.0	Inst. + scale effect	Bef.	Monotonic	F; U
	8FH	8FH-1	95	12.5	8.0	Inst. + scale effect	Bef.	Monotonic	F; U
	10FH	10FH-1	95	10	8.0	Inst. + scale effect	Bef.	Monotonic	F; U
2	8FH	8FH-1	96	12.5	8.0	Inst. + scale effect	In flight	Monotonic	F; U
	10FH	10FH-1	96	10	8.0	Inst. + scale effect	In flight	Monotonic	F; U
	8RH	8RH-1	96	12.5	8.0	Shaft friction	In flight	Monotonic	F; U
	10RH	10RH-1	96	10	8.0	Shaft friction	In flight	Monotonic	F; U
3	10RH	10RH-1	96	10	8.0	Shaft friction	In flight	Monotonic	F; U
	12FH	12FH-1	96	8.3	6.0	Shaft fr. + scale eff.	In flight	Monotonic	F; U
	10FH	10FH-1	96	10	8.0	Inst. + shaft + sc. eff.	In flight	Monotonic	F; U
4	12FH	12FH-1	96	8.3	6.0	Inst. eff. (excav.)	In flight	No loading	-
	10FH	10FH-2	96	10	7.4	Cyclic loading	In flight	Mult. monot.	F; U
	10FH	10FH-3	96	1	7.4	Cyclic loading	In flight	Cyc. + mon.	F; U
	10FH	10FH-4	96	1	7.4	Cyclic loading	In flight	Cyc. + mon.	F; U
	10FH	10FH-5	96	1	7.4	Cyclic loading	In flight	Cyc. + mon.	F; U
	10FH	10FH-6	96	1	7.4	Cyclic loading	In flight	Cyc. + mon.	F; U
	10RH	10RH-1	96	1	7.4	Shaft friction	In flight	Monotonic	F; U
5	10FH	10FH-1	95	1	7.4	Cyclic loading	In flight	Monotonic	F; U
	10FH	10FH-2	95	1	7.4	Cyclic loading	In flight	Cyc. + mon.	F; U
	10FH	10FH-3	95	1	7.4	Cyclic loading	In flight	Cyc. + mon.	F; U
	10FH	10FH-4	95	1	7.4	Cyclic loading	In flight	Cyc. + mon.	F; U
	10FH	10FH-5	95	1	7.4	Cyclic loading	In flight	Cyc. + mon.	F; U
	10FH	10FH-6	95	1	7.4	Cyclic loading	In flight	Cyclic	F; U
6	10FH	10FH-1	94	1	7.4	Cyclic loading	In flight	Cyc. + mon.	F; U
	10FH	10FH-2	94	1	7.4	Cyclic loading	In flight	Cyc. + mon.	F; U
	10FH	10FH-3	94	1	7.4	Cyclic loading	In flight	Cyc. + mon.	F; U
	10FH	10FH-4	94	1	7.4	Cyclic loading	In flight	Cyc. + mon.	F; U
	10FH	10FH-5	94	1	7.4	2 Cyclic loadings	In flight	Cyc. + mon.	F; U
	10FH	10FH-6	94	1	7.4	2 Cyclic loadings	In flight	Cyc. + mon.	F; U
7	10FH	10FH-1	95	1	7.4	Cyclic loading	In flight	Monotonic	F; U
	10FH	10FH-2	95	1	7.4	Cyclic loading	In flight	Monotonic	F; U
	8FH	8FH-1	95	12.5	10	Inst. eff. (excav.)	In flight	Monotonic	F; U
	12FH	12FH-1	95	8.3	6.0	Inst. eff. (excav.)	In flight	Monotonic	F; U
	10FH	10FH-3	95	1	7.4	Cyclic loading	In flight	Monotonic	F; U
	10FH	10FH-4	95	1	7.4	Cyclic loading	In flight	Monotonic	F; U
8	10FH	10FH-1	99	1	6.0	Scale effect	In flight	Monotonic	F; U
	10FH	10FH-2	99	1	6.0	Scale effect	In flight	Monotonic	F; U
	12FH	12FH-1	99	8.3	6.0	Scale effect	In flight	Monotonic	F; U
	12FH	12FH-2	99	8.3	6.0	Scale effect	In flight	Monotonic	F; U
	8FH	8FH-1	99	12.5	6.0	Scale effect	In flight	Monotonic	F; U
	8FH	8FH-2	99	12.5	6.0	Scale effect	In flight	Monotonic	F; U

Table 28. Summary of centrifuge tests with helical pile models (cont.)

Cont. No.	Model	Test No.	D_r (%)	G-level (×g)	z_D/D	Study	Installation	Type of load	Obtained measures
9	10FHi	10FHi-1	99	10	7.4	Mon. + cycl. load.	In flight	Monot. + cycl.	F; U
	10FHi	10FHi-2	99	10	7.4	Mon. + cycl. load.	In flight	Monot. + cycl.	F; U
	10FHi	10FHi-3	99	10	7.4	Cyclic loading	In flight	Cyc. + mon.	F; U
	10FHi	10FHi-4	99	10	7.4	Cyclic loading	In flight	Cyc. + mon.	F; U
	10FHi	10FHi-5	99	10	7.4	2 cyclic loadings	In flight	Cyc. + mon.	F; U; T
	10FHi	10FHi-6	99	10	7.4	2 cyclic loadings	In flight	Cyc. + mon.	F; U; T
10	10FHi	10FHi-1	98	10	7.4	Cyclic loading	In flight	Cyc. + mon.	F; U; T
	10FHi	10FHi-2	98	10	7.4	Cyclic loading	In flight	Cyc. + mon.	F; U; T
	10FHi	10FHi-3	98	10	7.4	Cyclic loading	In flight	Cyc. + mon.	F; U; T
	10FHi	10FHi-4	98	10	7.4	Cyclic loading	In flight	Cyc. + mon.	F; U; T
	10FHi	10FHi-6	98	10	7.4	Cyclic loading	In flight	Cyc. + mon.	F; U; T
	10FHi	10FHi-7	98	10	7.4	Cyclic loading	In flight	Cyc. + mon.	F; U; T
11	6FH	6FH-1	99	16.7	6.0	Scale effect	In flight	Monotonic	F; U; T
	6FH	6FH-2	99	16.7	8.0	Inst. effect	In flight	Monotonic	F; U; T
	6FH	6FH-3	99	16.7	6.0	Scale effect	In flight	Monotonic	F; U; T
	10FH	10FH-1	99	10	6.0	Scale effect	In flight	Monotonic	F; U; T
	10FH	10FH-2	99	10	6.0	Scale effect	In flight	Monotonic	F; U; T
	12FH	12FH-1	99	8.3	6.0	Scale effect	In flight	Monotonic	F; U; T
	10RH	10RH-1	99	10	6.0	Shaft friction	In flight	Monotonic	F; U; T
12	6FH	6FH-1	99	16.7	6.0	Scale effect	In flight	Monotonic	F; U; T
	8FH	8FH-1	99	12.5	6.0	Scale effect	In flight	Monotonic	F; U; T
	10FH	10FH-1	99	10	6.0	Scale effect	In flight	Monotonic	F; U; T
	12FH	12FH-1	99	8.3	6.0	Scale effect	In flight	Monotonic	F; U; T
13	10FHi	10FHi-1	99	10	7.4	Cyclic loading	In flight	Cyc. + mon.	F; U; T
	10FHi	10FHi-2	99	10	7.4	Cyclic loading	In flight	Cyc. + mon.	F; U; T
	10FHi	10FHi-3	99	10	7.4	Cyclic loading	In flight	Cyc. + mon.	F; U; T
	10FHi	10FHi-4	99	10	7.4	Cyclic loading	In flight	Cyc. + mon.	F; U; T
14	10FHi	10FHi-1	99	10	7.4	Cyclic loading	In flight	Cyc. + mon.	F; U; T
	10FHi	10FHi-2	99	10	7.4	Cyclic loading	In flight	Cyc. + mon.	F; U; T
	10FHi	10FHi-3	99	10	7.4	Cyclic loading	In flight	Cyc. + mon.	F; U; T
	10FHi	10FHi-4	99	10	7.4	2 Cyclic loadings	In flight	Cyc. + mon.	F; U; T
	10FHi	10FHi-5	99	10	7.4	2 Cyclic loadings	In flight	Cyc. + mon.	F; U; T
	6FHp	6FHp	99	16.7	7.5	Inst. eff. (tomogr.)	In flight	Monotonic	F; U; T

Appendix L. Installation torque in centrifuge tests, in model values

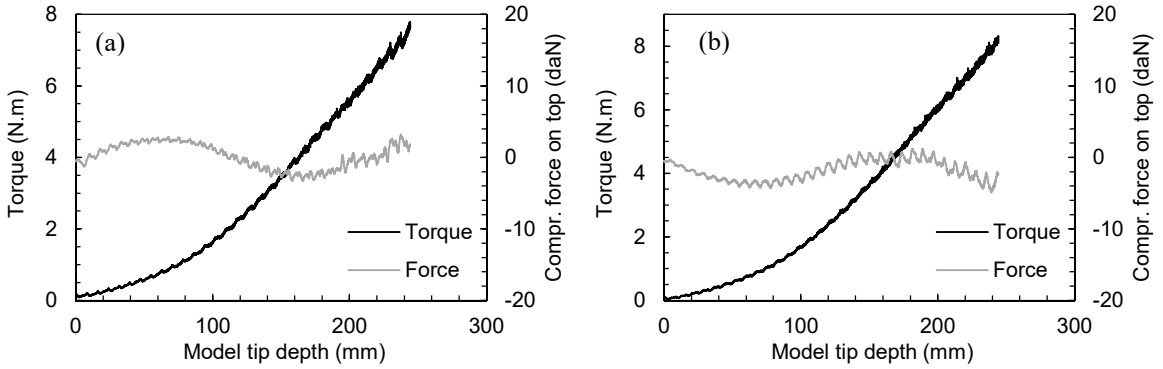

Figure 132. Installation torque of the 10FH model tested in container n. 9: (a) test 10FHi-5 and (b) test 10FHi-6.

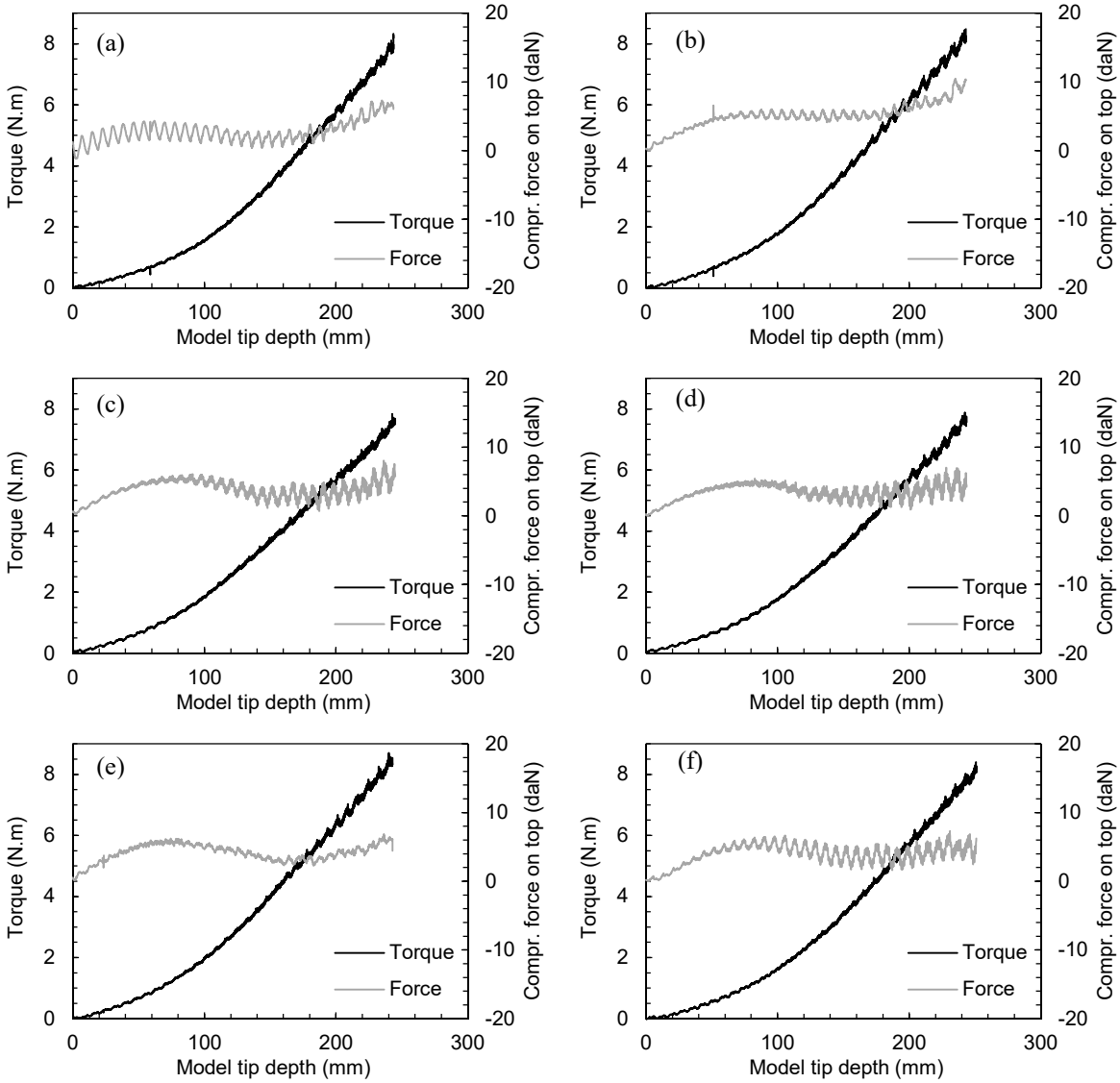

Figure 133. Installation torque of the 10FHi model tested in container n. 10: (a) test 10FHi-1; (b) test 10FHi-2; (c) test 10FHi-3; (d) test 10FHi-4; (e) test 10FHi-6 and (f) test 10FHi-7.

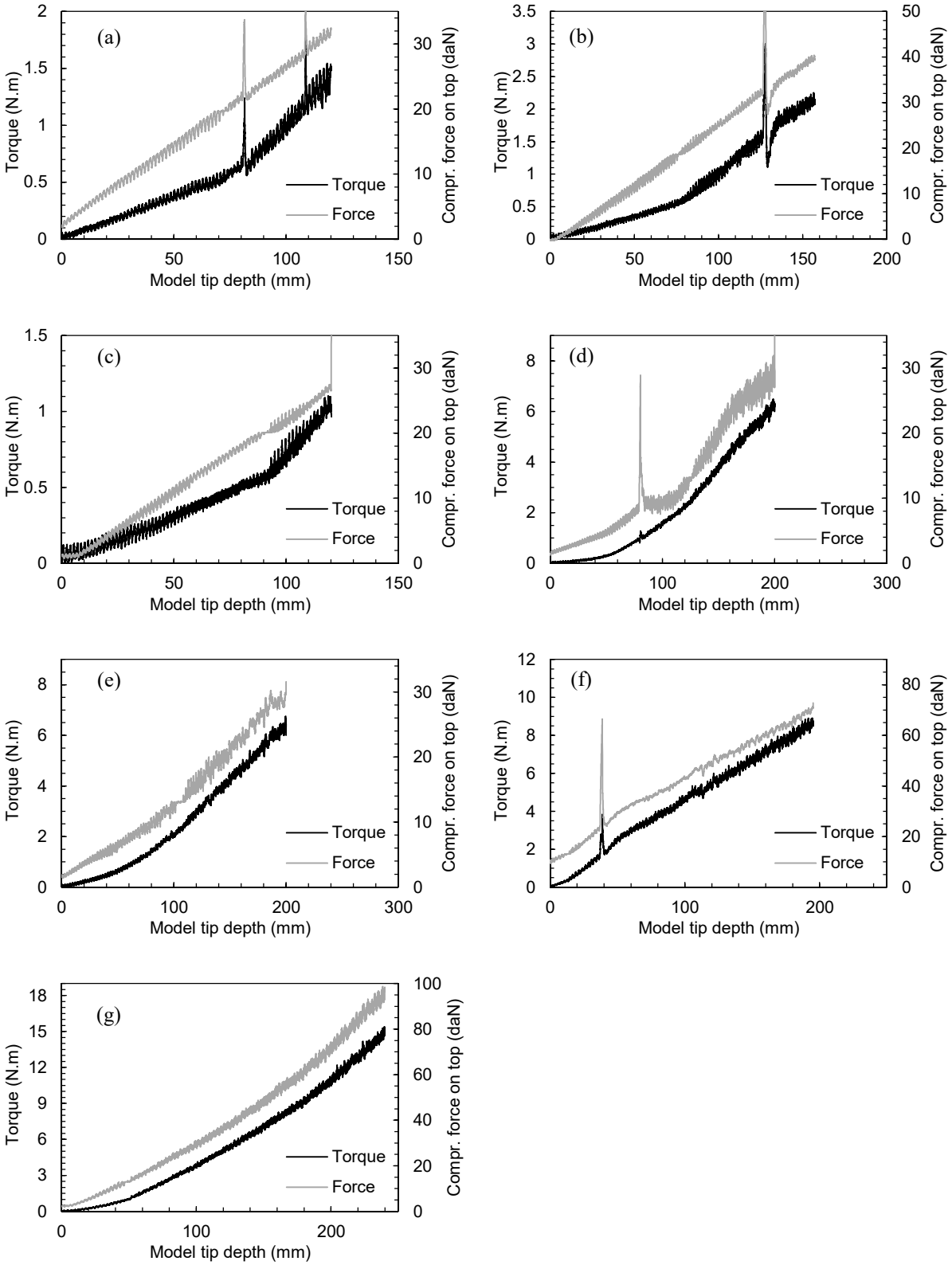

Figure 134. Installation torque of the anchor models tested in container n. 11: (a) test 6FH-1; (b) test 6FH-2; (c) test 6FH-3; (d) test 10FH-1; (e) test 10FH-2; (f) test 10RH-1 and (g) test 12FH-1.

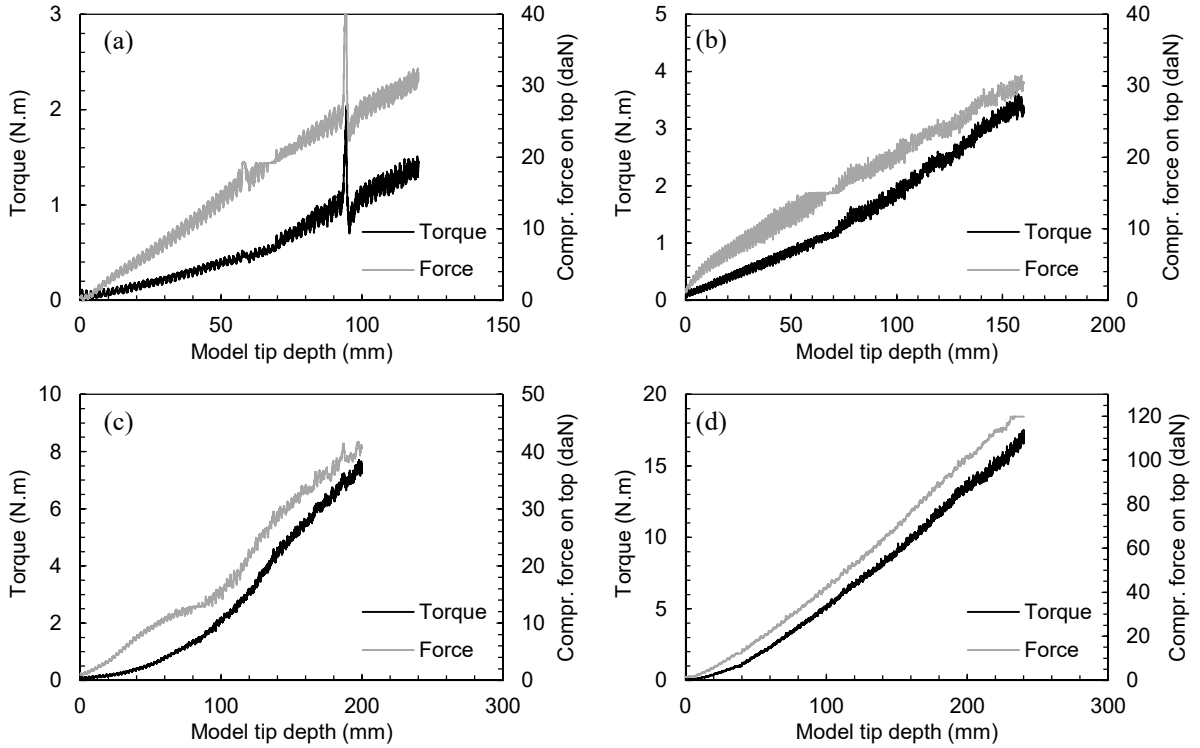

Figure 135. Installation torque of the anchor models tested in container n. 12: (a) test 6-1; (b) test 8FH-1; (c) test 10FH-1 and (d) test 12FH-1.

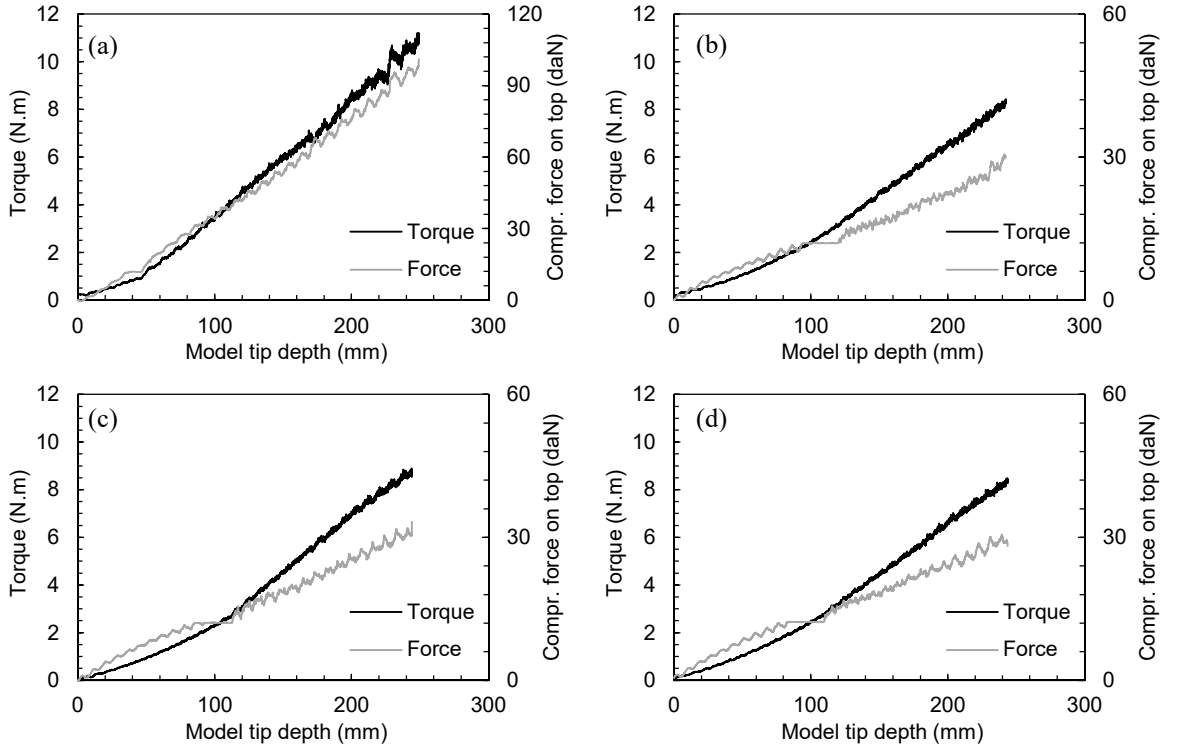

Figure 136. Installation torque of the anchor models tested in container n. 13: (a) test 10FHi-1; (b) test 10FHi-2; (c) test 10FHi-3; (d) test 10FHi-4;

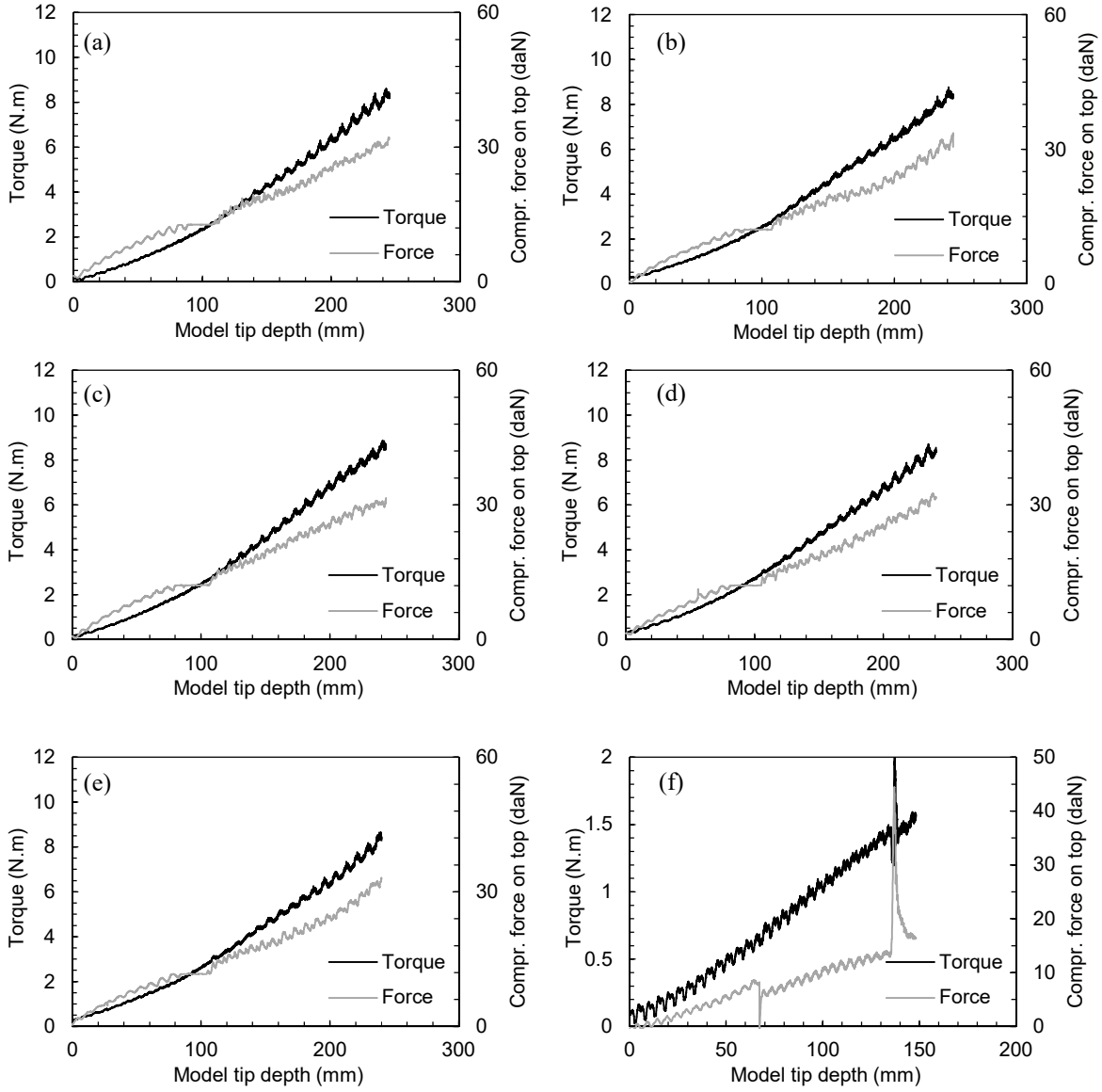

Figure 137. Installation torque of the 10FHi model tested in container n. 14: (a) test 10FHi-1; (b) test 10FHi-2; (c) test 10FHi-3; (d) test 10FHi-4; (e) test 10FHi-5 and (f) test 6FHp

Appendix M. Pre-cyclic load-displacement response after the end of the installation and before the cyclic loading on the model 10FHi

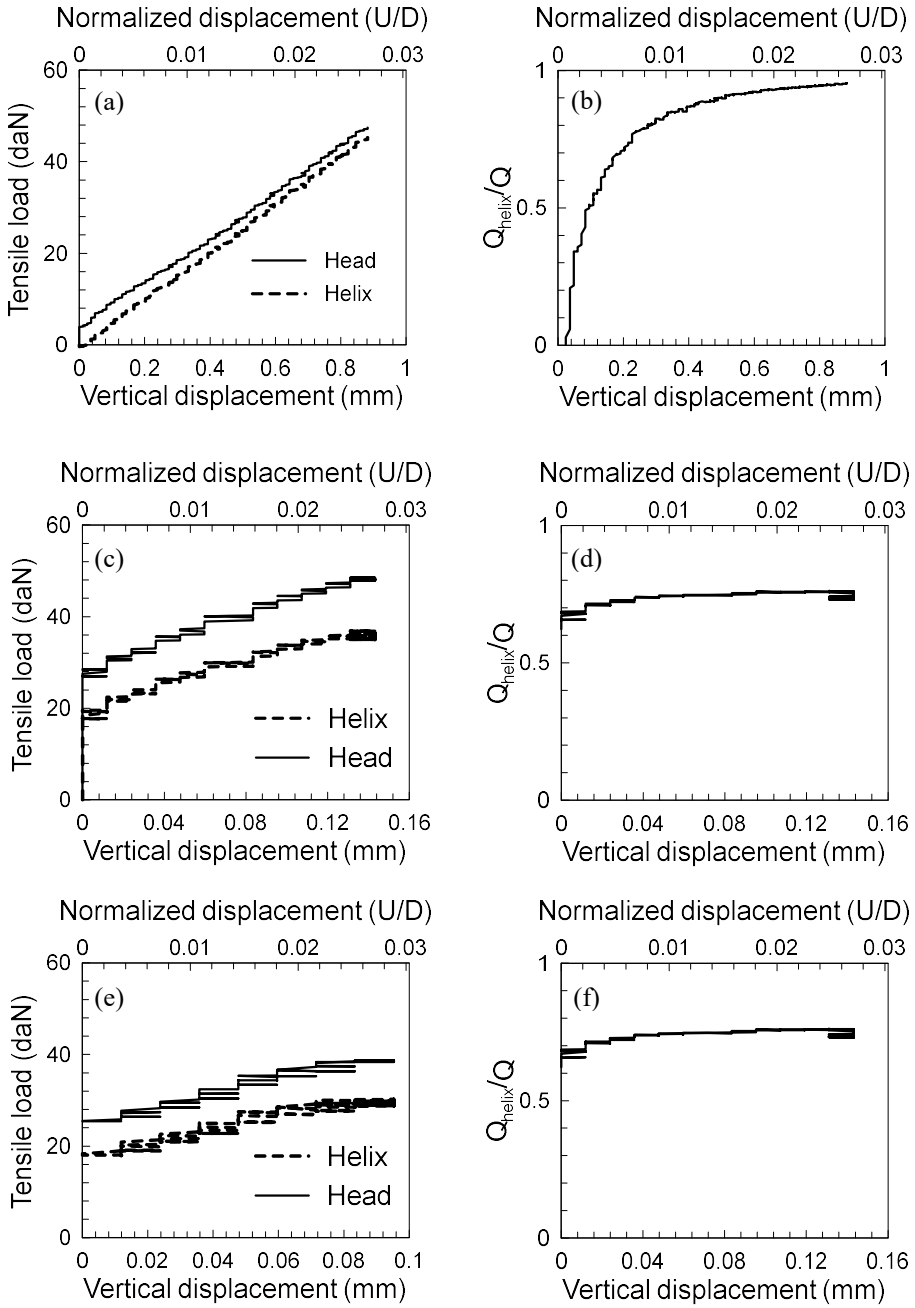

Figure 138. Load-displacement response 10FH model tested in container n. 10: (a) and (b) test 10FH-1; (c) and (d) test 10FH-2; (e) and (f) test 10FH-3.

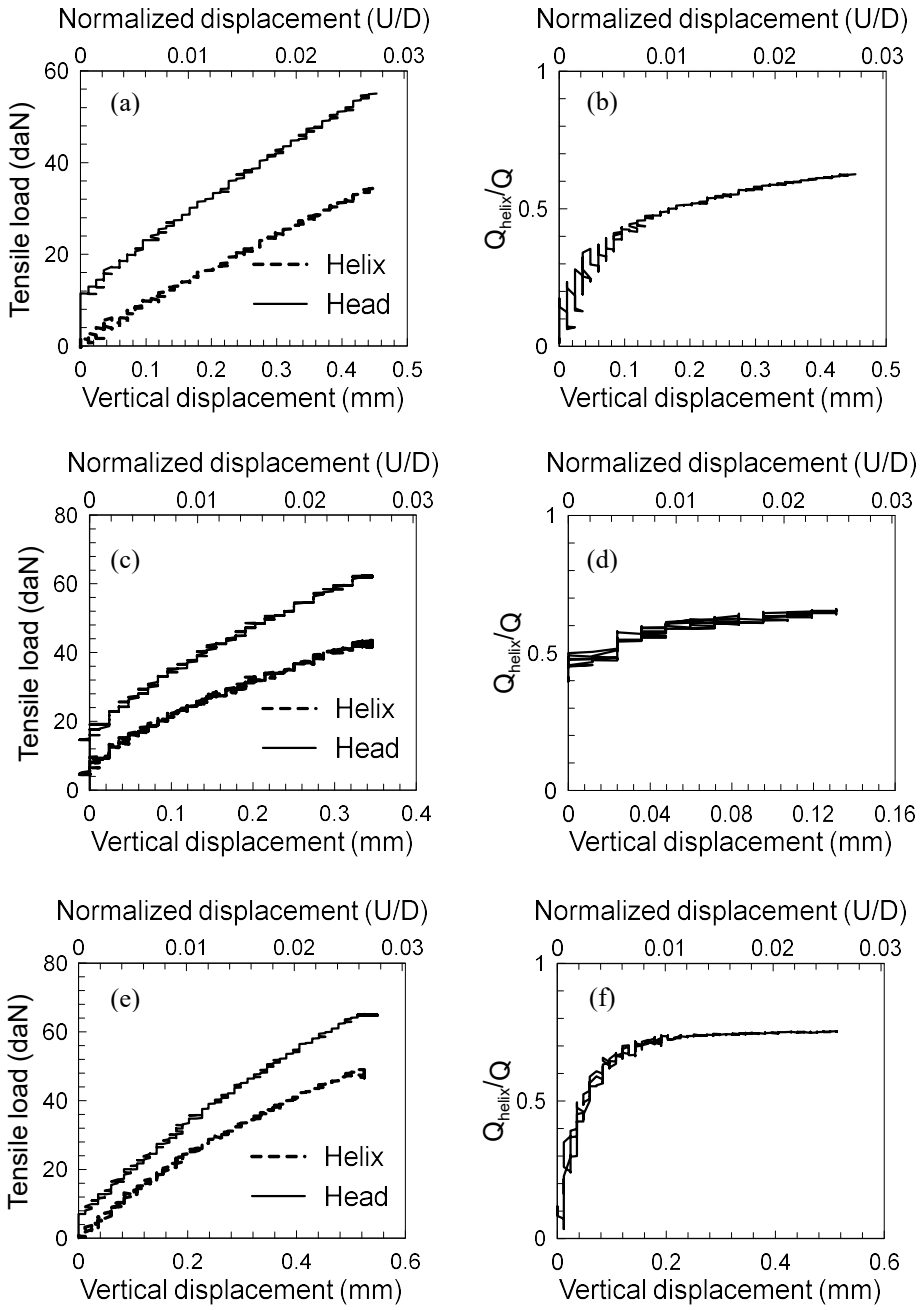

Figure 139. Load-displacement response 10FH model tested in container n. 10: (a) and (b) test 10FH-4; (c) and (d) test 10FH-6; (e) and (f) test 10FH-7.

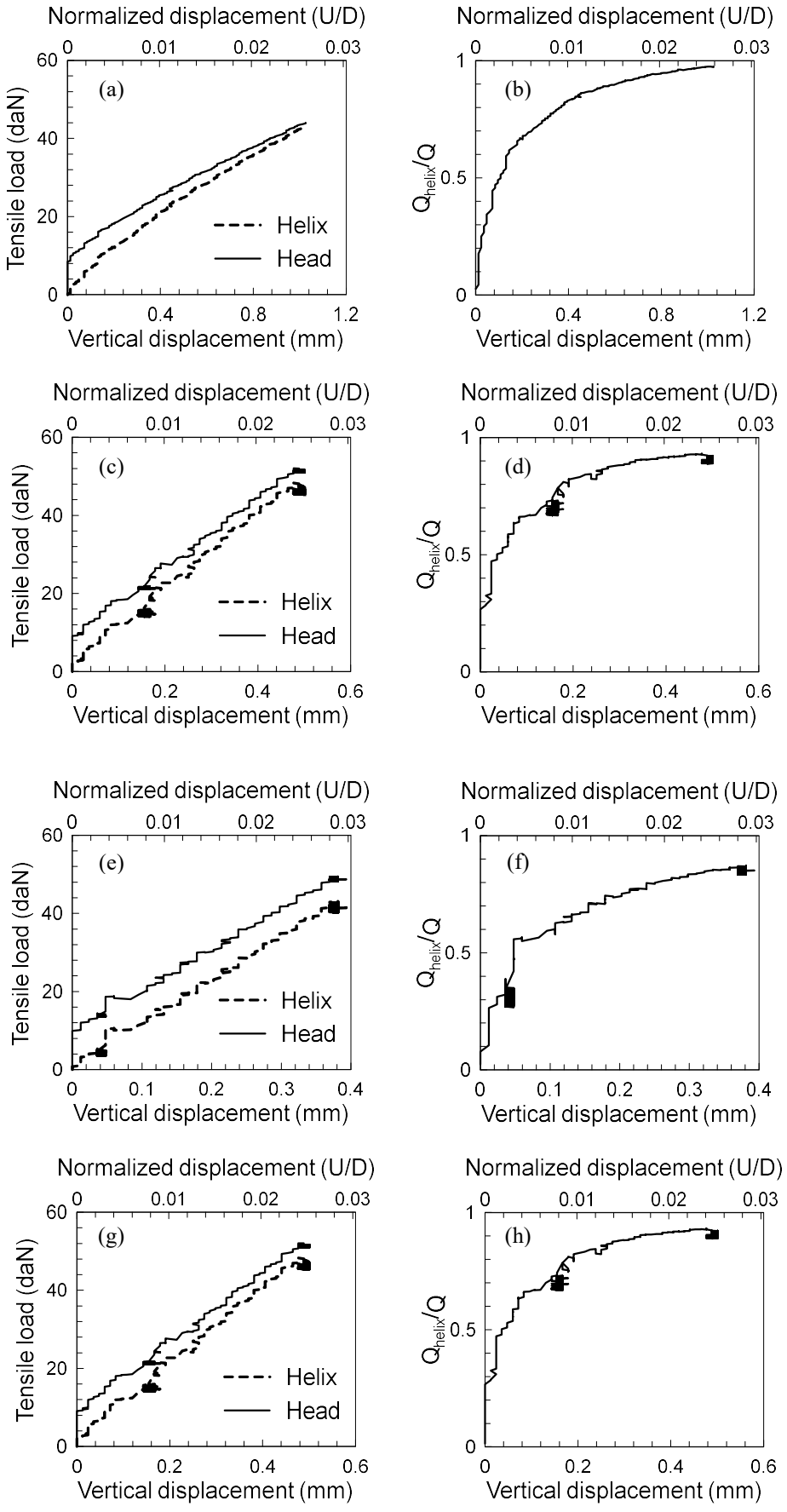

Figure 140. Load-displacement response 10FH model tested in container n. 13: (a) and (b) test 10FH-1; (c) and (d) test 10FH-2; (e) and (f) test 10FH-3; (g) and (h) test 10FH-4

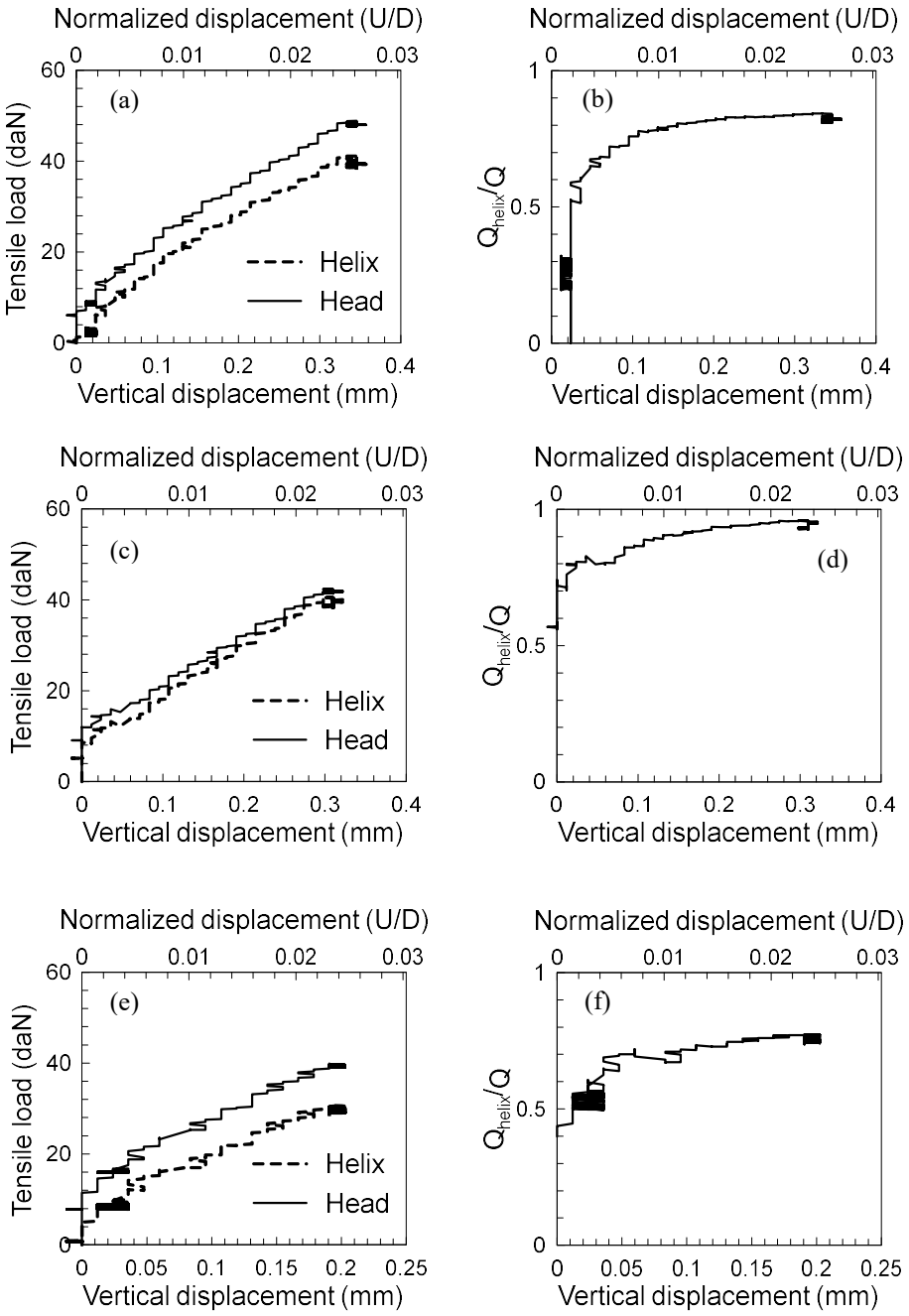

Figure 141. Load-displacement response 10FH model tested in container n. 14: (a) and (b) test 10FH-1; (c) and (d) test 10FH-2; (e) and (f) test 10FH-3.

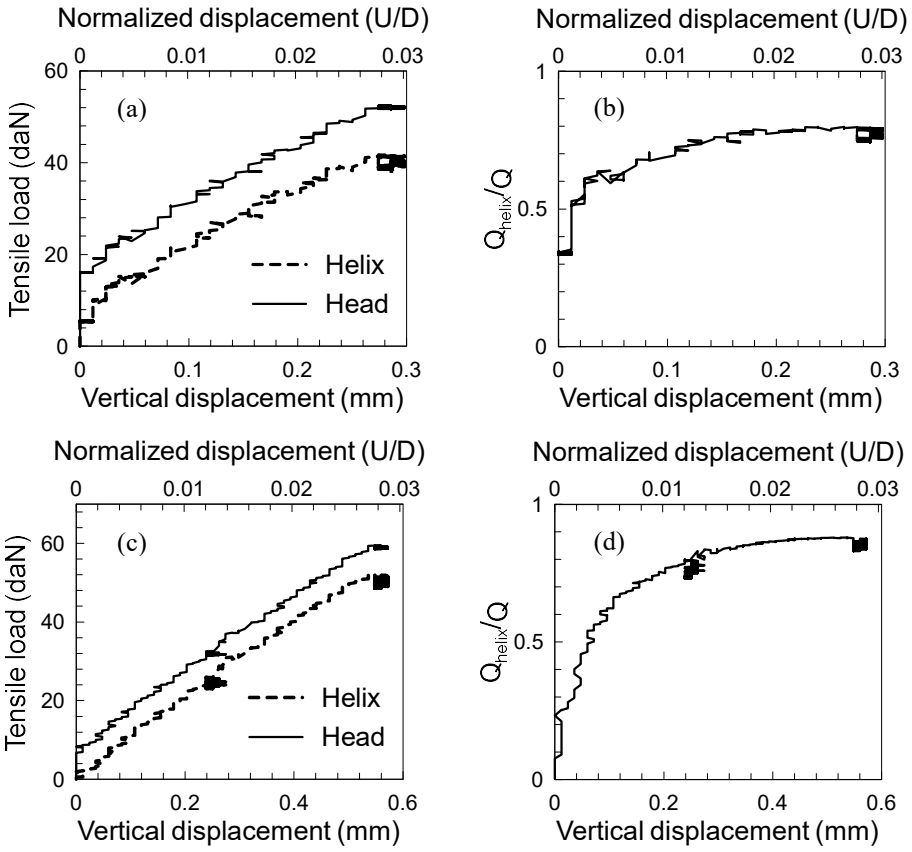

Figure 142. Load-displacement response 10FH model tested in container n. 14: (a) and (b) test 10FH-4; (c) and (d) test 10FH-5.

Appendix N. Results of the cyclic tests on 10FH and 10FHi in model values

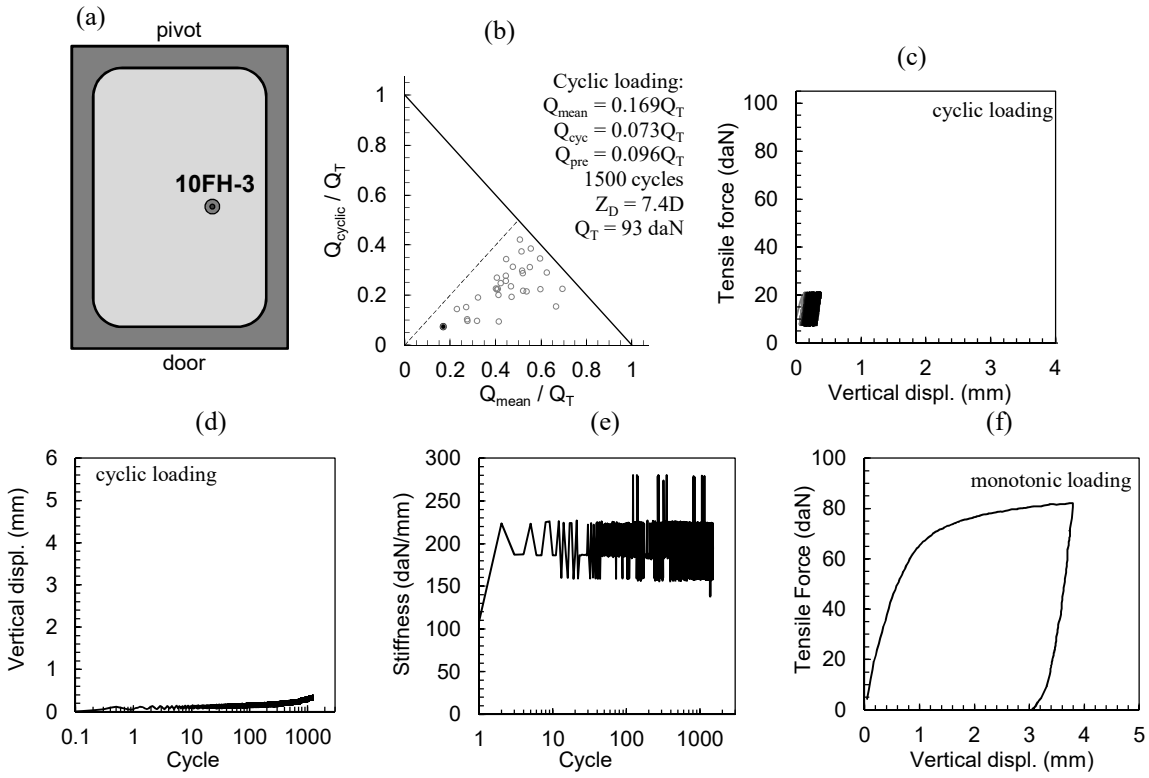

Figure 143. Cyclic loading and pull-out test nº 10FH-3 with 10FH model in the 4th container: (a) anchor location; (b) cyclic loading test on stability diagram; (c), (d) and (e) cyclic loading; (f) post-cyclic (results in model scale).

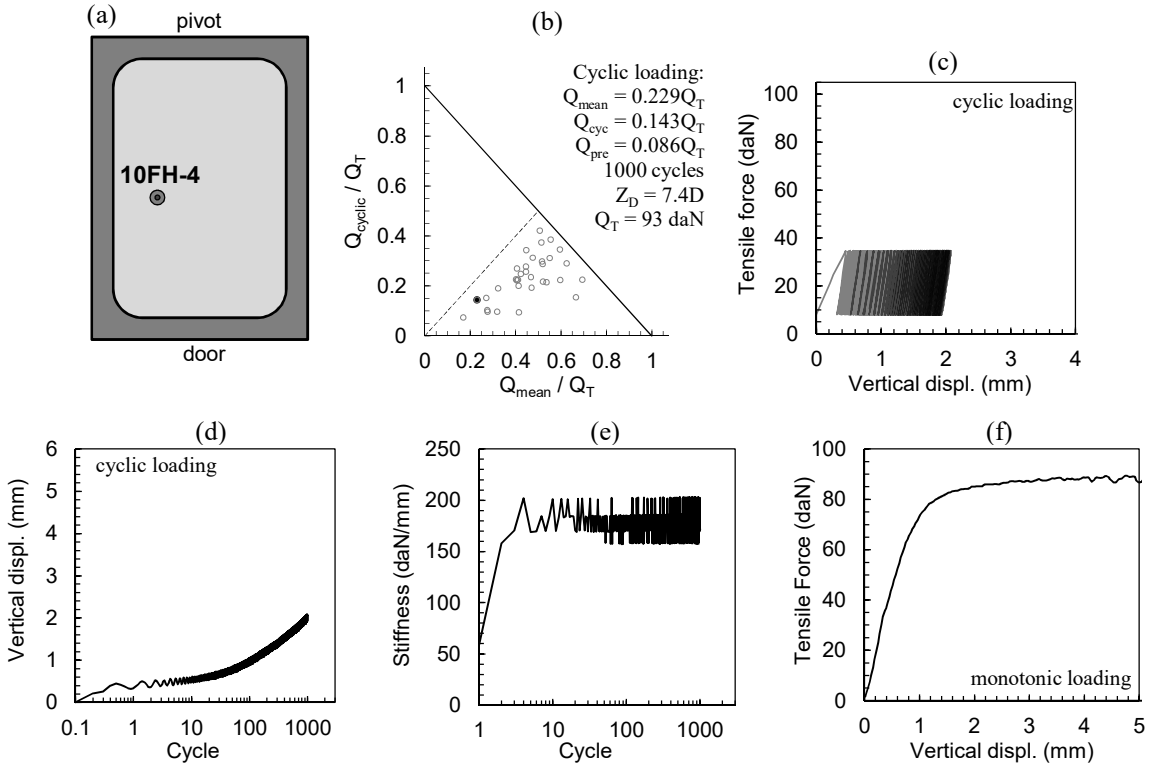

Figure 144. Cyclic loading and pull-out test nº 10FH-4 with 10FH model in the 4th container: (a) anchor location; (b) cyclic loading test on stability diagram; (c), (d) and (e) cyclic loading; (f) post-cyclic (results in model scale).

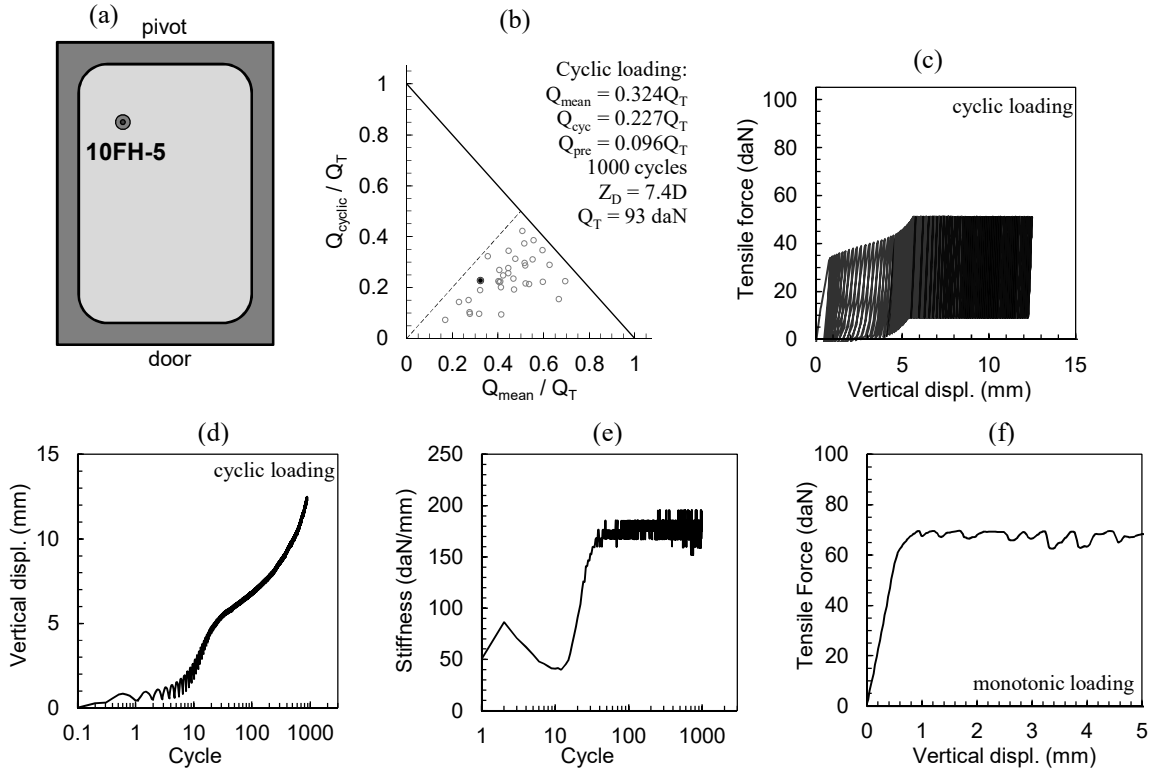

Figure 145. Cyclic loading and pull-out test nº 10FH-3 with 10FH model in the 4th container: (a) anchor location; (b) cyclic loading test on stability diagram; (c), (d) and (e) cyclic loading; (f) post-cyclic (results in model scale).

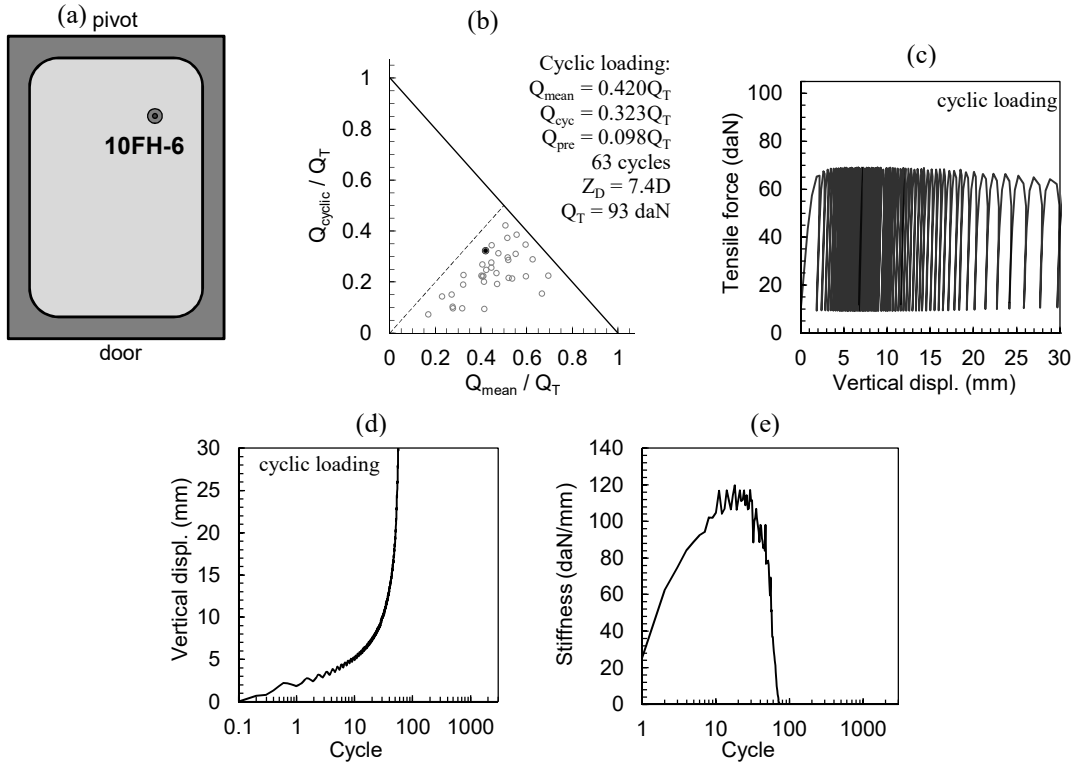

Figure 146. Cyclic loading and pull-out test nº 10FH-6 with 10FH model in the 4th container: (a) anchor location; (b) cyclic loading test on stability diagram; (c), (d) and (e) cyclic loading (results in model scale).

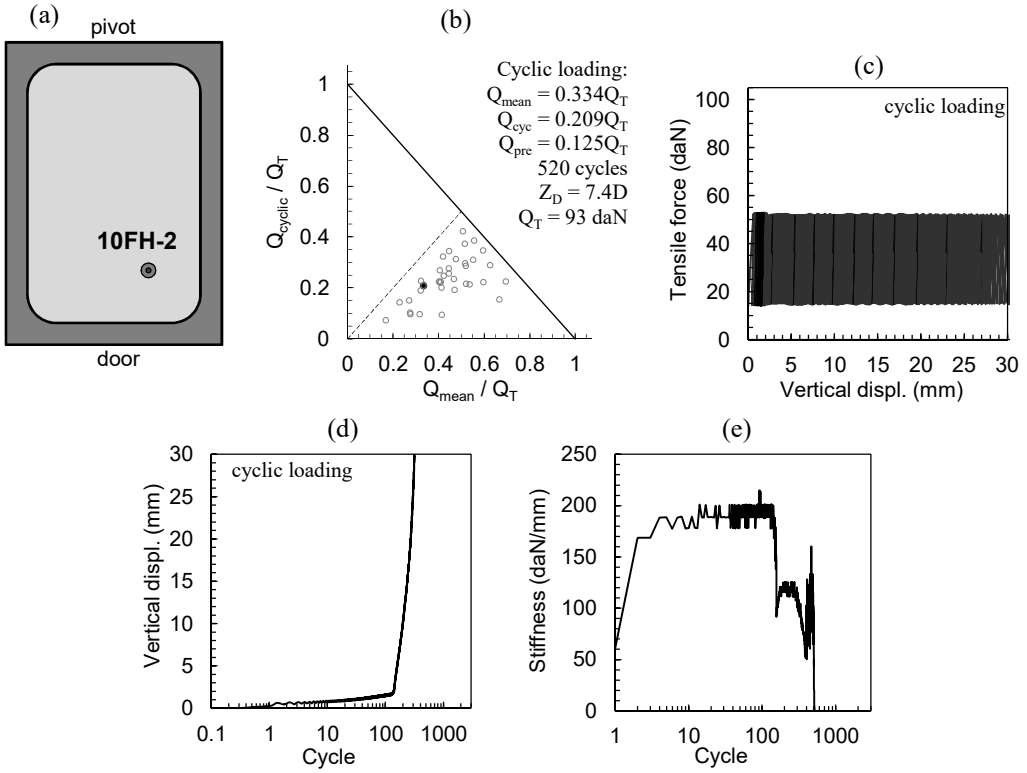

Figure 147. Cyclic loading and pull-out test nº 10FH-2 with 10FH model in the 5th container: (a) anchor location; (b) cyclic loading test on stability diagram; (c), (d) and (e) cyclic loading (results in model scale).

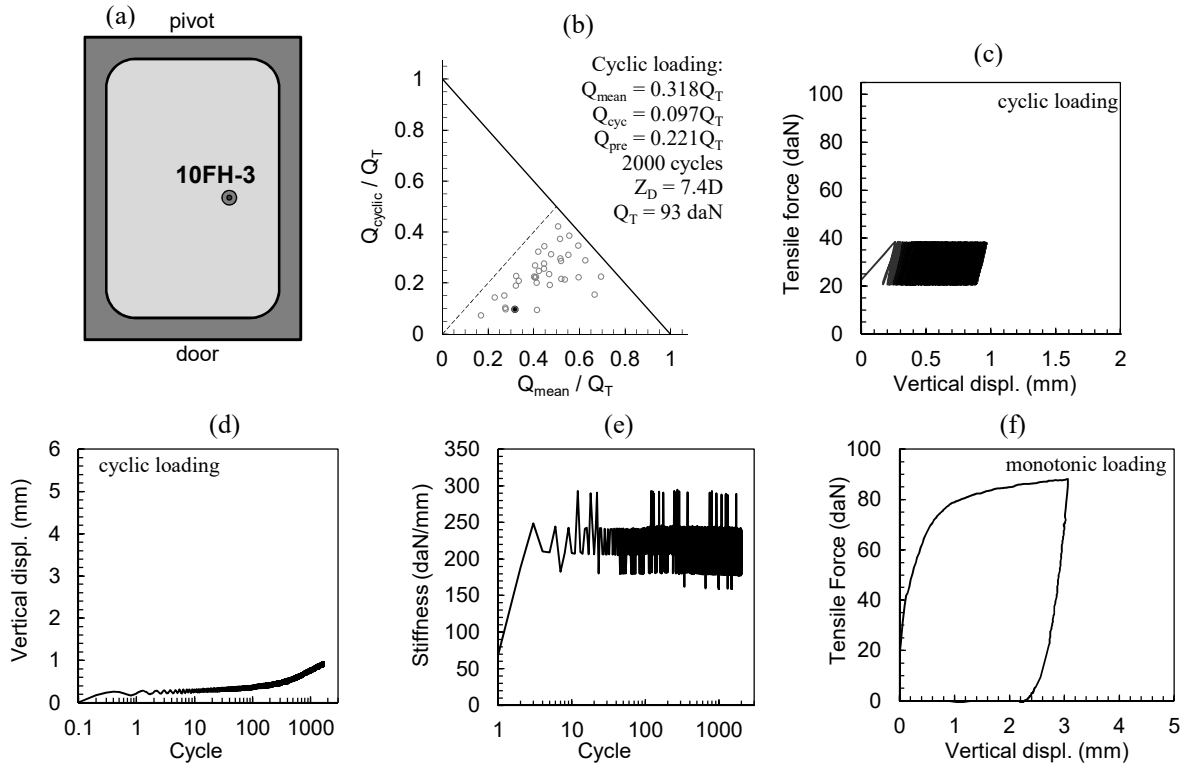

Figure 148. Cyclic loading and pull-out test nº 10FH-3 with 10FH model in the 5th container: (a) anchor location; (b) cyclic loading test on stability diagram; (c), (d) and (e) cyclic loading; (f) post-cyclic (results in model scale).

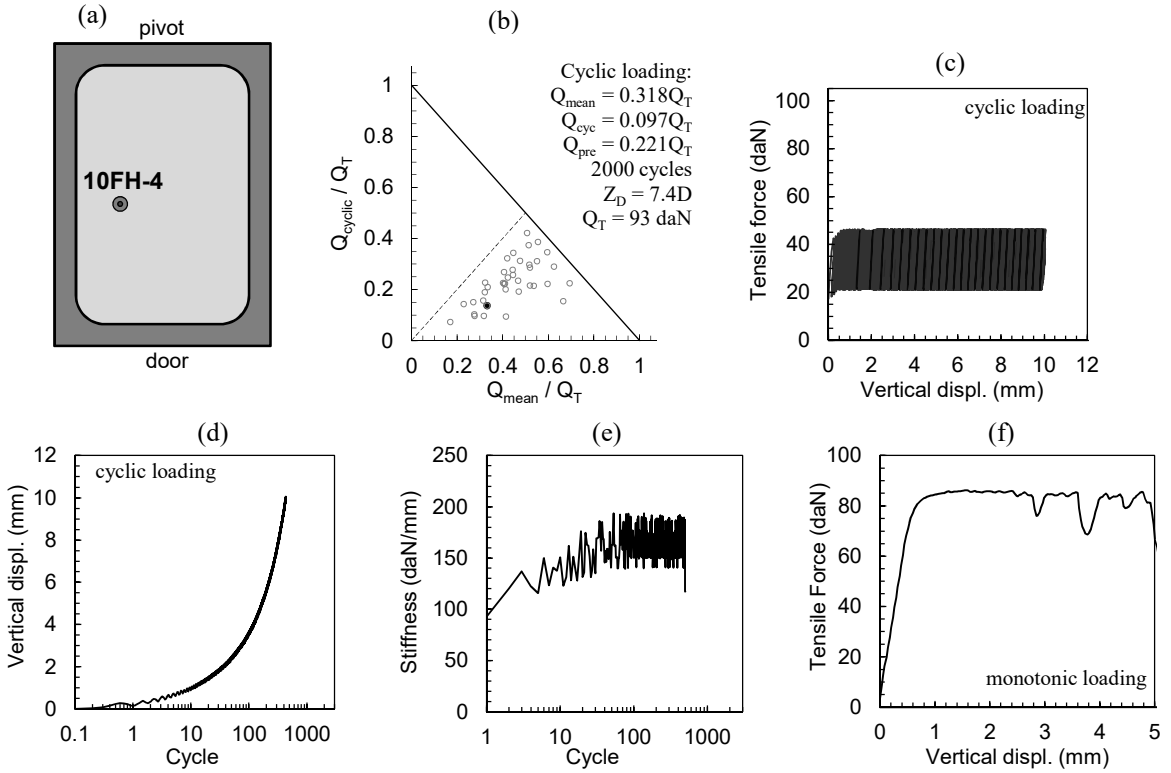

Figure 149. Cyclic loading and pull-out test nº 10FH-4 with 10FH model in the 5th container: (a) anchor location; (b) cyclic loading test on stability diagram; (c), (d) and (e) cyclic loading; (f) post-cyclic (results in model scale).

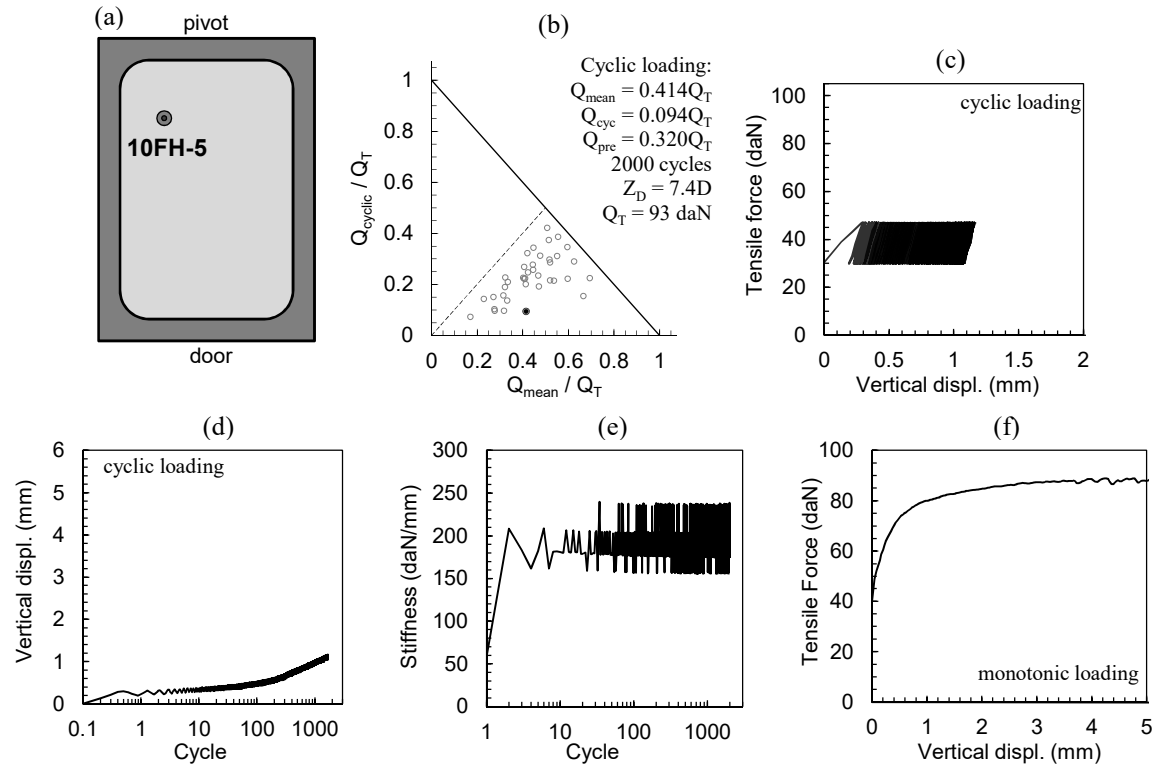

Figure 150. Cyclic loading and pull-out test nº 10FH-5 with 10FH model in the 5th container: (a) anchor location; (b) cyclic loading test on stability diagram; (c), (d) and (e) cyclic loading; (f) post-cyclic (results in model scale).

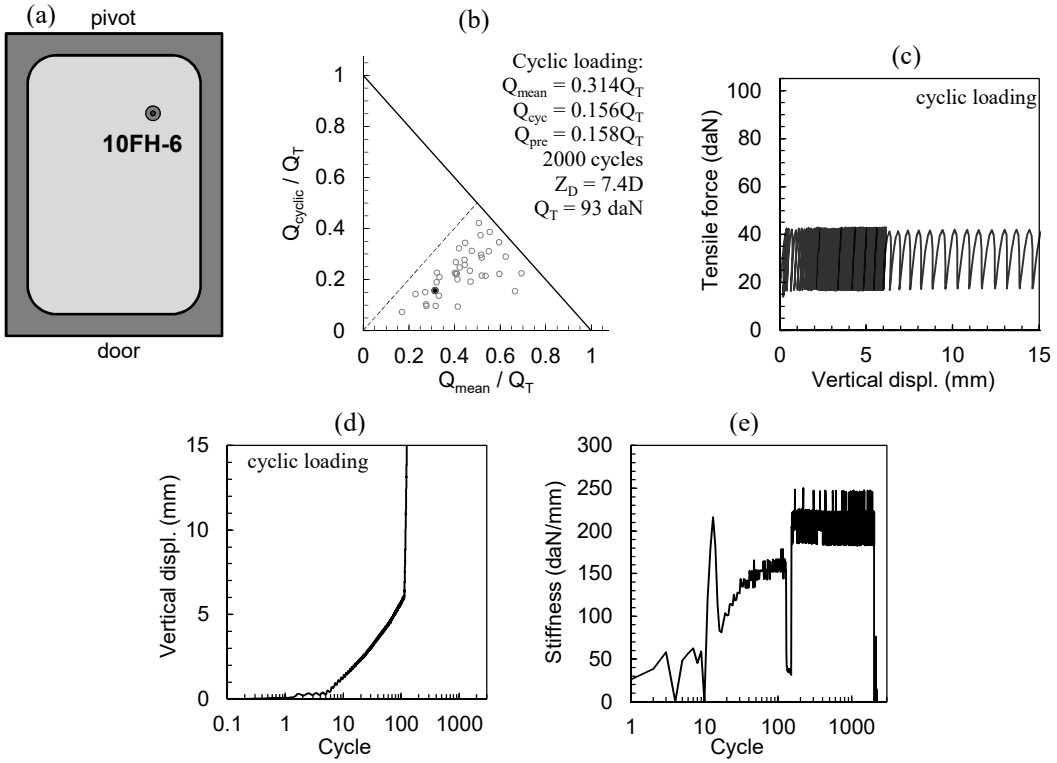

Figure 151. Cyclic loading and pull-out test nº 10FH-6 with 10FH model in the 5th container: (a) anchor location; (b) cyclic loading test on stability diagram; (c), (d) and (e) cyclic loading (results in model scale).

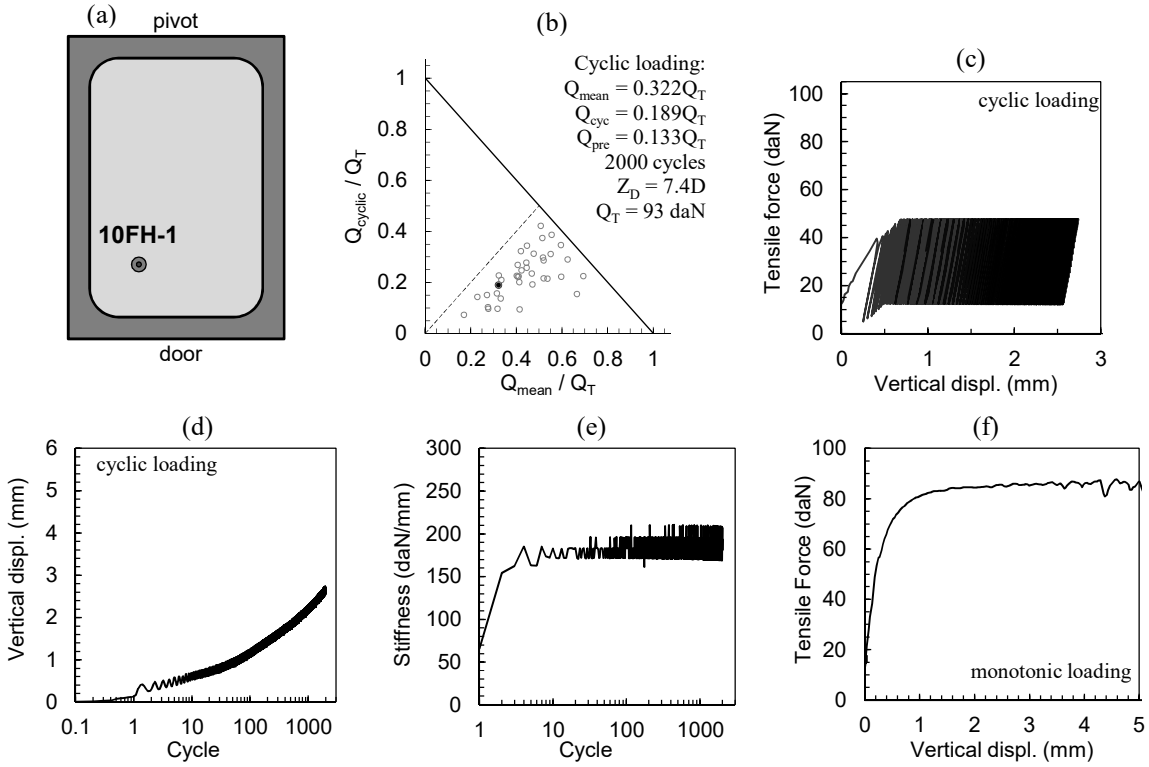

Figure 152. Cyclic loading and pull-out test nº 10FH-1 with 10FH model in the 6th container: (a) anchor location; (b) cyclic loading test on stability diagram; (c), (d) and (e) cyclic loading; (f) post-cyclic (results in model scale).

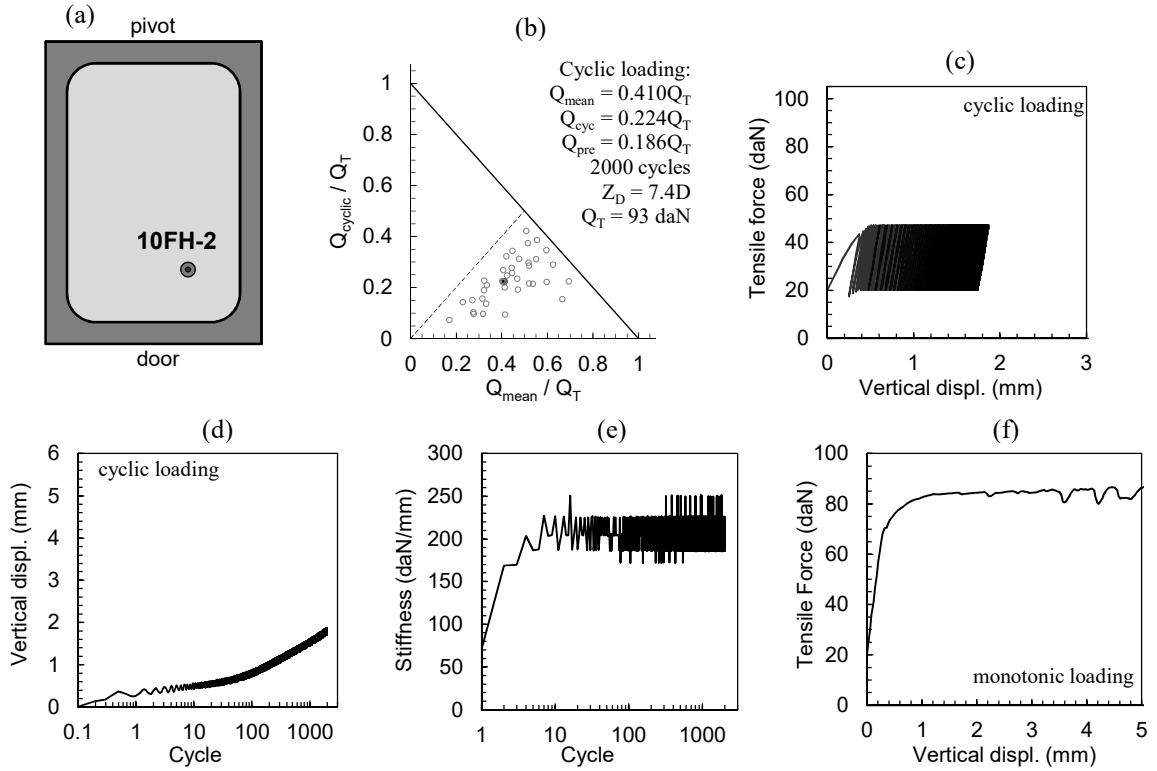

Figure 153. Cyclic loading and pull-out test nº 10FH-2 with 10FH model in the 6th container: (a) anchor location; (b) cyclic loading test on stability diagram; (c), (d) and (e) cyclic loading; (f) post-cyclic (results in model scale).

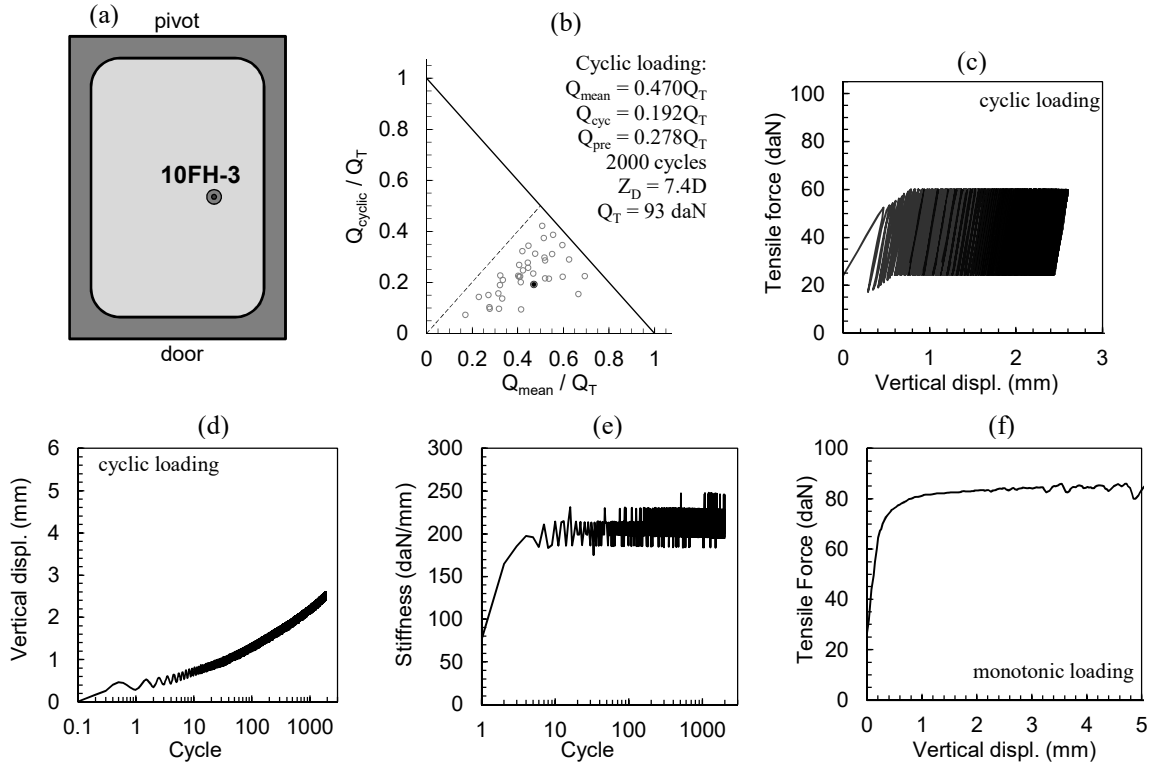

Figure 154. Cyclic loading and pull-out test nº 10FH-3 with 10FH model in the 6th container: (a) anchor location; (b) cyclic loading test on stability diagram; (c), (d) and (e) cyclic loading; (f) post-cyclic (results in model scale).

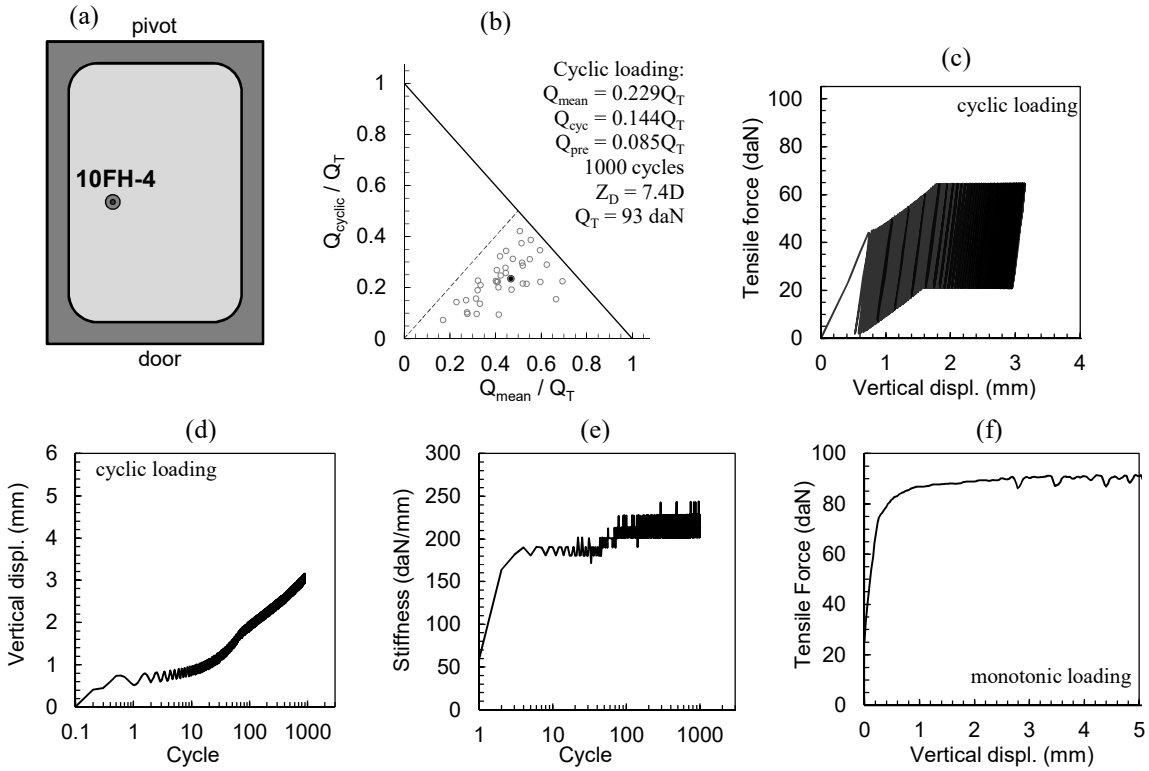

Figure 155. Cyclic loading and pull-out test nº 10FH-4 with 10FH model in the 6th container: (a) anchor location; (b) cyclic loading test on stability diagram; (c), (d) and (e) cyclic loading; (f) post-cyclic (results in model scale).

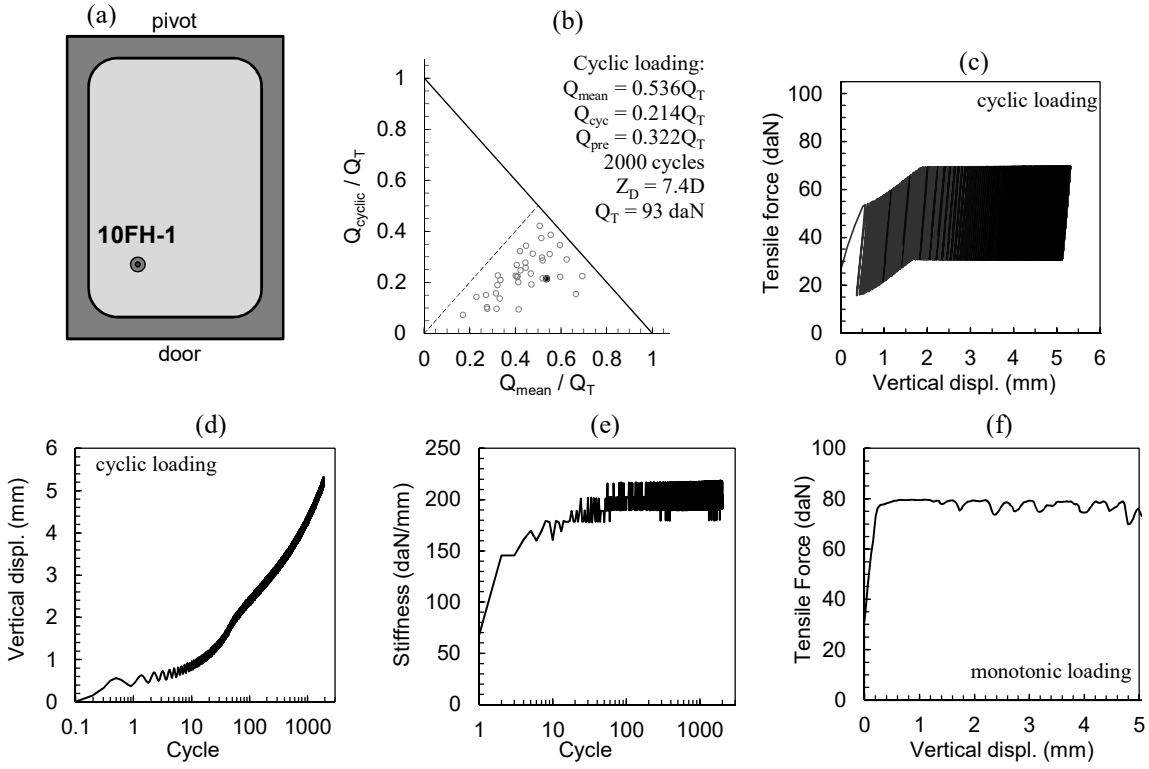

Figure 156. Cyclic loading and pull-out test nº 10FH-1 with 10FH model in the 7th container: (a) anchor location; (b) cyclic loading test on stability diagram; (c), (d) and (e) cyclic loading; (f) post-cyclic (results in model scale).

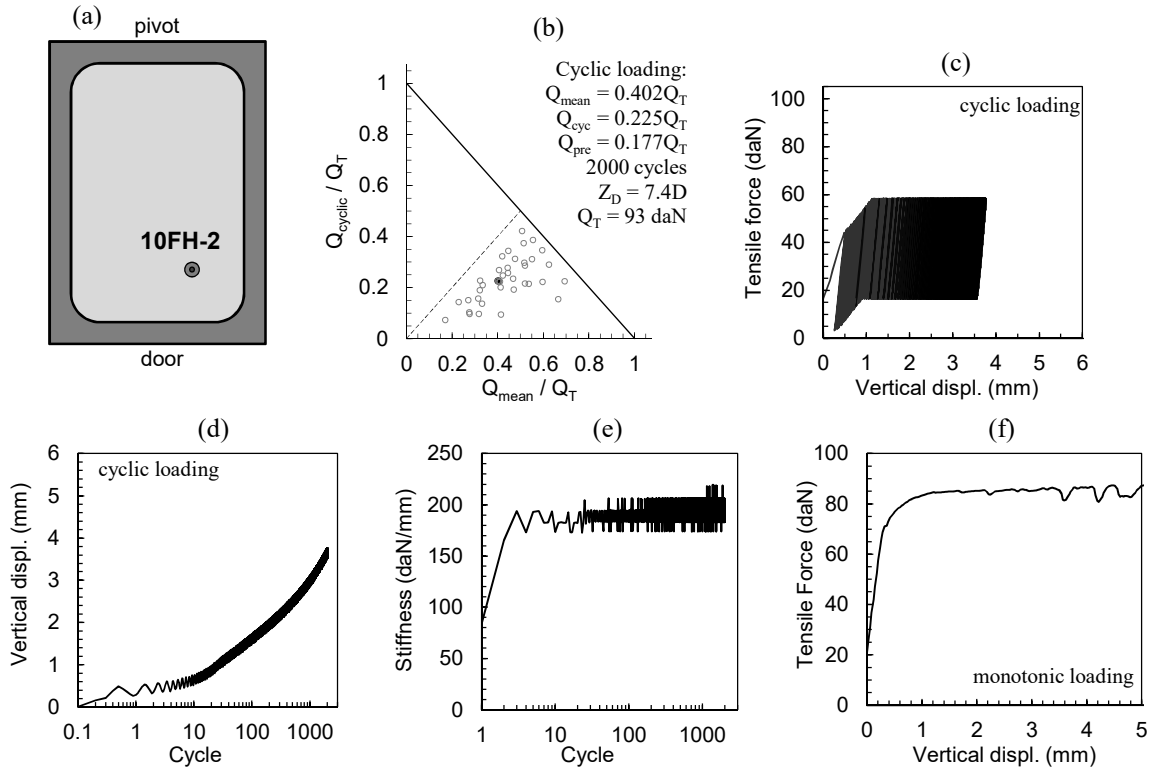

Figure 157. Cyclic loading and pull-out test nº 10FH-2 with 10FH model in the 7th container: (a) anchor location; (b) cyclic loading test on stability diagram; (c), (d) and (e) cyclic loading; (f) post-cyclic (results in model scale).

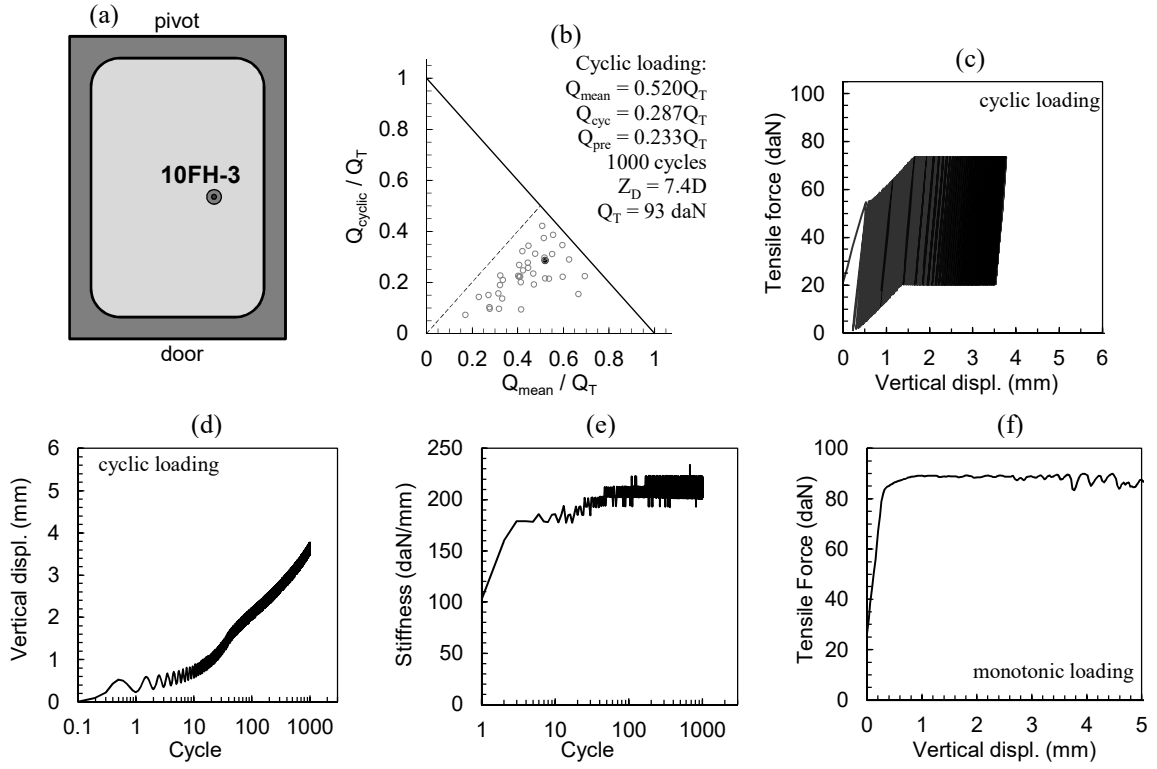

Figure 158. Cyclic loading and pull-out test nº 10FH-3 with 10FH model in the 7th container: (a) anchor location; (b) cyclic loading test on stability diagram; (c), (d) and (e) cyclic loading; (f) post-cyclic (results in model scale).

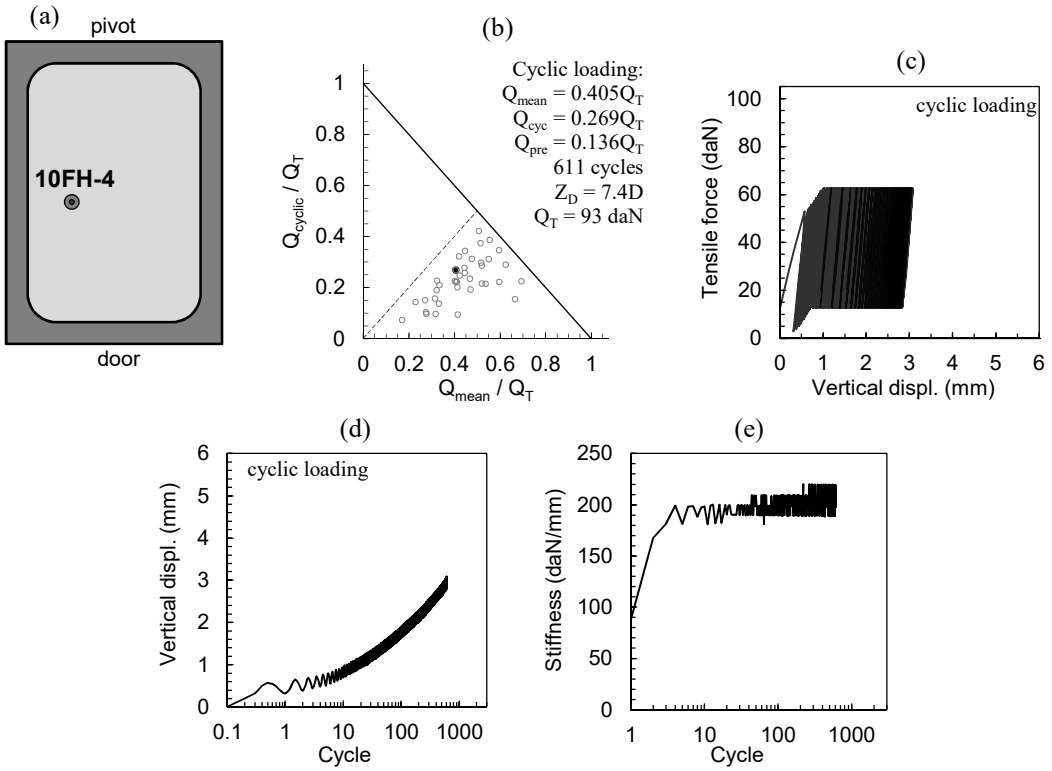

Figure 159. Cyclic loading and pull-out test nº 10FH-4 with 10FH model in the 7th container: (a) anchor location; (b) cyclic loading test on stability diagram; (c), (d) and (e) cyclic loading (results in model scale).

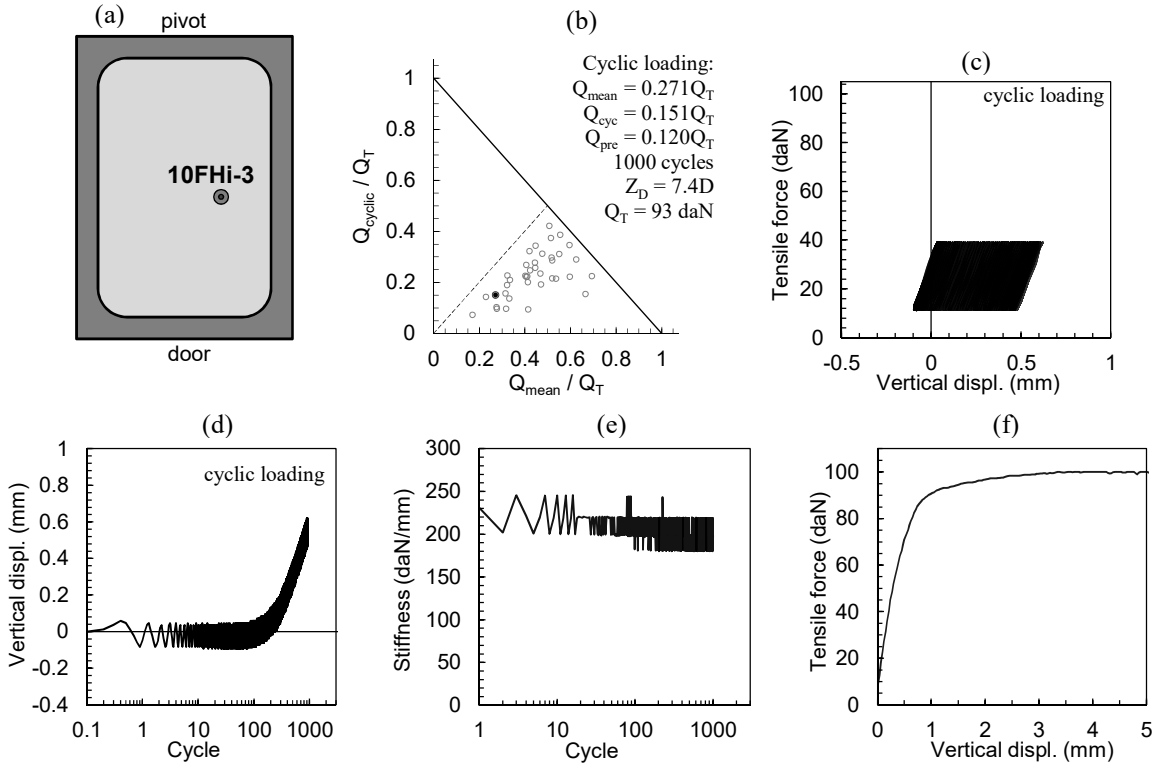

Figure 160. Cyclic loading and pull-out test nº 10FHi-3 with 10FHi model in the 9th container: (a) anchor location; (b) cyclic loading test on stability diagram; (c), (d) and (e) cyclic loading; (f) post-cyclic (results in model scale).

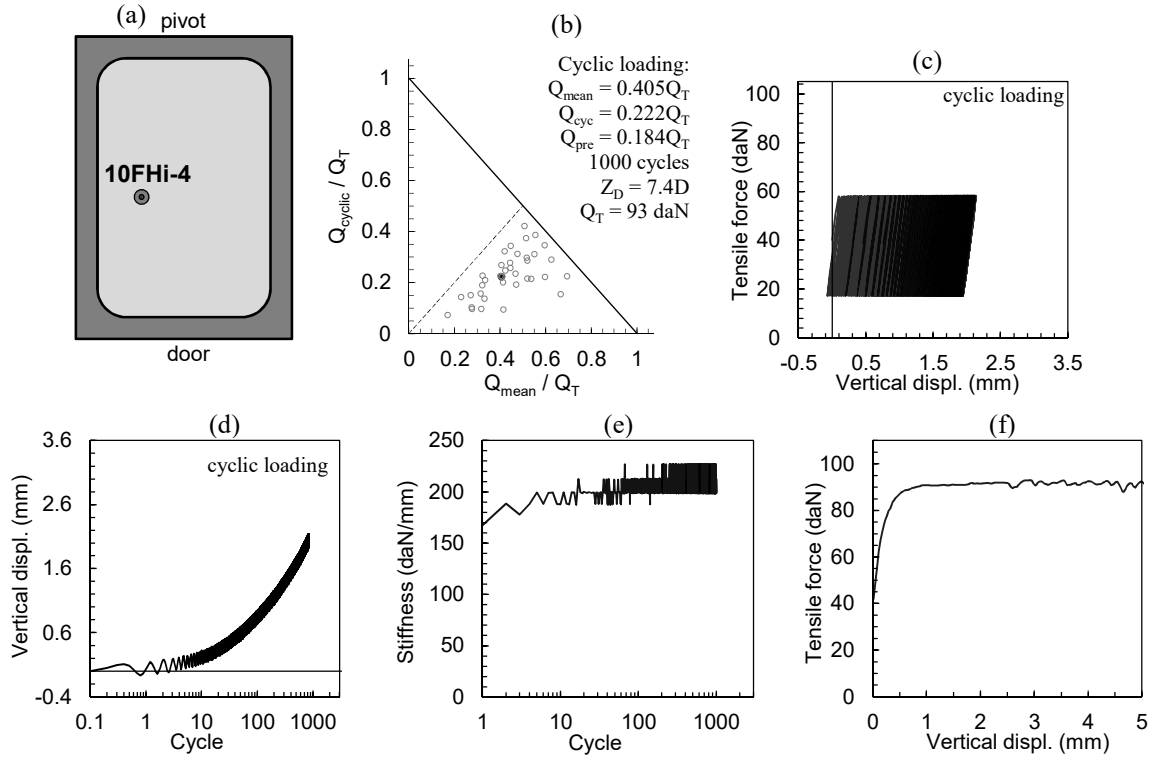

Figure 161. Cyclic loading and pull-out test nº 10FHi-4 with 10FHi model in the 9th container: (a) anchor location; (b) cyclic loading test on stability diagram; (c), (d) and (e) cyclic loading; (f) post-cyclic (results in model scale).

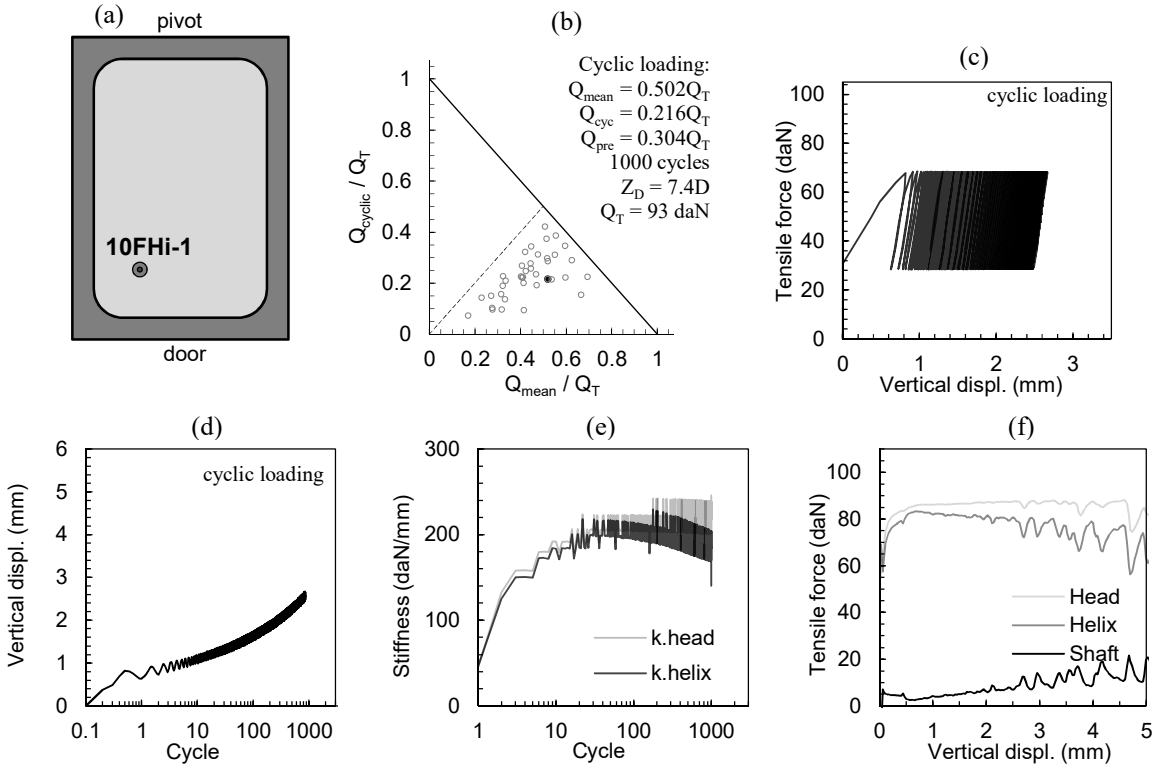

Figure 162. Cyclic loading and pull-out test nº 10FHi-1 with 10FHi model in the 10th container: (a) anchor location; (b) cyclic loading test on stability diagram; (c), (d) and (e) cyclic loading; (f) post-cyclic (results in model scale).

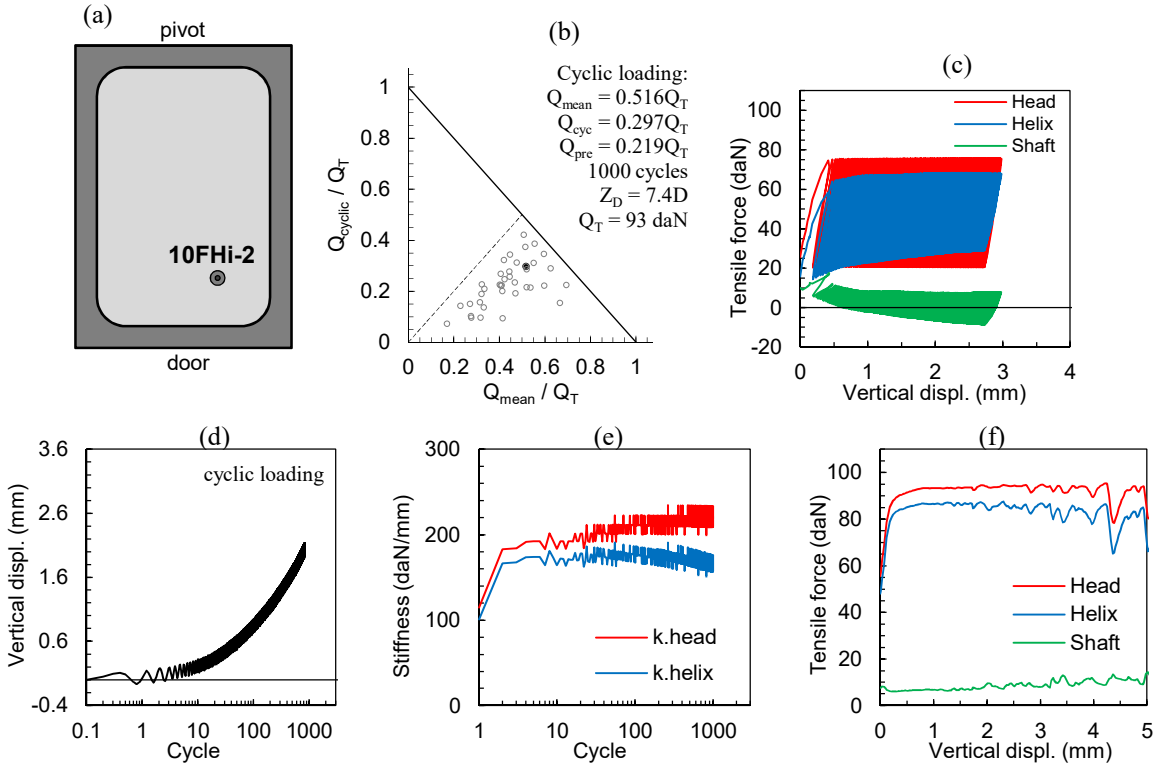

Figure 163. Cyclic loading and pull-out test nº 10FHi-2 with 10FHi model in the 10th container: (a) anchor location; (b) cyclic loading test on stability diagram; (c), (d) and (e) cyclic loading; (f) post-cyclic (results in model scale).

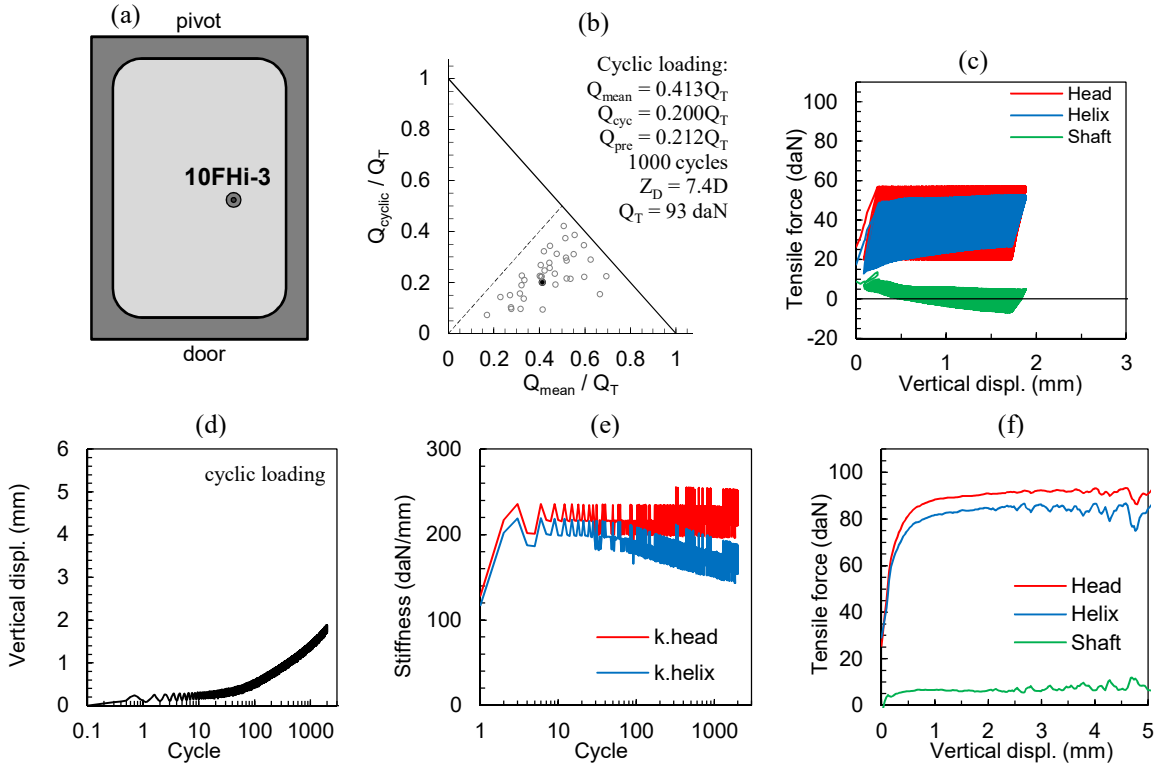

Figure 164. Cyclic loading and pull-out test nº 10FHi-3 with 10FHi model in the 10th container: (a) anchor location; (b) cyclic loading test on stability diagram; (c), (d) and (e) cyclic loading; (f) post-cyclic (results in model scale).

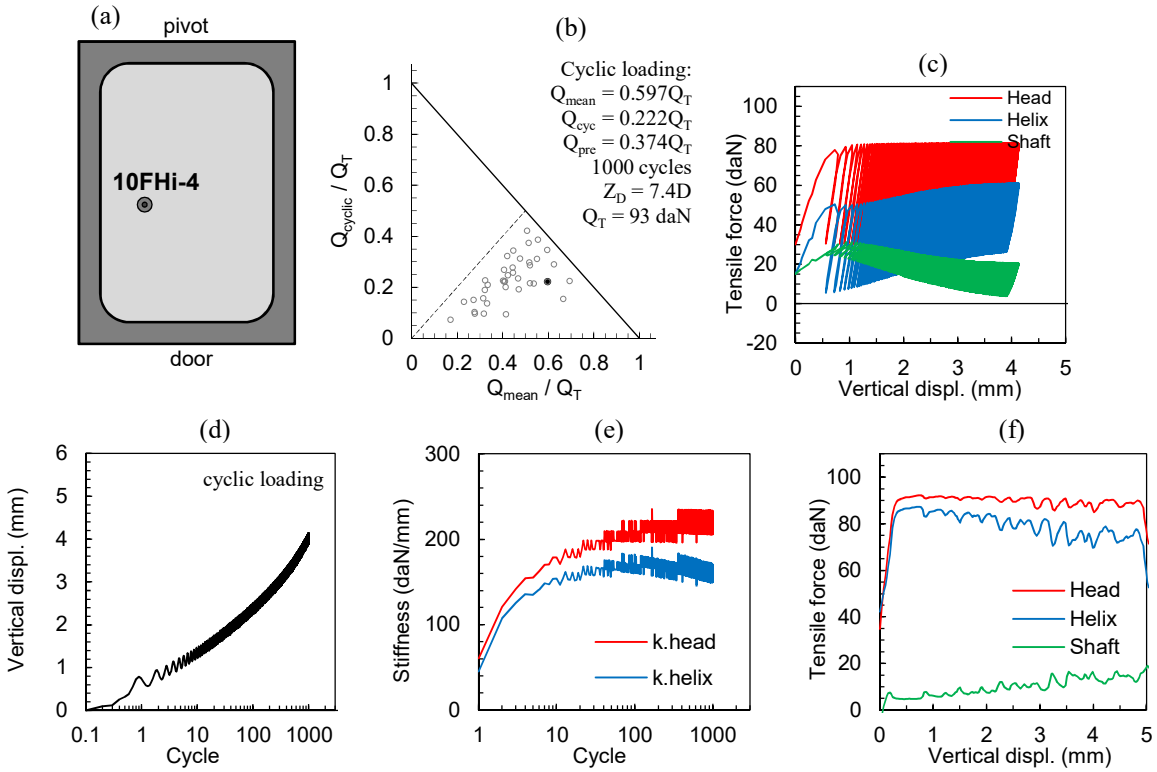

Figure 165. Cyclic loading and pull-out test nº 10FHi-4 with 10FHi model in the 10th container: (a) anchor location; (b) cyclic loading test on stability diagram; (c), (d) and (e) cyclic loading; (f) post-cyclic (results in model scale).

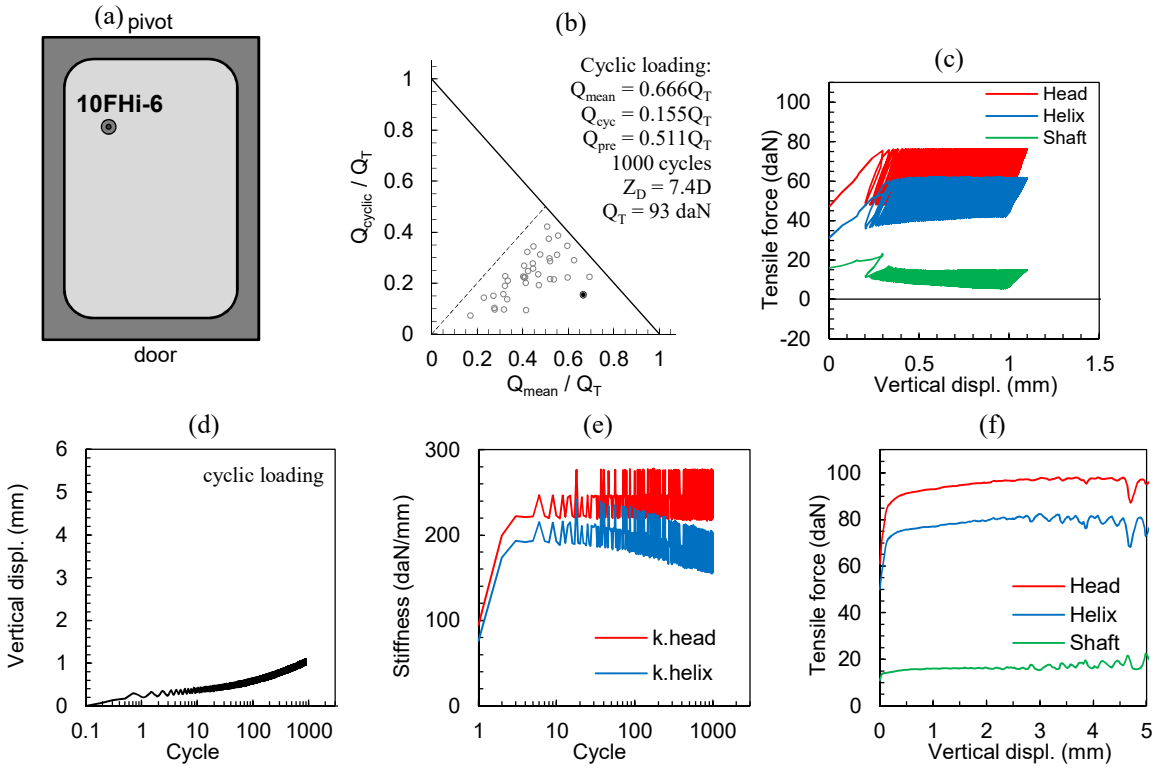

Figure 166. Cyclic loading and pull-out test nº 10FHi-6 with 10FHi model in the 10th container: (a) anchor location; (b) cyclic loading test on stability diagram; (c), (d) and (e) cyclic loading; (f) post-cyclic (results in model scale).

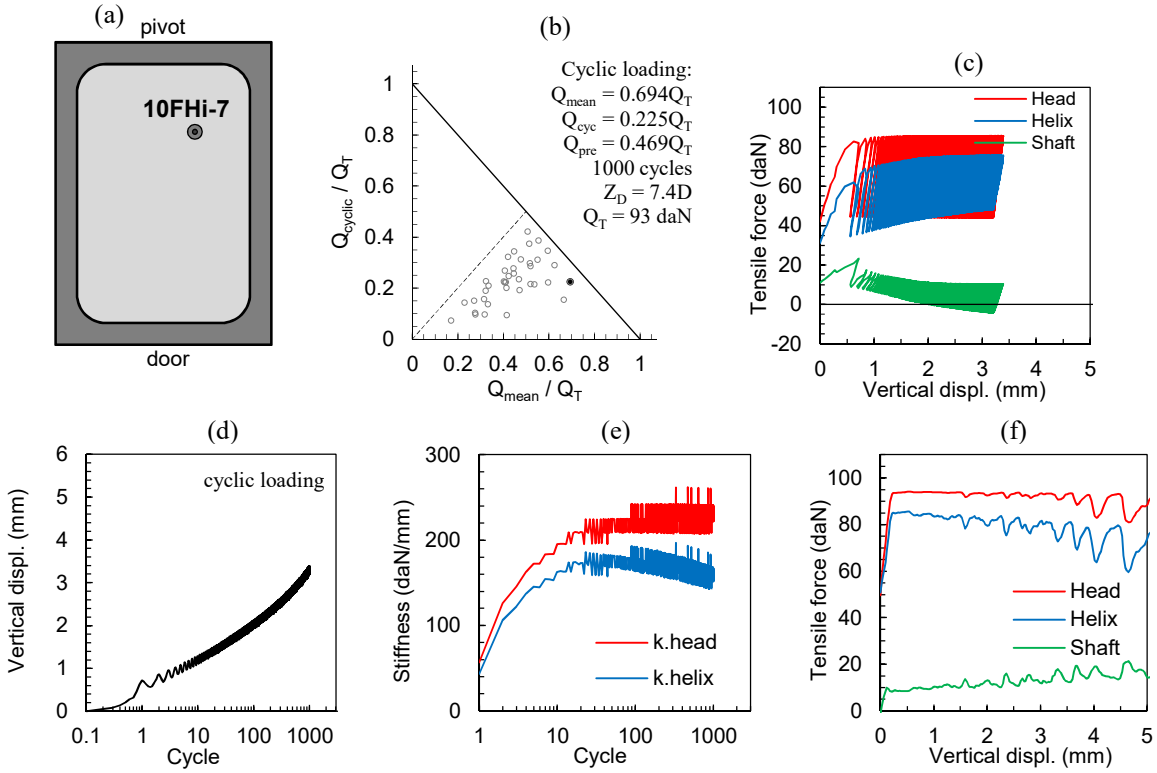

Figure 167. Cyclic loading and pull-out test nº 10FHi-7 with 10FHi model in the 10th container: (a) anchor location; (b) cyclic loading test on stability diagram; (c), (d) and (e) cyclic loading; (f) post-cyclic (results in model scale).

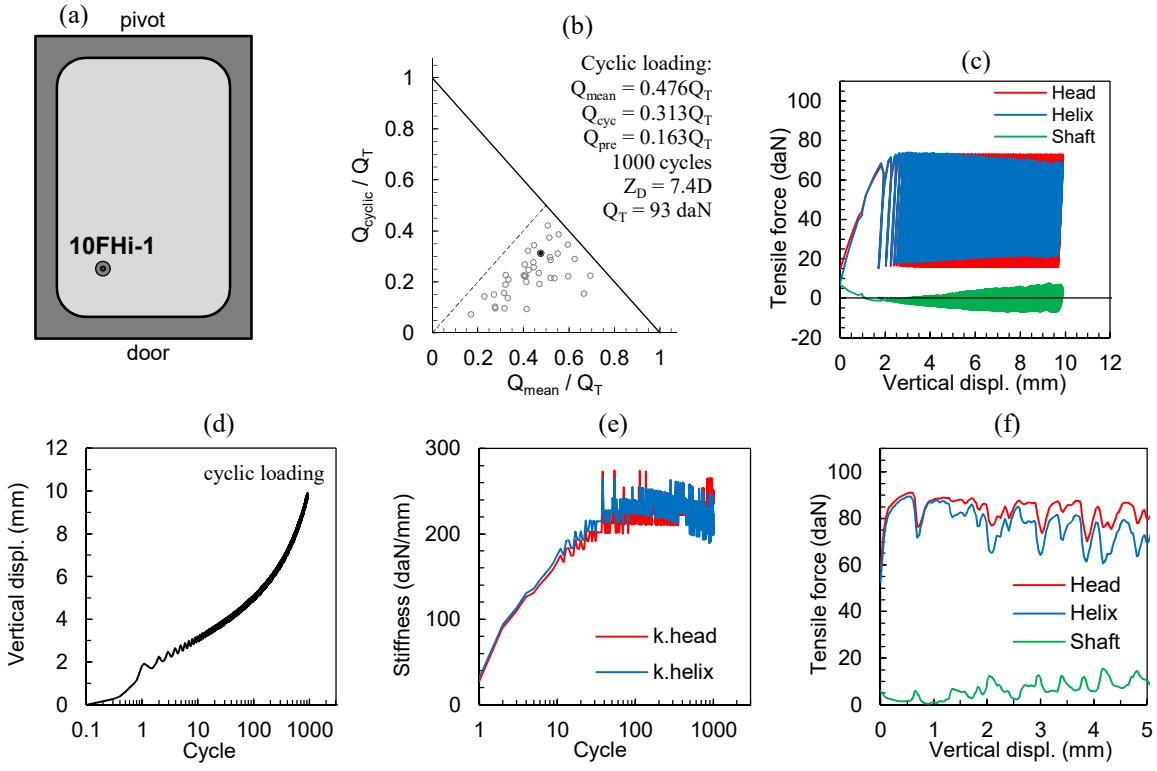

Figure 168. Cyclic loading and pull-out test nº 10FHi-1 with 10FHi model in the 13th container: (a) anchor location; (b) cyclic loading test on stability diagram; (c), (d) and (e) cyclic loading; (f) post-cyclic (results in model scale).

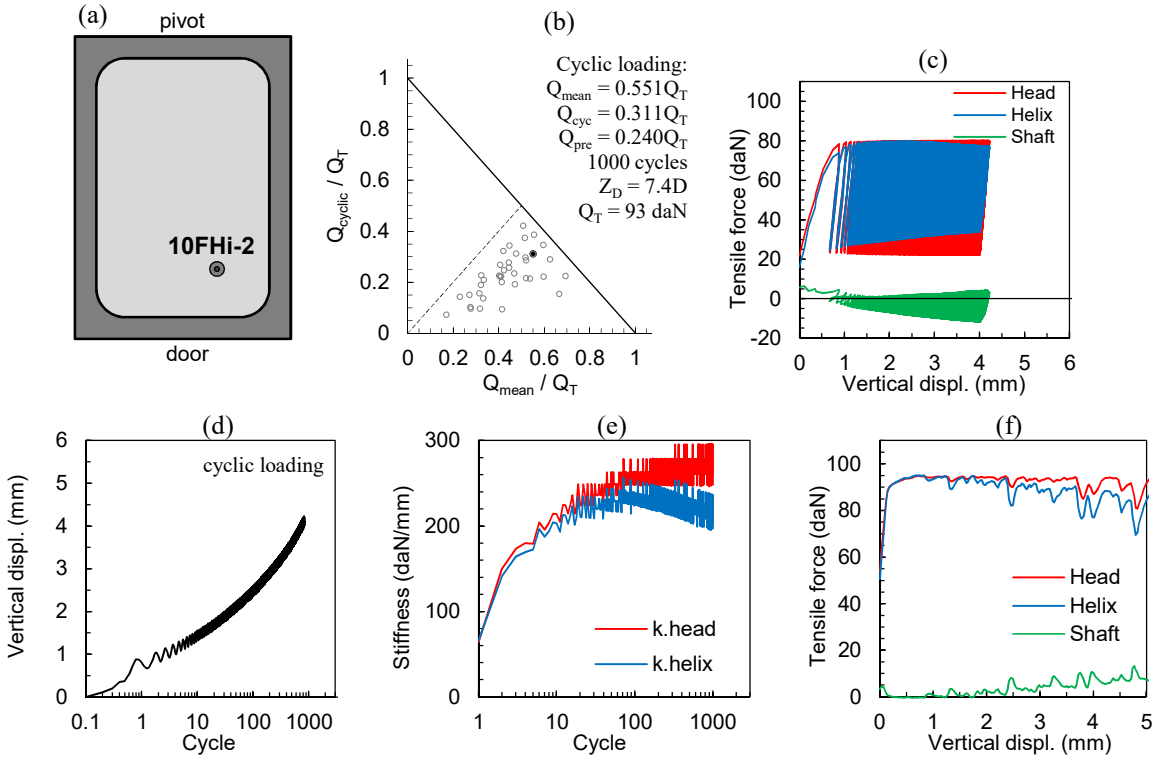

Figure 169. Cyclic loading and pull-out test nº 10FHi-2 with 10FHi model in the 13th container: (a) anchor location; (b) cyclic loading test on stability diagram; (c), (d) and (e) cyclic loading; (f) post-cyclic (results in model scale).

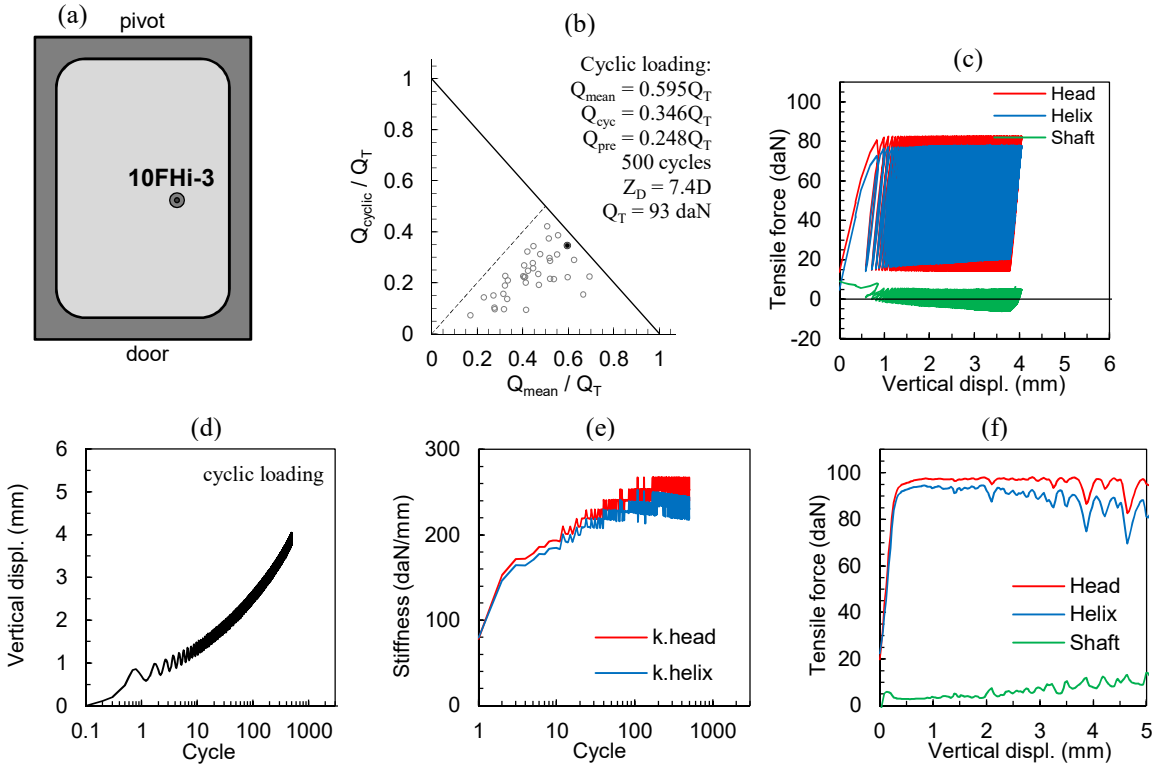

Figure 170. Cyclic loading and pull-out test nº 10FHi-3 with 10FHi model in the 13th container: (a) anchor location; (b) cyclic loading test on stability diagram; (c), (d) and (e) cyclic loading; (f) post-cyclic (results in model scale).

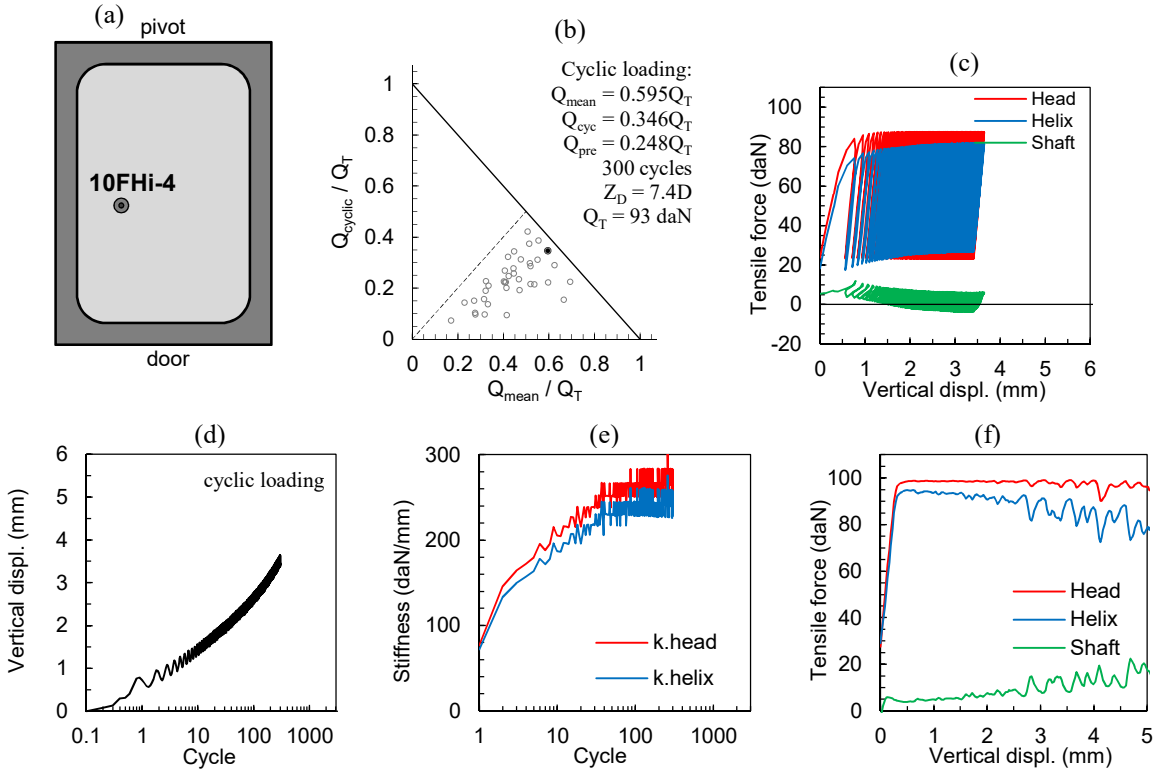

Figure 171. Cyclic loading and pull-out test nº 10FHi-4 with 10FHi model in the 13th container: (a) anchor location; (b) cyclic loading test on stability diagram; (c), (d) and (e) cyclic loading; (f) post-cyclic (results in model scale).

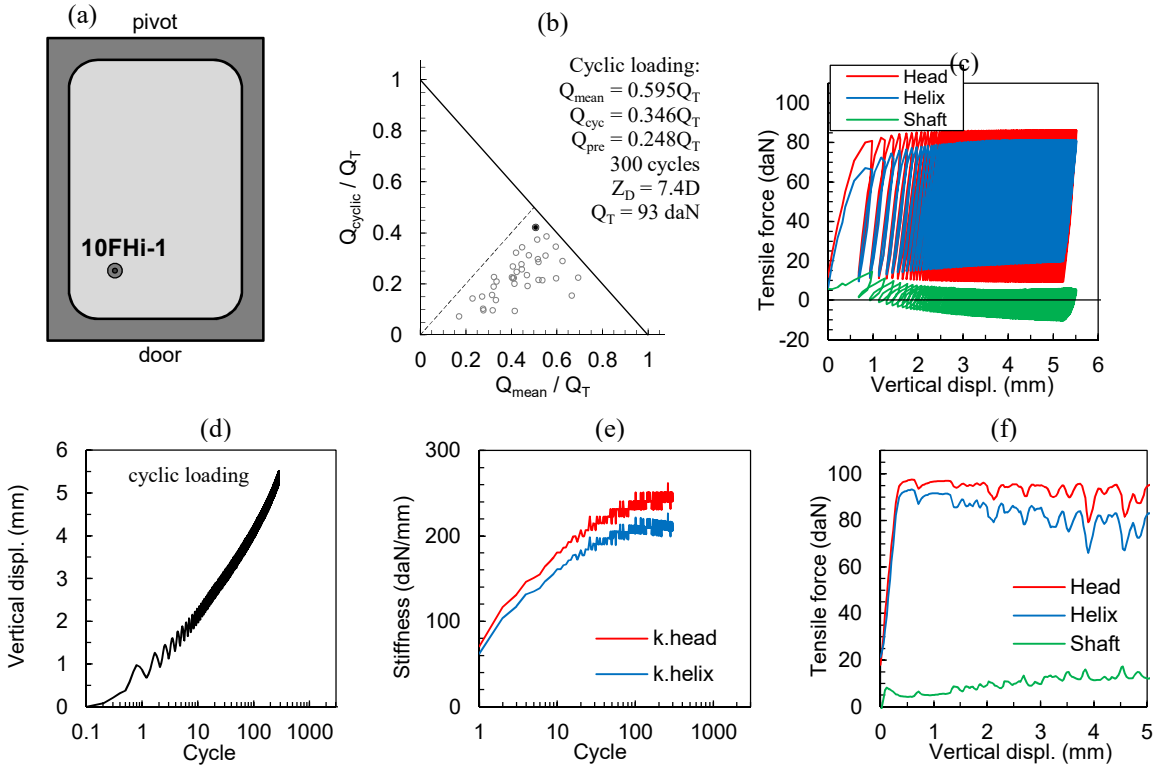

Figure 172. Cyclic loading and pull-out test nº 10FHi-1 with 10FHi model in the 14th container: (a) anchor location; (b) cyclic loading test on stability diagram; (c), (d) and (e) cyclic loading; (f) post-cyclic (results in model scale).

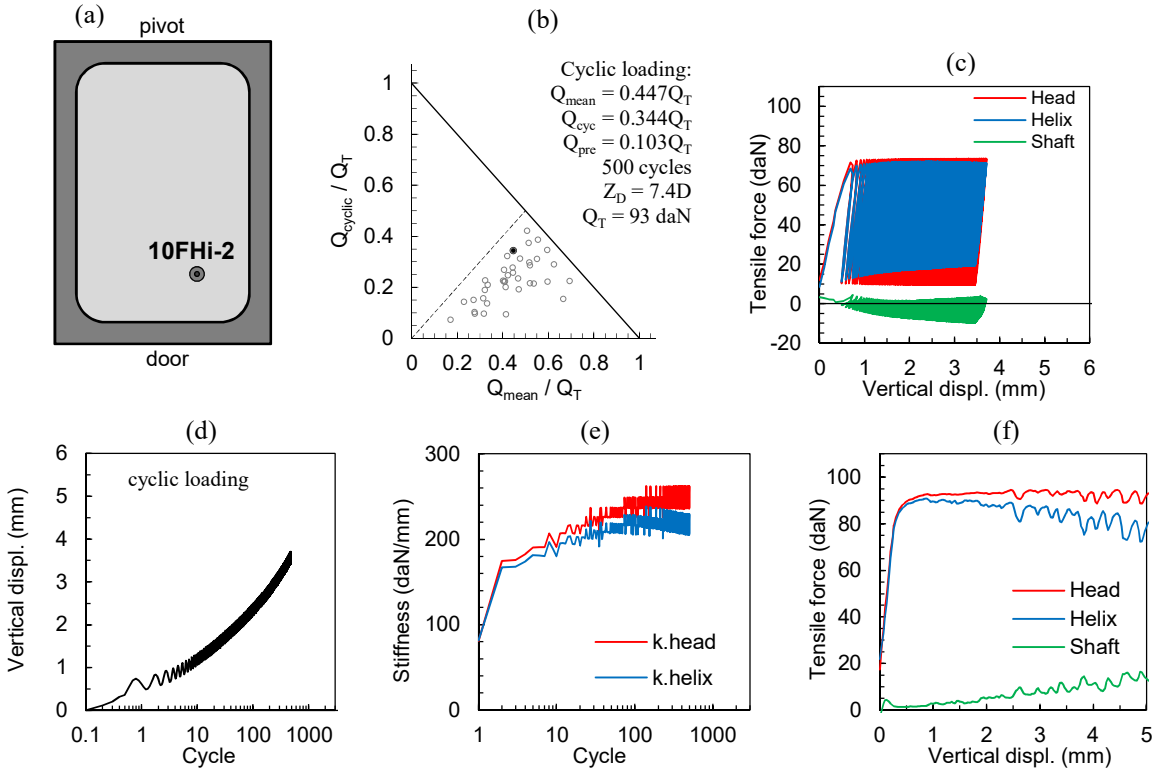

Figure 173. Cyclic loading and pull-out test nº 10FHi-2 with 10FHi model in the 14th container: (a) anchor location; (b) cyclic loading test on stability diagram; (c), (d) and (e) cyclic loading; (f) post-cyclic (results in model scale).

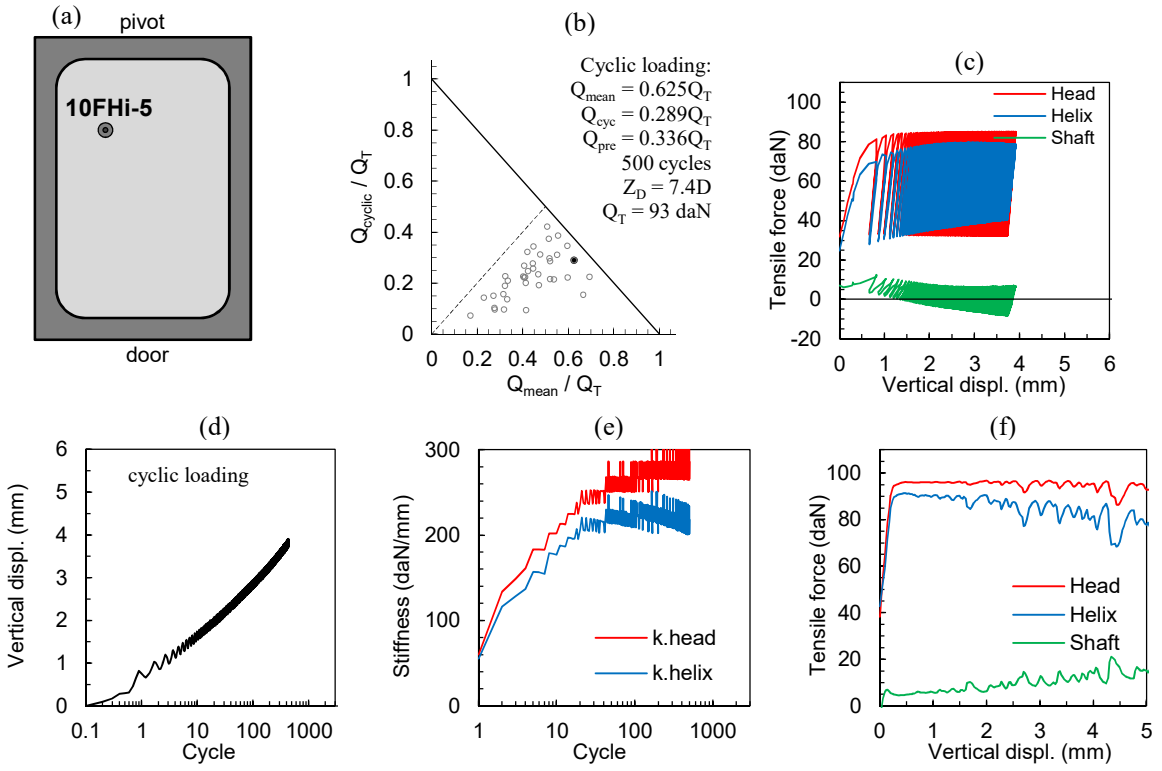

Figure 174. Cyclic loading and pull-out test nº 10FHi-5 with 10FHi model in the 14th container: (a) anchor location; (b) cyclic loading test on stability diagram; (c), (d) and (e) cyclic loading; (f) post-cyclic (results in model scale).

Appendix O. Cyclic degradation

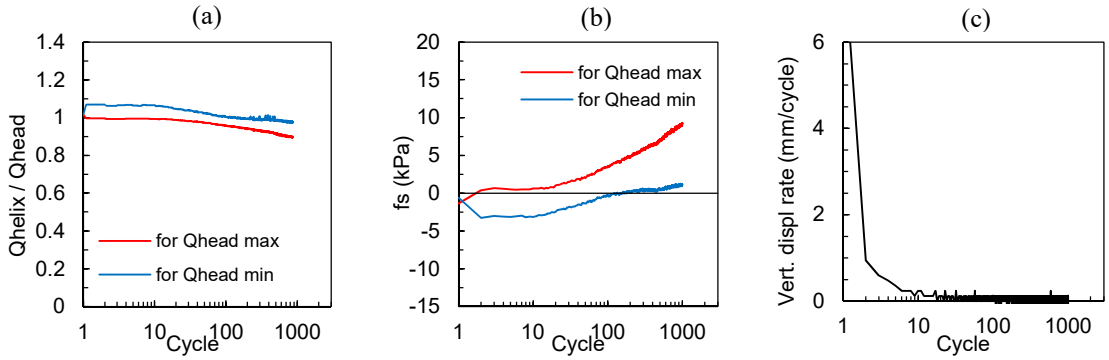

Figure 175. Cyclic loading test 10FHi-1 in the 10th container: (a) Q_{helix}/Q_{head} *versus* cycle number; (b) friction resistance *versus* cycle number; (c) displacement rate during the cyclic loading.

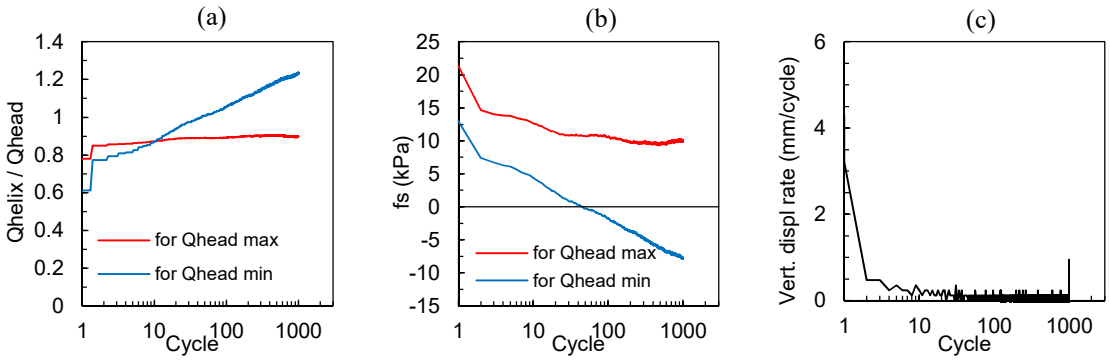

Figure 176. Cyclic loading test 10FHi-2 in the 10th container: (a) Q_{helix}/Q_{head} *versus* cycle number; (b) friction resistance *versus* cycle number; (c) displacement rate during the cyclic loading.

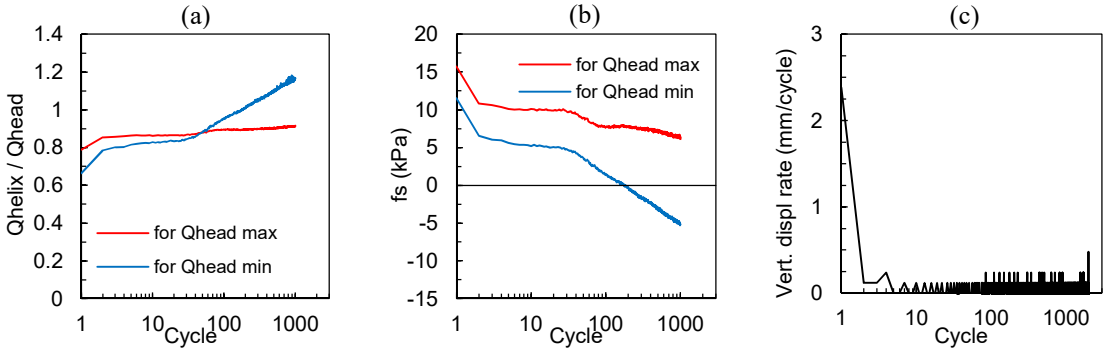

Figure 177. Cyclic loading test 10FHi-3 in the 10th container: (a) Q_{helix}/Q_{head} *versus* cycle number; (b) friction resistance *versus* cycle number; (c) displacement rate during the cyclic loading.

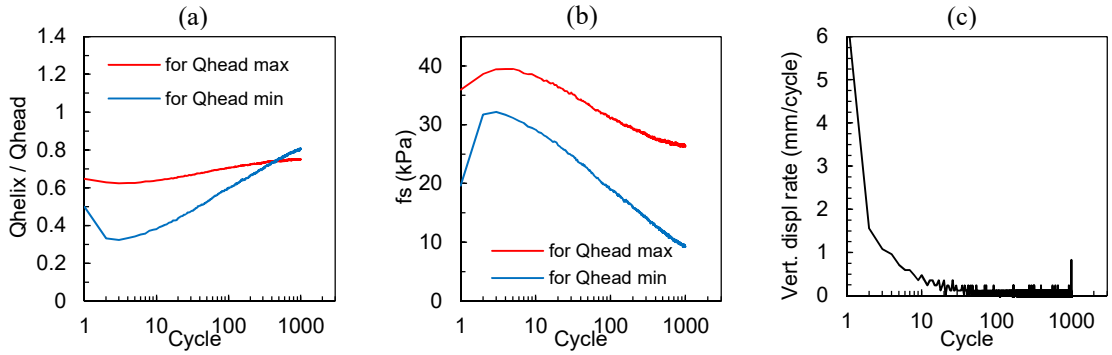

Figure 178. Cyclic loading test 10FHi-4 in the 10th container: (a) Q_{helix}/Q_{head} *versus* cycle number; (b) friction resistance *versus* cycle number; (c) displacement rate during the cyclic loading.

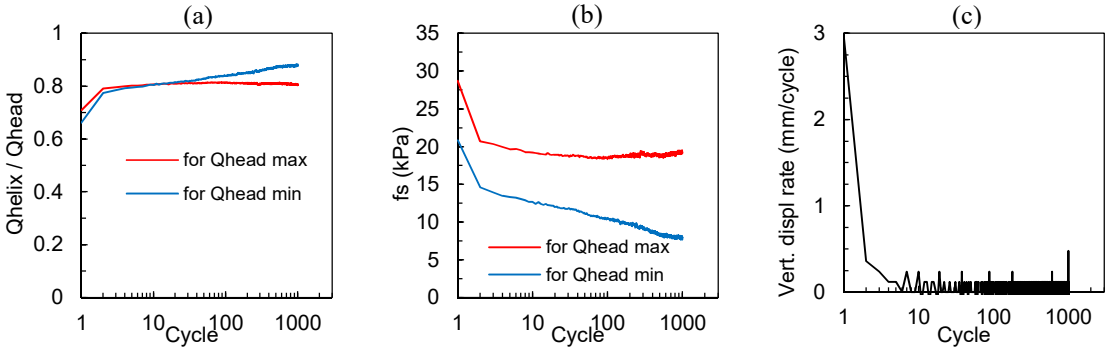

Figure 179. Cyclic loading test 10FHi-6 in the 10th container: (a) Q_{helix}/Q_{head} *versus* cycle number; (b) friction resistance *versus* cycle number; (c) displacement rate during the cyclic loading.

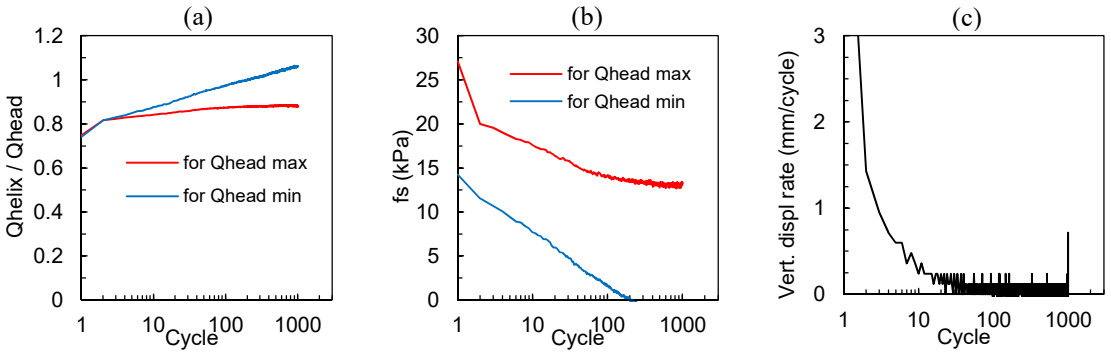

Figure 180. Cyclic loading test 10FHi-7 in the 10th container: (a) Q_{helix}/Q_{head} *versus* cycle number; (b) friction resistance *versus* cycle number; (c) displacement rate during the cyclic loading.

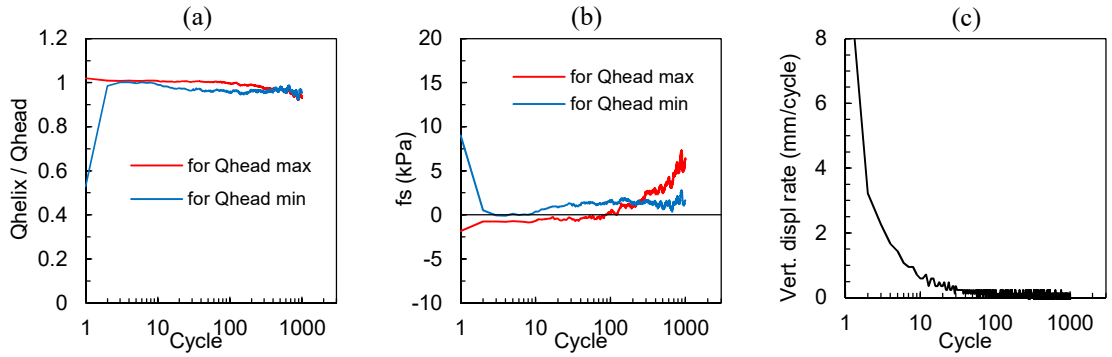

Figure 181. Cyclic loading test 10FHi-1 in the 13th container: (a) Q_{helix}/Q_{head} *versus* cycle number; (b) friction resistance *versus* cycle number; (c) displacement rate during the cyclic loading.

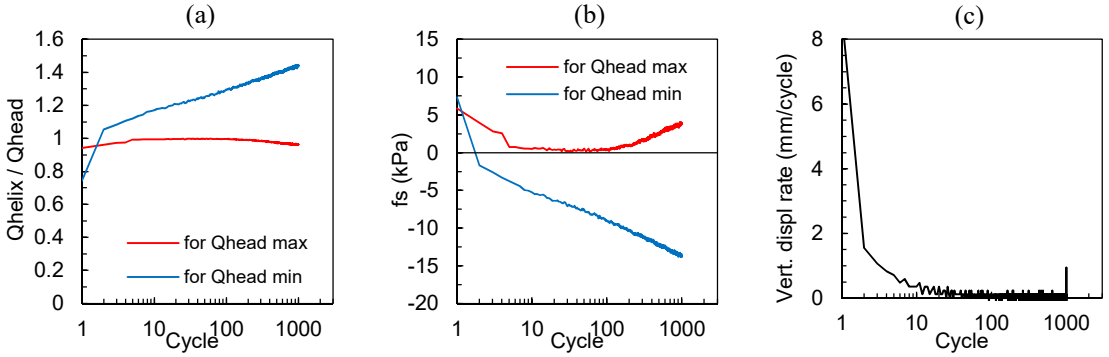

Figure 182. Cyclic loading test 10FHi-2 in the 13th container: (a) Q_{helix}/Q_{head} *versus* cycle number; (b) friction resistance *versus* cycle number; (c) displacement rate during the cyclic loading.

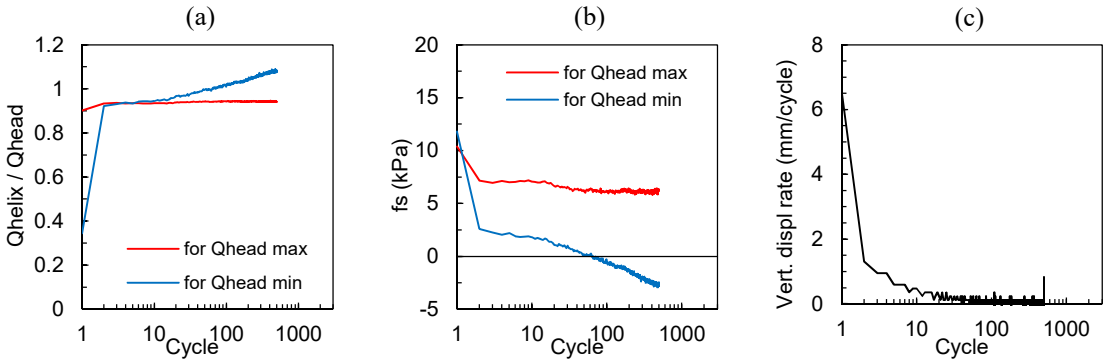

Figure 183. Cyclic loading test 10FHi-3 on 10FHi in the 13th container: (a) Q_{helix}/Q_{head} *versus* cycle number; (b) friction resistance *versus* cycle number; (c) displacement rate during the cyclic loading.

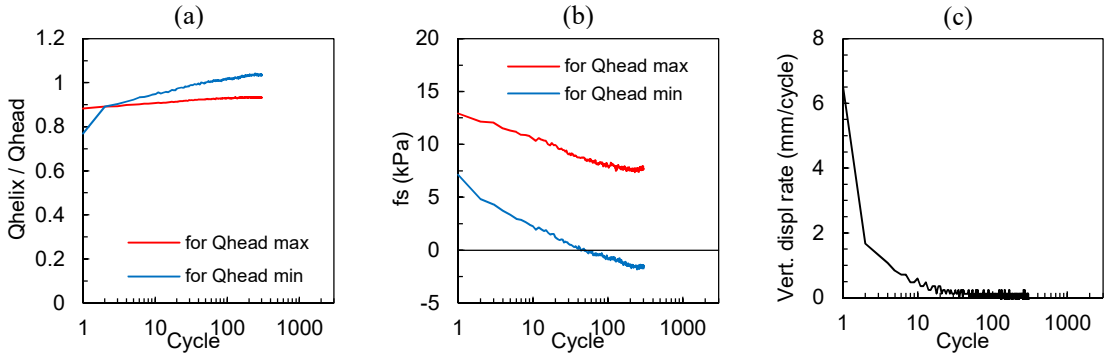

Figure 184. Cyclic loading test 10FHi-4 on 10FHi in the 13th container: (a) Q_{helix}/Q_{head} *versus* cycle number; (b) friction resistance *versus* cycle number; (c) displacement rate during the cyclic loading.

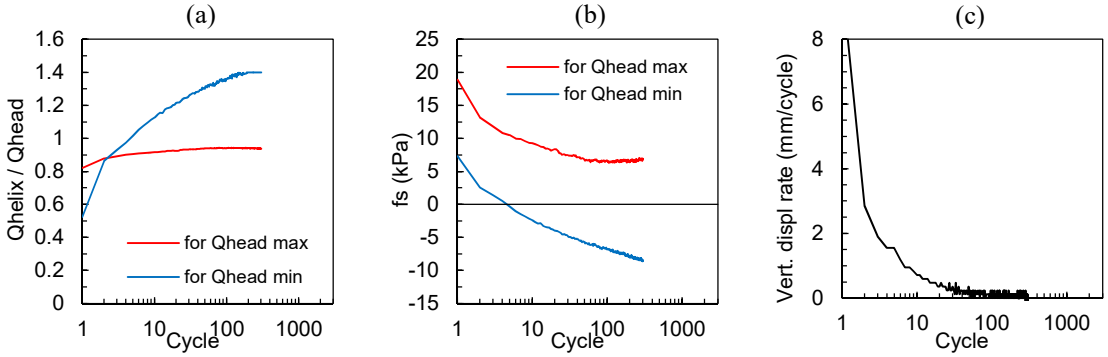

Figure 185. Cyclic loading test 10FHi-1 in the 14th container: (a) Q_{helix}/Q_{head} *versus* cycle number; (b) friction resistance *versus* cycle number; (c) displacement rate during the cyclic loading.

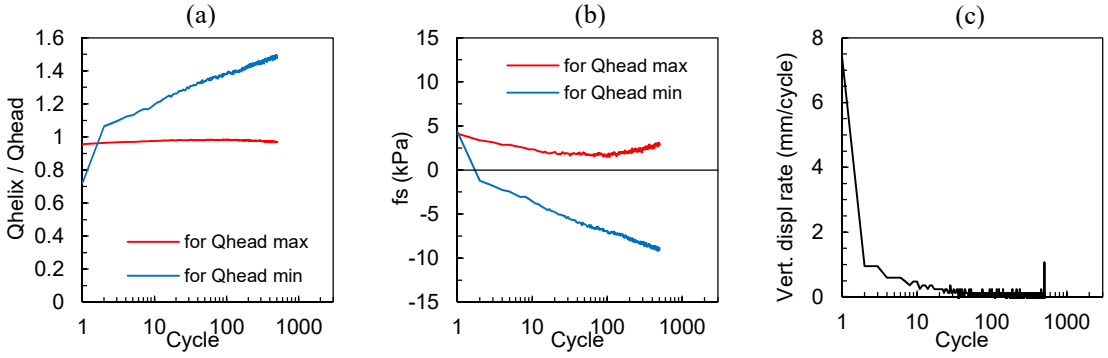

Figure 186. Cyclic loading test 10FHi-2 in the 14th container: (a) Q_{helix}/Q_{head} *versus* cycle number; (b) friction resistance *versus* cycle number; (c) displacement rate during the cyclic loading.

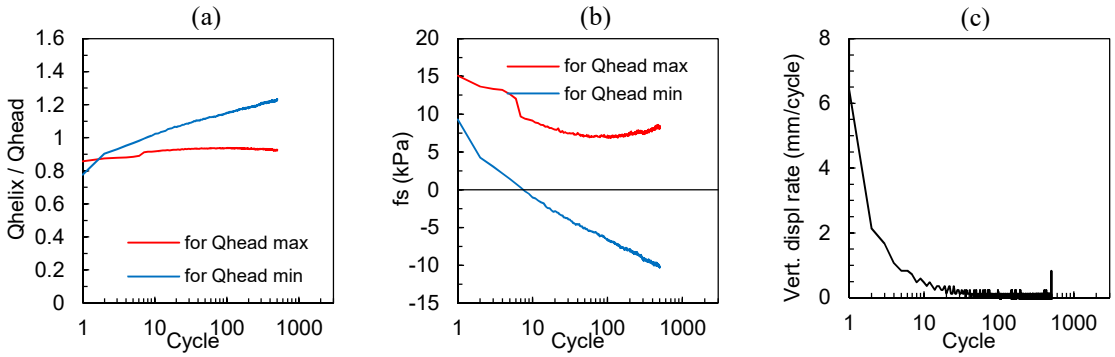

Figure 187. Cyclic loading test 10FHi-5 in the 14th container: (a) Q_{helix}/Q_{head} *versus* cycle number; (b) friction resistance *versus* cycle number; (c) displacement rate during the cyclic loading.

Appendix P. Helical pile models exhumation after testing (container No. 7)

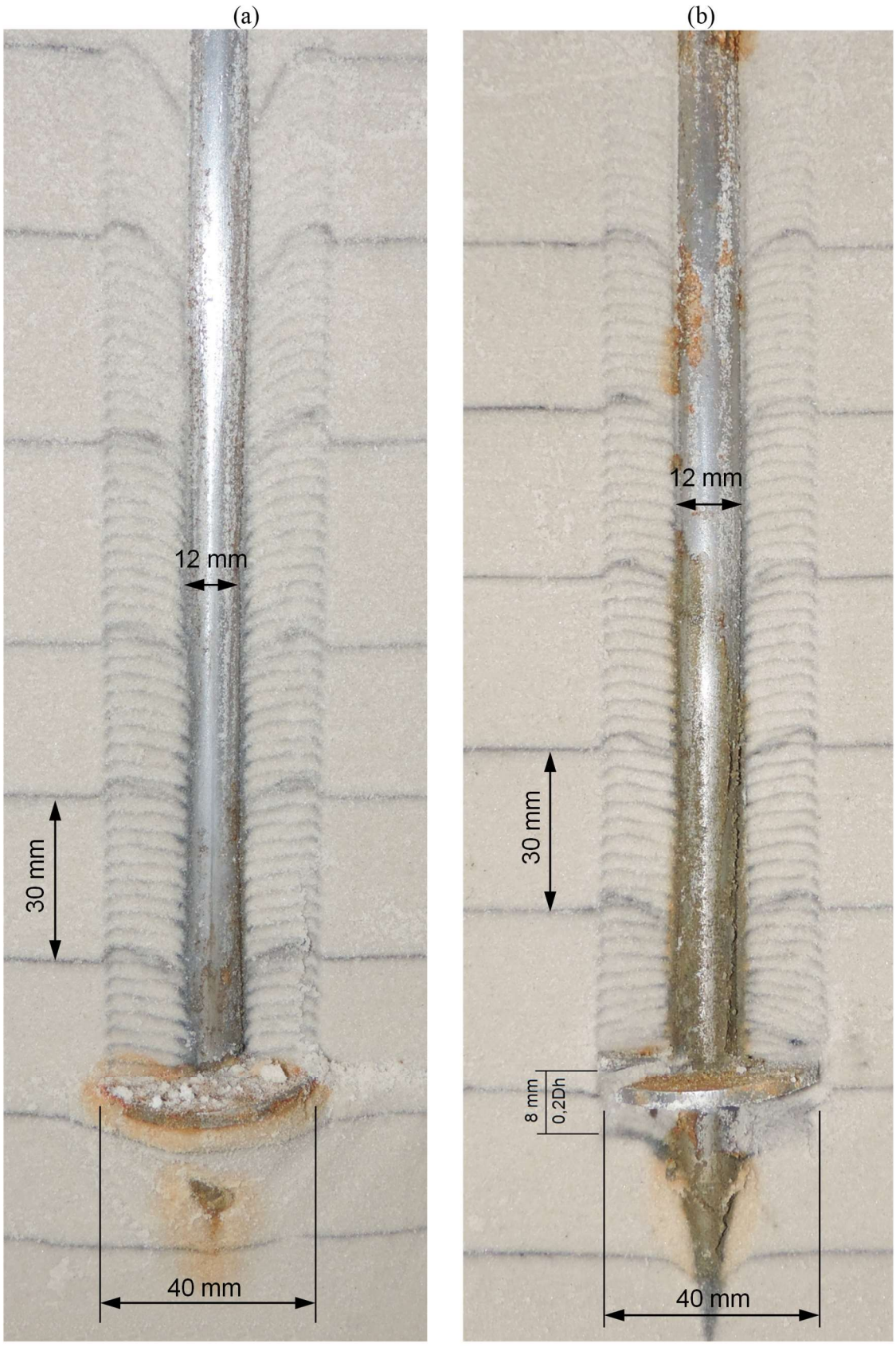

Figure 188. 12FH model exhumation after: (a) installation (b) uplift equals to 8 mm (0.2D).

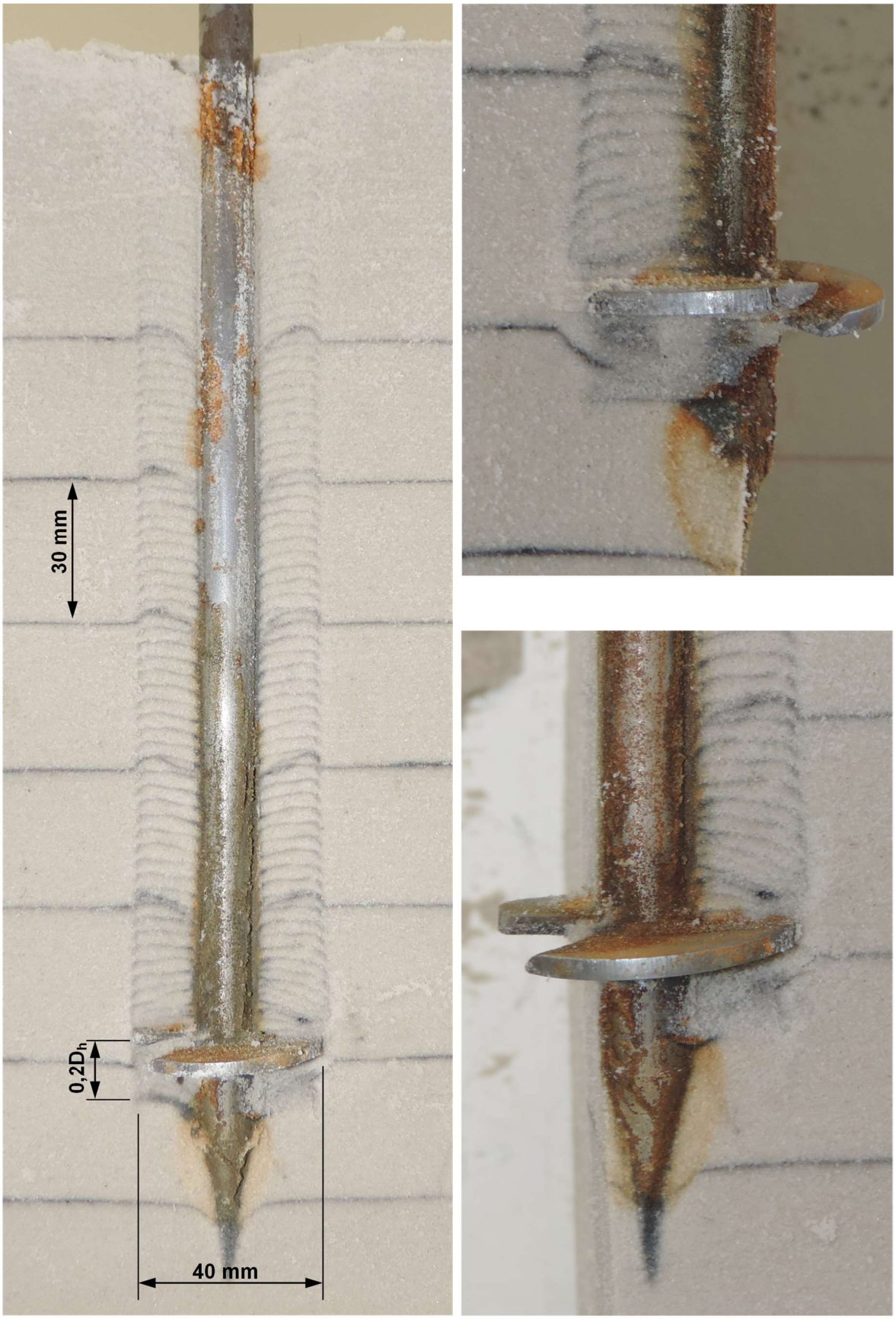

Figure 189. 12FH model exhumation after uplift equals to 8 mm (0.2D) with the helix in detail.

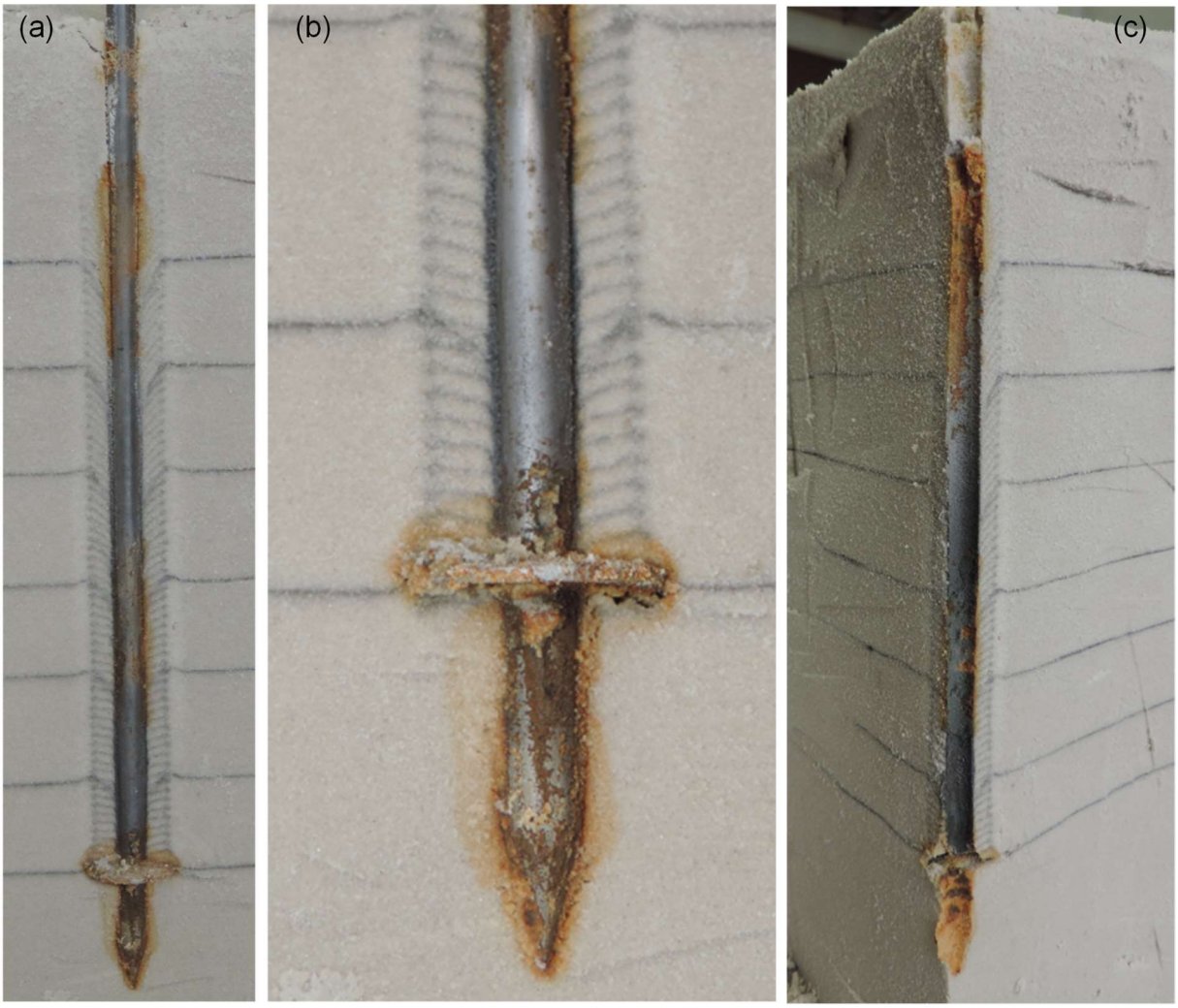

Figure 190. 8FH model exhumation after uplift equals to 5.3 mm (0.2D): (a) entire anchor model; (b) helix in detail; (c) after removing the model anchor.

Appendix Q. Comparison of the accumulated displacements calculated with the proposed equations of the current study and the experimental results

Table 29. Calculated and experimental results of accumulated displacements.

Container No.	Test	Cycle number					
		300		500		1000	
		Calculated U_{acc} (mm)	Experimental U_{acc} (mm)	Calculated U_{acc} (mm)	Experimental U_{acc} (mm)	Calculated U_{acc} (mm)	Experimental U_{acc} (mm)
4	10FH-4	12.8	15.5	14.1	17.5	-	-
5	10FH-3	8.1	4.1	9.0	5.0	10.0	6.7
	10FH-5	8.4	5.6	9.3	7.0	10.4	8.8
6	10FH-1	15.6	17.3	17.4	19.3	-	-
	10FH-2	17.9	10.6	19.9	12.3	22.5	14.7
	10FH-3	17.0	17.9	19.0	19.4	-	-
	10FH-4	18.6	18.6	21.1	21.2	24.3	25.3
	10FH-5	7.8	10.8	8.6	12.5	-	-
	10FH-6	22.1	21.6	24.9	24.6	28.3	29.6
7	10FH-1	20.1	29.9	22.5	34.1	25.5	41.4
	10FH-2	18.9	20.6	21.3	23.7	24.1	28.7
	10FH-3	24.8	26.0	28.2	29.4	32.4	35.3
	10FH-4	22.9	22.9	25.8	26.5	-	-
10	10FHi-1	22.8	21.1	25.2	23.1	-	-
	10FHi-2	24.6	18.6	27.6	21.9	31.7	27.5
	10FHi-3	14.5	8.0	16.2	10.0	18.6	13.1
	10FHi-4	23.5	29.2	26.1	32.9	29.5	39.3
	10FHi-6	14.3	7.0	16.1	8.2	18.4	9.9
	10FHi-7	24.5	27.2	27.4	29.8	-	-
13	10FHi-1	42.0	63.8	45.7	74.1	50.2	96.8
	10FHi-2	31.9	33.5	35.8	37.1	-	-
	10FHi-3	36.0	33.0	40.1	38.3	-	-
	10FHi-4	34.7	34.6	-	-	-	-
14	10FHi-1	41.5	52.2	-	-	-	-
	10FHi-2	30.7	29.9	34.2	34.7	-	-
	10FHi-3	19.8	13.2	22.1	15.6	25.1	19.5
	10FHi-4	38.5	42.5	-	-	-	-
	10FHi-5	30.9	30.8	34.7	33.5	-	-

Appendix R. Manuscript submitted to the International Journal of Physical Modelling in Geotecnics

DOI: 10.1680/jphmg.15.00047

Scale effect in centrifuge tests of helical anchors in sand

Author 1

- José Antonio Schiavon, MSc
- DSc Candidate, Department of Geotechnical Engineering, University of São Paulo at São Carlos, São Carlos, Brazil

Author 2

- Cristina de Hollanda Cavalcanti Tsuha, MSc, DSc
- Professor, Department of Geotechnical Engineering, University of São Paulo at São Carlos, São Carlos, Brazil

Author 3

- Luc Thorel, Ing, HDR, PhD
- Senior Researcher, IFSTTAR, GERS, Earthworks & Centrifuge Laboratory, LUNAM University, Bouguenais, France

Abstract

Centrifuge modelling is an advantageous technique to simulate the behaviour of helical anchors in sand. The uplift capacity of a single-helix anchor is the sum of the helix bearing resistance plus the shaft resistance; therefore, the recommendations to avoid the grain-size effect of previous model tests on plate anchors and on regular piles appear to be reasonable for helical anchor model tests. However, there are two important differences between centrifuge models of plate anchors and helical anchors: the ratio of the helical plate to the shaft diameter and the plate installation procedure. Consequently, the shaft friction and the plate bearing resistance of helical anchors can be affected by the scaling effect in a different manner. To clarify this uncertainty, this study was proposed to investigate the grain size effect on the results of uplift capacity of helical anchor models in sand. Anchor models with different scales were tested to simulate the same prototype in very dense dry sand in a centrifuge. These experiments showed that no scale effect was found for models with the ratio of the effective helical radius to the average grain-size greater than 58. The findings obtained here could guide future centrifuge model studies on helical anchors.

Keywords

Anchors & anchorages; sands; centrifuge modelling.

List of notations

d is the shaft diameter

d_{50} is the average grain-size

e_{max} is the maximum void ratio

e_{min} is the minimum void ratio

p is the helix pitch

t_h is the helical plate thickness

w is the effective helical radius

z_D is the helix embedment depth

B is the square plate width

C_u is the coefficient of uniformity

D is the regular plate or helical plate diameter

D_r is the relative density of sand

G_s is the specific gravity of the sand particles

Q is the tensile load on the anchor head

Q_T is the ultimate tensile load

R_{max} is the maximum surface roughness

$T_{avg\text{-}3D}$ is the average torque for the final distance of penetration equal to three times the helix diameter

T_f is the final installation torque

U is the vertical displacement at failure

$\gamma_{d(max)}$ is the maximum dry unity weight

$\gamma_{d(min)}$ is the minimum dry unity weight

$\gamma_{d(avg)}$ is the average unity weight of the sand samples

ϕ' is the effective angle of the internal friction

1. Introduction

Helical piles have been used extensively to support tensile and compressive loads in a wide range of applications, such as transmission towers, pipeline anchors, foundations for commercial and residential buildings, solar panels, foundation repair, and retaining wall systems. These foundations are normally applied onshore; however, recently, the use of helical piles has been suggested as an innovative and attractive solution for foundations of offshore wind turbines (Byrne and Houlsby 2015, Spagnoli and Gavin 2015, Spagnoli *et al.* 2015). This type of foundation is composed of one or more helix welded to a steel shaft and is installed into the ground by rotation, causing the helical plate to screw through the soil. During the installation of a helical anchor, the cylindrical volume of the soil penetrated by the helices is disturbed by screwing the anchor into the ground, and these changes influence its uplift performance (Mitsch and Clemence, 1985). This installation effect depends on the soil type and on the soil initial condition.

The helical anchors, according to the plate relative depth and mode of failure, could be classified as shallow anchor or deep anchor. Different from the shallow anchor, the deep condition occurs when the failure surface does not extend to the ground surface. In this case, the anchor capacity is a combination of the helix bearing resistance and the shaft resistance (Lutenegger, 2013). Normally, the bearing resistance is the predominant portion of the total capacity.

The uplift behaviour of helical anchors has been extensively investigated using laboratory 1 g models tests (Clemence and Pepe 1984; Mitsch and Clemence 1985; Narasimha Rao *et al.* 1989; Ghaly *et al.* 1991; Ghaly and Clemence 1998; etc.). However, to simulate cases where the anchor response is highly dependent on the confining stress, the use of geotechnical centrifuges is more appropriate to compensate for the soil self-weight stresses.

Centrifuge modelling allows for parametric studies with relatively small effort and low-cost compared to full-scale tests. For this reason, this modelling technique has been used successfully to investigate the performance of plate anchors (Ovesen 1981, Dickin and Leung 1983, Dickin 1988, Tagaya *et al.* 1988) and helical anchors (Levesque 2002, Tsuha *et al.* 2007, Bian *et al.* 2008, Wang *et al.* 2013). However, the occurrence of scale effects could influence the results of model experiments of geotechnical problems in granular soils. The reduced scale of models can induce scale effect in relation to the grain-size (Balachowski, 2006). Dilation, roughness, and grain crushing influence the behaviour of granular soils, and the smaller the model is, the larger the contribution of these phenomena on the model capacity (Klinkvort *et al.,* 2013). Therefore, as the uplift capacity of a deep single-helix anchor is the sum of the shaft skin friction and the helix bearing capacity, for the centrifuge simulation of helical anchors in sand, it is fundamental to verify the occurrence of scale effects on the results of both parts of anchor capacity. To address this need, this paper presents an experimental study with the aim of finding the appropriate dimensions of helical anchor models to simulate adequately the behaviour of single helix anchors in sand using centrifuge tests.

2. Scale effect on helical anchor models in sand

The occurrence of the scale effect in centrifuge model tests on helical anchors in granular soils can be interpreted in terms of two different mechanisms: the particle-size effect on the shaft resistance and the particle-size effect on the helical plate bearing resistance.

2.1 Particle-size effects on the shaft resistance

Scale effects observed on shaft resistance are related to the soil tendency to dilate at the interface, which is a function of soil mineralogy, soil density, stress level, grain-size, pile diameter and interface roughness (Foray, 1991). The particle size effect on the skin resistance of piles is associated with shear band formation along the shaft. The ratio of the dilatant zone thickness to the pile diameter is responsible for the large shaft resistance observed in small diameter piles; however, for relatively smooth steel piles, the dilatant properties of the soil may be less important (Houlsby, 1991). Thus, an adequate model simulation of the pile-sand interface should to be assured by following a minimum ratio of the pile shaft diameter to the average grain-size (d/d_{50}). Previous studies on the scaling effect on the shaft friction have presented different limits of the ratio d/d_{50}. Foray *et al.* (1998) reported that size effects are negligible when d/d_{50} is greater than 200. Garnier and König (1998) found no significant grain-size effect when d/d_{50} is larger than 100 for pile models with a rough shaft. Fioravante (2002) commented that scaling effects can be neglected for d/d_{50} greater than 30 to 50, despite the dispersion observed in the results.

The scale effects on the shaft friction of helical anchors are related to the shaft diameter d, similar to the case of regular piles. However, the relationships of the pile shaft diameter to d_{50} recommended to prevent scale effects on model tests are not appropriate for the simulation of shaft resistance of helical anchors, as the soil mass around the shaft (also the dilatant zone) is influenced by the previous installation of the helix.

Figure 1 shows a photograph of a helical anchor after installation, in flight, in the centrifuge of IFSTTAR (Bouguenais). This figure shows the disturbed sand around the anchor model installed in very dense HN38 Hostun sand. Therefore, based on the previous observation that the installation of the helix can influence the confining stresses around the shaft and the dilation mechanism, the values of the d/d_{50} ratio found in the literature for regular piles are not adequate for modelling the shaft resistance of helical anchors in sand.

2.2 Particle-size effects on the helical plate bearing resistance

Because there is no study available on the particle size effects on the bearing plate resistance of helical anchor models, the recommendations of previous centrifuge model test investigations on footings and on plate anchors in sand were used in Tsuha *et al.* (2007) to define the minimum ratio D/d_{50} (D is plate diameter) to provide a satisfactory simulation of helical plate bearing resistance.

Yamaguchi *et al.* (1977) found no difference in the results of the bearing capacity factor and the load-settlement response of shallow foundations with the ratio of foundation width (B) to the average grain size (d_{50}) greater than

36. Ovesen (1979) investigated scaling effects in centrifuge tests on footing models in sand and found no scale effect in experiments on footing model diameters (D) larger than $30d_{50}$. Lau (1988) observed no evidence of serious particle size effects on footing models in sand with B/d_{50} ratios ranging from 165 to 8333. The results of Tatsuoka *et al.* (1997) showed good agreement between the footing models with D/d_{50} ratio of 33 and 50.

Three different scales of square plate anchors were tested by Ovesen (1981) in dense sand (g-levels ranging from 167 g to 56 g). In this cited work, no scale errors were observed in models with the B/d_{50} larger than 25.

In the case of plate anchor models tested in a centrifuge, the sand above the plate is placed in the container after the plate installation. Differently, in the case of centrifuge tests on helical anchors, the helical plate is penetrated into the soil by rotation after sand placement, and consequently, significant disturbance occurs within the cylindrical installation zone of the anchor, as shown in Figure 1. In addition, the range of the ratio of plate to shaft diameters (D/d) is far superior for plate anchors compared to helical anchors. Therefore, these two differences probably result in different values of the minimum ratio D/d_{50} necessary to avoid scale effects on helical anchor tests compared to the case of plate anchor and footing models.

Centrifuge model investigations on helical anchors in sand can produce reliable simulations of the anchor behaviour without the influence of scale effects. For such simulations, some relationships of the grain to the model size should be established to provide an accurate reproduction of the prototype anchor-soil interaction. In the case of helical anchors, the helix-shaft-soil interaction is influenced by the grain-size in a particular manner.

In the case of the helix bearing resistance, it is necessary to establish a helical plate component (e.g., helix diameter or effective helical radius) that can be related to particle size effects. In the case of plate anchors, the ratio of the plate diameter D to the average grain size d_{50} appears to be a good parameter and is commonly used to evaluate scale effects. However, in the case of helical anchors, the net projected area of the helix is reduced in comparison to a plate anchor of same plate diameter. In addition, the ratio of the helical plate to the shaft diameters is variable, typically varying from 1.5 to 7.5. Therefore, the ratio of the helix diameter D to d_{50} is not the best parameter to explain the particle size effects on the helical plate bearing resistance. Accordingly, in the current work, the particle size effect on the bearing resistance is proposed to be correlated to the effective helical radius w:

$$w = 0.5(D - d) \quad (1)$$

Thus, it is necessary to verify the minimum value of w/d_{50} ratio (Figure 2) to prevent any scale effect on helical anchor model in sand.

The values for the ratios D/d_{50} (plate diameter/average grain size) and d/d_{50} (shaft diameter/average grain size) observed in previous studies to avoid scale effects on bearing plate resistance and shaft resistance indicate that the shaft diameter should restrict the helical anchor model dimensions (greater d/d_{50} ratios are suggested

compared to D/d_{50}). However, the shaft friction resistance contributes to a very small portion of the total capacity of a helical anchor in sand as demonstrated in Schiavon (2016). This author performed a series of pull-out tests on an instrumented model of a single-helix anchor, installed in the same sand sample used in the current investigation; in this case, the shaft capacity varied from 12 to 22% of the total uplift capacity of the helical anchor. Therefore, noting that the predominant portion of the uplift capacity of the investigated helical anchor is related to the helical plate bearing resistance; the scale effects evaluated in the current study are predominantly influenced by the ratio of the effective helical radius to the average grain size.

3. Experimental programme

The current study aims to verify the particle size effect on the uplift response of helical anchor models in sand tested in a centrifuge. To achieve this objective, four different helical anchor models, fabricated to simulate the same prototype of a helical anchor, were installed in dry dense sand samples and tested in a centrifuge. The pull-out tests were performed on each model anchor at least three times to verify the repeatability and reproducibility of the measured results of uplift capacity. Therefore, three containers were equally prepared to allow the number of tests required for this purpose.

The scale effects on the helical anchor capacity were verified from the experimental results using the technique "modelling of models" described in Ovesen (1979). In this cited work, anchor models of different sizes and g-levels were used to simulate the same prototype response in the same sand, and the full similarity is achieved when an identical response is observed between model and prototype. This author used this technique to evaluate scale effects on the bearing resistance.

The helical anchor models were installed and tested in three reconstituted sand samples prepared by a raining deposition technique. The sand samples were placed in a rectangular container of 1200 mm in length, 800 mm in width, and 360 mm in depth.

The centrifuge experiments were performed in reconstituted dry HN38 Hostun sand, which is a fine silica sand consisting of angular particles (sand extracted in Hostun, France). The Hostun sand is used in other laboratory investigations, and its physical properties are well established (Flavigny *et al.*, 1990). The experiments were performed in sand samples with sand relative density of 99%. Table 1 illustrates the characteristics of HN38 Hostun sand. Figure 3 shows the results of mini-CPT tests (cone diameter = 12 mm) carried out in a preliminary container, prepared only to evaluate the vertical and horizontal homogeneity of the sand sample tested in the current investigation. The experiments were conducted in the IFSTTAR geotechnical centrifuge (Corté and Garnier 1986), which has a radius of 5.50 m, a maximum payload of 2000 kg, and a maximum acceleration of 200 g (Figure 4).

3.1 Test system

The anchor model installations and pull-out tests were performed using a servo-control system fixed over the sand container. As illustrated in Figure 5, a motor was coupled to the system to rotate the helical anchor models

during the installation. The installation torque was measured by a torquemeter (indicated in Figure 5) only in two of the three containers tested in this investigation. The axial movement and loading on the anchor models were monitored by displacement and force transducers. The measurements of installation torque, displacement, and force were obtained by an automatic data acquisition system installed in the centrifuge swinging basket. More details regarding the IFSTTAR centrifuge can be found in Thorel *et al.* (2008).

3.2 Helical anchor models

Figure 6 shows the four different single-helix anchor models tested in this investigation. The anchor models were composed of a steel helical plate welded to a round steel shaft, both fabricated with a maximum steel surface roughness R_{max} of 4.87 μm.

Four different scaling factors were estimated to provide a helical anchor prototype with a 100 mm of shaft diameter and a 330 mm helical plate diameter (D/d ratio equals to 3.3). The embedment depth of the helical plate was equal to 6 times the plate diameter (1.98 m depth). The dimensions of the helical anchor models and their corresponding g-levels are presented in Table 2.

3.3 Anchor installation and pull-out tests

The installation of the helical anchor models into the sand sample was performed in flight, applying a constant rotation to the model of 5.3 rpm (the field rotation rate normally varies from 5 to 20 rpm). The results of the final installation torque (T_f) and of the average torque measured at the final penetration of 3 helical plate diameters ($T_{avg\text{-}3D}$) are presented in Table 3. During installation by rotation, the vertical displacement rate was controlled to permit the helix to screw down through the sand sample with a rate of penetration of one pitch per revolution. In each container, a minimum centre-to-centre spacing of 10 times the helix diameter was kept between anchors to ensure no influence on the results.

The pull-out tests were performed three minutes after the end of anchor installations. The anchor models were loaded at a vertical displacement rate of 0.3 mm/s. When the pull-out was completed, the centrifuge was stopped to move the servo-control system over the following test location.

4. Test results

In the present study, the ultimate uplift capacity was assumed to be the peak tensile force measured during the pull-out test on the anchor model. As shown in Table 3, the peak capacity, $Q_{T\ (peak)}$, is very close to the tensile capacity related to a displacement of 10% of the plate diameter, $Q_{T\ (0.1D)}$. Figure 7 presents the load-displacement curves (in prototype values) obtained from the tensile loading tests on the anchor models. This figure shows that the results of ultimate uplift capacity obtained from the tests in containers 1 and 3 are more uniform than the results of the container 2 (Figure 7c). The variability of the results of the container 2 is probably due to the sample heterogeneity, as the other two samples provided uniform results for all models tested. Table 3 shows the results of ultimate uplift capacity (Q_T) and displacement (U) at failure found in Figure 7.

Figure 8 and Table 3 compare the ultimate uplift capacity obtained from different model sizes (different w/d_{50}). The average ultimate load obtained from the 13 tests is 61 kN, with a small coefficient of variation (COV) of 11%. The variation in the Q_T results probably occurred due to the variability in the sand samples and may not be attributed to particle size effect because there is no clearly defined trend.

The estimated uplift capacity of the prototype simulated in this study, using Terzaghi's equation as proposed in Adams and Klym (1972) for single-helix anchors, and the uplift capacity factor N_{qu} presented in Mitsch and Clemence (1985) for single-helix anchors in sand, was 120 kN, which is approximately twice the measured uplift capacity. A similar difference was observed in the numerical simulation of the field experiments of Gavin *et al.* (2014) on a single-helix anchor in dense sand. The prediction of these authors provides a result of the uplift capacity two times greater than the field measurements. These significant differences between the estimates and the measurements suggest that there is an important installation effect, not considered in the p rediction methods, that influences the single-helix uplift capacity in dense sand, as illustrated in Figure 1.

Table 3 and Figure 9 show that the ultimate load was reached at a vertical displacement in the range of 10% to 16% of the helical plate diameter. The larger anchor models required slightly smaller displacements to attain the ultimate load; however, as shown in Figure 9, no clear trend was observed.

The findings reported in Ovesen (1979 and 1981), Foray *et al.* (1998), Garnier and König (1998), and in other studies indicate that the results of bearing capacity and shaft resistance increases as the model size decreases. Therefore, the almost horizontal trend line plotted in Figure 8 suggests that no scale effect was identified for the range of models evaluated in this investigation: $d/d_{50} \geq 50$, and $w/d_{50} \geq 58$.

The results of the installation torque of the anchor models tested in the containers 2 and 3 are presented in Figure 10 and 11. Figure 11 shows that the values of the final installation torque obtained for the models 10H and 12H (in prototype value) are slightly greater than the results found for the other models. The models 10H and 12H were fabricated with greater helix thickness (18.0 and 25.0 mm in prototype scale, respectively) compared to the models 6H and 8H (8.4 and 8.8 mm) to prevent bending during the installation (see Table 2); therefore, as the installation torque increases with the helix thickness (Sakr, 2014), this torque gain probably is not caused by a scale effect. Accordingly, Figure 11 indicates that the installation torque was not influenced by scale effects for the range of w/d_{50} and d/d_{50} evaluated, as observed in Figure 8 for the uplift capacity. This finding is important because the average torque measured at the final penetration of 3 times the helix diameter is used to predict and to verify the ultimate capacity during anchor installation. Hoyt and Clemence (1989) proposed an empirical relationship of the installation torque to the axial uplift capacity of helical piles, given by Eq. 2:

$$Q_T = K_t \times T_{avg-3D} \quad (2)$$

where

T_{avg-3D} = average of the torque measured along the final distance corresponding to 3 times the helix diameter

K_t = torque correlation factor that varies with the shaft diameter

Therefore, to verify if the physical modelling well reproduced the field behaviour of helical anchors during installation and under tensile loading, the K_t values were determined in this investigation, as presented in Table 3. The centrifuge tests produced results of similar magnitude to the field-measured value presented in Gavin *et al.* (2014) for a single-helix anchor of similar shaft diameter installed in dense sand. These authors found a K_t value of 13 m^{-1}, and the current centrifuge tests provide a mean K_t value of 15 m^{-1}. In addition, as shown in Table 3, for the range of model sizes tested, no scale effect was observed on the simulation of a prototype K_t factor. However, the results of the coefficient of variation of the installation torque (and K_t factor) indicate that the resisting forces acting on the helical anchor during installation are more variable than the forces acting on the anchor under loading (Table 3).

5. Conclusions

The use of a geotechnical centrifuge to investigate helical anchor behaviour is advantageous because field tests are time consuming, expensive, and difficult to be repeated or compared due to the natural soil variability. However, scaling issues in modelling helical anchors have not been investigated previously. To address this problem, in the current study, pull-out tests on different reduced models of helical anchor in sand were performed in a centrifuge. All tested models simulated the same single-helix anchor prototype, with D = 330 mm, z_D = 6D, and $d = D/3.3$. The findings presented here are valid for helical anchor models with D/d (helix/shaft diameters) ratios similar or greater than the one tested in this study. The performance of helical anchor models with smaller D/d ratios may be affected by scaling effect in a different manner due to the increase of the shaft resistance contribution to the total capacity. The main conclusions of this study are:

- A new parameter or relationship (ratio of the effective helical radius to the average grain size, w/d_{50}) is proposed in this work to evaluate the scale effects on the results of the helical anchors uplift capacity in sand.

- The results of uplift capacity of all tested anchor models with the ratio w/d_{50} greater than 58 are comparable (mean value of 61 kN, with a coefficient of variation of 11%). Therefore, for the range of model sizes investigated, the influence of scale effects on tests results can be considered negligible.

- Although the minimum value of the shaft diameter/average grain size ratio evaluated in this study is 50 (much inferior to the recommended values in previous investigations regarding scale effects on shaft resistance), no scale effect on the uplift capacity results was observed. Accordingly, it is reasonable to assume that the particle size effects on helical anchor models in sand is related to effective helical radius /grain size ratio because the plate bearing capacity is the principal portion of the total capacity.

- The results of installation torque and torque correlation factor K_t obtained for the range of model sizes tested were not affected by scale effects. In addition, this centrifuge modelling study provides results of the torque correlation factor K_t comparable to the field.

Acknowledgements

This research was supported by the program USP-COFECUB grant No. UcMa 132/12, by the Brazilian Agency CAPES (Ministry of Education) and by the French Institute of Science and Technology for Transport, Development and Networks (IFSTTAR), France. The authors would like to thank to P. Gaudicheau, P. Audrain, S. Lerat, A. Neel, D. Macé and C. Favraud for their valuable contributions.

References

Adams JI and Klym WT (1972) A study of anchorages for transmission tower foundations. *Canadian Geotechnical Journal* **9(1)**: 89-104.

Bałachowski L (2006) Scale effect in shaft friction from the direct shear interface tests. *Archives of Civil and Mechanical Engineering* **6(3)**: 13-28.

Bian Y, Hutchinson TC, Wilson D *et al.* (2008) Experimental investigation of grouted helical piers for use in foundation rehabilitation. *Journal of Geotechnical and Geoenvironmental Engineering* **134(9)**: 1280-1289.

Byrne BW and Houlsby GT (2015) Helical piles: an innovative foundation design option for offshore wind turbines. *Philosophical Transactions Royal Society A* **373** : 20140081, http://dx.doi.org/10.1098/rsta.2014.008.

Clemence SP and Pepe FD Jr (1984) Measurement of lateral stress around multihelix anchors in sand. *Geotechnical Testing Journal* **7(3)**: 145-152.

Corté JF and Garnier J (1986) Une centrifugeuse pour la recherche en géotechnique. *Bulletin de Liaison des Laboratoires des Ponts et Chaussées* **146**: 5-28.

Dickin EA (1988) Uplift behavior of horizontal anchor plates in sand. *Journal of Geotechnical Engineering* **114(11)**: 1300-1317.

Dickin EA and Leung CF (1983) Centrifugal model tests on vertical anchor plates. *Journal of Geotechnical Engineering* **119(12)**: 1503-1525.

Fioravante V (2002) On the shaft friction modelling of non-displacement piles in sand. *Soils and Foundations* **42(2)**: 23-33.

Flavigny E, Desrues J and Palayer B (1990) Le sable d'Hostun RF. *Revue Française de Géotechnique* **53**: 67-70.

Foray P (1991) Scale and boundary effects on calibration chamber pile tests. In *Proceedings of the 1st International Symposium on Calibration Chamber Testing*. Elsevier, New York, USA, pp. 147-160.

Foray P, Balachowski L and Rault G (1998) Scale effect in shaft friction due to the localisation of deformations. In *Proceedings of the International Conference Centrifuge 98*. Balkema, Rotterdam, the Netherlands, vol. 1, pp. 211-216.

Garnier J and König D (1998) Scale effects in piles and nails loading tests in sand. In *Proceedings of the International Conference Centrifuge 98*. Balkema, Rotterdam, the Netherlands, vol. 1, pp. 205-210.

Gavin K, Doherty P and Tolooiyan A (2014) Field investigation of the axial resistance of helical piles in dense sand. *Canadian Geotechnical Journal* **51(11)**: 1343-1354.

Ghaly AM and Clemence SP (1998) Pullout performance of inclined helical screw anchors in sand. *Journal of Geotechnical and Geoenvironmental Engineering* **124(7)**: 617-627.

Ghaly AM, Hanna AM and Hanna MS (1991) Uplift behavior of screw anchors in sand - Part I: dry sand. *Journal of Geotechnical Engineering* **117(5)**: 773-793.

Houlsby GT (1991) How the dilatancy of soils affects their behaviour. In *Proceedings of the 10th European Conference on Soil Mechanics and Foundation Engineering*. Taylor & Francis, London, UK, vol. 4, pp. 1189-1202.

Hoyt RM and Clemence SP (1989) Uplift capacity of helical anchors in soil. In *Proceedings of the 12th International Conference on Soil Mechanics and Foundation Engineering*. Balkema, Rotterdam, the Netherlands, vol. 1, pp. 1019-1022.

Klinkvort RT, Hededal O and Springman SM (2013) Scaling issues in centrifuge modelling of monopiles. *International Journal of Physical Modelling in Geotechnics* **13(2)**: 38-49.

Lau, CK (1988) *Scale effects in tests on footings*. PhD thesis, University of Cambridge, Cambridge, UK.

Levesque CL (2002) *Centrifuge modelling of helical anchors in sand*. MSc. Thesis, University of New Brunswick, Canada.

Lutenegger AJ (2013) Uplift of shallow single-helix screw-piles. In *Proceedings of the 1st International Geotechnical Symposium on Helical Foundations*. International Society for Helical Foundations, Amherst, USA, pp. 200-210.

Mitsch MP and Clemence SP (1985) The uplift capacity of helical anchors in sand. In *Uplift behavior of anchor foundations in soil*. ASCE, New York, USA, pp. 26-47.

Narasimha Rao S, Prasad YVSN, Shetty MD *et al.* (1989) Uplift capacity of screw pile. *Geotechnical Engineering* **20(2)**: 139-159.

Ovesen NK (1979) The scaling law relationship. In *Proceedings of the 7th European Conference on Soil Mechanics and Foundation Engineering*. Britsh Geotechnical Society, London, UK, vol. 4, pp. 319-323.

Ovesen NK (1981) Centrifuge tests of the uplift capacity of anchors. In *Proceedings of the 10th International Conference on Soil Mechanics and Foundation Engineering*. Balkema, Rotterdam, the Netherlands, vol. 1, pp. 717-722.

Sakr M (2014) Relationship between installation torque and axial capacities of helical piles in cohesionless soils. *Canadian Geotechnical Journal* **52 (6)**: 747-759.

Schiavon JA (2016) *Experimental investigation on the helical pile behaviour under cyclic tensile loading*. PhD thesis (in preparation), University of São Paulo, São Carlos, Brazil.

Spagnoli G and Gavin K (2015) Helical piles as a novel foundation system for offshore piled facilities. In *Proceedings of the 2015 SPE Abu Dhabi International Petroleum Exhibition and Conference*. Society of Petroleum Engineers, Abu Dhabi, United Arab Emirates, http://dx.doi.org/10.2118/177604-MS.

Spagnoli G, Gavin K, Brangan C *et al.* (2015) In situ and laboratory tests in dense sand investigating the helix-to-shaft ratio of helical piles as a novel offshore foundation system. In *Proceedings of the 3rd International Symposium on Frontiers in Offshore Geotechnics*. Taylor & Francis, London, UK, vol. 1, pp. 643-648.

Tagaya K, Scott RF and Aboshi H (1988) Pullout resistance of buried anchor in sand. *Soils and Foundations* **28(3)**: 114-130.

Tatsuoka F, Goto S, Tanaka T *et al.* (1997) Particle size effects on bearing capacity of footing on granular material. In *Proceedings of the International Symposium on Deformation and Progressive Failure in Geomechanics*. Elsevier, New York, USA, pp. 133-138.

Thorel L, Rault G, Garnier J *et al.* (2008) Mesures en macrogravité sur modèles réduits d'ouvrages géotechniques. Bulletin des Laboratoires des Ponts et Chaussées **273**: 93-131.

Tsuha CHC, Aoki N, Rault G *et al.* (2007) Physical modelling of helical pile anchors. *International Journal of Physical Modelling in Geotechnics* **7(4)**: 1-12.

Wang D, Merifield RS and Gaudin C (2013) Uplift behaviour of helical anchors in clay. *Canadian Geotechnical Journal* **50(6)**: 575-584.

Yamaguchi H, Kimura T and Fujii N (1977) On the scale effect of footings in dense sand. In *Proceedings of the 9th International Conference on Soil Mechanics and Foundation Engineering*. Japanese Society of Soil Mechanics and Foundation Engineering, Tokyo, Japan, vol. 1, pp. 795-798.

Figures

Figure 1. Photograph of a helical anchor model in very dense sand after installation.

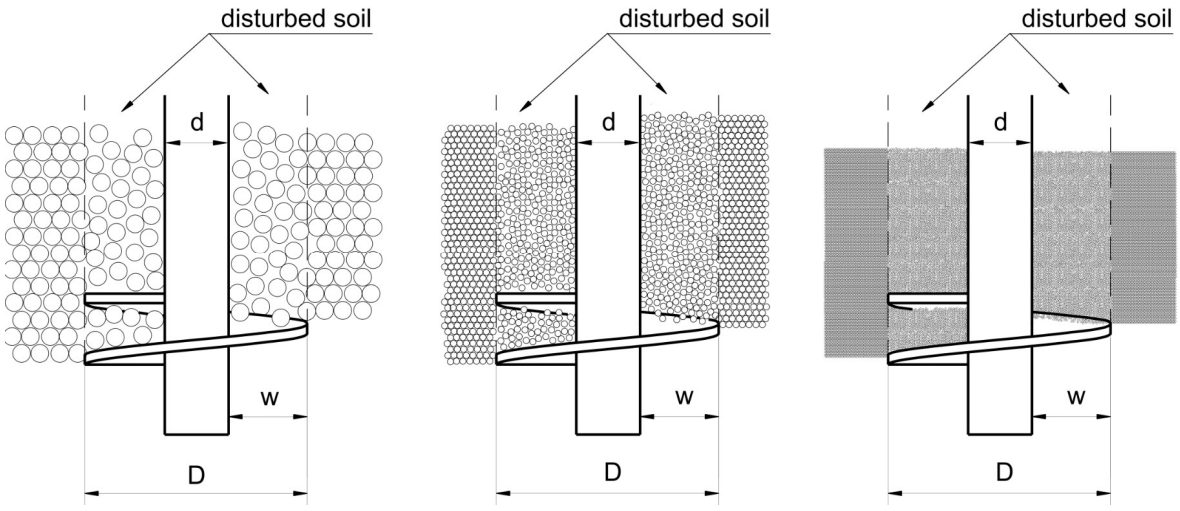

Figure 2. Helical anchor prototype simulated by anchor models of different w/d_{50} ratios (different model sizes in the same sand sample).

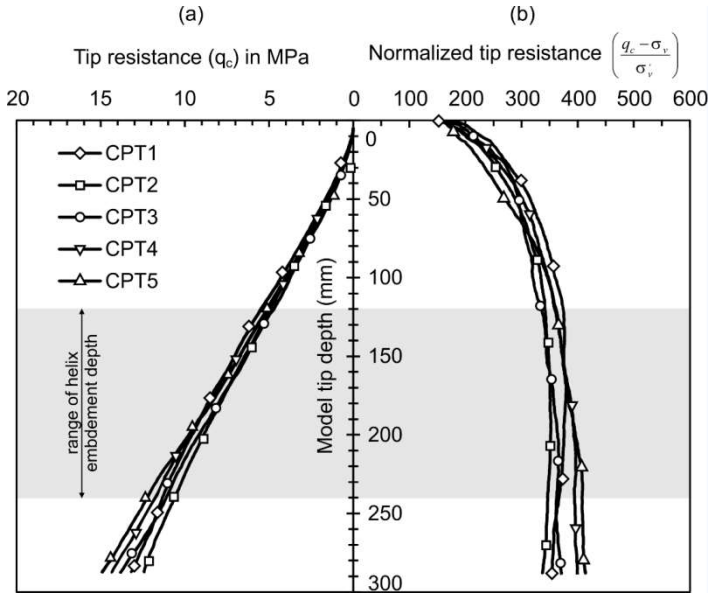

Figure 3. Mini-CPT results: (a) q_c *vs* tip depth, (b) normalized tip resistance *vs* depth.

Figure 4. IFSTTAR centrifuge.

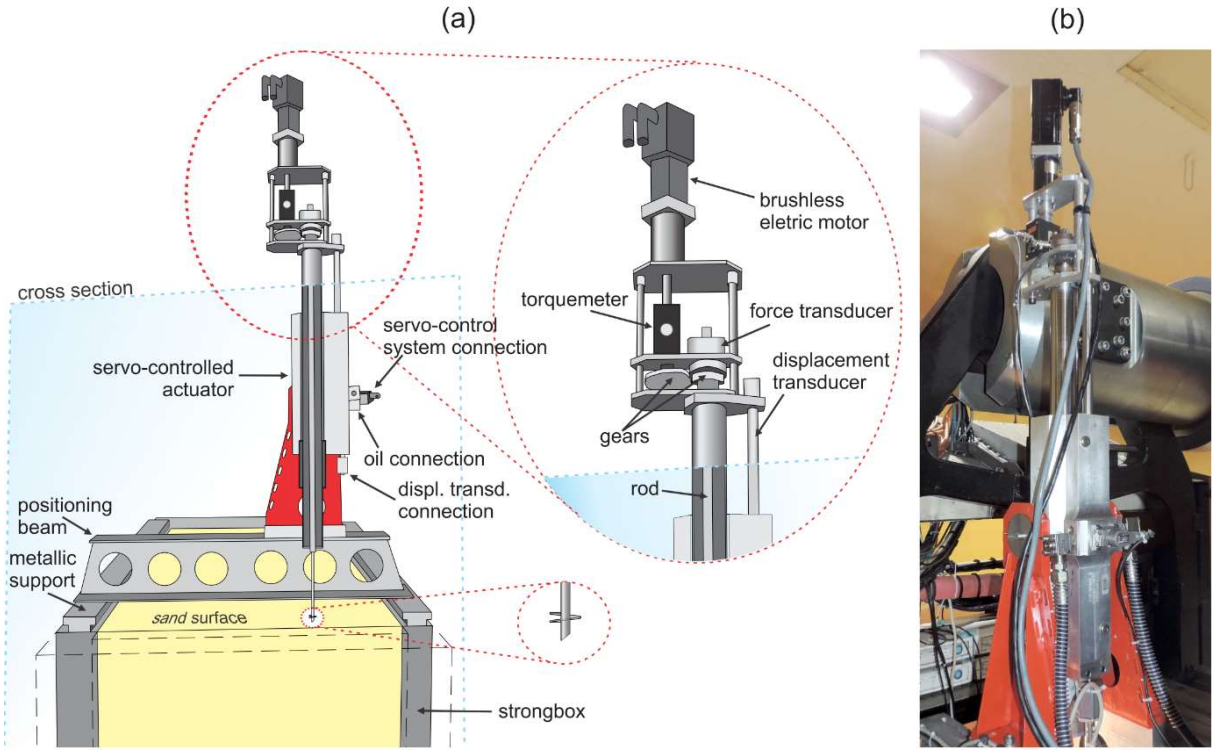

Figure 5. (a) test system; (b) servo-controlled actuator.

Figure 6. Helical model anchors.

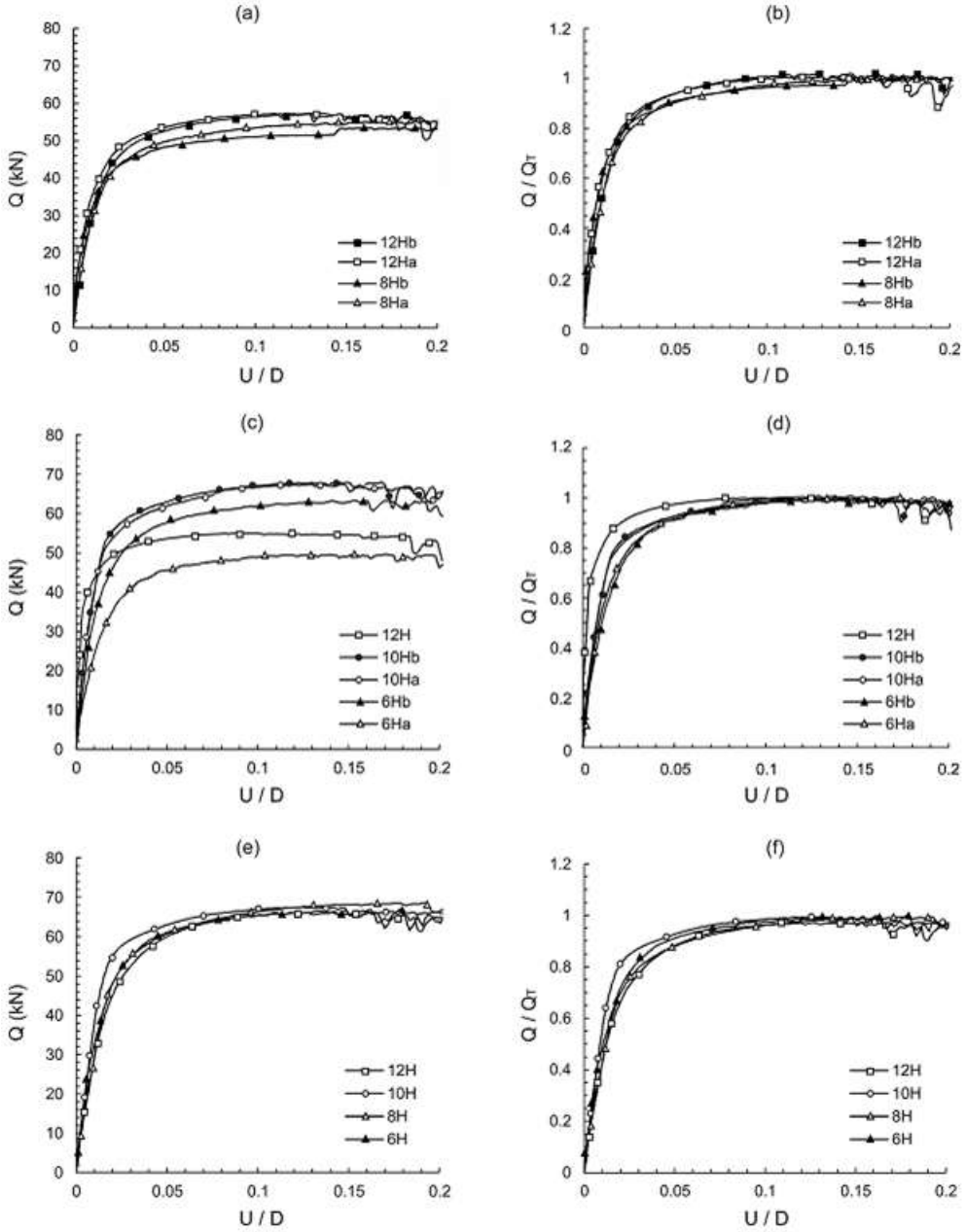

Figure 7. Load-displacement curves of the tensile load tests: (a) and (b) container 1, (c) and (d) container 2, (e) and (f) container 3.

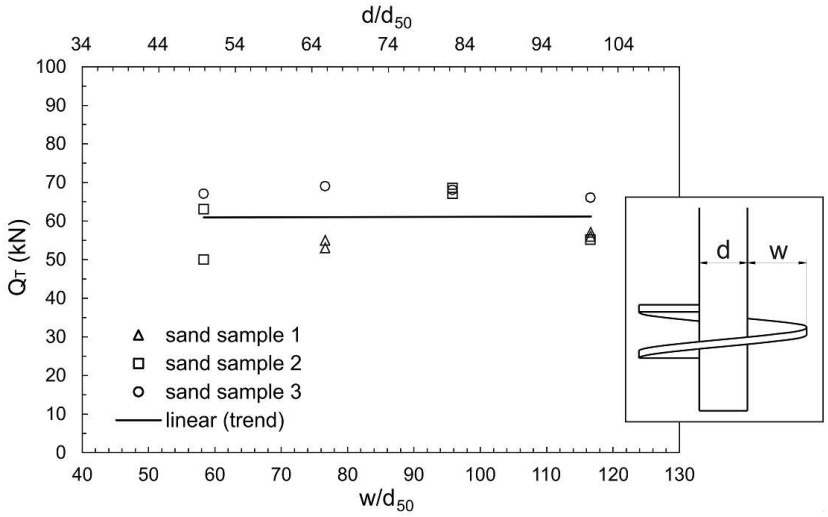

Figure 8. Ultimate tensile load of helical anchor models of different sizes.

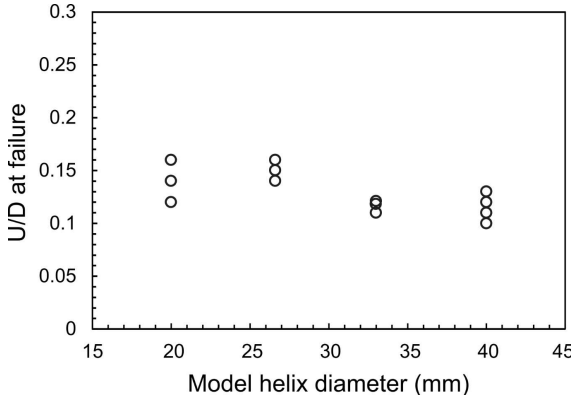

Figure 9. Relationship between the dimensionless ultimate displacement and helical plate diameter.

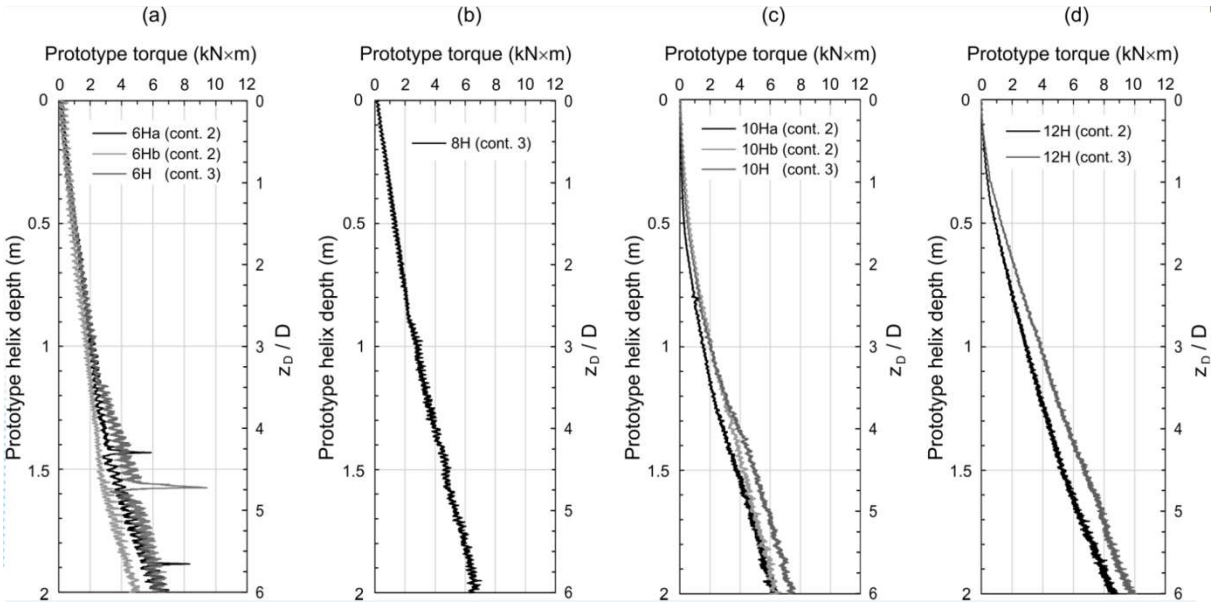

Figure 10. Installation torque *vs* depth, in prototype scale: (a) 6H, (b) 8H, (c) 10H, and (d) 12H.

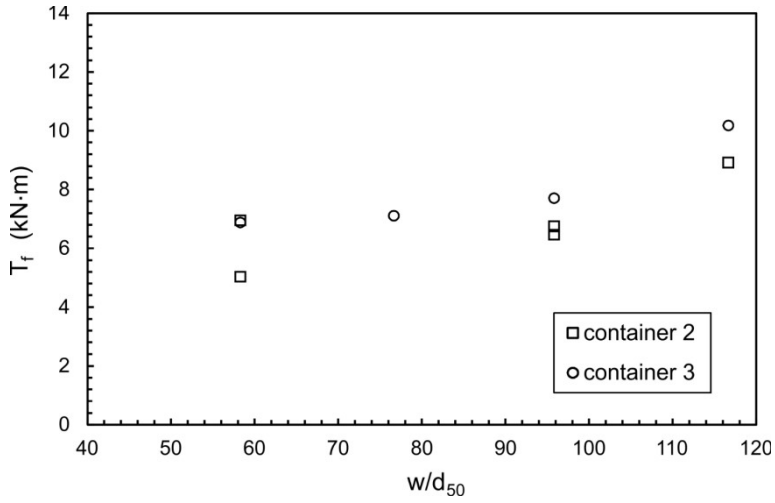

Figure 11. Installation torque of helical anchor models of different sizes.

Tables.

Table 1. HN38 Hostun sand characteristics.

Specific gravity of the sand particles	G_s	2.64[a]
Maximum dry unity weight (kN/m^3)	$\gamma_{d(max)}$	15.24
Minimum dry unity weight (kN/m^3)	$\gamma_{d(min)}$	11.63
Average unity weight of sand samples	$\gamma_{d(avg)}$	15.22[b]
Maximum void ratio	e_{max}	1.23
Minimum void ratio	e_{min}	0.70
Average grain-size (mm)	d_{50}	0.12
Coefficient of uniformity	C_u	1.97
Relative density (%)	D_r	99
Angle of internal friction (°)	ϕ'	42[c]

[a] Provided from tests performed by Unisol Laboratories

[b] Estimated from at least two calibrated boxes placed on the bottom of each container

[c] Measured from direct shear tests

Table 2. Anchor models characteristics.

Model anchor designation	Shaft diameter (d) in mm		Helix diameter (D) in mm		Helix pitch (p) in mm		Helical plate thickness (t_h) in mm		Helix embedment (z_D) in mm		G-level (×g)	d/d_{50}	D/d_{50}	p/D
	Model	Prototype	Model	Prototype	Model	Prototype	Model	Prototype	Model	Prototype				
6H	6.0	100	20.0	330	1.6	26.7	0.5	8.4	120	1980	16.7	50	167	0.080
8H	8.0	100	26.6	330	1.4	17.5	0.8	10.0	160	1980	12.5	67	222	0.053
10H	10.0	100	33.0	330	2.5	25.0	1.8	18.0	198	1980	10.0	83	275	0.076
12H	12.0	100	40.0	330	3.0	25.0	3.0	25.0	240	1980	8.3	100	333	0.075

Table 3. Results of the centrifuge tests

Sand sample	Model	d/d_{50}	D/d_{50}	w/d_{50}	T_f (kN·m)	$T_{avg\text{-}3D}$ (kN·m)	K_t (m^{-1})	$Q_{T\ (0.1D)}$ (kN)	$Q_{T\ (peak)}$ (kN)	$U_{(peak)}$ (mm)	U/D
Container 1	8Ha	67	220	77	-	-	-	54	55	52.9	0.16
	8Hb	67	220	77	-	-	-	51	53	48.3	0.15
	12Ha	100	333	117	-	-	-	57	57	36.6	0.11
	12Hb	100	333	117	-	-	-	56	57	42.7	0.13
Container 2	6Ha	50	167	58	6.9	3.7	17	62	63	46.5	0.14
	6Hb	50	167	58	5.1	2.9	17	49	50	38.5	0.12
	10Ha	83	275	96	6.5	3.8	18	67	67	36.5	0.11
	10Hb	83	275	96	6.8	4.3	16	67	68	40.4	0.12
	12H	100	333	117	8.9	8.9	6	55	55	32.7	0.1
Container 3	6H	50	167	58	6.9	4.3	16	65	67	53	0.16
	8H	67	220	77	7.1	4.7	15	66	69	47.4	0.14
	10H	83	275	96	7.8	5.0	14	67	68	38.3	0.12
	12H	100	333	117	10.2	6.9	10	65	66	38	0.12
				Mean value	7.4	4.9	14	60	61	42.4	
				Standard deviation	1.5	1.9	3.9	7	7	6.6	
				Coefficient of variation	20%	37%	27%	12%	11%	16%	

ANNEX

Annex A. Roughness of 10FH helical pile model

Alicona Imaging GmbH
Dr.-Auner Strasse 21a
A-8074 Raaba/Graz

alicona

Measurement Report

Mesure de profil

image1

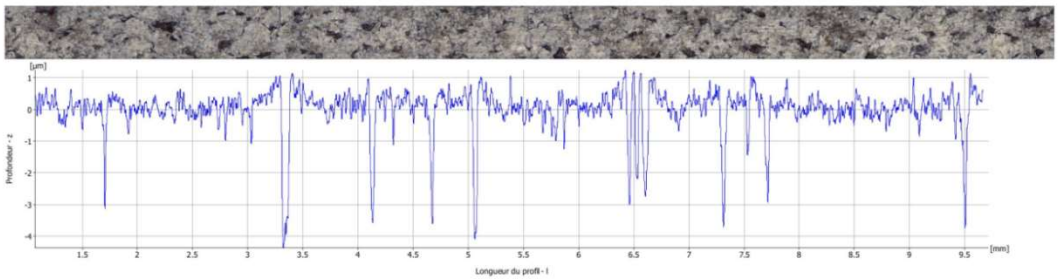

Ra: 400.5542nm
Rq: 703.3010nm
Rz: 4.8702µm

Filtre : passe-haut - profil de rugosité
Lc := 800.0000µm

Measurement performed by Alicona InfiniteFocus, 12/05/2015 10:16:19 1

Alicona Imaging GmbH
Dr.-Auner Strasse 21a
A-8074 Raaba/Graz

alicona

Measurement Report

Mesure de Rugosité de Profil

Paramètres du profil de rugosité

image1

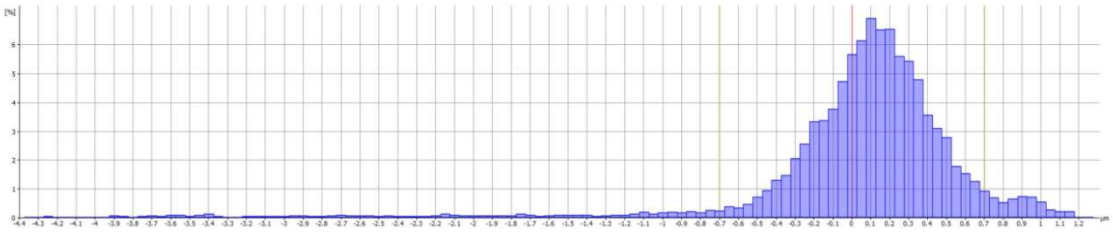

Histrogramme Paramètres de l'histogramme

Nombre de classes : 113
Valeur minimum : -4.3733µm
Valeur Maximum : 1.2767µm
Largeur de classe : 0.0500µm

Statistiques

Nom	Valeur	[u]
Eléments	26216	
Classes	113	
Valeur moyenne	0.0021	µm
Ecart type	0.7033	µm

Paramètres

Nom	Valeur	[u]	Description
Ra	400.5542	nm	moyenne rugosité du profil
Rq	703.3010	nm	moyenne quadratique rugosité du profil
Rt	5.6090	µm	Hauteur maximum de pic à vallée du profil de profil de rugosité
Rz	4.8702	µm	Hauteur moyenne de pic à vallée de profil de rugosité
Rmax	5.5200	µm	Hauteur maximum de pic à vallée du profil de profil de rugosité dans les limites d'une longueur d'évaluation
Rp	1.2358	µm	Hauteur du pic maximal de profil de rugosité
Rv	4.3733	µm	Profondeur de creux maximal du profil de rugosité
Rc	2.7679	µm	Hauteur moyenne des irrégularités de profil de rugosité
Rsm	347.4853	µm	Espacement moyen des irrégularités de profil de rugosité
Rsk	-3.1200		Skewness asymétrie du profil de rugosité
Rku	15.6654		Kurtosis applatissement du profil de rugosité
Rdq	0.0605		Pente de profil de rugosité calculée par la méthode des moindres carrés
Rt/Rz	1.1517		Valeur extrême de rayure / pic du profil de rugosité, (>=1), les valeurs élevées représentent les grandes rayures ou pics extrêmes
l	1.0736	cm	Longueur du profil

Measurement performed by Alicona InfiniteFocus, 12/05/2015 10:17:13 1

Alicona Imaging GmbH
Dr.-Auner Strasse 21a
A-8074 Raaba/Graz

alicona

Measurement Report

Mesure de profil

image2

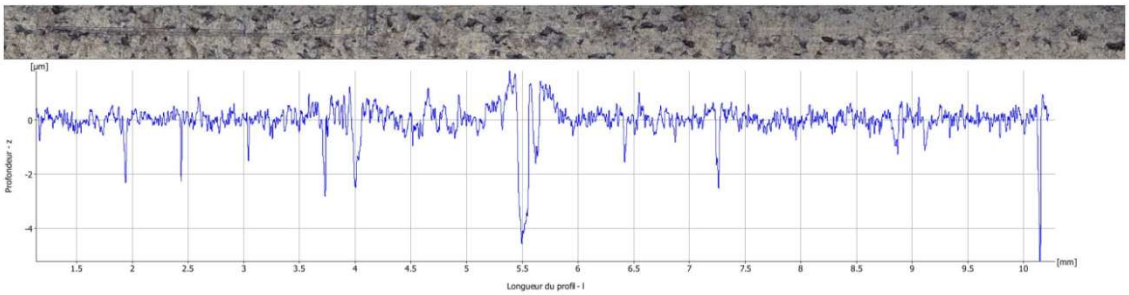

Ra: 343.2504nm
Rq: 617.0060nm
Rz: 4.5877µm

Filtre : passe-haut - profil de rugosité
Lc := 800.0000µm

Alicona Imaging GmbH
Dr.-Auner Strasse 21a
A-8074 Raaba/Graz

alicona

Measurement Report

Mesure de Rugosité de Profil

Paramètres du profil de rugosité

image2

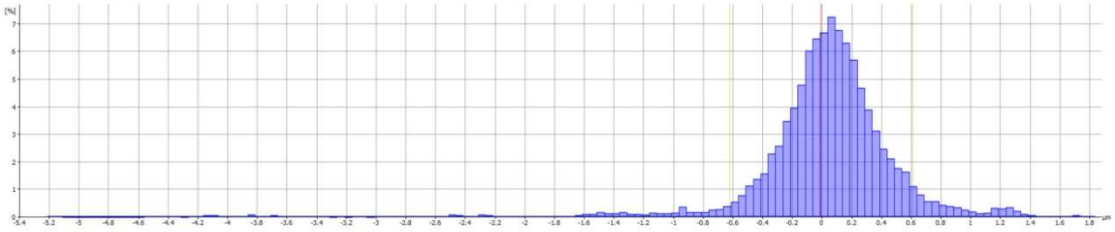

Histrogramme Paramètres de l'histogramme

Nombre de classes : 141
Valeur minimum : -5.2130µm
Valeur Maximum : 1.8370µm
Largeur de classe : 0.0500µm

Statistiques

Nom	Valeur	[u]
Eléments	26216	
Classes	141	
Valeur moyenne	-0.0039	µm
Ecart type	0.6170	µm

Paramètres

Nom	Valeur	[u]	Description
Ra	343.2504	nm	moyenne rugosité du profil
Rq	617.0060	nm	moyenne quadratique rugosité du profil
Rt	7.0172	µm	Hauteur maximum de pic à vallée du profil de profil de rugosité
Rz	4.5877	µm	Hauteur moyenne de pic à vallée de profil de rugosité
Rmax	6.3674	µm	Hauteur maximum de pic à vallée du profil de profil de rugosité dans les limites d'une longueur d'évaluation
Rp	1.8041	µm	Hauteur du pic maximal de profil de rugosité
Rv	5.2130	µm	Profondeur de creux maximal du profil de rugosité
Rc	3.5053	µm	Hauteur moyenne des irrégularités de profil de rugosité
Rsm	823.0910	µm	Espacement moyen des irrégularités de profil de rugosité
Rsk	-3.3561		Skewness asymétrie du profil de rugosité
Rku	22.4912		Kurtosis applatissement du profil de rugosité
Rdq	0.0616		Pente de profil de rugosité calculée par la méthode des moindres carrés
Rt/Rz	1.5296		Valeur extrême de rayure / pic du profil de rugosité, (>=1), les valeurs élevées représentent les grandes rayures ou pics extrêmes
l	1.1362	cm	Longueur du profil

Annex B. Features of the force gauge in the model 10FHi

measurement SPECIALTIES

FICHE TECHNIQUE

TECHNICAL DATA SHEET

MEAS France SO : FA61563

Mesurande : *Measurand :*	Force	
Caractéristiques/*Characteristics*	**Capteur** / *Sensor*	**Electronique** / *Electronics*
Spécifications : *Specifications :*	XF3063-2KN_Rev A	-
Modèle : *Model :*	XF3063-2KN_Rev A	-
N° de série : *Serial number :*	Z140JF	-
Voie : *Channel :*	-	-
Etendue de mesure (EM) : *Range :*	2000 N	-
Alimentation : *Excitation :*	+10 Vdc	-
Déséquilibre initial (typique) : *Offset (typ) :*	+/- 10 mV	-
Valeurs mesurées / *Measured values*		
Signal pour l'EM : *FSO :*	99.96 mV	-
Impédance d'entrée / consommation *Input impedance / Current consumption :*	1396 Ohm	-
Impédance de sortie : *Output impedance :*	455 Ohm	-
Cran de calibration : *Shunt cal :*	-	-
Résistance de calibration : *Calibration resistor :*	-	-
Entre les bornes : *Connected between :*	-	-
Connectique / *Connections*		
+ Alimentation : *+ Excitation :*	Rouge (Red)	-
- Alimentation : *- Excitation :*	Noir (Black)	-
+ Mesure : *+ Signal :*	Vert (Green)	-
- Mesure : *- Signal*	Blanc (White)	-
Blindage : *Shield :*	Tresse (Braid)	-
Observations / *Notes*		

Préconisations d'utilisation et de montage disponibles sur www.meas-spec.com, rubrique « Resources Library / manuals »

Visa QC : QC10 **Date :** 26/01/2015

Ce capteur a été étalonné par rapport à un étalon de travail raccordé aux étalons nationaux. Le certificat d'étalonnage de l'étalon de référence, l'instruction de vérification de l'étalon de travail et la documentation du banc d'étalonnage sont gérés suivant les règles définies par notre système d'assurance Qualité. Cette documentation est disponible pour consultation. Nous certifions que ce produit est conforme aux spécifications de MEAS France.

The above instrument has been calibrated against a working standard which is directly traceable to a National Standard. All data interpreted per Measurement Specialties Instruction Manual unless otherwise indicated. The calibrated values do not exceed the data sheet specifications, value shown is the data sheet, unless purchase order specifies otherwise.

DGQ250

measurement SPECIALTIES

RELEVE DE MESURE

TEST RESULTS

MEAS France SO : FA61563

Mesurande / *Measurand*	Force	
Caractéristiques / *Characteristics*	**Capteur** / ***Sensor***	**Electronique** / ***Electronics***
Modèle / *Model*	XF3063-2KN_Rev A	-
Etendue de mesure (EM) / *Range*	2000 N	-
N° de série / *Serial number*	Z140JF	-
Voie / *Channel*	-	-

Conditions de test / *test conditions*

Température / *Temperature*	23°C ± 3°C
Alimentation / *Excitation*	10 Vdc
EM d'essai / *Full scale test*	2000 N
Sens de l'essai / *Calibration mode*	Traction (Tension)
Equipements / *Equipments*	M434-2kN

Valeurs mesurées / Results

Mesurande (N)	(mV)	( )
0	6.46	-
400	26.07	-
800	45.82	-
1200	65.82	-
1600	86.05	-
2000	106.42	-
1600	86.13	-
1200	65.85	-
800	45.74	-
400	25.89	-
0	6.51	-
Signal pour l'EM / *Full scale output*	99.96 mV	-
Linéarité / *Linearity*	± 0.335 %FSO	-
Hystérésis / *Hysteresis*	± 0.09 %FSO	-

Observations / *Notes*

Cran de calibration / *Shunt cal*	-	-
R. calibration / *Calibration R.*	-	-
Entre les bornes / *Connected between*	-	-

Visa QC : QC10 **Date :** 26/01/2015

Ce capteur a été étalonné par rapport à un étalon de travail raccordé aux étalons nationaux. Le certificat d'étalonnage de l'étalon de référence, l'instruction de vérification de l'étalon de travail et la documentation du banc d'étalonnage sont gérés suivant les règles définies par notre système d'assurance Qualité. Cette documentation est disponible pour consultation.

The above instrument has been calibrated against a working standard which is directly traceable to a National Standard. All data interpreted per Measurement Specialties Instruction Manual unless otherwise indicated.

DGQ251A